NASA CR-54079

RAD-TR-64-42

THIRTY KILOWATT PLASMAJET ROCKET ENGINE DEVELOPMENT

THIRD YEAR DEVELOPMENT PROGRAM

prepared for

NATIONAL AERONAUTICS AND SPACE ADMINISTRATION

Contract NAS 3-2593

FACILITY FORM 602

N65 14402	
(ACCESSION NUMBER)	(THRU)
245	1
(PAGES)	(CODE)
CR-54079	28
(NASA CR OR TMX OR AD NUMBER)	(CATEGORY)

GPO PRICE $ ______

OTS PRICE(S) $ ______

Hard copy (HC) 6.00

Microfiche (MF) 1.50

RESEARCH AND ADVANCED DEVELOPMENT DIVISION
AVCO CORPORATION
Wilmington, Massachusetts

NOTICE

This report was prepared as an account of Government sponsored work. Neither the United States, nor the National Aeronautics and Space Administration (NASA), nor any person acting on behalf of NASA:

A.) Makes any warranty or representation, expressed or implied, with respect to the accuracy, completeness, or usefulness of the information contained in this report, or that the use of any information, apparatus, method, or process disclosed in this report may not infringe privately owned rights; or

B.) Assumes any liabilities with respect to the use of, or for damages resulting from the use of any information, apparatus, method or process disclosed in this report.

As used above, "person acting on behalf of NASA" includes any employee or contractor of NASA, or employee of such contractor, to the extent that such employee or contractor of NASA, or employee of such contractor prepares, disseminates, or provides access to, any information pursuant to his employment or contract with NASA, or his employment with such contractor.

Requests for copies of this report should be referred to

National Aeronautics and Space Administration
Office of Scientific and Technical Information
Attention: AFSS-A
Washington, D.C. 20546

CASE FILE COPY

NASA CR-54079

RAD-TR-64-42

SUMMARY REPORT

THIRTY KILOWATT PLASMAJET ROCKET ENGINE DEVELOPMENT

THIRD YEAR DEVELOPMENT PROGRAM

prepared for

NATIONAL AERONAUTICS AND SPACE ADMINISTRATION

2 July 1964

CONTRACT NAS 3-2593

Technical Management
NASA Lewis Research Center
Cleveland, Ohio
Electric Propulsion Office
Henry Hunczak

RESEARCH AND ADVANCED DEVELOPMENT DIVISION
AVCO CORPORATION
Wilmington, Massachusetts

ABSTRACT

14402

Thirty kilowatt radiation cooled arcjet engines have been tested for 30 days at 1000 second I_{sp}, 10 days at 1300 second I_{sp}, and 120 hours at 1500 second I_{sp}. The measured efficiency range was 40-45 percent. Results of an extensive high temperature bonding study are reported. At the 200 kilowatt power level a specific impulse level of 2000 seconds has been reached with a radiation cooled engine, and 7400 seconds with a liquid cooled engine, also in the 40 percent efficiency range. Probe measurements have been made in the 30 kilowatt engine exhaust, and are compared with predictions of the core flow model. Measurements have been made of the constricted arc voltage gradient.

SUMMARY

This report is the Summary Report for the third year of 30-kilowatt Plasmajet Rocket Engine Development. Engine development was pursued both at the 30-kilowatt level and at power levels ranging to 200 kilowatts.

At the 30-kilowatt power level a series of radiation cooled engines with added regenerative cooling passages has been developed for operation in the specific impulse range of 1000 to 1500 seconds. A 30 day life has been demonstrated at the 1000 second level, while life tests of 10 days and 120 hours have been completed at the 1300 and 1500 second levels, respectively. Difficulty in the life test was experienced only at the 1500 second specific impulse level. Over the range of specific impulse investigated engine efficiencies of 40 to 45 percent were achieved, with no apparent correlation of specific impulse and efficiency.

An extensive investigation has been made of bonding techniques suitable for joining refractory metals (tungsten and molybdenum). A diffusion bonding technique has been developed which appears to be very satisfactory. Brazing has been accomplished with powdered iron and with Cr-V brazing materials. A study has been made of electron beam welding with essentially negative results to this date.

A number of experiments were performed to aid in understanding the details of energy addition and loss processes in the 30-kilowatt arcjet engine. In particular, impact pressure and mass flux profile measurements were made with specially developed probes; measurements were made of the voltage gradient in the constricted arc column; the engine configuration was tested with a number of different gases; and, a partial study was made of arc attachment phenomena. The results of these investigations were compared with the previously proposed 'core flow model' of arc engine operation, with generally satisfactory agreement. Sufficient data have now been accumulated on this program and on earlier programs to demonstrate that the arc discharge occupies only a portion of the constrictor flow area; a portion of the propellant passes through the discharge and achieves extremely high temperatures, while another portion of the propellant flows around the discharge and reaches a much lower temperature. As a result the flow at the throat and at the nozzle exit plane is characterized by strong radial gradients of temperature, composition, density and velocity. In the specific impulse range to 1500 seconds, at least, this appears to be advantageous. The momentum loss introduced by the radial velocity profile appears to be overcome by large improvements in frozen flow efficiency over the one-dimensional case.

Insofar as they have been measured, the characteristics of the arc discharge column are in approximate agreement with the predictions of the Heller-Elenbaas equation. The measurements have been sufficiently sensitive to detect departures

from strict Heller-Elenbaas behavior, but to first order this simple equation is a useful guide to arc behavior.

At the higher power levels two developments have been pursued. A radiation cooled engine has been operated at a specific impulse level of 2000 seconds with an efficiency of nearly 40 percent. A liquid cooled engine has been operated at a specific impulse value of 7400 seconds and an efficiency of 35 percent. The former engine is a scaled up version of the 30 kilowatt series, but the latter departs siginficantly from this design. It is thought that self induced $\vec{j} \times \vec{B}$ forces play a major role in its performance. It appears to be a most attractive electric propulsion device, combining high specific impulse and high thrust density. Further development may result in improved efficiencies.

CONTENTS

I. Introduction 1

II. Engine Development 3

- A. Introduction 3
- B. R-4 Engine 3
    - 1. Configuration 3
    - 2. Construction 7
    - 3. Test Procedures 8
    - 4. Performance 8
    - 5. Discussion 16
    - 6. Conclusions 19
- C. X-1 High Specific Impulse Engine 20
    - 1. Configuration 20
    - 2. Performance 21
    - 3. Conclusions 22
- D. X-2 High Impulse Engine Development 25
    - 1. Introduction 25
    - 2. Engine Design 25
    - 3. Engine Performance 27
    - 4. Analysis of Performance 27
    - 5. Conclusions 34
- E. Engine Materials and Bonding 34
    - 1. Introduction 34
    - 2. Material Choice 35
    - 3. Brazing 35
    - 4. Diffusion Bonding 39
    - 5. Electron Beam Welding 42
- F. Conclusions on Status of Engine Development 52

CONTENTS (Cont'd)

III. Applied Research 60

- A. Introduction 60
- B. Engine Optimization 60
  - 1. Introduction 60
  - 2. Cathode Shape and Gap-Length 61
  - 3. Nozzle Angle 78
- C. Arc Column Studies 84
  - 1. Introduction 84
  - 2. Voltage Gradient Measurements 84
  - 3. Two Fluid Model for the Constricted Arc Column 98
  - 4. Dissociative Non-equilibrium in the Constrictor 101
  - 5. Arc-Engine Voltage in Hydrogen, Nitrogen, Ammonia, and Helium 106
  - 6. Arc Attachment Phenomena in a Supersonic Nozzle 121
- D. Exhaust Jet Diagnostics 125
  - 1. Introduction 125
  - 2. Impact Pressure Profiles 130
  - 3. Mass Flux Profiles 139
  - 4. Velocity and Density Profiles 141
  - 5. Arc Engine Power Balance 145
- E. Summary and Conclusions of Applied Research 151

IV. Program Direction 153

Appendixes

- A. Test System Considerations 156
- B. Arcjet Surface Temperature Measurement Using an Optical Pyrometer 162
- C. Interactions of Current Distributions with the Self Magnetic Field 176

CONTENTS (Concl'd)

Appendixes
(Cont'd)

D. Composite Engine 186
E. Analysis of Two-Fluid Model for the Constricted Arc 188
F. Theory of the Impact Pressure Probe 200
G. Mass Flow Probe 209
H. Nonequilibrium in Nozzle Exhaust 215
I. Effect of Supersonic Heat Addition on Arcjet Engine Performance 219

ILLUSTRATIONS

Figure 1 R-4 Radiation Cooled Arcjet Engine 4

2 Photograph of R-4 Radiation Cooled Arcjet Engine 5

3 Constricted Arcjet Engine Schematic 6

4 Thrust, Efficiency, and Voltage versus Time; Endurance Test of R-4 Mod 1 9

5 Thrust, Efficiency, and Voltage versus Time; Endurance Test of R-4 Mod 2 10

6 Thrust, Efficiency, and Voltage versus Time; Endurance Test of R-4 Mod 3 11

7 X-1 High Specific Impulse Arcjet Engine Schematic 23

8 Efficiency versus Specific Impulse; X-1 High Specific Impulse Engine and R-4 Engines 24

9 X-2 High Specific Impulse Arcjet Engine; Schematic...... 26

10 Thrust versus Product of Chamber Pressure and Throat Area, X-2 Engine................................. 29

11 Chamber Pressure versus Mass Flow Rate, X-2 Engine .. 30

12 Non-Aerodynamic Thrust versus Square of Arc Current, X-2 Engine 33

13 Phase Diagram for Molybdenum and Tungsten 40

14 Partial Phase Diagrams for Molybdenum-Nickel and Tungsten-Nickel 43

15 Nickel Diffusion Bond after 46 hours at the 1500 Second Specific Impulse Level; R-4 Mod 3 (Engine 68), Bond at Upstream End of Nozzle............................ 44

16 Nickel Diffusion Bond after 46 hours at the 1500 Second Specific Impulse Level; R-4 Mod 3 (Engine 68), Bond at Downstream End of Plenum.......................... 44

ILLUSTRATIONS (Cont'd)

17 Gas Injector-Plenum Bond after 46 hours at the 1500 Second Specific Impulse Level; R-4 Mod 3 (Engine 68), TZM Inlet Tube, Iron Braze 45

18 Electron Beam Welding Samples; Photomicrographs of the First Group 47

19 Electron Beam Welding Samples; Photomicrographs of the Second Group 53

20 Efficiency versus Specific Impulse; R-4, X-1, and X-2 Arcjet Engines 59

21 Schematic Arc Engine Operation 63

22 Schematic Drawing Indicating the Geometric Meaning of Gap Setting 64

23 Schematic Drawing showing Four Cathode Shapes......... 65

24 Modification of Engine 41 to Obtain Sharp Corner......... 66

25 Position of Regular Cathode for Four Gap Settings 67

26 Position of Pointed Cathode for Four Gap Settings 68

27 Position of Flat Cathode for Four Gap Settings 69

28 Position of Hollow Cathode for Four Gap Settings......... 70

29 Arc Voltage, Efficiency, and Thrust versus Current; Gap 0.090 inch 75

30 Arc Voltage, Efficiency, and Thrust versus Current; Gap 0.110 inch 76

31 Arc Voltage, Efficiency, and Thrust versus Current; Gap 0.125 inch 77

32 Specific Impulse versus Mass Flow Rate; Gap 0.090 inch 81

33 Specific Impulse versus Mass Flow Rate; Gap 0.110 inch 82

34 Specific Impulse versus Mass Flow Rate; Gap 0.125 inch 83

ILLUSTRATIONS (Cont'd)

35 Measured Thrust versus Nozzle Half Angle for Various Mass Flow Rates 85

36 Efficiency versus Nozzle Half Angle for Various Mass Flow Rates 86

37 Total Arc Voltage versus Nozzle Half Angle for Various Mass Flow Rates 87

38 Schematic Drawing of Voltage Probe Test System 89

39 Photograph of Voltage Probe Measuring System 90

40 Voltage Probe Measurements at the 30 kw Power Level 91

41 Longitudinal Distribution of Local Voltage Gradient According to Stine-Watson Theory 97

42 Schematic Drawing of the Two Fluid Model 100

43 Assumed Constrictor Temperature Profile 105

44 Experimental Arcjet Engine for Observation of the Arc Discharge 107

45 Arc Column in Hydrogen, Ammonia, Nitrogen, and Helium 109

46 Arc Voltage versus Molar Flow Rate, Arc Current 100 amperes 112

47 Arc Voltage versus Molar Flow Rate, Arc Current 200 amperes 113

48 Enthalpy versus Temperature for Hydrogen, Ammonia, Nitrogen, and Helium 117

49 Column Cooling Rate versus Voltage Gradient for the Fully Developed Arc Column in Hydrogen 119

50 Column Energy Flow Rate versus Current for a Fully Developed Hydrogen Arc Column 122

51 Schematic Drawing of Circuit to Obtain Overall AC Characteristics 126

ILLUSTRATIONS (Cont'd)

52 Typical AC Voltage Fluctuation 127

53 Effect of Power Level on AC Voltage Fluctuation 127

54 Effect of Mass Flow Rate on AC Voltage Fluctuation 128

55 Typical Time-Coincident AC Voltage Current Fluctuation 129

56 Front Portion of Experimental Impact Pressure Probe.... 131

57 Front View of Probe Insertion Unit 133

58 Rear View of Probe Insertion Unit 134

59 Closeup of Microswitch for Gilman Slide Drive Assembly 135

60 Impact Pressure Probe with Supporting Structure 136

61 Impact Pressure Profiles at 20 and 25 kilowatts 138

62 Mass Flux Profiles at 20 and 25 kilowatts 140

63 Derived Velocity Profiles at 20 and 25 kilowatts.......... 143

64 Derived Density Profiles at 20 and 25 kilowatts 144

65 Block Representation of Power Distribution in Arcjet Engine 147

A-1 Schematic of Engine Test System 159

A-2 Cutaway Drawing of Liquid Cooled Thrust Stand 160

A-3 Photograph of Liquid Cooled Thrust Stand 161

B-1 Schematic Drawing of System for Engine Temperature Measurement.. 165

B-2 Image Displacement by Glass Plate 165

B-3 Calibration Curves for Brightness Temperature 174

C-1 Force Resulting from Interaction Between a Current and its Own Magnetic Field in an Arcjet Engine Configuration....................................... 181

ILLUSTRATIONS (Cont'd)

C-2 Force between Current and Self Magnetic Field, Purely Radial Discharge 181

C-3 Pinch Force, Uniform Axial Discharge 182

C-4 Pinch Force, Axial Sheet Discharge 182

C-5 Pinch Force Including Effect at the Anode 182

D-1 Thirty Kilowatt Composite Arc Assembly 187

E-1 K/C_p versus Temperature for Hydrogen 194

E-2 Electrical Conductivity versus Enthalpy for Hydrogen 195

E-3 Arc Voltage versus Axial Position as Given by the Two Fluid Model 196

E-4 Core Radius versus Axial Position as Given by the Two Fluid Model 198

E-5 Pressure Distribution in the Constrictor as Given by the Two Fluid Model 199

F-1 Representation of Impact Pressure Probe in Supersonic Stream 202

F-2 Plot of $P_{02}/ \ _1 u_1^2$ versus M_1 203

F-3 Geometrical Considerations in Design of Impact Pressure Probe 207

G-1 Schematic Drawing of Mass Flux Probe and Associated Equipment 213

G-2 Mass Flux Probe Tip Geometries 214

G-3 Mass Flux Probe Tip Geometries 214

G-4 Mass Flux Probe Tip Geometries 214

ILLUSTRATIONS (Concl'd)

I-1 Arc Engine Configuration 220

I-2 Mach No. versus Axial Position, as a Function of Heating in the Supersonic Nozzle 227

I-3 Exit Velocity and Specific Impulse Ratios As a Function of Heating of the Supersonic Nozzle 228

TABLES

Table 1 Dimensions and Bonding of R-4 Series, 30 KW Arcjet Engines 7

2 Performance of R-4 Series 30 KW Arcjet Engines During Endurance Tests 12

3 Dimensions of the X-1 High Specific Impulse Engine 21

4 Performance of the X-1 High Specific Impulse Arcjet Engine 22

5 Performance of X-2 Engine 28

5A Performance of X-2 Engine 32

6 Leaktight Alloys After Brazing Tungsten and Molybdenum at 50-PSI Gas Pressure 36

7 Results of Remelt Temperature Investigation 38

8 Welding History of Second Group of Electron Beam Welding Samples 50

9 Operation and Performance Characteristics for the Regular Cathods with Different Gap Settings 71

10 Operation and Performance Characteristics for the Pointed Cathode with Different Gap Settings 72

11 Operation and Performance Characteristics for the Flat Cathode with Different Gap Settings 73

12 Operation and Performance Characteristics for the Hollow Cathode with Different Gap Settings 74

13 Operation and Performance Characteristics for the 0.090 Inch Radius and Sharp Corner Configuration with a Constant Gap Setting of 0.125 Inch 79

14 Area Ratio Corresponding to Nozzle Half-Angle 80

TABLES (Concl'd)

Table 15 Variation of Heller-Elenbaas Solution with Transport Properties 95

16 Engine Operating Conditions for Figure 45.......... 108

17 Estimated Voltage Gradients for Ammonia, Hydrogen, Nitrogen and Helium 114

18 Calculated Column Cooling Rates for Arc Columns in Hydrogen, Nitrogen, Ammonia, and Helium for Currents of 100 and 200 Amperes and Select Voltage Gradients 115

19 Thermal Conductivities of Ammonia, Hydrogen, Nitrogen, and Helium at one Atmosphere 116

20 Operating Conditions Used for the Diagnostic Study of Exhaust Jet 130

21 Comparison of Measured Mass Flow Rate and Integration of Mass Flux Profile 139

22 Experimentally Measured Kinetic Power 148

23 Incomplete Expansion Power Loss 150

I. INTRODUCTION

This is the Summary Report on the Third Year Development Program on Thirty Kilowatt Plasmajet Rocket Engine Development. It covers the period 1 June 1963 through 31 May 1964. At the conclusion of the Second Year Development Program[1] a lifetime of at least 723 hours had been demonstrated for a 30-kilowatt arcjet engine operated at a specific impulse of 1000 seconds, and a phenomenological model of arc engine operation (the 'core flow' model) had been proposed. The objectives of the Third Year Development Program included

i) further demonstration of arcjet engine life at specific impulse values up to 1500 seconds at the 30-kilowatt power level, and improved efficiency,

ii) investigations of materials and bonding processes to secure improved engine life at high temperatures,

iii) diagnostic measurements which could be compared with the predictions of the core flow model, and,

iv) attempts to obtain significantly higher specific impulse values with arcjet engines not restricted to the 30-kilowatt power level.

Items (i), (ii), and (iv) above are discussed in section II of this report (Engine Development): endurance runs of 250 hours at the 1300 second specific impulse level and 120 hours at the 1500 second specific impulse level are described; results of investigations of brazing, electron beam welding, and diffusion bonding are presented; and, two high power high specific impulse arcjet engines which have been developed are described along with the performance which has been obtained so far from each. Item (iii) is discussed in section III of this report (Applied Research); the results of a program of aerodynamic probing of the engine exhaust are given and compared with core flow model predictions. A number of additional experiments which elucidate in some measure the mechanisms of energy addition and loss in the 30-kilowatt thermal arcjet engine are reported. These include investigations of the anode attachment phenomena, engine operation in different gases, arc column voltage gradient measurements, and systematic variations of the engine configuration.

The conclusions which may be drawn as a result of the work reported here are that

i) a radiation-regeneration cooled 30-kilowatt arcjet engine can be run for periods of the order of hundreds of hours in the specific impulse range of 1000 to nearly 1500 seconds, with an efficiency of approximately 40-45 percent;

ii) a diffusion bonding technique appears to offer advantages over conventional brazing and electron beam welding for high temperature bonding of refractory metals (tungsten and molybdenum);

iii) the core flow model describes to a first order approximation the effects of radial non-uniformities on the propellant flow in the 30-kilowatt engine; and,

iv) at high currents the thermal arcjet engine benefits from certain $\vec{j} \times \vec{B}$ forces which greatly enhance its specific impulse capability. As a result, the arcjet engine may prove effective at specific impulse values in the range 3,000 to 10,000 seconds which had until recently been thought beyond its capabilities.

The participants in this research have been, along with their fields of principal contribution: Dr. W. Bade, Dr. J. Yos, Mr. Y. Chiu, Interaction of the Flow with the Discharge, and Energy Transfer from the Arc Column; Dr. L. A. Cass, Mr. A. Mironer, Mr. K. Clark, Arcjet Engine Aerodynamics and Probing of the Exhaust; Dr. A. Tuchman, Anode Phenomena; Mr. J. T. Smith, Mr. R. Kane, Engine Materials and Bonding; Mr. K. Coughlin, Mr. R. Reynolds, Engine Design; Mr. G. Enos, Mr. J. Malenda, Arcjet Engine Performance Testing; Mr. J. Connors, Project Engineer; Dr. S. Bennett, Assistant Project Director; and, Dr. R. R. John, Project Director. The Project Manager for Lewis Research Center was Mr. Henry Hunczak.

The following papers were generated during the past year as a result of work performed under this contract:

"Arcjet Engine Performance - Experiment and Theory," AIAA Journal, Vol. 1, pp 2517-2525, 1963, by R. R. John, S. Bennett, and J. F. Connors.

"Theory and Experiment of a Gas Stabilized Constricted Arc," Proceedings of the I.E.E.E. Professional Technical Group on Nuclear Sciences, Vol. NS-11, pp 109-118, 1964, by S. Bennett and J. F. Connors.

Under a separate task of this contract Avco RAD personnel traveled to Lewis Research Center to aid in installing and testing several 30-kilowatt arcjet engines of the types developed under this program and earlier programs.

II. ENGINE DEVELOPMENT

A. INTRODUCTION

This section of the report summarizes activities concerned with development of arcjet engines, as distinct from research studies which are summarized in section III. Development activities during this contract period were pursued for three different engine configurations. These are (i) the 30-kilowatt R-4 series of radiation-regeneration cooled engines, (ii) the 200-kilowatt X-1 high specific impulse radiation cooled engine, and (iii) the 70-250 kilowatt X-2 liquid cooled high specific impulse engine. Several endurance tests were made of the R-4 engine series. Performance data are presented for each engine configuration. A discussion is given of the results of the engine bonding program. A description of the engine test system and estimates of the experimental errors associated with each measurement are given in appendix A.

B. R-4 SERIES OF 30-KILOWATT ARCJET ENGINES

1. Configuration

The general configuration of the R-4 series of 30-kilowatt arcjet engines is sketched in figure 1. A photograph is presented as figure 2. The cathode is rod shaped with a rounded cone tip and made of 2 percent thoriated tungsten. The nozzle-anode is also 2 percent thoriated tungsten. The plenum section is molybdenum. The insulators are boron nitride. The main joint is between the nozzle-anode and the plenum section; a secondary joint is between the molybdenum plenum and the gas supply tube. The joints are required to be gas-tight; a full discussion of the bonding procedures is given below, in the paragraph on engine bonding.

Propellant enters the plenum section through the gas supply tube and then passes through a set of channels cut through into the nozzle-anode before returning to the plenum section. From this point the propellant is introduced through four sonic orifices into the region around the cathode, swirls down over the cathode tip through the constrictor, and then out through the supersonic nozzle. The purpose of introducing the propellant flow into the body of the nozzle is twofold; first, the propellant absorbs some heat which might otherwise be radiated from the engine surface, and, second, the engine temperatures near the propellant flow paths are reduced. The latter effects can be important in terms of the lifetime of the brazed joint between the plenum and the nozzle-anode.

The major dimensions of the R-4 series of 30-kilowatt engines are defined in the sketch of figure 3, and listed for the different models of this series in table 1 below.

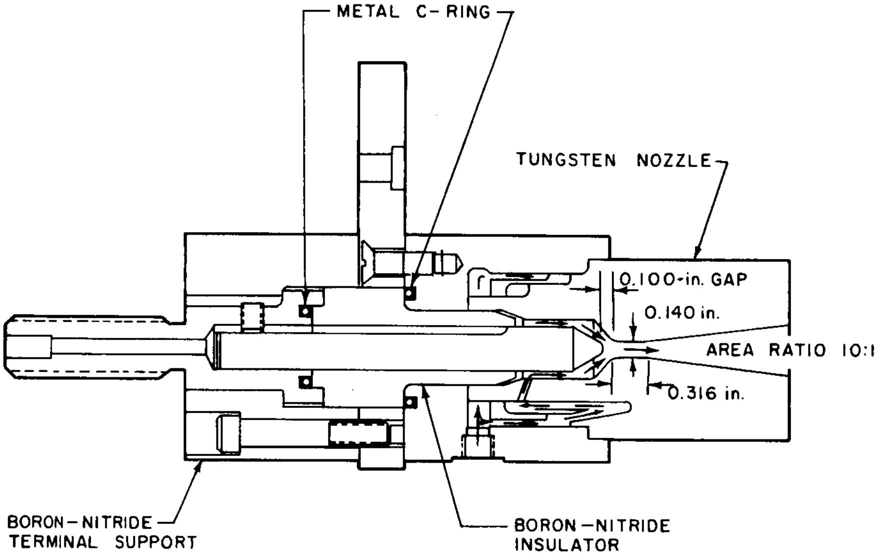
METAL C-RING
TUNGSTEN NOZZLE
0.100-in. GAP
0.140 in.
AREA RATIO 10:1
0.316 in.
BORON-NITRIDE TERMINAL SUPPORT
BORON-NITRIDE INSULATOR

63-10708

Figure 1 R-4 RADIATION COOLED ARCJET ENGINE

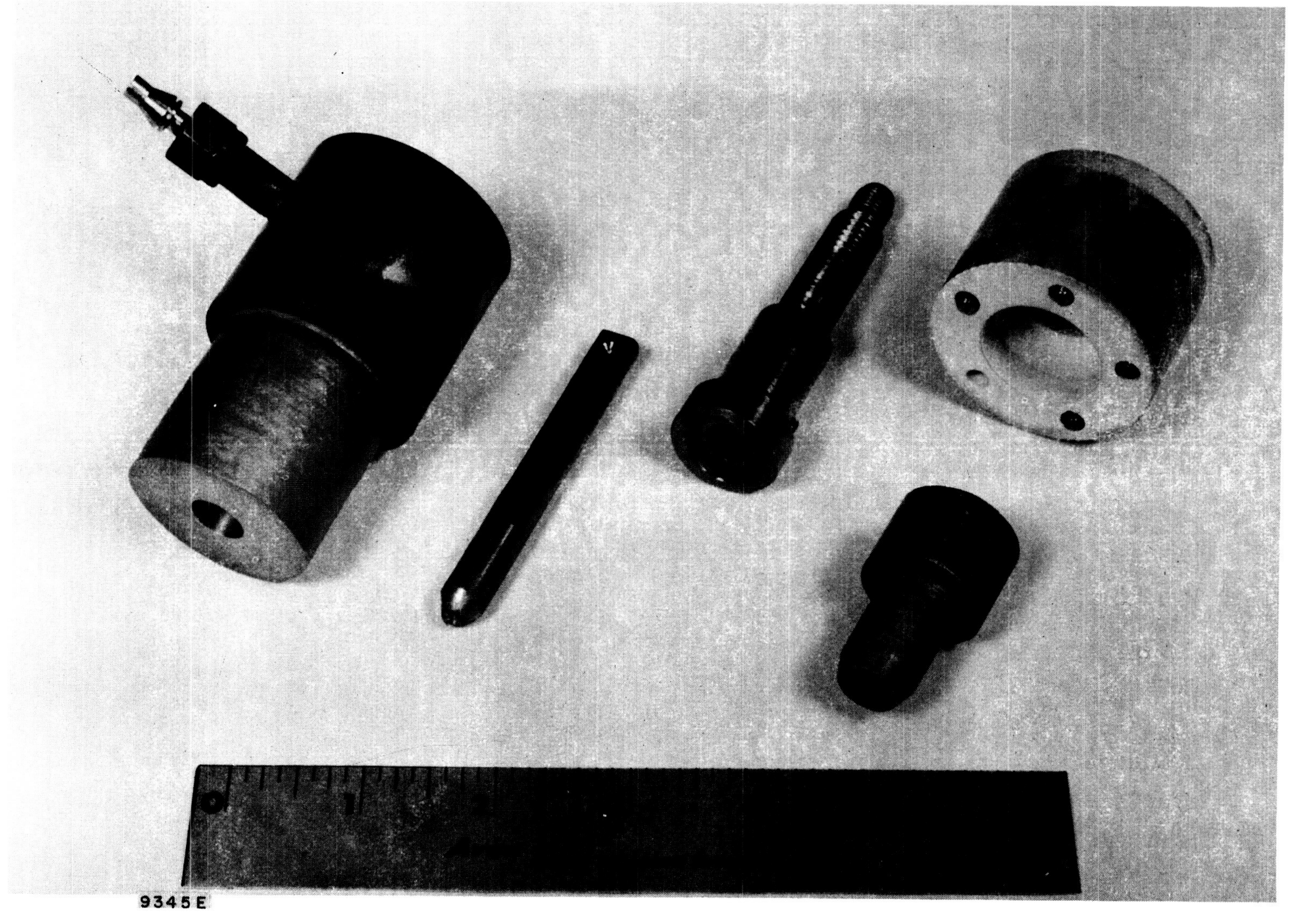

Figure 2 PHOTOGRAPH OF R-4 RADIATION COOLED ARCJET ENGINE

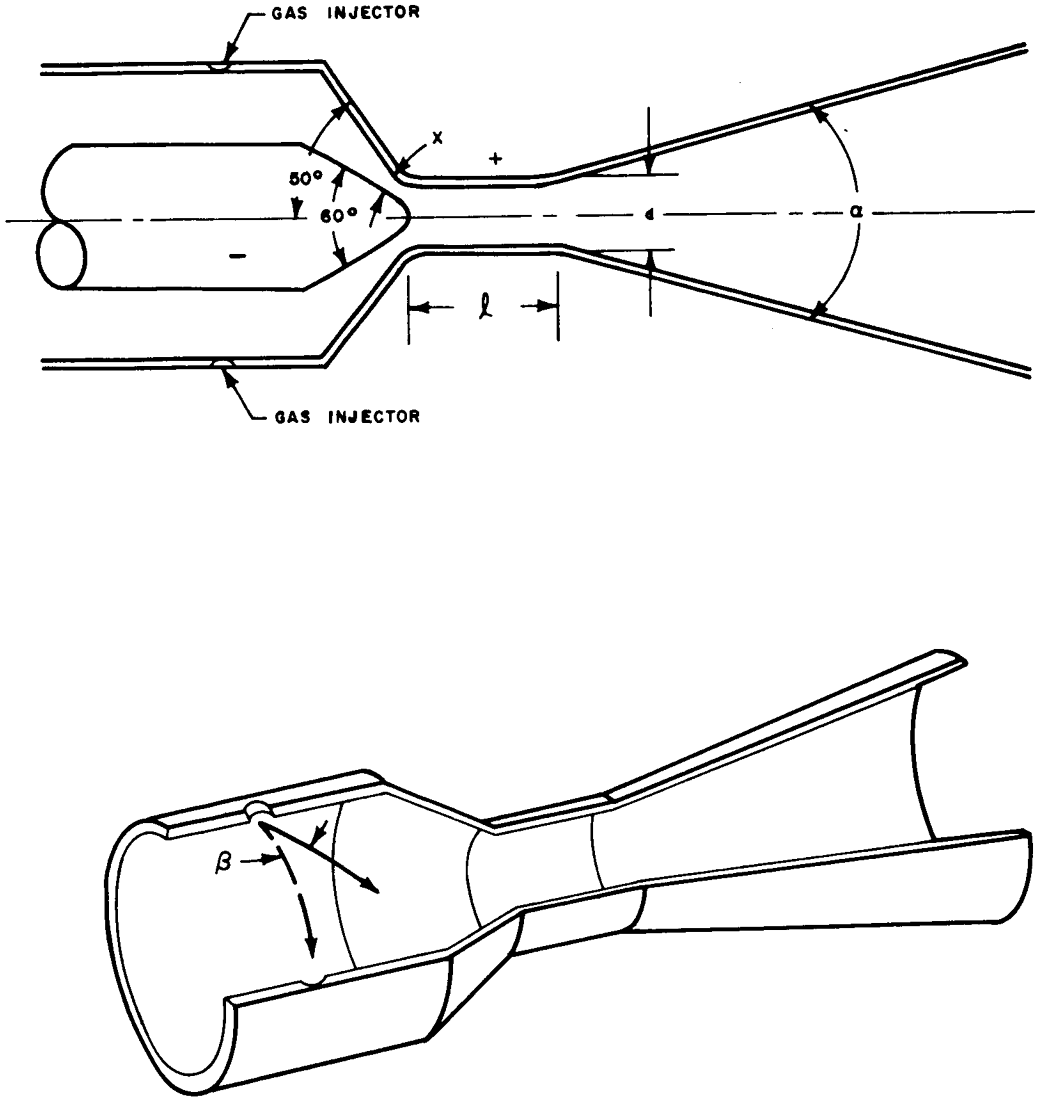
GAS INJECTOR
x
+
50°
60°
−
ℓ
d
α
GAS INJECTOR
β

64-14226

Figure 3 CONSTRICTED ARCJET ENGINE SCHEMATIC

TABLE 1

DIMENSIONS AND BONDING OF R-4 SERIES 30 Kw ARCJET ENGINES

	R-4 Mod 1	R-4 Mod 2	R-4 Mod 3
Constrictor Length	0.889 cm	0.804 cm	0.610 cm
Constrictor Diam.	0.444 cm	0.356 cm	0.305 cm
Length/Diam.	2	2.26	2
Nozzle half angle	7°	7°	7°
Exit Diameter	1.15 cm	1.075 cm	1.065 cm
Area Ratio	6.7	9.2	12.2
Injection Angle	60°	60°	60°
No. Regen Passages	9	9	9
Gas Inlet Tube Material	Steel	Steel	TZM
*Gas Inlet Tube Braze	50% Pt- 50% Cu	50% Pt- 50% Cu	Iron
*Nozzle-Plenum Bond	Iron	75% Cr- 25% V	Nickel Diffusion Bond

*See Section II E

2. Construction

The materials used in the R-4 series engines are thoriated tungsten for the anode-nozzle and cathode, molybdenum for the plenum section, boron nitride for all insulators, and either carbon steel or TZM alloy (an alloy of titanium, zirconium, and molybdenum) for the gas injector tube. TZM alloy was used in later models of the R-4 series, including the R-4 Mod 3, for its superior high temperature properties.

For the most part these materials permit normal machining techniques, with the exception of producing deep, small diameter holes in the thoriated tungsten anode-nozzle; these holes are required for the inlet orifices and for the regenerative cooling passages. Such holes are readily produced by starting with a drill and finishing with an Elox machine.

The two high temperature seals (between the nozzle-anode and the molybdenum plenum, and between the gas inlet tube and the molybdenum plenum) are either brazed or diffusion bonded (see section II-E). Lower temperature seals at the upstream end of the engine are made with stainless steel C-rings.

3. Test Procedures

Engine test procedures are discussed in detail in appendix A. Briefly, the engine is suspended from a liquid-cooled direct force measuring thrust stand, within an evacuated test cell. The natural frequency of the thrust stand is of the order of 2 cycles per second. Calibration is static and is accomplished with standard pully and weight techniques. Thrust is sensed as a displacement of the engine platform by a linear differential transformer (Sanborn 581-251) and recorded on a Sanborn recorder. Mass flow rate is measured with calibrated rotameter type flowmeters (Fisher-Porter Co.). Power is calculated from measurements made with D.C. precision voltmeters and ammeters. Chamber pressure is measured with a Bourdon Gauge and manually recorded. Engine surface temperatures are measured with an optical pyrometer, and manually recorded (details of pyrometer calibration are given in appendix B.). From the measured values of input power, thrust, and mass flow rate, the specific impulse and efficiency are calculated. Engine surface temperatures along with the known engine surface area allow estimates of engine radiation to be made.

In certain special tests measurements other than those listed above are made, generally for research purposes. However, the measurements indicated comprise the minimum set for performance tests.

4. Performance

The R-4 Mods 2 and 3 engines were developed under this Third Year Development Program, while the R-4 Mod 1 was developed during the previous year's effort.[1] Performance for each of the R-4 series engines is summarized in table 2 below. The entries in table 2 represent average or steady state values of the recorded quantities measured during endurance tests of each of the engines. Figures 4, 5, and 6 show the detailed variation of thrust, efficiency, and voltage during the endurance tests; figure 4 refers to the 723 hour run of the R-4 Mod 1, figure 5 to the 250 hour run of the R-4 Mod 2, and figure 6 to the 120 hour run of the R-4 Mod 3.

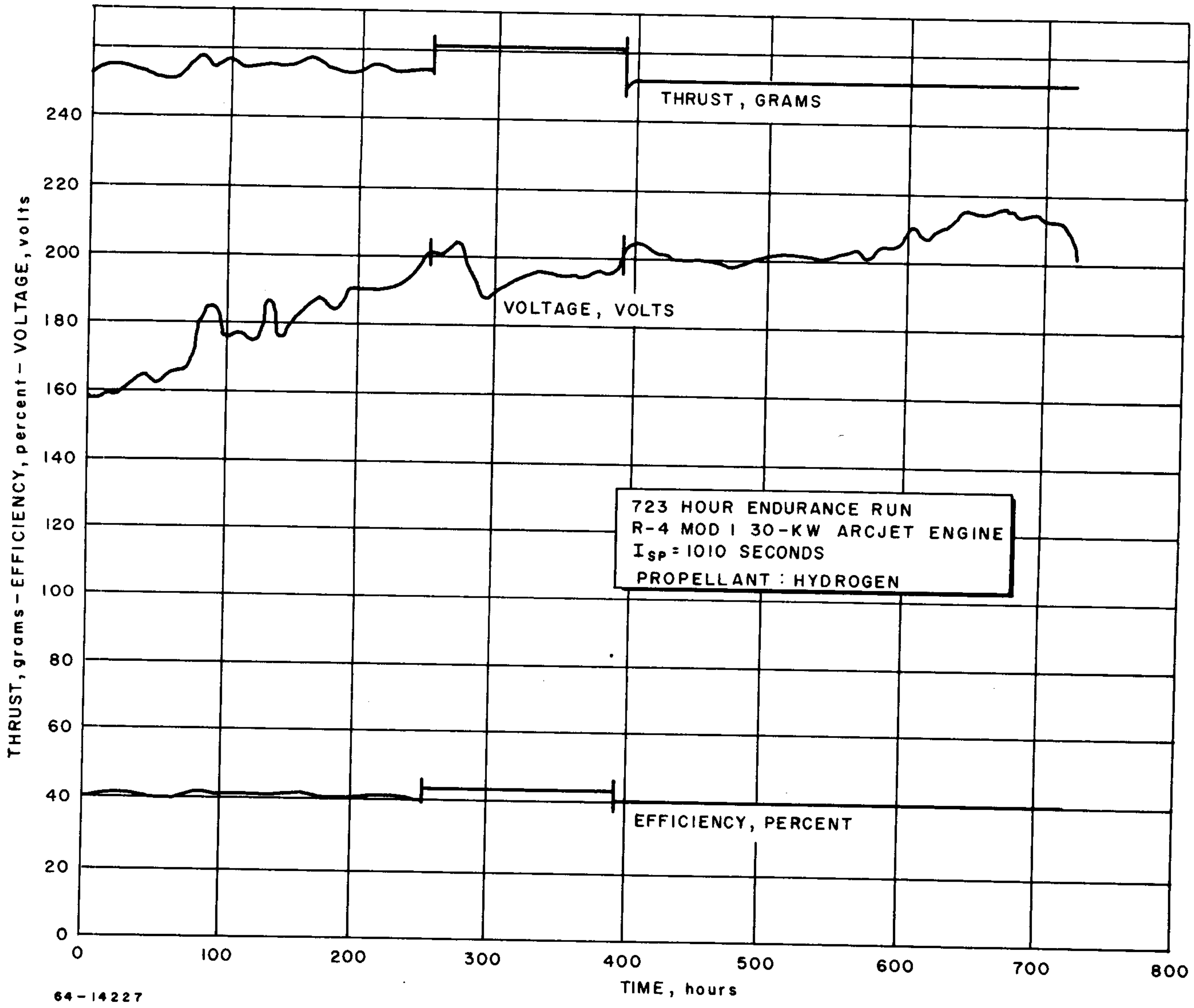

Figure 4 THRUST, EFFICIENCY, AND VOLTAGE VERSUS TIME; ENDURANCE TEST OF R-4 MOD 1

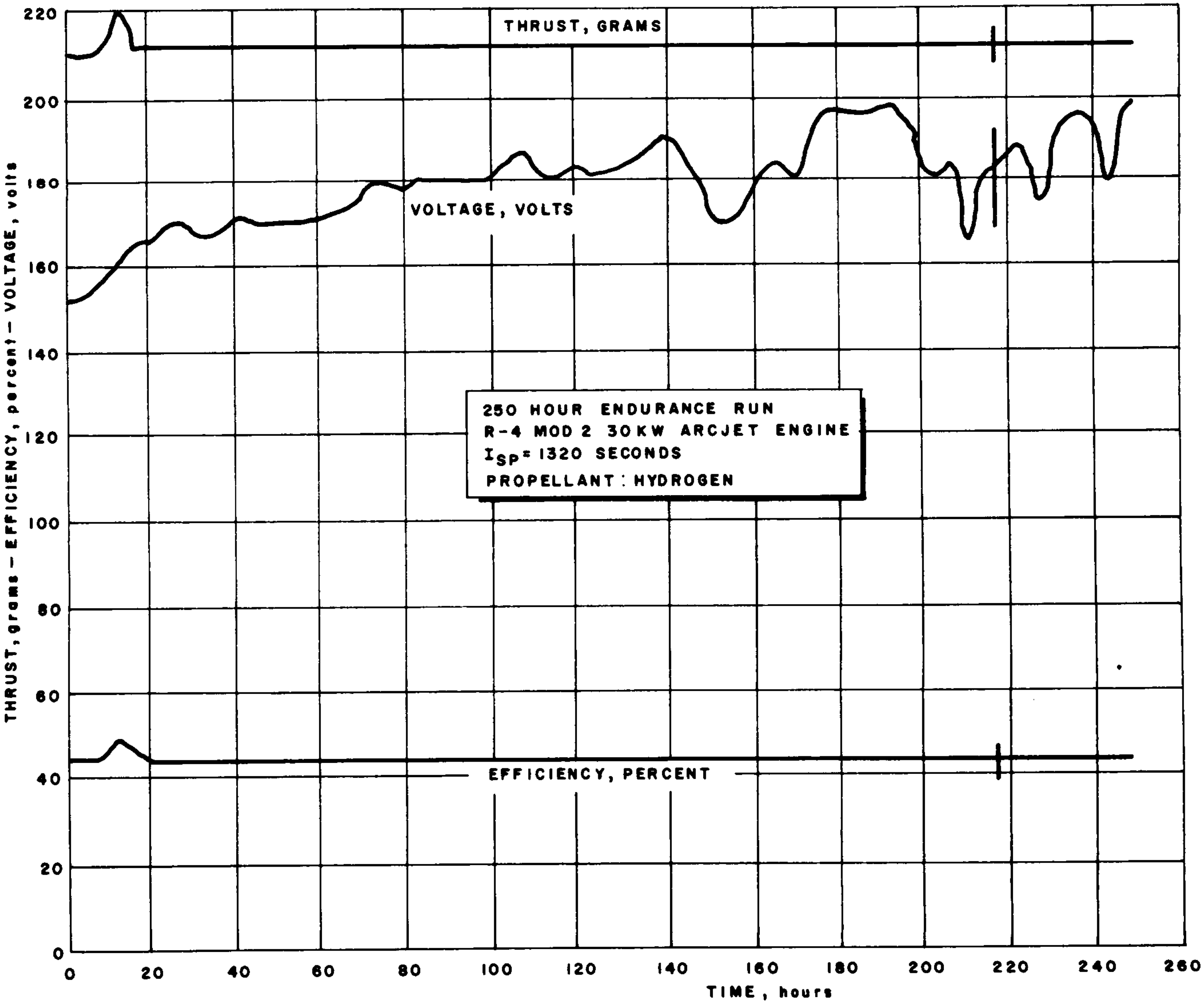

64-14228

Figure 5 THRUST, EFFICIENCY, AND VOLTAGE VERSUST TIME; ENDURANCE TEST OF R-4 MOD 2

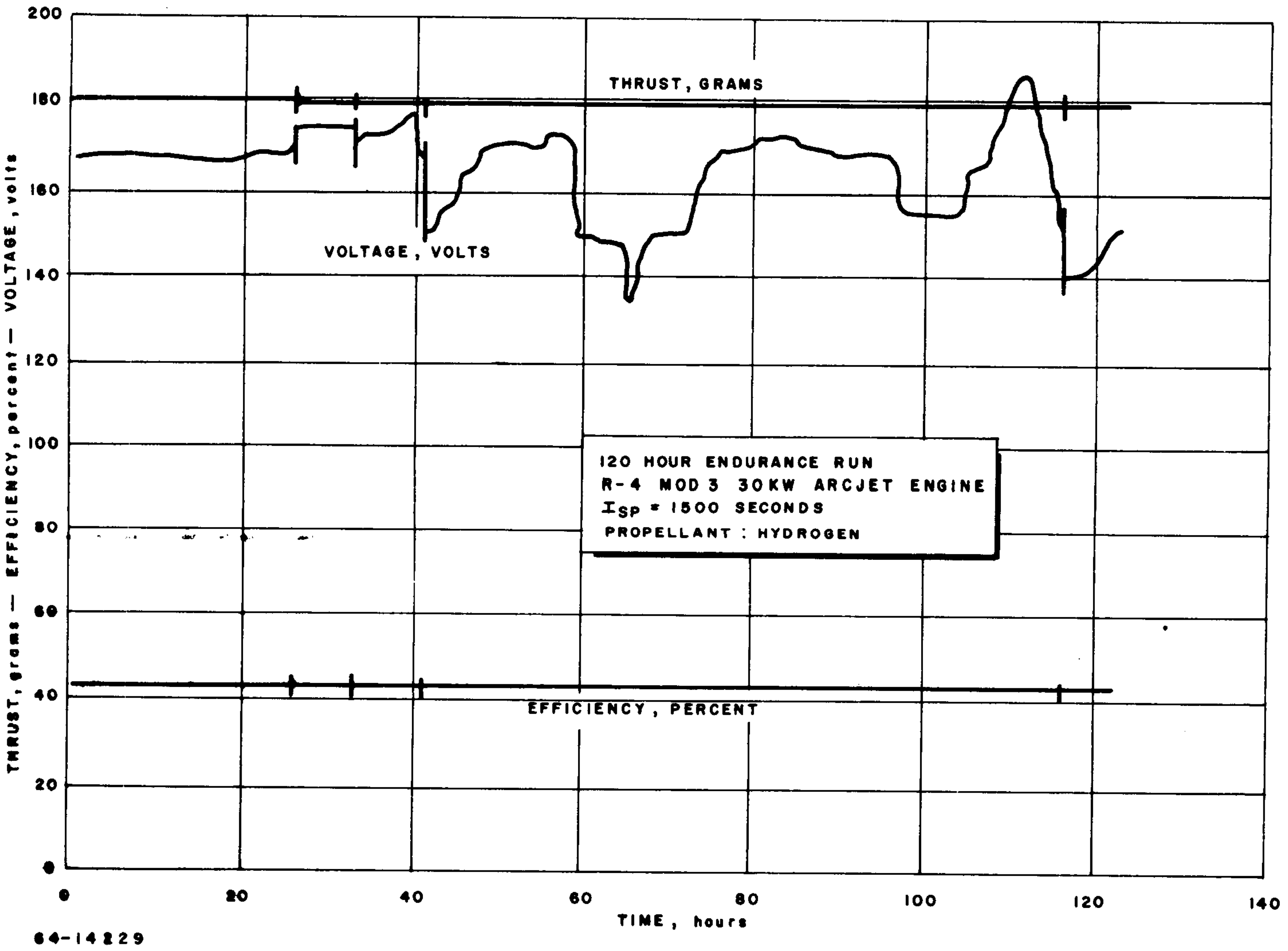

Figure 6 THRUST, EFFICIENCY, AND VOLTAGE VERSUS TIME; ENDURANCE TEST OF R-4 MOD 3

TABLE 2

PERFORMANCE OF R-4 SERIES 30 Kw ARCJET ENGINES DURING ENDURANCE TESTS

	R-4 Mod 1	R-4 Mod 2	R-4 Mod 3
Test Length	723 Hours	250 Hours	120 Hours
Thrust	252 grams	211 grams	180 grams
Mass Flow Rate	0. 25 gm/sec	0. 16 gm/sec	0. 12 gm/sec
Specific Impulse	1010 sec	1320 sec	1500 sec
Efficiency	40. 7%	44.6%	43. 2%
Voltage	200 volts	198 volts	170
Current	150 amperes	151 amperes	177
Power	30 kw	30 kw	30 kw
Weight Loss			
Cathode		0.6 gm	0. 3 gm
Anode		0	10.6 gm
Total		0.6 gm	10. 9 gm
Peak Nozzle Temp.	1850°K	2200°K	2280°K
Braze Temperature	1200°K	1870°K	1940°K

a. Engine Lifetime

Details of the 723 hour endurance run of the R-4 Mod 1 engine were reported in reference 1. The 250 hour endurance run of the R-4 Mod 2 engine took place in July, 1963. The test commenced at approximately 1300, 9 July, and the engine was brought to full power and a specific impulse in excess of 1300 seconds by 1330. The test continued uninterrupted until 1550, 18 July, when a local rainstorm caused interruption of power into the laboratory. The engine was restarted after power became available, at 1636, 18 July, and the test continued until it was voluntarily terminated at approximately 0010, 20 July. During the power interruption of 18 July no servicing was performed on the engine or the associated test equipment.

Considerably more difficulty was experienced with the 120 hour test of the R-4 Mod 3 engine at 1500 second specific impulse. A total of three endurance tests at this specific impulse level were attempted, in May, 1964, with three different engines. The entries in Tables 1 and 2 describe the engine used for the third test, which was the most successful. The first test was terminated after 46 hours of operation at a specific impulse level over 1500 seconds; a power interruption occurred at the 27th hour, owing to a power failure outside the plant, necessitating a restart. During the last 10 hours of the test, operation was erratic in terms of arc current and voltage and the visual appearance of the exhaust jet. Termination came about as a result of a current surge which caused a gouge in the nozzle just downstream of the throat.

It was thought that the power failure at the 27th hour might have caused engine damage resulting in the failure after 46 hours. Therefore, another test was instituted directly, using an engine only slightly different from that used in the first test, and without modification of the test system. The engine used in the second test had been used in the earlier development program for the Mod 3 engine, and had suffered minor damage in the constrictor and nozzle. The constrictor and nozzle were remachined to remove the slight gouges, with the result that the constrictor diameter was increased from 0.305 cm to 0.318 cm, the constrictor length from 0.610 cm to 0.635 cm, and the nozzle half angle from 7° to 7.5°. It was thought that these minor variations in configuration would not greatly effect engine performance, and, in fact, the operating characteristics of this modified engine were only negligibly different from those of a standard Mod 3 engine, with the exception that the voltage tended to be low by about 15 percent.

The second test lasted only 33 hours at a specific impulse level in excess of 1500 seconds. After 24 hours a current surge caused the arc engine to be shut down automatically by a current limiting circuit which is part of the test system, and after restart the operating voltage fell slowly but steadily. To maintain the 30-kw level the current was increased until a point was reached where burnout was believed to be imminent and the run was terminated. At this time the current was in excess of 250 amperes, and no further increases could be obtained without visible erosion of the electrodes.

Attention was then focussed on the arc engine power supply. It was observed in both attempted long runs at the 1500 second specific impulse level that the power delivered to the arc engine tended to fluctuate. Fluctuations resulting in a smaller current resulted in momentary operation at low power, and could be corrected by the operation without damage. However, fluctuations tending to increase the current and the operating power level, even if momentary, could cause damage to the anode, eventual gouging, and could result in an abort of the test. The power supply was an unmodified Miller welding rectifier. At the higher mass flow rates characteristic of lower specific impulse operation the engine current is generally below 175 amperes for 30 kilowatt operation, and fluctuations need not be harmful if they are not too large. However, when the average value of the current is in excess of 175 amperes, fluctuations become more important.

The power supply was modified to improve regulation, so that a variation of the line voltage would be damped out at the power supply output terminals. Sufficient regulation was supplied to the Miller welding units so that when they were driving an arcjet engine at the 30 kilowatt level, a 40 kilowatt extra load could be dropped on and off the power supply input without causing appreciable surges in the arc engine current or voltage.

With this improvement of the power supply accomplished, a third attempt at a long run at the 1500 second specific impulse level was initiated. This run is summarized in Table 2 and in figure 6, and the engine data are given in table 1. The configuration is the standard Mod 3.

During this third attempt the engine performed more satisfactorily, but the test system behavior was unsatisfactory. There were two major difficulties with the test system. First, an intermittent short to ground developed at one of the mercury pots where electrical connection is made to the engine. This short caused excessive current to be drawn from the power supply (although not through the engine), and tended to activate the automatic engine shutdown controls. Second, the vacuum pump broke away from its attachment to the concrete floor; various methods were employed to stabilize the pump without interrupting the operation but eventually the run had to be terminated while the pump mounting was repaired. Visual inspection of the engine during this shutdown revealed a crack in the nozzle, and the run was not reinitiated. No information is available to determine exactly when the crack occurred, but it is conceivable that if the engine did not have to undergo so many restarts because of support system failures it could have run much longer.

The first shutdown owing to the partial short at the mercury pot came after 26 hours of operation; the second 8 hours later; the third after an additional 8 hours; at this time the source of the intermittent short was discovered, and several hours were used to repair it; there followed 75 hours of uninterrupted operation, ending in a current surge which again automatically shut down the engine; after restarting an additional 5 hours was logged before the pump required a shutdown.

b. Engine Radiation

An approximate value for the energy radiated from the R-4 series engines can be obtained by assuming that all the radiation is from the nozzle-anode (downstream of the braze to the molybdenum plenum) and that the entire nozzle anode is at the temperature of the downstream end. The first assumption tends to underestimate the radiation, since there is radiation also from the plenum section and even the upstream end of the engine, but the second assumption tends to overestimate the radiation and to cancel the effect of the first assumption. Comparisons of the estimated radiation calculated in this way have been made with estimates calculated from detailed temperature distributions, with good agreement.

The surface area of that portion of the engine assumed to radiate is approximately 60 cm^2. Using an emissivity [2] of 0.3, the radiated power for the Mod 1 engine at a temperature of 1850°K is approximately 1.2 kw; for the Mod 3 engine at 2280°K, the radiation is 2.8 kw. This suggests that the arc heater efficiency is measurably higher at a mass flow rate of 0.25 gm/sec than at 0.16 or 0.12 gm/sec, but that the difference at the latter two values of mass flow rate is small. In each case the arc heater efficiency is in excess of 90 percent.

c. Chamber Pressure

In each of the R-series engines a chamber pressure tap is constructed upstream of the cathode. These taps are valuable in diagnosing engine behavior, particularly with regard to leaks in propellant flow path. It is also tempting to use the measured chamber pressure values to evaluate nozzle performance, and in earlier work[1] engine thrust coefficients have been calculated as the ratio of thrust to the product of chamber pressure and throat area. It is now believed that the chamber pressure measurements are only roughly indicative of engine pressure levels, owing to the vorticity of the flow and the effects of the regenerative cooling passages 'upstream' of the chamber. The thrust coefficients calculated for the R-4 Mods 1, 2 and 3 engines from the thrust data of table 2 and the measured chamber pressures of approximately 8 PSIG in each case vary from approximately 1.0 for the Mod 1 engine to 1.5 for the Mod 2 and 1.8 for the Mod 3 engines. It does not seem consistent with the relatively small changes in nozzle geometry from one engine to the next that there should be such large changes in the thrust coefficient. The nozzle lengths are all nearly the same, the opening angles are exactly the same, and the area ratios vary by less than a factor of two in a regime of area ratio (around 10) where nozzle performance is relatively insensitive to this parameter.

Within one engine model the chamber pressure is sensitive to the mass flow rate and to the power when these parameters are varied. In this sense the thrust coefficient is meaningful. However, in comparing two different models the geometry near the cathode tip is changed slightly, and it is thought that the change in recorded pressure when the geometry is changed may obscure any change in nozzle effectiveness.

5. Discussion

It has been previously proposed[1] that the R-series 30-Kilowatt arcjet engines operate in the core flow mode. In this mode of engine operation the arc discharge extends from the cathode tip through the constrictor section, terminating either diffusely or in a moving spot in the anode-nozzle. The cross sectional area of the discharge is small compared with the cross sectional area of the constrictor section, and the column is stabilized in the center of the constrictor by the gas flow which has associated with it some degree of vorticity. A portion of the flow passes longitudinally through the discharge, and is heated to extremely high temperatures. A larger portion of the flow passes around the discharge and is heated by conduction from the discharge as from a hot wire. As a result the flow at the nozzle exit plane is highly non-uniform, consisting of a high velocity core surrounded by a coaxial flow of lower velocity.

In sections III C and D, analyses and the results of experiments are presented which shed some light on details of the core flow mode of arc engine operation. Reference is made to the core flow mode at this point in order to discuss propulsion results obtained with the R-4 series engines, and the engine design.

a. Scaling

In the R-4 series engines there is no electrical separation between the constrictor section and the nozzle; these are formed of one piece of thoriated tungsten. As a consequence, the arc discharge is free to terminate in the nozzle, or to draw back into the constrictor. The flow in effect "blows" the discharge through the constrictor. Reduction in the mass flow rate tends to be accompanied by a shortening of the arc discharge column unless the configuration is adjusted for different mass flow rates. The scaling law which has proved successful in adjusting the configuration to the mass flow rate involves keeping the mass flux at the throat constant. In the Mod 1 of the R-4 series, designed to operate at a mass flow rate of 0.25 gm/sec of hydrogen, the constrictor diameter is 0.444 cm, while in the Mod 3 engine it is only 0.305 cm. The ratio of throat areas for the two engines is approximately two, as is the ratio of design mass flow rates. The Mod 2 engine was also scaled in this way, so that the mass flux rates are approximately the same for all of the R-4 series engines. Similarly, it has been learned empirically that a constrictor length to diameter ratio of two is most satisfactory both from the point of view of engine performance and life. A small length to diameter ratio (one or even less) does not allow the arc discharge to be stably established, and it tends to fluctuate. A much larger length to diameter ratio produces an arc attachment in the anode nozzle quite close to the engine throat, so that small fluctuations in power or mass flow result in the arc drawing back into the constrictor; this is nearly always destructive of the engine.

The nozzle serves not only an aerodynamic function, but an electrodynamic one as the anode. Hence, its configuration cannot be determined on purely aerodynamic grounds. Further, the flow is not one dimensional. Straightforward calculations of optimum nozzle geometries for one dimensional flow characterized by the bulk values of enthalpy, etc., characteristic of the R-series engines indicate that some gain in performance could be realized by increasing the area ratio and the nozzle angle. This has been attempted experimentally, both in earlier phases of the program and during this Third Year Development Program (see section III), with results that indicate that the 7° half angle is near optimum, and that variation of the area ratio between 5 and 15 affects performance very little. For this reason the R-4 series engines are all made from nozzle-anode blanks of the same length; the varying throat sizes cause the geometric area ratio of the nozzle to vary from approximately 12 in the Mod 3 down to nearly 7 in the Mod 1.

b. Efficiency

Perhaps the most striking feature of the performance reported in table 2 is that the efficiencies of the three engines are very nearly the same. The entire range of efficiency can be expressed as 42.7 ± 2 percent. This margin of difference is within the experimental uncertainties (see appendix A.) It is thought that this insensitivity of efficiency to specific impulse arises as a result of several competing phenomena. A complete discussion of the arc engine energy balance will be found in section III E, but that discussion can be summarized briefly as follows: The input power (30 kilowatts) is invested in several channels; these are

i) Thrust power

ii) Non-uniform velocity profile power loss

iii) Frozen flow power loss

iv) Residual thermal power loss

v) Radiation from the engine structure.

The first four channels listed above include all the power transferred to the gas while the fifth accounts for power input which is not contained in the gas at the nozzle exit plane. The sum of the first and second channels is the kinetic energy flow per unit time. The third and fourth channels account for power delivered to the gas which is not converted to kinetic energy; it resides either in chemical degrees of freedom (frozen flow loss) or in random thermal motion and excitation (residual thermal loss).

The results of a detailed investigation of the exhaust with aerodynamic probes are given in section III D. Certain features of these results are excerpted for use in this discussion. In particular, the probe investigation reveals that the power loss associated with the non-uniform velocity distribution is a small fraction of the thrust power, of the order of 10 to 20 percent. Since a 40 percent overall efficiency at the 30 kilowatt input power level requires a thrust power of 12 kilowatts, this indicates that the velocity profile power loss is of the order of 1 to 2 kilowatts. Engine surface temperature measurements lead to estimates of the radiated power of 2 to 3 kilowatts, varying rather slowly with specific impulse level. Hence, the sum of the frozen flow power and the residual thermal power is approximately 13 to 15 kilowatts. In order that the efficiency not vary significantly between engine operation at 1000 seconds and at 1500 seconds, it is necessary that this figure also be relatively constant.

With regard to the residual thermal loss, two mechanisms are operative which tend to cancel. For, while the average temperature of the gas at the outlet tends to increase with decreasing mass flow rate at constant power input, the power loss which comes from incomplete expansion is determined by the product of mass flow rate and the mass flow normalized thermal energy content. At least to a first approximation it would be expected that this product of the mass flow rate and a quantity which varies oppositely to the mass flow rate would remain nearly constant as the mass flow rate is varied.

If, indeed, the thermal power content of the gas flow does not vary greatly as the specific impulse is varied from 1000 to 1500 seconds, it is necessary to conclude that the frozen flow power loss also does not vary greatly, for it has been shown that the sum of the two is nearly constant. This suggests that the degrees of ionization and of dissociation increase as the specific impulse level increases, but that they do not increase rapidly. For example, if the mass flow rate of 0.25 gm/sec in the R-4 Mod 1 engine is characterized by a degree of dissociation of 15 percent, then the power loss associated with disssociation is approximately 8 kilowatts. This power loss is equivalent to a degree of dissociation of 31 percent at the R-4 Mod 3 mass flow rate of 0.12 gm/sec, so that the degree of dissociation approximately doubles in going from 1000 seconds to 1500 seconds specific impulse.

These investigations of the arc engine energy balance suggest that operation in the core flow mode at the 30 kilowatt power level is beneficial for performance. The major advantages of the core flow mode are that the non-uniformities introduced by the arc column tend to improve the frozen flow efficiency over the one dimensional case in the specific impulse range of 1000 to 1500 seconds, and that the use of the nozzle as the anode tends to alleviate anode heating problems by providing an anode root which is either diffuse or diffuse in a time average sense (moving spot). The major drawback of operation in the core flow mode is the introduction of a velocity profile loss associated with the very high central velocities; however, measurements reported in section III-D indicate that this loss is relatively small (order of 10 to 20 percent of the thrust power, or 4 to 8 percent of the input power).

A second drawback of core flow mode operation is associated with the fact that, if the flow sonic point is the nozzle entrance, then some of the heating of the propellant is accomplished in the supersonic region, for the arc attachment point is downstream of the throat. This problem has been investigated analytically, and is presented in appendix I. The major conclusions of appendix I are that the decrease in specific impulse owing to heating in the supersonic nozzle as compared with the specific impulse which would be obtained if all the heating were done upstream of the throat is of the order of 3 percent for as much as 25 percent of the heating in the supersonic region. Hence, it is believed that this effect is not important with regard to propulsion performance.

6. Conclusions

a. 30-kw arcjet engines have been operated in the range of specific impulse of 1000 to 1500 seconds. Efficiencies of 40-45 percent have been obtained, and there seems to be little dependence of efficiency on the specific impulse level in this range.

b. Lifetime demonstrations at the 1000 second and 1300 second specific impulse levels were successfully concluded, but life at the

1500 second specific impulse level is still uncertain. A test of 120 hours duration was made, but the engine was damaged during the course of the test.

c. Further improvements in the area of engine materials may be necessary to run satisfactory life tests at the 1500 second specific impulse level.

d. Engine performance is consistent with operation in the core flow mode.

C. X-1 HIGH SPECIFIC IMPULSE ENGINE

Preliminary investigations have been made of the possibility of utilizing an arcjet engine configuration to obtain specific impulse values in hydrogen in excess of 1500 seconds. For the purposes of these investigations the power limit of 30 kilowatts was relaxed. Two engines operating at higher power levels were developed during the course of this program. The first of these was a radiation cooled engine, with a general configuration patterned after that of the 30 kilowatt R-series of engines. This high power engine is designated X-1, and is discussed in the remainder of this section. The second configuration, with which significantly improved specific impulse values were achieved, is designated X-2, and is discussed in the following section.

1. Configuration

As indicated above, the X-1 radiation cooled high specific impulse engine is a scaled up version of the R-series of 30 kilowatt engines. The engine configuration is sketched in figure 7. The major differences between the X-1 and R-4 configurations are that:

a. The anode-nozzle of the X-1 engine is not regeneratively cooled. This design decision was made largely on the basis of ease of construction, since this engine model is at an early stage of development. Further development of this engine resulting in a configuration which is optimum in terms of constrictor length to diameter ratio, etc., could then justify addition of regeneration.

b. The cathode of the X-1 engine is regeneratively cooled. Experience with uncooled cathodes at the high current levels characteristic of X-1 engine operation indicated that cathode lifetime was a problem. Addition of regenerative cooling passages allowed significant cathode lifetime improvement.

c. The outer surface of the anode-nozzle is integral from the upstream end of the engine to the nozzle exit plane, without interruption by a brazed joint. Sealing is in part accomplished by brazes within the engine interior, and in part by stainless steel C-rings. An exterior braze of such a large structure as the X-1 engine would have been extremely difficult with the available brazing furnaces. For preliminary testing of the type which was accomplished with the X-1 engine, the use of C-rings was acceptable.

Referring to figure 7, the cathode is regeneratively cooled copper tubing with a thoriated tungsten tip. The propellant injector tube is stainless steel, brazed to the molybdenum plenum section with 50 percent copper-50 percent platinum. The molybdenum plenum is brazed to the tunsten anode nozzle with powdered iron. The C-rings are stainless steel. The cathode holder is boron nitride. The important dimensions of the X-1 engine are listed in table 3. The constrictor l/d ratio was maintained at nearly two. The somewhat larger cross sectional areas in the X-1 engine compared with the R-series engines motivated an increase in area ratio which was achieved in part by making the expansion angle larger. Finally, the constrictor diameter was chosen for a mass flow rate of 0.50 grams/sec., although the engine was later run at smaller mass flow rates. The mass flux at a flow rate of 0.50 grams/ sec. is the same as for the R-4 engines.

TABLE 3

DIMENSIONS OF THE X-1
HIGH SPECIFIC IMPULSE ENGINE

Constrictor Length	1.27 cm
Constrictor Diameter	0.602 cm
l/d	2.11
Nozzle 1/2 Angle	10°
Nozzle Exit Diameter	2.61 cm
Area Ratio	19
Cathode Gap	0.384 cm

2. Performance

Performance data obtained with the X-1 high specific impulse engine are given in table 4. These data have been used to plot figure 8, which shows X-1 engine efficiency versus specific impulse. For comparison data from long runs of the R-4 series 30 kilowatt engines are also plotted on figure 8, as is the one-dimensional frozen flow efficiency curve. The major indications of figure 8 are that specific impulse values of approximately 2,000 seconds can be reached with a conventional arcjet configuration at overall efficiencies which compare reasonably well with the efficiencies achieved at much lower impulse values, and that the overall trend of efficiency versus specific impulse in the range 1,000 to 2,000 seconds for this type of design is rather flat; indeed, although the efficiencies at the higher specific impulse values are somewhat lower than those obtained with the R-4 series of engines, it should be recalled that the X-1 engine is not regeneratively cooled to a significant extent and that some efficiency improvement should be possible by optimization. Further, the efficiency trend with specific impulse has little correlation with the one-dimensional frozen flow curve.

3. Conclusions

A conventional radiation cooled arcjet engine run at power levels in the 200 kilowatt range has yielded specific impulse values of approximately 2,000 seconds. The efficiency is comparable with efficiencies obtained at the 30 kilowatt level, especially considering the preliminary stage of development of the high power engine. No data were obtained on lifetime, nor was the experimental configuration well suited to long engine runs, owing to the use of C-rings for seals in engine regions expected to reach high temperatures after several hours of operation.

TABLE 4

PERFORMANCE OF THE X-1 HIGH SPECIFIC IMPULSE ARCJET ENGINE

Arc Voltage Volts	Arc Current Amp	Arc Power KW	$\dot{m}$ GM/Sec	Thrust GM	Isp Sec	Eff 70
162	928	150	0.143	660	1600	33.7
163	928	151	0.396	650	1640	33.9
163	928	151	0.376	640	1702	34.6
162	948	153	0.347	635	1830	36.4
159	964	153	0.327	630	1925	38.1
160	1080	173	0.327	660	2080	37.0
161	1232	198	0.327	693	2120	35.6
160	1350	216	0.327	724	2210	35.6

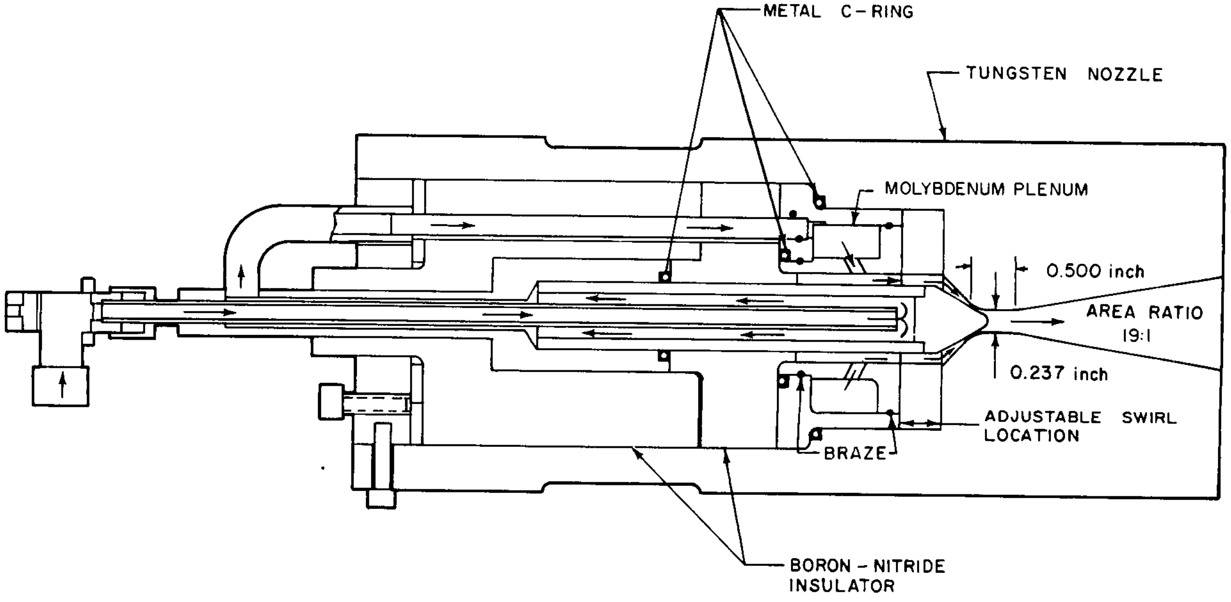
METAL C-RING
TUNGSTEN NOZZLE
MOLYBDENUM PLENUM
0.500 inch
AREA RATIO
19:1
0.237 inch
ADJUSTABLE SWIRL LOCATION
BRAZE
BORON - NITRIDE INSULATOR

63-10707

Figure 7 X-1 HIGH SPECIFIC IMPULSE ARCJET ENGINE SCHEMATIC

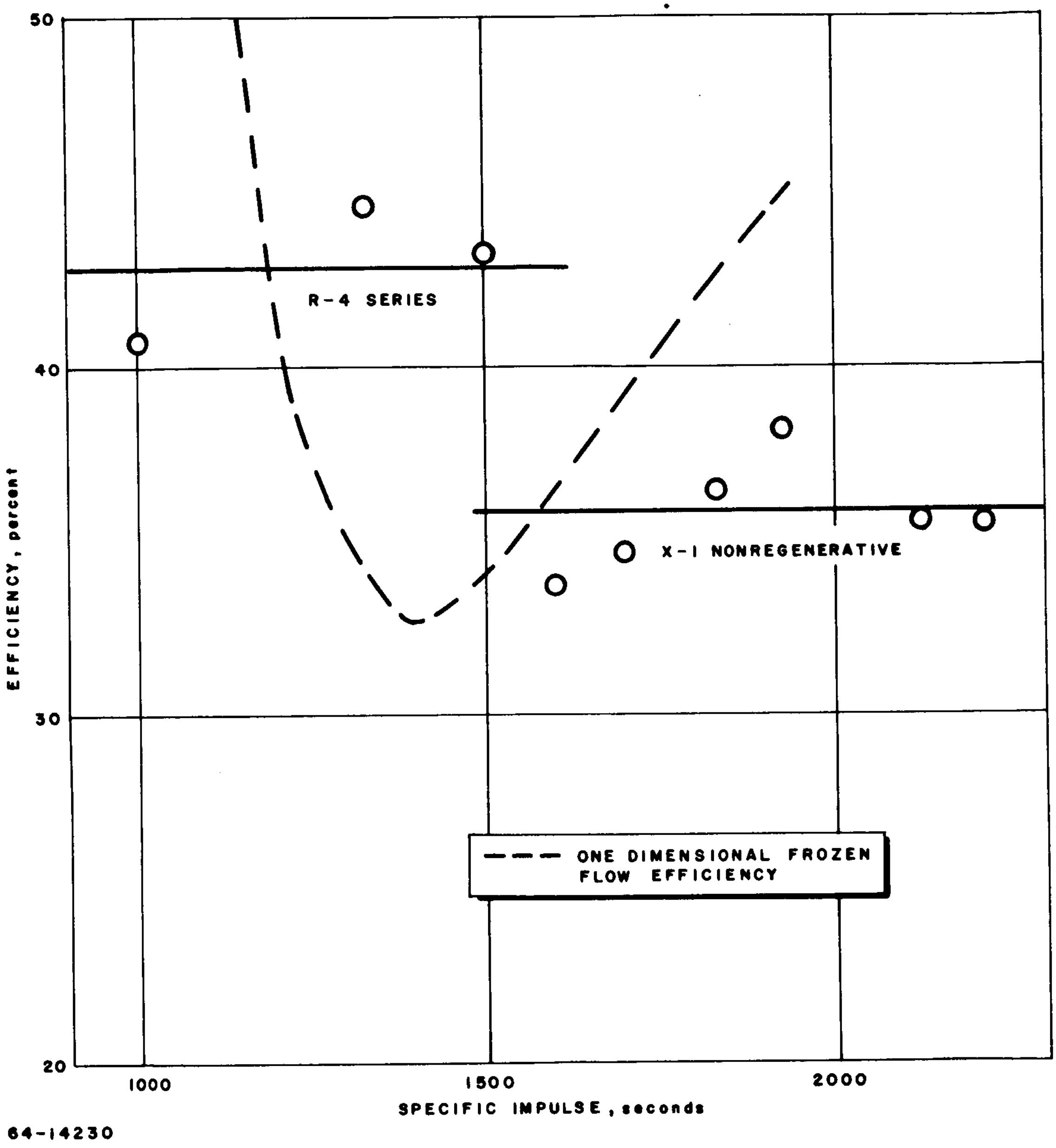

Figure 8 EFFICIENCY VERSUS SPECIFIC IMPULSE; X-1 HIGH SPECIFIC IMPULSE ENGINE AND R-4 ENGINES

D. X-2 HIGH-IMPULSE ENGINE DEVELOPMENT

1. Introduction

Following the X-1 engine development (section II C), tests were made with an engine based on a design concept significantly different from the 30-kw constricted arcjet engine. This new design is designated as X-2. In the following paragraphs the engine design is described and test results are reported. A hypothesis describing the mode of engine operation is advanced. Experimental testing of this engine is in the preliminary stage, but data so far obtained indicate that specific impulse values of 7400 seconds at efficiencies in excess of 30 percent have been achieved, using hydrogen as the propellant. A small number of tests have also been made in nitrogen and argon resulting in specific impulses of 2000 and 1000 seconds respectively.

2. Engine Design

A sketch of the X-2 engine design is given in figure 9. The cathode is water-cooled copper with a thoriated tungsten tip. The anode is water cooled copper. Propellant is injected tangentially upstream of the cathode, swirls over the cathode tip, through the throat, and is ejected immediately. The major differences between this design and that of the X-1 engine (or, in fact, of the R-series of 30 kilowatt engines) are that:

a. The constrictor section is absent in the X-2 design. The arc discharge between the cathode tip and the anode is not confined or constricted over any appreciable length by a straight section;

b. The conical exit nozzle is absent in the X-2 design. The nozzle exit plane is very close to the throat (which is relatively large), and joined to the throat by a rounded contour.

The design changes for the experimental engine were made to allow engine operation with extremely low mass flow rates of propellant. Experience with the R-series of 30-kilowatt engines indicated that reduction of the mass flow rate in a constricted arc engine tends to move the anode attachment zone upstream; reduction of the flow rate below some minimum value tends to move the anode attachment zone into the constricted section, which results in heavy constrictor damage and eventual engine failure. The practical lower limit of mass flow rate observed for the R-series of 30-kilowatt engines has been in the range 0.09 to 0.10 gm/sec of hydrogen. At the 30-kilowatt power level this corresponds to a specific impulse value of approximately 1500 seconds, at efficiencies typical of the R-series of radiation-cooled engines (40 percent). The desire to run an engine with significantly lower mass flow rates prompted elimination of the constrictor section in an experimental engine.

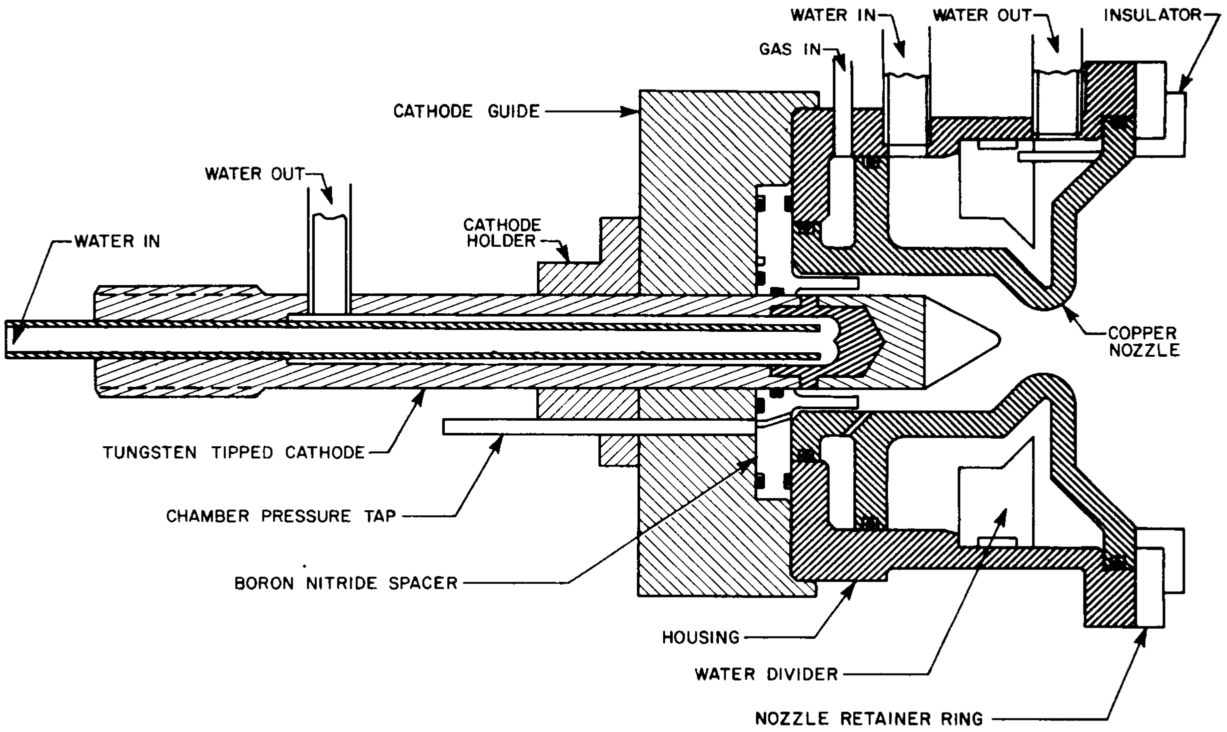
WATER IN
GAS IN
WATER OUT
INSULATOR
CATHODE GUIDE
WATER OUT
CATHODE HOLDER
WATER IN
COPPER NOZZLE
TUNGSTEN TIPPED CATHODE
CHAMBER PRESSURE TAP
BORON NITRIDE SPACER
HOUSING
WATER DIVIDER
NOZZLE RETAINER RING
64-2979

Figure 9 X-2 HIGH SPECIFIC IMPULSE ARCJET ENGINE; SCHEMATIC

As the mass flux and operating pressure are reduced, viscous effects become more important. For this reason the nozzle was severely truncated.

Finally, it was thought that experimental tests of the engine could be facilitated by liquid cooling techniques. Proper design of an engine for radiation cooling is in itself a substantial engineering task, and it was desirable in the experimental engine to uncouple this portion of the problem to allow timely investigation of the propulsion performance.

3. Engine Performance

The X-2 engine (figure 9), was tested in an environmental system like those which have been used for development of the R-series of 30-kilowatt engines. Power was supplied by two silicon diode rectifiers connected to give an open circuit voltage of 500 volts, with a current capability in excess of 3000 amperes at a load voltage of approximately 100 volts. Engine starting was accomplished with Paschen's Law breakdown. Thrust was measured with a water-cooled direct-force-measuring thrust stand, calibrated by a pulley and weight technique. Mass flow was monitored with a rotameter type flow gauge calibrated by the manufacturer (Fischer-Porter Co.), with a calibration check performed at this laboratory. The environmental tank is water cooled and contains a heat exchanger to reduce the propellant enthalpy to tolerable levels before it enters the vacuum pumping system. The vacuum pump capacity is 6000 ft^3/min, sufficient to maintain an ambient pressure in the environmental tank of less than 1 mm Hg during engine operation.

Measured and computed performance parameters are listed in table 5. The directly measured quantities are thrust, mass flow rate, input power, engine chamber pressure, and heat extracted by the anode and cathode cooling water. The derived quantities include specific impulse and efficiency.

4. Analysis of X-2 Engine Performance

In the absence of a significant nozzle expansion region, it is expected that the thrust produced by a conventional arcjet engine should be closely related to the product of chamber pressure and throat area. This is not the case for the data of table 5. Figure 10 is a plot of measured thrust versus the product of chamber pressure and throat area, demonstrating that the correlation is quite poor. Chamber pressure has been measured with a variety of gages, and with a mercury manometer as well, yielding quite reproducible values. The measured values of chamber pressure can be correlated with the propellant mass flow rate, as is indicated in figure 11. As a result, there is reasonable confidence that the chamber pressure measurements are accurate, at least in indicating trends. There exists the possibility that the high currents involved in the operation of the X-2 engine set up magnetic fields

TABLE 5

PERFORMANCE OF X-2 ENGINE

(PROPELLANT: HYDROGEN)

Run Number	$\dot{m}$ (gm/sec)	I (amperes)	V (volts)	P_{in} (kw)	T (grams)	P_{Thrust} (kw)	E_{ff} (percent)	I_{sp} (seconds)	P_{cool} (kw)	Chamber Pressure (mm Hg)
1	0.050	1140	63	72	100	9.6	13.3	2000	24.6	46
2	0.050	1450	68	98	132	16.8	17.1	2640	29.8	29
3	0.050	1560	69	108	136	17.8	16.5	2720	31.1	50
4	0.050	1700	70	119	156	23.4	19.7	3120	34.1	50
5	0.050	1870	72	134	172	28.4	21.1	3440	37.1	50
6	0.050	2000	74	148	197	37.2	25.1	3950	38.2	50
7	0.050	2200	76	167	221	46.8	28	4420	41.3	50
8	0.040	2120	72	153	197	47.2	30.8	4980	40.6	40
9	0.026	2360	82	196	192	68.2	35.3	7400	36	14

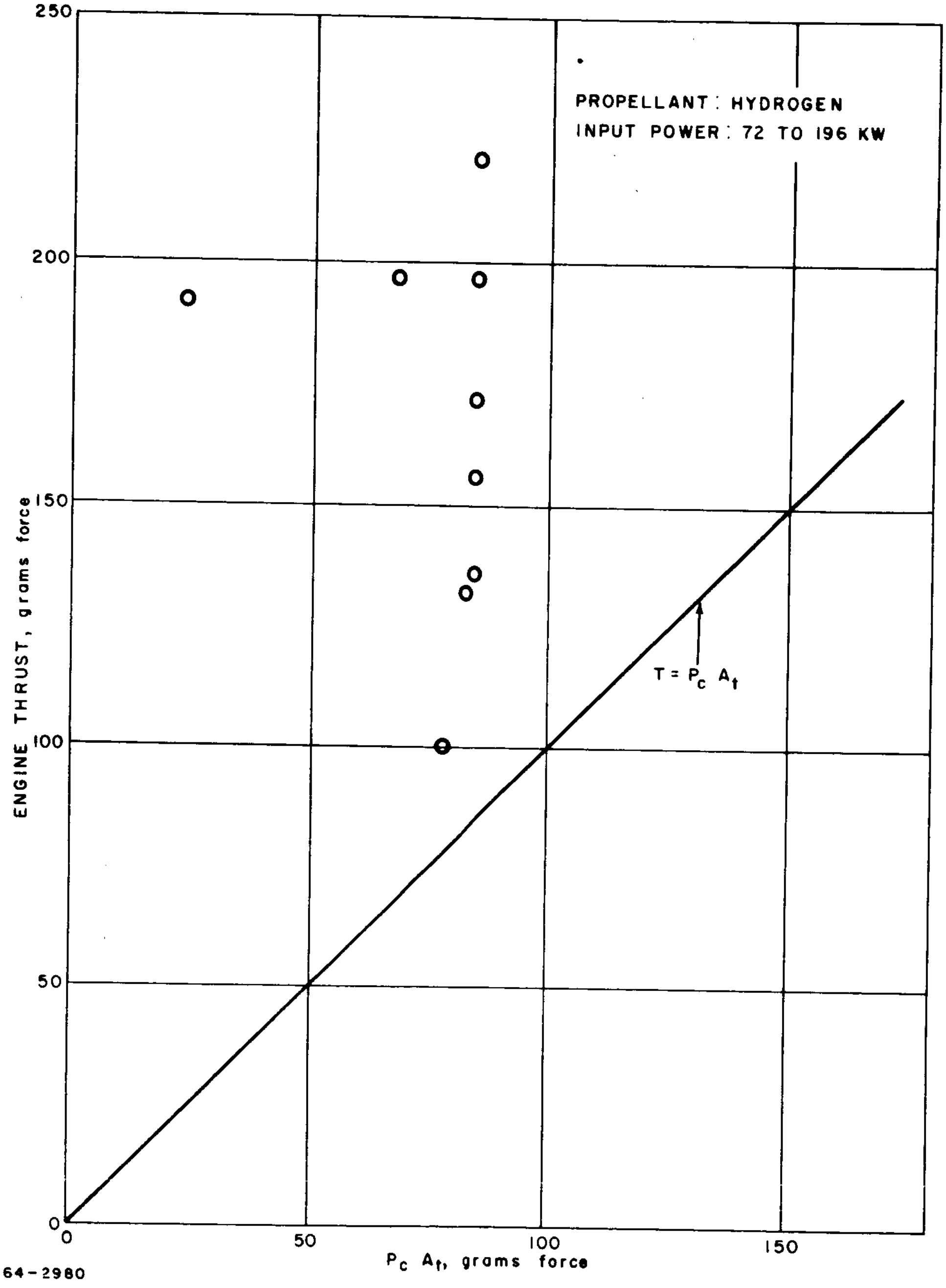

Figure 10 THRUST VERSUS PRODUCT OF CHAMBER PRESSURE AND THROAT AREA, X-2 ENGINE

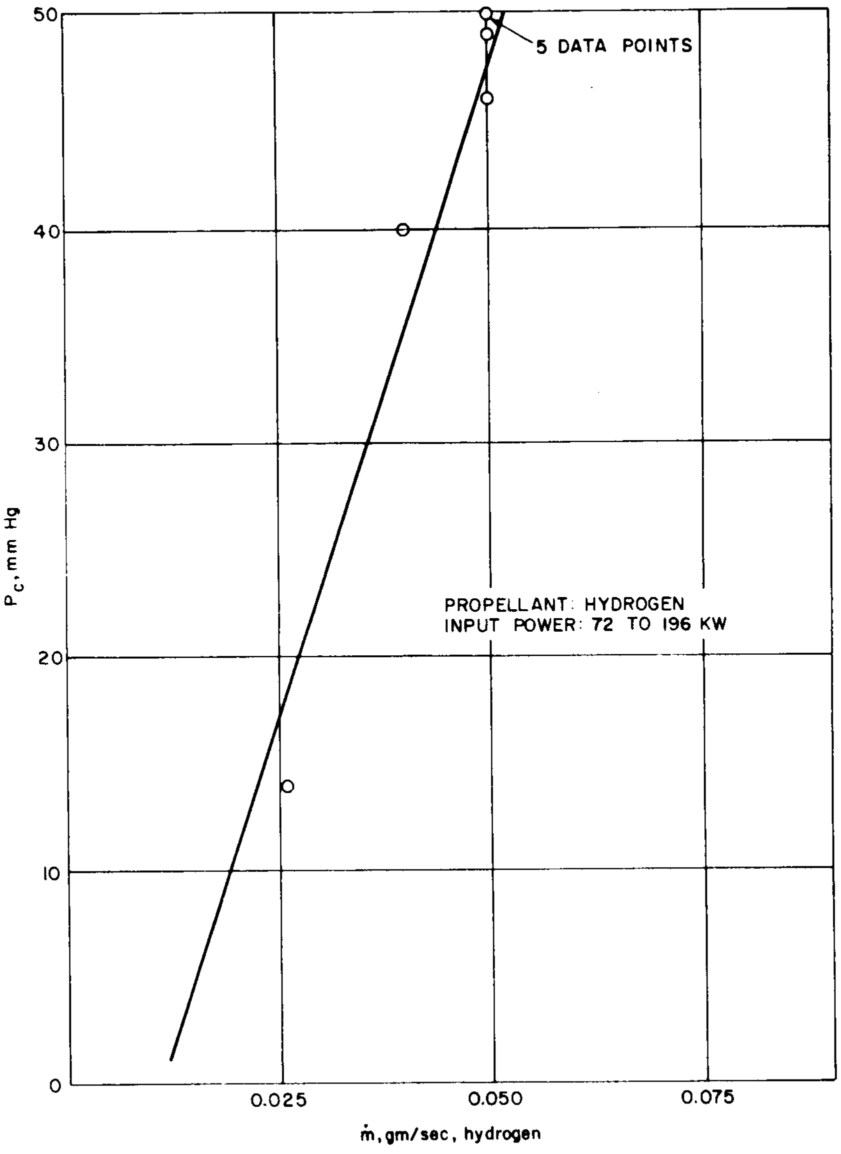

64-2981

Figure 11 CHAMBER PRESSURE VERSUS MASS FLOW RATE, X-2 ENGINE

which then interact with the environmental tank or with the thrust stand, causing spurious deflections and erroneous thrust readings. This possibility has been checked by shorting the cathode of the X-2 engine to the anode, and duplicating the operating currents in the absence of propellant flow. The thrust readings which are observed under these conditions are much too small to account for the discrepancy between measured thrust and chamber pressure, and are in fact in the wrong direction; this interaction appears to simulate drag.

The tentative conclusion has been reached, on the basis of (1) the data of table 5 (2) the poor correlation between chamber pressure and thrust, and (3) the checks which have been made of the instrumentation, that there is a mechanism operative which produces thrust but which does not reflect itself in an increase in pressure near the surface of the arc chamber.

If this mechanism involves an interaction between the arc current and its own magnetic field, it is anticipated that the resulting thrust will depend upon the square of the current (the current enters once in setting up the magnetic field and again in interacting with it). To investigate this possibility the data of table 5 were used to form table 5A.

The entries in table 5A are defined as follows:

T_{total} = measured thrust, grams force

T_{aero} = product of chamber pressure and throat area, converted to grams force

T_{arc} = $T_{total} - T_{aero}$, grams force

I^2 = square of arc current, ampere^2.

Figure 12 has been plotted from table 5A showing T_{arc} versus I^2. The apparently good correlation between T_{arc}, the "extra" thrust, and I^2 gives some confidence to the idea that T_{arc} originates in an interaction between the arc and its own magnetic field, although it certainly does not demonstrate this in any conclusive manner.

In Appendix C several mathematical analyses are presented based upon possible physical models of the arc discharge interaction with its own magnetic field. Basically, two types of effects are noted. If a radial current component interacts with an azimuthal magnetic field, the resulting force is axial.[3, 4] Such a force can directly accelerate the propellant

TABLE 5A

VARIATION OF THRUST WITH
(ARC CURRENT)^2
(PROPELLANT: HYDROGEN)

Run No.	T_{total} (gmf)	T_{aero} (gmf)	T_{arc} (gmf)	I^2 (amperes)^2
1	100	77	23	1.29×10^6
2	132	82	50	2.09
3	136	84	52	2.41
4	156	84	72	2.87
5	172	84	88	3.49
6	197	84	113	4.00
7	221	84	137	4.81
8	197	67	130	4.49
9	192	23	169	5.52

in the manner of a blower. It is also possible for an axial current component to interact with the azimuthal magnetic field, producing a radial inward acceleration. In this case the effect is to increase the pressure in the propellant, leading then to acceleration in a conventional aerodynamic manner. The extent to which either or both of these mechanisms is operative depends upon the current distribution in the discharge and at the electrode which is unknown at this time. It is shown in appendix C that, based upon reasonable assumptions about the nature of the discharge, the forces which would be produced by either mechanism are at least of the correct order of magnitude to account for the observed thrust.

It should also be pointed out that it has proved useful in terms of prolonging X-2 engine life to supply an auxiliary magnetic field to swirl the discharge near the anode. This has been done both by self-excitation and by separate excitation. In the first case the current lead to the cathode was wrapped

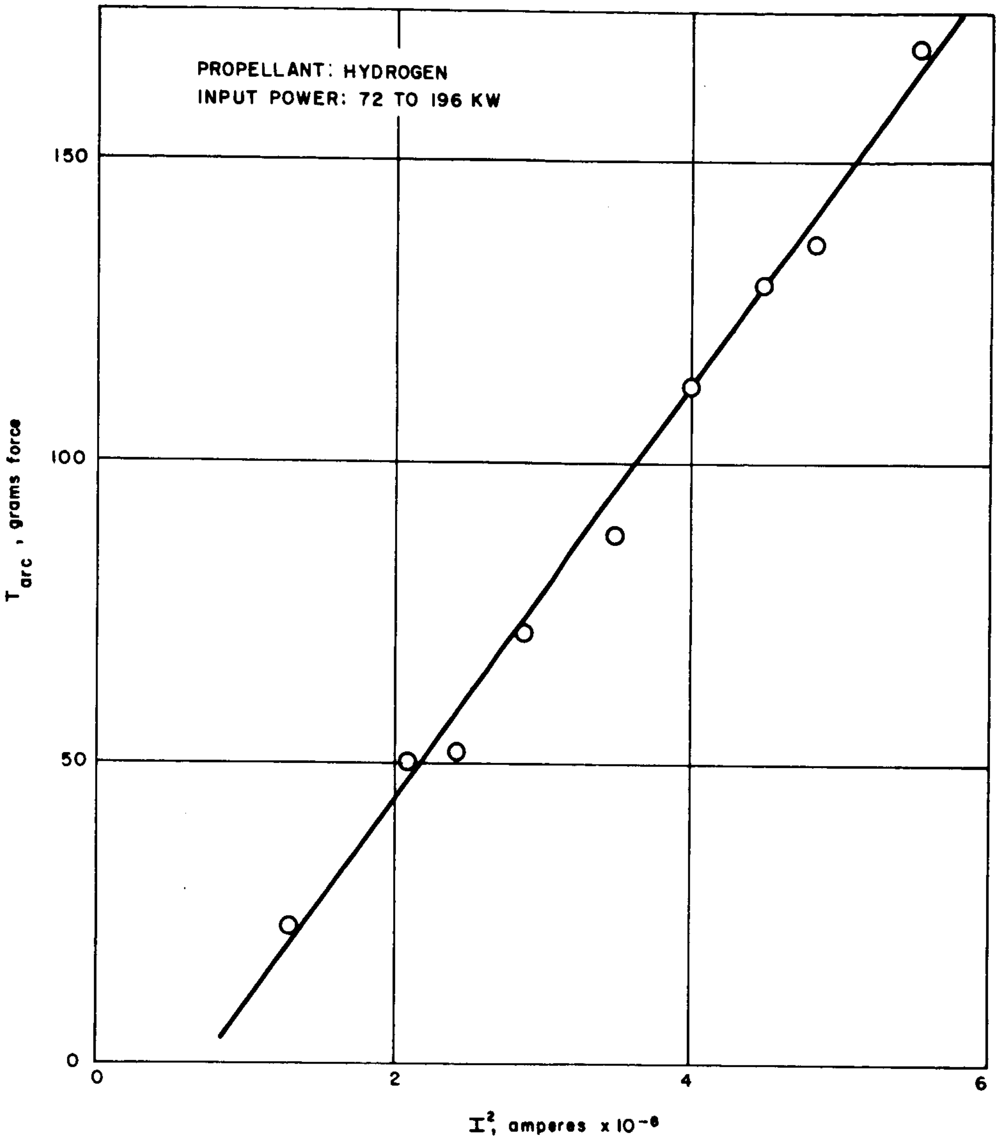

64-2982

Figure 12 NON-AERODYNAMIC THRUST VERSUS SQUARE OF ARC CURRENT, X-2 ENGINE

several times about the engine exterior before it was connected to the cathode. In the second case an entirely separate magnetic field coil was used. In the first case the coil was of necessity attached physically to the engine and hence to the thrust stand. In the second case the coil was mounted firmly to the vacuum tank, independently of the thrust stand. Measured engine performance in the two cases is the same within the limits of experimental uncertainty (approximately 15 percent for these preliminary measurements). In addition, with the separately excited magnetic field coil, it has proved possible to vary the magnet excitation independently of the main arc current. No systematic effect upon thrust has been discovered as a result of this variation. It is tentatively concluded that, unlike the Hall accelerator, the high specific impulse X-2 arcjet engine performance is not dependant upon the external magnetic field, except insofar as life time is concerned.

5. Conclusions

As a result of the work described above and the mathematical analyses of appendix C, it can be tentatively concluded that:

a. At high currents and low mass flow rates the self electromagnetic forces associated with the thermal arcjet engine are significant in terms of propulsion performance.

b. Probably as a result of these forces at reasonable power and mass flow rates (that is, at rates easily achievable in the laboratory without unusual equipment) arcjet engines can produce specific impulse values in the range heretofore available only to the ion engine or, in concept, to mhd devices.

c. Apart from the basic propulsion performance data, very little has so far been discovered about the arcjet engine operating in this high specific impulse mode. In particular, information about the nature of the discharge and the effect of propellant properties upon the discharge would be of great value in elucidating the thrust mechanism.

E. ENGINE MATERIALS AND BONDING

1. Introduction

The high temperatures characteristic of radiation-regeneration cooled arcjet engine operation restrict the list of materials which may be used in engine construction and bonding to only a few possibilities. Experience in earlier phases of the 30-kilowatt development program indicated that tungsten with a thoria additive is most suitable for the electrodes, molybdenum for portions of the engine which do not reach electrode temperatures, and steel for those parts of the engine which are relatively cool during engine operation. In each case a balance must be struck between performance at high temperature and ease of machining. Boron nitride has proved to be a reliable high temperature insulator. During this Third Year Development program attention has been focussed on the specific type of each of the refractory metals to use (i. e., wrought, sintered, or arc-cast tungsten, and on the methods used to join the engine sections. The following paragraphs describe criteria upon which the material type choice is made, and discuss progress in the bonding program for each of the two high temperature joints which must be made.

2. Material Choice

Three forms of tungsten have been considered. These are sintered, arc-cast and wrought.

a. sintered tungsten (2 percent Thoria) -- this material is readily available, and relatively inexpensive and easy to machine. It is especially suitable for brazing. However, it is susceptible to cracking during welding. The material contains voids 5-8 volume percent, which make welding difficult.

b. arc-cast tungsten -- this material has high density and is relatively inexpensive. However, it is not readily available, and it has a columnar grain structure making it extremely susceptible to thermal shock failure.

c. wrought tungsten -- this material has good thermal and electrical properties and good mechanical properties owing to random orientation of grains. It has good joining properties but is extremely difficult to machine.

Arc-cast molybdenum has been selected because it is relatively inexpensive and easy to machine, and can be both brazed and welded.

3. Brazing Investigations

In the initial phase of the brazing program attention was concentrated on the joint between the thoriated tungsten anode nozzle and the molybdenum plenum section, with the objective of increasing the temperature limit at which this joint would remain leak tight in operation with hydrogen or ammonia. After some progress was made in this direction the work was extended to the joint between the gas inlet tube and the molybdenum plenum which was also upgraded in its temperature capability.

A brazing sample was designed which could be easily leak tested after brazing and after diffusion anneals which simulated actual run conditions of an engine. A number of brazing alloys were then used to join sintered tungsten and molybdenum. Those which were found to be leak tight at 50 psi pressure after brazing are listed in table 6.

TABLE 6

LEAK TIGHT ALLOYS AFTER BRAZING TUNGSTEN AND MOLYBDENUM AT 50-PSI GAS PRESSURE

Braze Alloy	Braze Temperature °C	Braze Atmosphere
Coast 62 (68 Manganese-16 Cobalt-16 Nickel	1150	Hydrogen
Ge J-8600 (38 Nickel-33 Chromium-25 Palladium-4 Silicon)	1200	Hydrogen
70 Platinum-30 Copper	1550	Hydrogen
70 Platinum-30 Copper	1550	Argon
85 Platinum-15 Copper	1700	Argon
50 Chromium-50 Nickel	1375	Argon
50 Chromium-50 Nickel	1475	Argon
100 Iron	1550	Hydrogen
100 Chromium	1900	Argon
100 Vanadium	1900	Argon
75 Chromium-25 Vanadium	1900	Argon
75 Vanadium-25 Chromium	1900	Argon

These joints were then annealed in hydrogen at temperatures in the range 900° to 1200°C. Leak checks were made at regular intervals to determine the length of time a particular braze would remain leaktight. At 900°C, the 50-chromium 50-nickel alloy was quite satisfactory. At higher temperatures, the nickel reacts with tungsten forming cracks and/or voids with resultant leaking. Therefore, both the 50-chromium 50-nickel alloy and J-8600 alloy were not acceptable above 900°C. The Coast 62 alloy was not satisfactory as leaks, caused by the vaporization of manganese from the braze alloy and by the tungsten-nickel reaction, developed. The platinum-copper alloys were unsatisfactory because of the embrittlement of platinum in hydrogen. Vanadium and vanadium-25 chromium were discounted because of the hydrogen embrittlement of vanadium. Iron is a satisfactory braze for service temperatures of about 1000°C. At 1200°C, chromium-25 vanadium is an excellent braze material. The low rate of diffusion of chromium and vanadium in the base metals for this temperature range is the major factor contributing to a sound brazed joint after a diffusion anneal. Since long-run times are required in the 30-kilowatt engine, it was felt that the low reported values of diffusion rates of chromium and vanadium into tungsten and molybdenum should be verified, particularly because grain boundary diffusion, known to be 10^3 to 10^4 times faster than bulk diffusion, might create voids at the interface.

Test specimens were submitted to the Advanced Metals Research Corporation for electron-beam microanalysis. The specimens were tungsten and molybdenum disks joined at 1900°C for two minutes in an argon atmosphere. The samples were given different diffusion anneals after brazing to simulate operating conditions of an arc-jet engine (annealed 250 hours at 1000°C in hydrogen and 50- and 225-hour anneals at 1200°C in hydrogen).

The results of the microanalysis are summarized as follows:

Molybdenum diffuses readily into the brazing alloy while the tungsten diffusion rate is considerably lower. The presence of molybdenum and tungsten in the brazing alloy is a beneficial effect since the solidus temperature of the alloy is raised by the presence of the higher melting elements. The chromium and vanadium diffused into the molybdenum and tungsten at about the same rate for the two temperatures studied. Data also indicated trace amounts of tungsten to be present in the molybdenum and molybdenum in the tungsten.

The results of the electron-beam microanalysis indicate that the Cr-V brazing alloys are not likely to form voids at the brazing alloy-base metal interface due to rapid diffusion of an alloy element into the base metal.

Finally, a program was undertaken to evaluate the remelt temperatures of iron and Cr-V brazes. In the remelt temperature study, samples of tungsten and molybdenum were brazed in the same manner as the tungsten anode and molybdenum plenum sections of the 30-kw arc-jet engine. Some samples were annealed at 1200°C in a hydrogen atmosphere for varying time periods. The samples were then put into a furnace and the temperature recorded at which the braze started to flow.

The results of the remelt study, given in table 7, show that of the chromium-vanadium brazes, the pure chromium braze has the highest remelt temperature and that annealing (which is done in a hydrogen atmosphere to simulate actual running conditions) has a somewhat mixed effect. It is pointed out that although the composition 75 percent chromium 25 percent vanadium showed a slightly lower remelt temperature than the other chromium-vanadium alloy brazes, it is considered a better brazing alloy. Upon annealing, pure vanadium suffers from embrittlement by hydrogen and/or the formation of vanadium hydride which has virtually no strength. The pure chromium braze causes cracks in the tungsten thus producing a braze which was not leaktight after annealing for about 50 hours. The alloy 25 percent chromium 75 percent vanadium showed improved performance but also showed leaking at the braze after annealing for about 100 hours. The 75 percent chromium 25 percent vanadium braze alloy shows no tendency towards either hydrogen embrittlement or the formation of cracks.

TABLE 7

RESULTS OF REMELT TEMPERATURE INVESTIGATION

Composition	Braze Treatment*	Remelt Temperature (°C)
75 CR-25V	As Brazed	1785
75 CR-25V	160 hr Anneal	1750
75 CR-25V	240 hr Anneal	1790
75V -25 Cr	As Brazed	1800
75V -25 Cr	56 hr Anneal	1820
75V -25 Cr	222 hr Anneal	1810
50 Cr-50V	As Brazed	1800
Cr	As Brazed	1850
Cr	88 hr Anneal	1950
Cr	160 hr Anneal	1950
Cr	362 hr Anneal	1860
Iron	As Brazed	1500
Iron	100 hr Anneal	1535

*Annealing is done in hydrogen atmosphere at 1200°C

The indication that the Cr-V brazes would permit higher engine operating temperatures than had been possible with the powdered iron braze, along with a measure of success in the diffusion bonding program (reported in the next section) motivated a study to increase the temperature capability of the joint at the base inlet tube entrance into the molybdenum plenum.

In earlier work, molybdenum inlet tubes had recrystallized during brazing and proved to be brittle, so low carbon steel tubing was used for the gas inlet. The braze to the molybdenum plenum chamber was made with a brazing alloy of 50 percent copper 50 percent platinum which melts at a temperature of approximately 1200° C. This relatively low temperature was necessitated by the melting point of the steel tubing. It proved possible by employing an alloy of molybdenum with 0. 5 percent titanium and 0. 1 percent zirconium (the alloy is known as TZM) to produce inlet tubes with greatly reduced brittleness when compared with pure molybdenum. At the same time, the increase in melting point over that of steel allows use of a powdered iron braze which flows at 1450 to 1500° C. These modifications of material and braze were adopted for all 30-kw engines, starting with the R-4 Mod 3. (This engine was used for the attempted long runs at the 1500 second specific impulse level.)

The conclusions of this brazing investigation are that for the main joint between the thoriated tungsten anode nozzle and the molybdenum plenum chamber, a braze material of 75 percent Chromium-25 percent Vanadium is most satisfactory. For lower temperature operation (as in the R-4 Mod 1 test at 1000 second specific impulse) powdered iron is also satisfactory. The joint between the gas inlet tube and the molybdenum plenum can be brazed successfully with 50 percent Platinum-50 percent copper, or with iron for better high temperature performance if the inlet tube is made of TZM alloy.

4. Diffusion Bonding

During the course of this Third Year Development Program a diffusion bonding technique for forming the joint between the nozzle and the plenum section was developed. It appears to offer better high temperature performance than any of the braze materials developed so far. The basis of the diffusion bonding technique is that tungsten and molybdenum form a continuous solid solution for all temperatures below the melting point of molybdenum (see figure 13).

The formation of a tungsten-molybdenum solid-solution alloy at the interface of the engine nozzle and engine cap would represent the most satisfactory joining technique since such an alloy would be compatible with both metals and would have a melting range higher than that of the unalloyed molybdenum.

One method for forming this type of alloy is a solid-state diffusional process at relatively high temperatures and with the application of pressure to bring the mating surfaces into intimate contact. A second method would be to melt the tungsten and molybdenum by electron-beam techniques, and weld the components together. Both of these techniques are complicated experimentally.

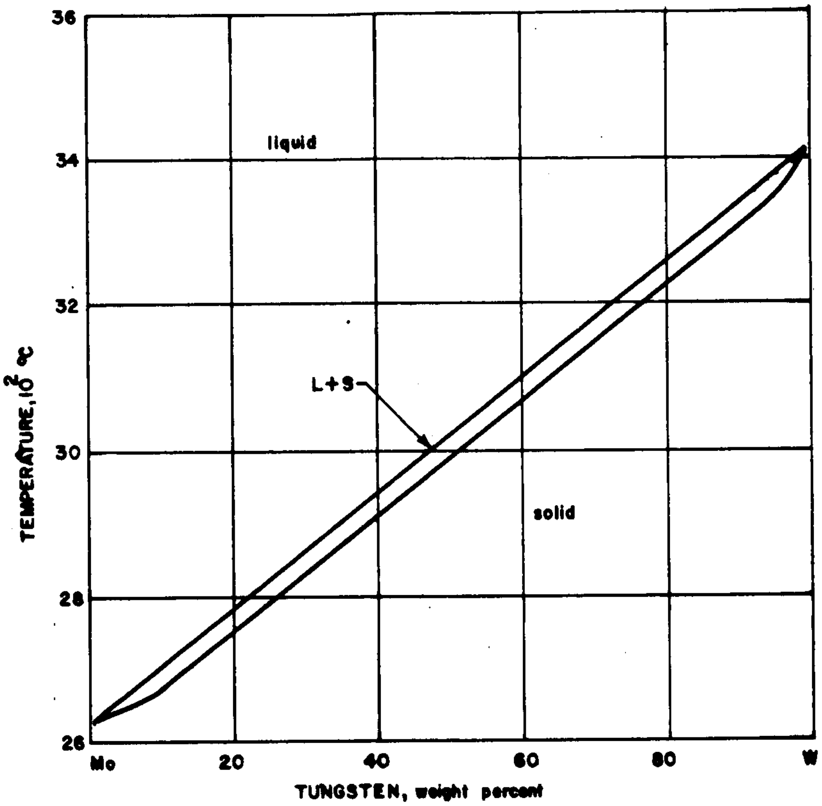

Figure 13 PHASE DIAGRAM FOR MOLYBDENUM AND TUNGSTEN

A method which proved very successful with small laboratory specimens, and which was then employed in an engine, is a modified diffusion-bonding method employing nickel as a bonding agent. The tungsten and molybdenum faces to be joined are lapped with diamond dust to a high surface finish. These lapped faces are then vaporplated with nickel to a few Angstrom thickness. The mating surfaces are brought into contact and held in place by a fixture. The entire assembly is heated to 1525°C for 8 hours. As seen in figure 14, this temperature is above the molybdenum-nickel and tungsten-nickel eutectic temperatures; therefore, at the interface, a tungsten-molybdenum-nickel liquid is formed. Subsequent diffusion of the nickel into the base metals, by lattice and grain-boundary mechanisms, leaves a solid-solution tungsten-molybdenum interface which joins the two base metals.

A 30-kw arc-jet engine was joined by a diffusion-bonding method utilizing vapor-plated nickel as a bonding agent, but separated after being run a few hours under conditions where the joint reached an optical temperature of 1650° to 1700°C. The two components were studied to determine the cause of the joint failure.

Metallographic examination revealed that the tungsten and molybdenum remained bonded after the failure. The cause of the separation was a crack in the tungsten immediately adjacent to the bond line and around the entire circumference of the anode. Vaporization of nickel from the joint was not likely as a ring of tungsten had remained bonded to the molybdenum.

The crack which caused failure was tentatively attributed to one of two sources: (a) thermal shock caused by the mismatch in expansion coefficients of the two metals, or (b) by the embrittlement of the tungsten by the nickel. Studies were undertaken to correct this cracking problem. First, the amount of nickel used for bonding was reduced by vapor plating only the molybdenum prior to joining. Second, after joining the pieces, a furnace anneal of about 50 hours was used to diffuse the nickel more completely away from the bonding interface. Both of these procedures reduce the nickel concentration in the tungsten adjacent to the joint and lessen the possibility of embrittlement.

After affecting these changes in the bonding technique, another engine was fabricated and tested. During this test, the engine was deliberately abused, being operated at both high-power levels (60 kw) and low-mass flow rate in order to subject the joint to high temperatures. In all, the engine was operated intermittently slightly in excess of 10 hours. A crack finally developed in the nozzle section well away from the bond area and it is believed to have been caused by a flaw in the original material.

This successful bond resulted in adoption of the diffusion bonding technique for engines fabricated for operation at high temperatures, particularly involving the specific impulse range to 1500 seconds. Engine 68, in particular, was diffusion bonded. After it had been in operation at the 1500 second specific impulse level for a total time of 46 hours it was subjected to metallographic analysis.

Prior to metallographic study the engine was tested for gas tightness and all the joints proved to be leak free. The engine was then appropriately sectioned for preparation of the individual joint areas. The joint between the end of the tungsten anode and the molybdenum plenum was very well formed and free of voids and cracks. A typical portion of this joint is shown in figure 15, where the tungsten is the upper portion of the photomicrograph. The microstructural soundness of the joint is very evident in this figure.

The second tungsten-molybdenum joint is located approximately at the midpoint of the anode and the base of the plenum. A typical microstructure from this area is shown in figure 16, again with the tungsten uppermost. This joint was also very sound as can be seen by the absence of voids or cracks in figure 16.

The brazed joint microstructure between the TZM alloy (left portion) and the molybdenum is illustrated in figure 17. It can be seen that the iron flowed into the threads to join the two components. A few voids are apparent in the thread area but are not open to the surface as this area was leak tight.

In summary, following 46 hours of operation, the two diffusion bonded areas were structurally sound and well bonded (even after machining) indicating that satisfactory joints can be achieved by this technique. Iron is satisfactory for obtaining the gas tight joints between molybdenum and the TZM alloy.

5. Electron Beam Welding

An initial metallographic study of electron beam welded tungsten to molybdenum has been completed. The samples were joined at Electron Beam Techniques, Inc., Plainville, Connecticut. The sample geometry was a half circle about 1/16-inch thick. Arc cast molybdenum was used with three forms of tungsten; arc cast, sintered, and sintered and wrought. Past experience at Avco RAD with electron beam welding had shown arc test molybdenum to be superior to other types of molybdenum. It was free of pores which apparently released gas into the molten weld metal to create voids when the weld alloy solidified.[5] The objective of this investigation was to determine the weldability of several types of tungsten with arc cast molybdenum. Six samples of each form of tungsten electron beam welded to molybdenum have been returned to RAD for evaluation, in two groups. The first group contained two samples of each form of tungsten, while the second group contained four samples of each. The results of the metallographic study[6] are summarized below.

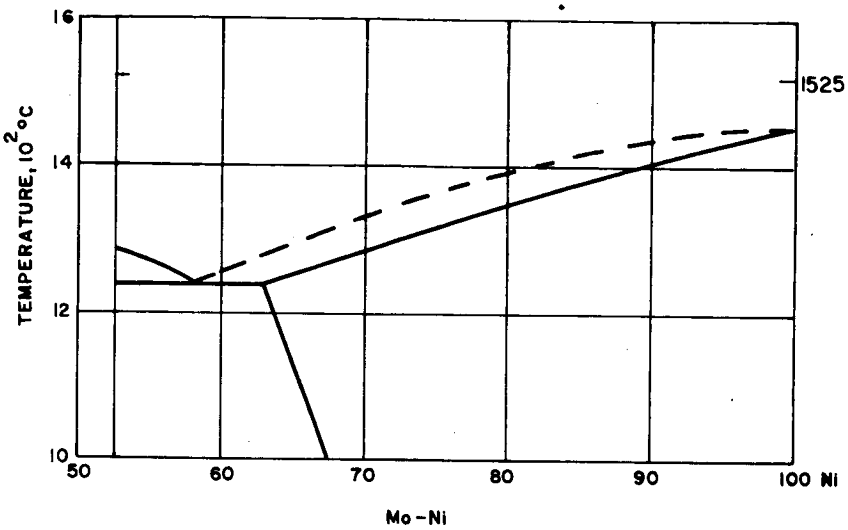

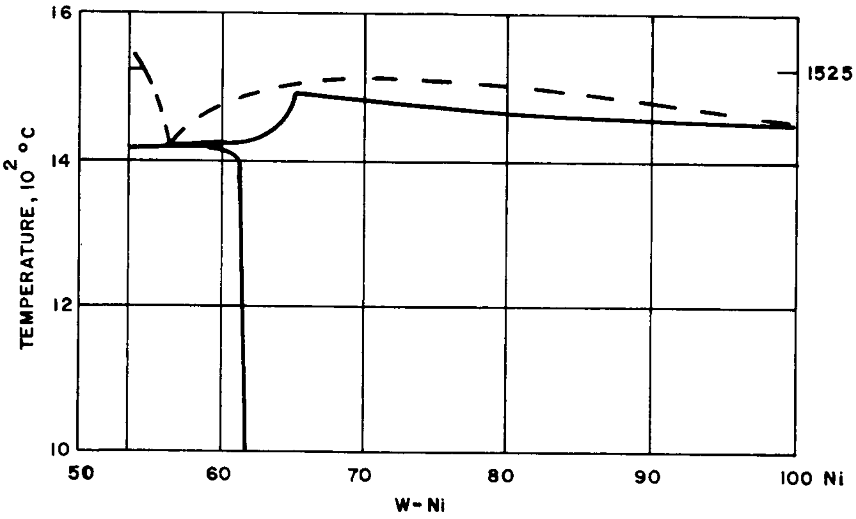

Figure 14 PARTIAL PHASE DIAGRAMS FOR MOLYBDENUM-NICKEL AND TUNGSTEN-NICKEL

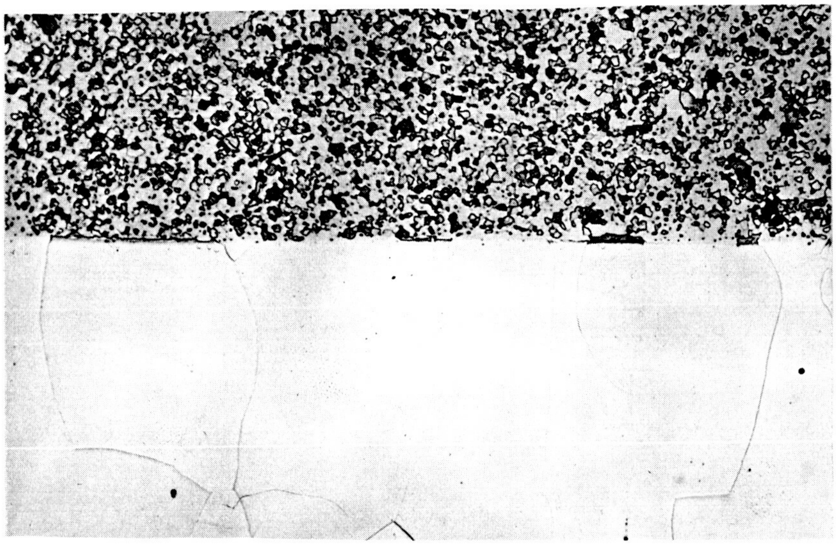

P3533C
250X

Figure 15 NICKEL DIFFUSION BOND AFTER 46 HOURS AT THE 1500 SECOND SPECIFIC IMPULSE LEVEL; R-4 MOD 3 (ENGINE 68), BOND AT UPSTREAM END OF NOZZLE

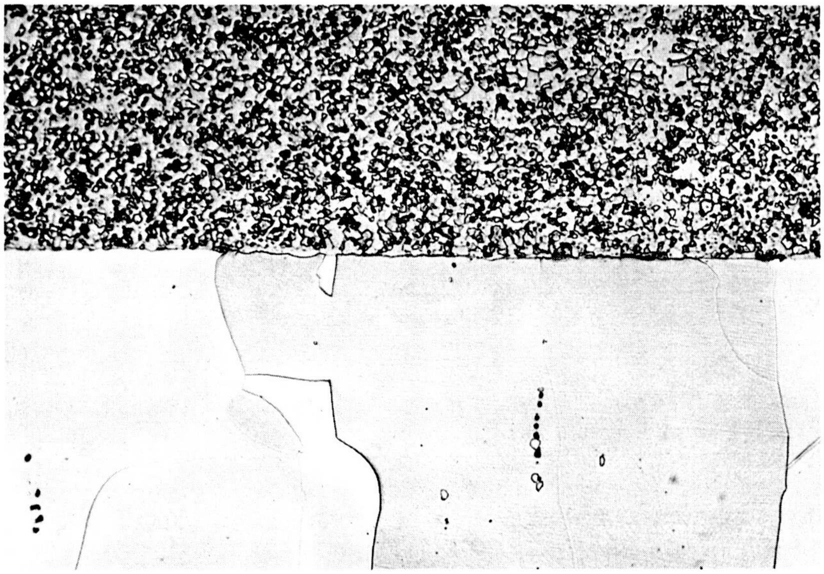

P3533D
250 X
64-14231

Figure 16 NICKEL DIFFUSION BOND AFTER 46 HOURS AT THE 1500 SECOND SPECIFIC IMPULSE LEVEL; R-4 MOD 3 (ENGINE 68), BOND AT DOWNSTREAM END OF PLENUM

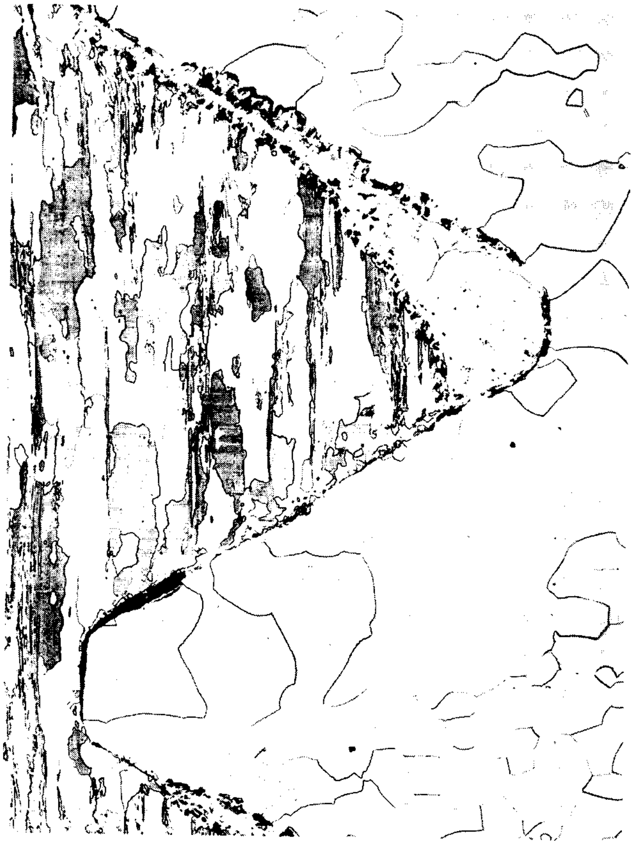
P35338

75X

64-14232

Figure 17 GAS INJECTOR-PLENUM BOND AFTER 46 HOURS AT THE 1500 SECOND SPECIFIC IMPULSE LEVEL; R-4 MOD 3 (ENGINE 68), TZM INLET TUBE, IRON BRAZE

a. First Group

The weld cross section of sample A-5 (sample designations originated with vendor) arc cast molybdenum to arc cast tungsten is shown in figure 18a. The open portion of the weld area at the bottom of the weld zone indicates lack of penetration by the electron beam during joining. No porosity is evident in the weld metal and no cracks are apparent. The heat affected zone (hereafter termed haz) in the tungsten is evidenced by the recrystallized structure which is quite different from the original acicular arc cast structure, oriented vertically in this specimen. The haz width in the tungsten extends from 0.005 to 0.015 inch from the weld while in the molybdenum it extends to 0.020 inch. The second specimen of this group, A-4 is a better weld exhibiting a finer grain size, which should be less brittle than the large grain size of A-5, and complete penetration, figure 18b. The haz is not as large in this sample, being about 0.010 in both base metals. No cracks are evident.

The weld zone microstructure of sample S-6, sintered tungsten to arc cast molybdenum, is shown as figure 18c. It is not possible to readily differentiate between the weld zone and haz for this sample. This sample was not welded through the entire cross section. This lack of penetration suggests that the total heat input to this sample was less than for the other samples and, consequently, the haz is quite small. The solidified weld metal is free of porosity and of cracks. Sample S-7, figure 18d, is joined through essentially the entire cross section although the very bottom of the weld does not exhibit a cast structure. Two large pores are evident in this weld presumably from the entrapped gases in the pores of sintered tungsten. The haz in the tungsten is negligible and extends about 0.005 to 0.010 inch maximum into the molybdenum. The sample showed no cracks.

The last set of welds examined were sintered and wrought tungsten to arc cast molybdenum. The deformation process closed most of the pores in the sintered tungsten thereby eliminating the source of potentially troublesome entrapped gases. Sample W-1 lacked complete penetration during welding, see figure 18e. The weld area is a mixture of coarse and fine grain sizes but is free of porosity and cracks. The haz is about 0.005 to 0.015 inch in both parent metals. A portion of this sample was dropped onto the floor during metallographic preparation and fractured in the weld metal.

This serves as a qualitative indication of the brittleness of the weld. The weld microstructure of the second sample of this group, W-2, appears as figure 18f. It appears to be the best weld of the six examined. There is complete penetration, no porosity, no cracking, and the haz is not unduly large, being about 0.010 inch maximum in either base metal.

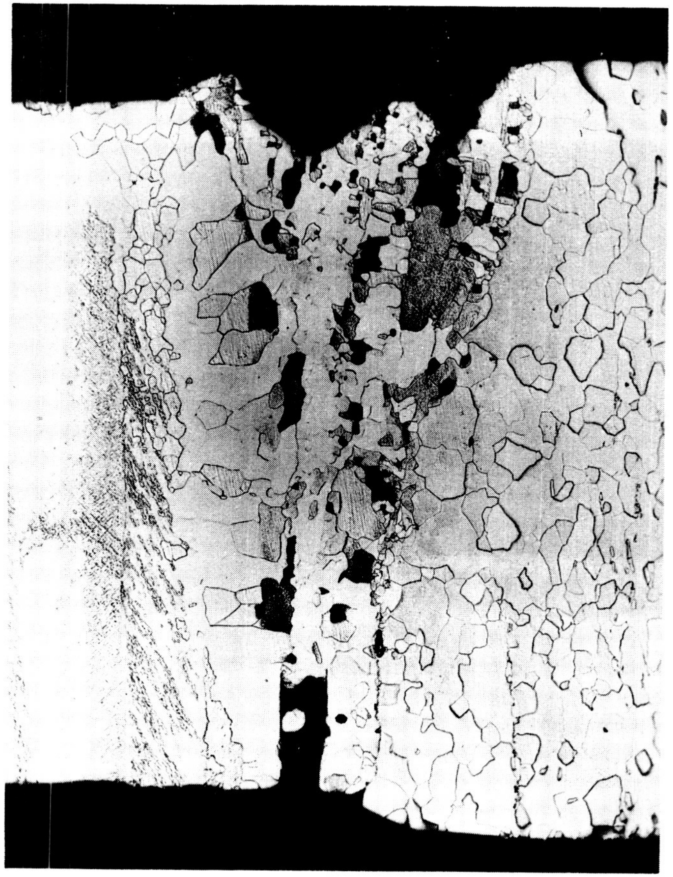

3523 B 75 X

Figure 18A

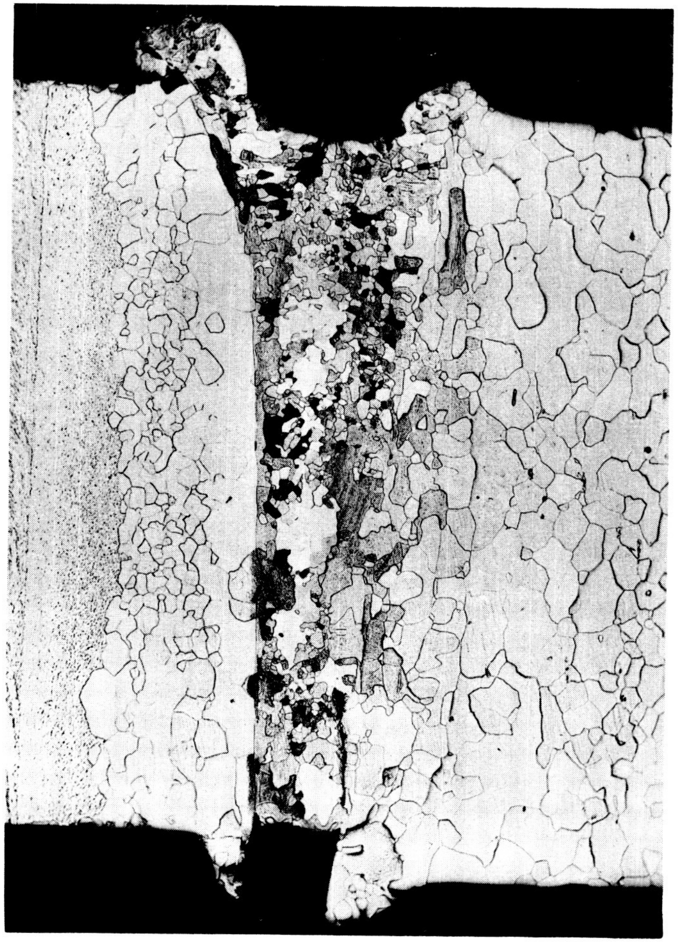

3523 C 75 X

Figure 18B

64-6229

ELECTRON BEAM WELDING SAMPLES; PHOTOMICROGRAPHS OF THE FIRST GROUP

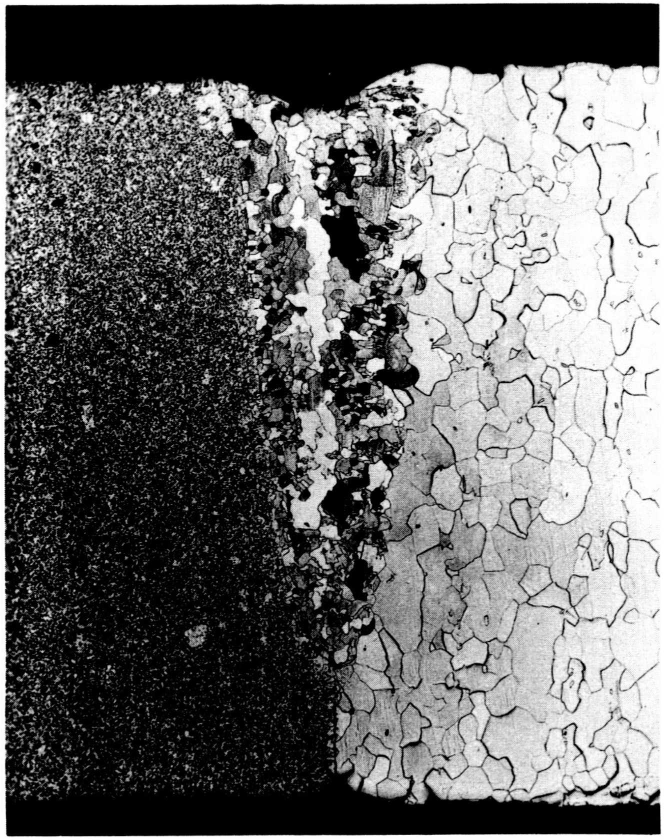

3523 A 75 X

Figure 6a PHOTOMICROGRAPH OF WELD CROSS SECTION; ARC CAST MOLYBDENUM AND SINTERED TUNGSTEN

64-6230

Figure 18C

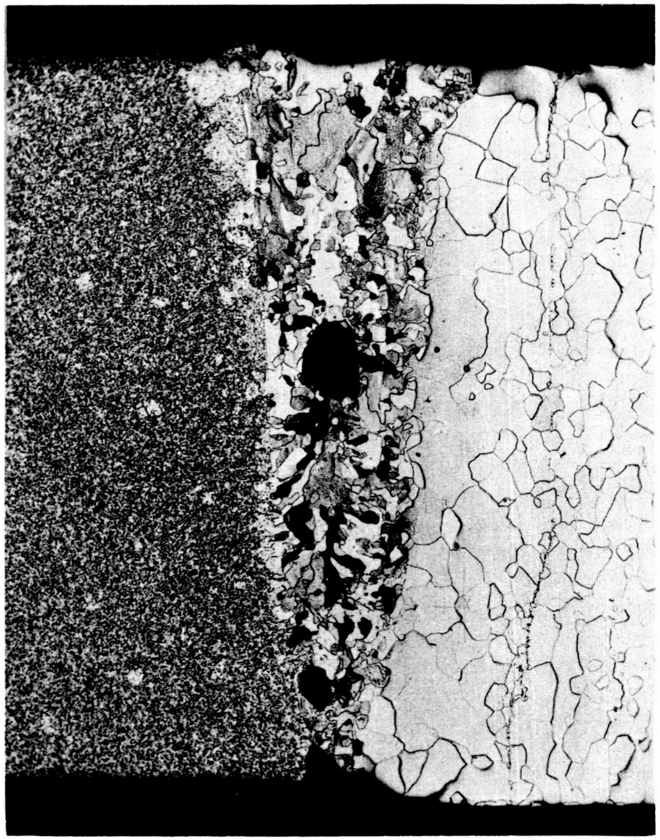

3523 75 X

Figure 6b PHOTOMICROGRAPH OF WELD CROSS SECTION; ARC CAST MOLYBDENUM AND SINTERED TUNGSTEN

Figure 18D

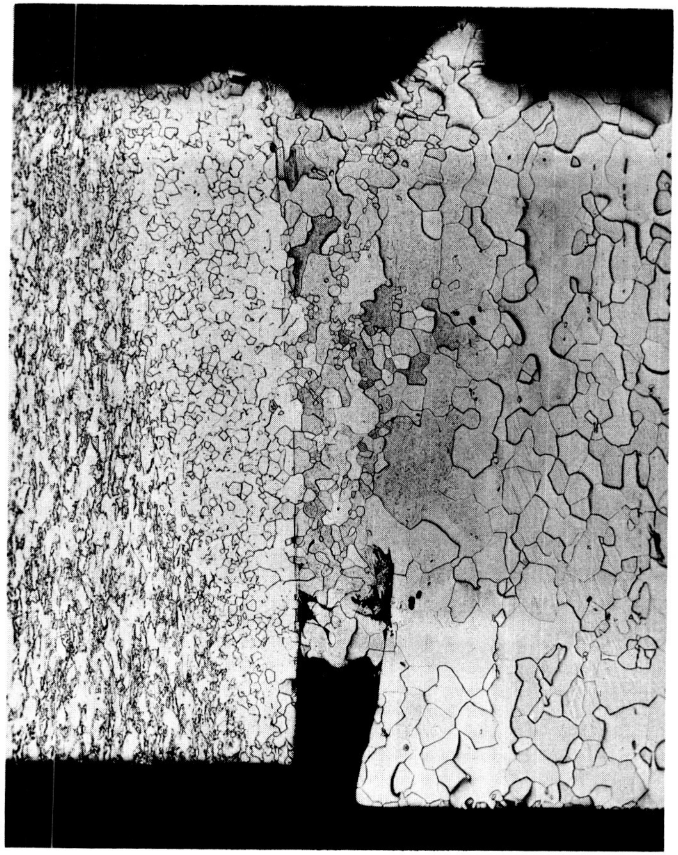

3523 E 75 X

Figure 7a PHOTOMICROGRAPH OF WELD CROSS SECTION; ARC CAST MOLYBDENUM AND SINTERED PLUS WROUGHT TUNGSTEN

64-6231

Figure 18E

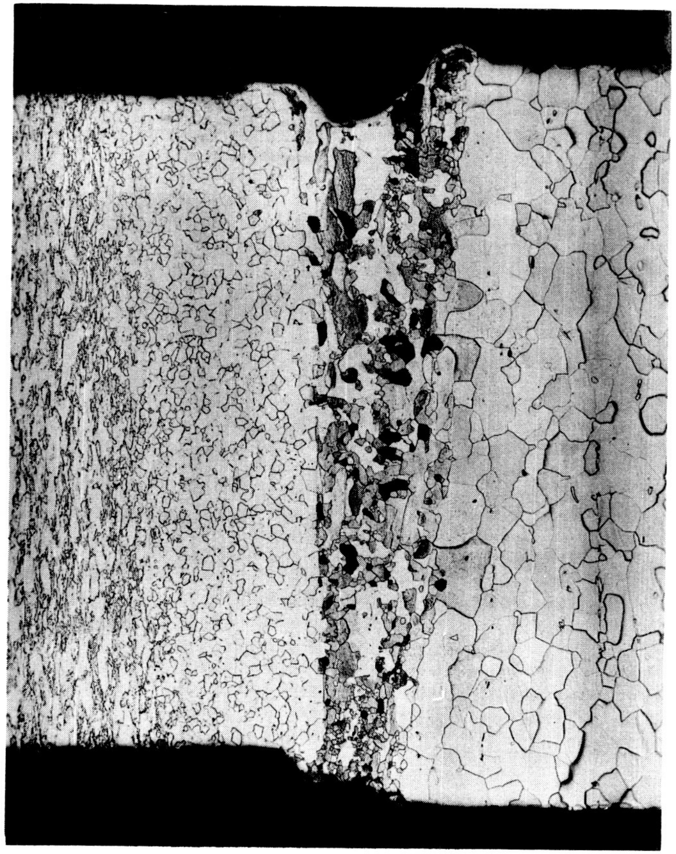

3523 D 75 X

Figure 7b PHOTOMICROGRAPH OF WELD CROSS SECTION; ARC CAST MOLYBDENUM AND SINTERED PLUS WROUGHT TUNGSTEN

Figure 18F

Concurrent with the weldability determinations, machinability tests of three forms of tungsten were conducted. The sintered tungsten with 2 percent thoria machines readily and is the material currently used for the 30-kw engine program. The cast and the sintered and wrought tungsten contained no thoria. These materials were extremely difficult to machine, to the extent that diamond tooling was necessary. The machining time was extended relative to that for sintered tungsten.

b. Second Group

An additional 12 samples of electron beam welded tungsten to molybdenum were then processed. Table 8 details the welding history of the samples as supplied by the vendor. The heat affected zone (haz) width was determined at RAD. The sample letter designations refer to the type of tungsten used, as follows: A-arc cast, S-sintered, W-wrought. In all cases arc cast molybdenum was employed. The figure number for each sample photomicrograph is also given.

TABLE 8

WELDING HISTORY OF SECOND GROUP OF ELECTRON BEAM WELDING SAMPLES

Sample Number	Figure Number	Number of Weld Passes	Filler Material	Comments	Haz Width	
					W(in x 10^3)	Mo(in x 10^3)
S-8	19a	1		cracked	0-5	6-8
S-9		2		cracked		
S-10	19b	1	Re		0-5	6-12
S-11	19c	2	Re	cracked	0-5	9-12
W-3	19d	1			15-20	12-15
W-4	19e	2		cracked	18-22	15-20
W-5	19f	1	Re	cracked	15-20	15-20
W-6	19g	2	Re	cracked	15-20	15-20
A-6	19h				12-14	14-16
A-7	19i	2			18-20	18-20
A-8	19j	1	Re		9-12	9-12
A-9	19k	2	Re		9-12	9-12

After reviewing the samples, certain general comments can be made. The second group of samples are all welded through the entire cross section, an improvement relative to the first group of samples. No detectable microstructural improvement resulted from the second weld pass used with some of the above samples. In general, the heat affected zones were larger for the present samples than for those joined initially. This is a result of the more complete weld penetration for these samples which increased the heat input. However, the extent of the haz does not appear excessive. The addition of rhenium has little microstructural effect in the weld area. Its purpose is to impart a needed mechanical property, ductility, to the weld. This property has not been experimentally evaluated.

The vendor indicated that many of the sintered tungsten (2 percent thoria) samples were cracked after welding. Figures 19a, b, and c are representative of these welds. No cracks are apparent in the particular cross section shown in figure 19a but cracks are easily seen in figure 19b and in figure 19c. The crack has traversed the entire specimen. Sample S-9 separated along the entire weld length during metallographic preparation and is not shown. A small amount of porosity is evident in all the welds but is not of an excessive amount. The sintered tungsten appears to be unsatisfactory for electron beam welding.

The weld cross sections for the wrought tungsten samples are shown in figures 19d, e, f, and g. The cracks present in the samples do not appear in those particular cross sections. Minor amounts of porosity are present in the welds. The rhenium alloying addition resulted in a slightly more homogeneous weld metal but did not eliminate the cracking. Wrought tungsten did not weld satisfactorily in this series.

The series of weld samples employing arc cast tungsten are shown in figures 19h, i, j, and k. These samples are both crack free and free from porosity. Again the rhenium alloying addition made a more homogeneous weld metal. These are the superior welds for this series of 12 samples.

Thus, two groups of weld samples, a total of 18 specimens, have been examined macroscopically and microscopically. The superior welds were obtained with the arc cast tungsten to the arc cast molybdenum. The sintered and the wrought tungsten when welded to arc cast molybdenum displayed sufficient amounts of porosity and cracks to make them poor choices for additional study. The rhenium addition should impart some ductility to the weld metal, but this property has not been determined. Microstructurally, the rhenium exerts no great effect. However, of the three types of tungsten welded, only the sintered displays good machining properties. It is necessary to evaluate weldability and machinability when selecting a material for use in the engine. If the machining characteristics of arc cast and wrought tungsten are such as to rule them out of the program, then one is forced to further evaluate sintered material for welding. If the former two materials can be machined satisfactorily, then arc cast tungsten has proved to be the superior material for welding.

F. CONCULSIONS ON STATUS OF ENGINE DEVELOPMENT

1. Engine Performance

At the conclusion of this Third Year Development Program engines at various stages of development have been operated in the specific impulse range from 1000 to 7400 seconds, using hydrogen as the propellant. Particular attention has been paid to the range 1000 to 1500 seconds, which is at the furthest development stage. Here a series of 30 kilowatt radiation cooled engines (the R-4 series) have been run continuously for significantly long times. At the 2000 second specific impulse level a 200 kilowatt radiation cooled engine (X-1) has been tested. Finally, in the specific impulse range to 7400 seconds a liquid cooled arcjet engine (X-2) has been tested for short periods of time.

The performance of each of these engines is summarized in figure 20, which displays the variation of efficiency with specific impulse. Some of the information in figure 20 is also contained in figure 8. From figure 20 it can be seen that over almost the entire range of specific impulse arcjet engines achieve efficiencies of the order of 40 percent. There is a strong indication that the efficiency of the X-2 engine increases with specific impulse; further, since this engine is at the earliest stage of development, there is reason to believe that improvements in efficiency may be forthcoming with additional development.

2. Engine Lifetime

Up to a specific impulse level of 1300 seconds arcjet engine life of at least 10 days has been demonstrated, and at 1000 seconds a life of 30 days has been established. Both the test at the 1300 second specific impulse level (10 days) and the 1000 second specific impulse level (30 days) were voluntarily terminated with no signs of imminent engine failure, so that these values should be considered as lower limits. At the 1500 second specific impulse level of a life of 120 hours was demonstrated, but this test was ended by engine failure. As a consequence, the situation with regard to lifetime demonstration at the 1500 second specific impulse level is considered not satisfactory. It is probably that some further work in the engine materials area may be necessary to obtain long life at the high temperatures characteristic of 1500 second operation.

At the higher specific impulse levels no attention has yet been devoted to demonstrating engine life. For the X-1 engine the likelihood is that its lifetime can be improved by the same methods utilized in the R-series engine programs. The X-2 engine appears to operate according to different principles, and it is thought to be too early to speculate about lifetime for this propulsion configuration.

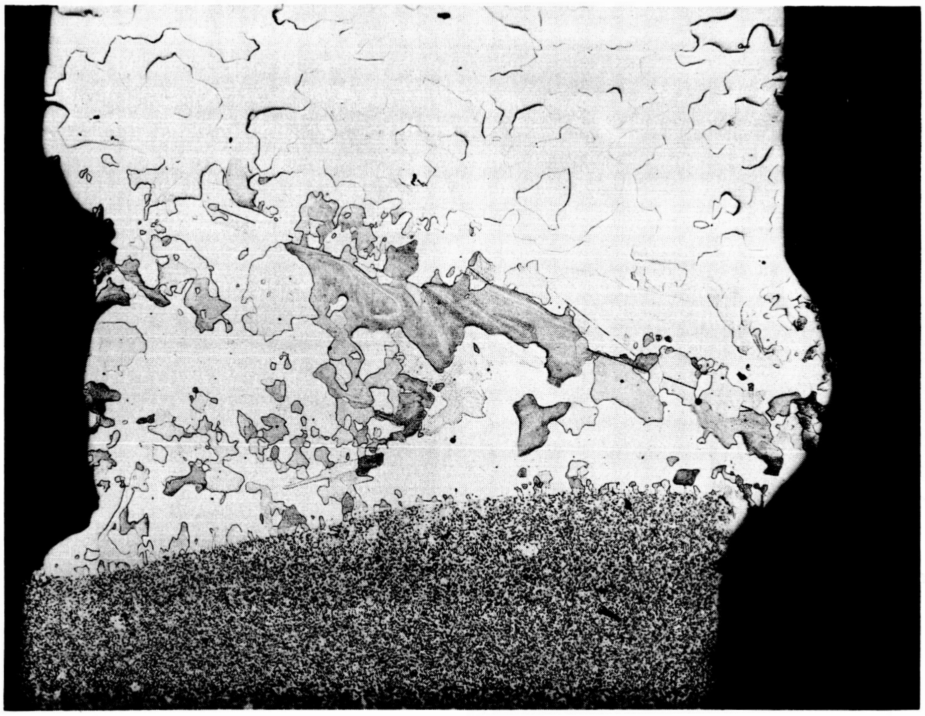

3535 G

Figure 19A

75 X

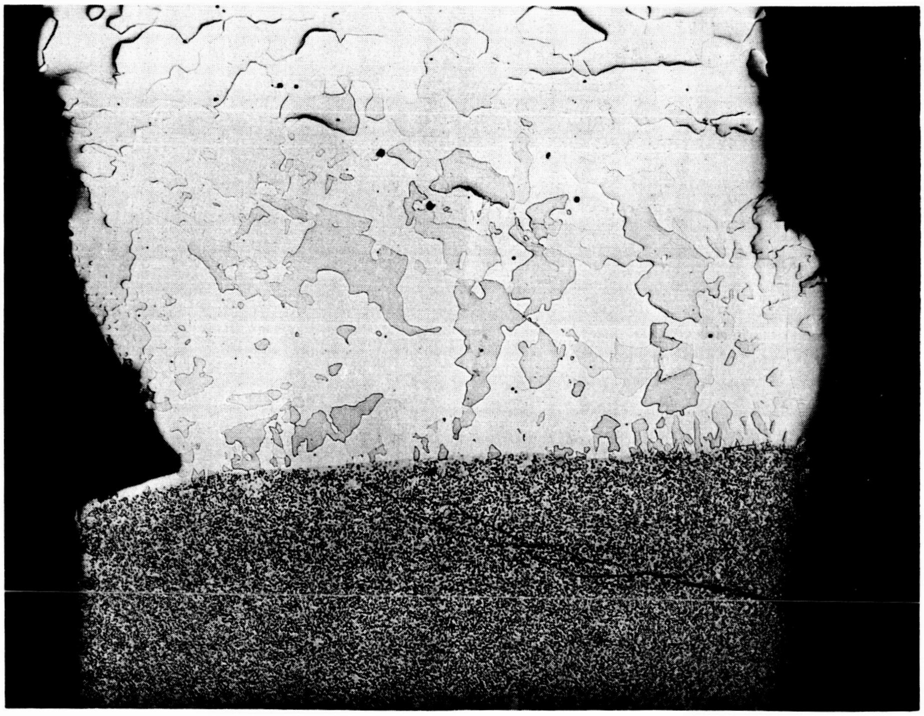

64-14233

3535 I

Figure 19B

75 X

ELECTRON BEAM WELDING SAMPLES; PHOTOMICROGRAPHS OF THE SECOND GROUP

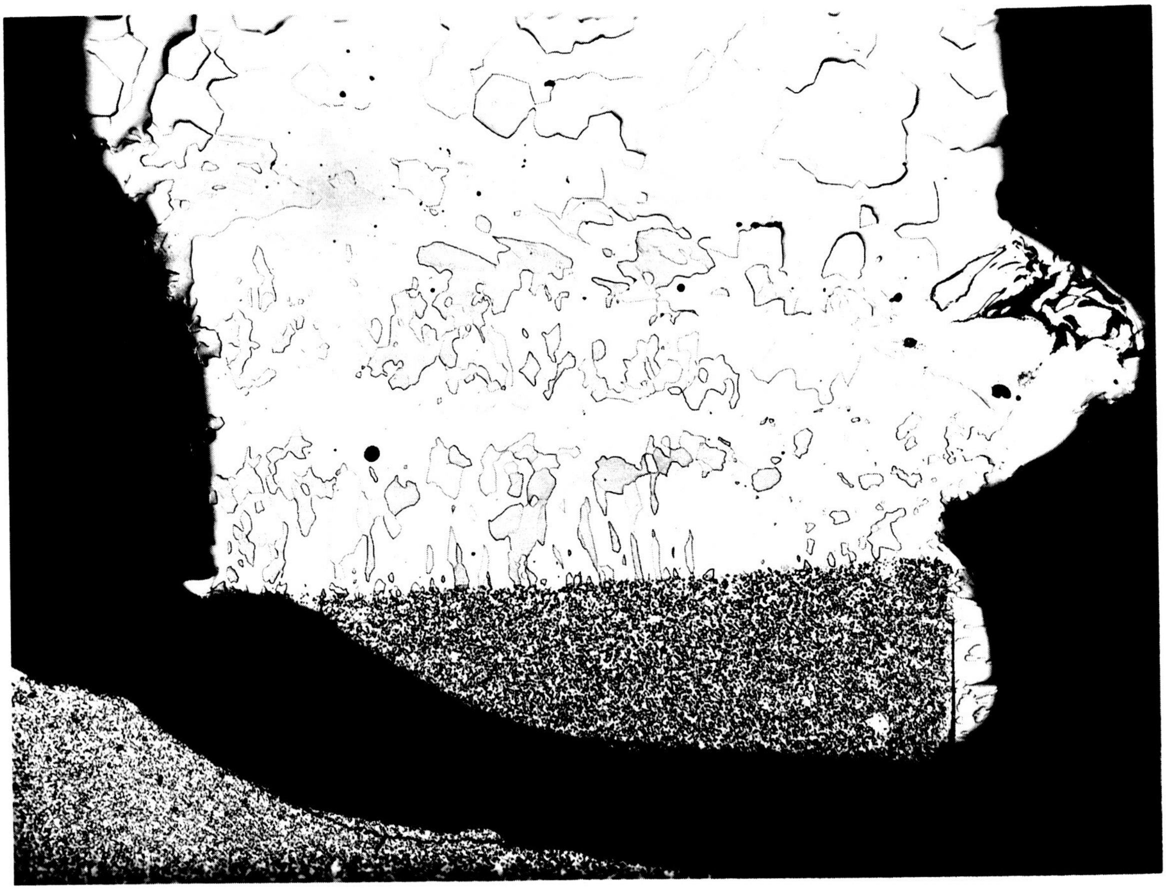

3535 J

75 X

64-14234

Figure 19C

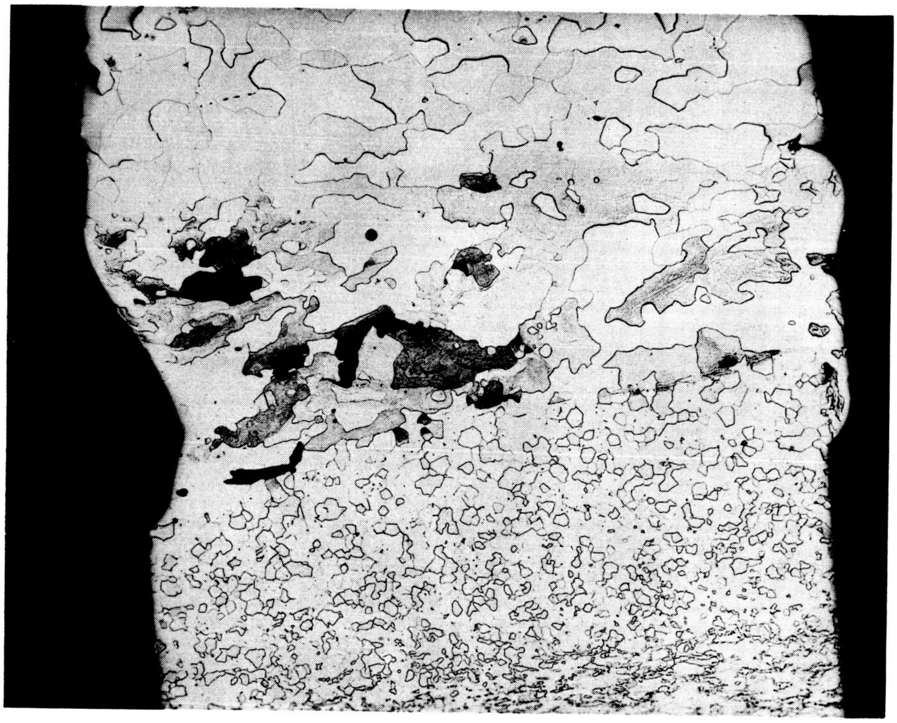

3535

Figure 19D

75 X

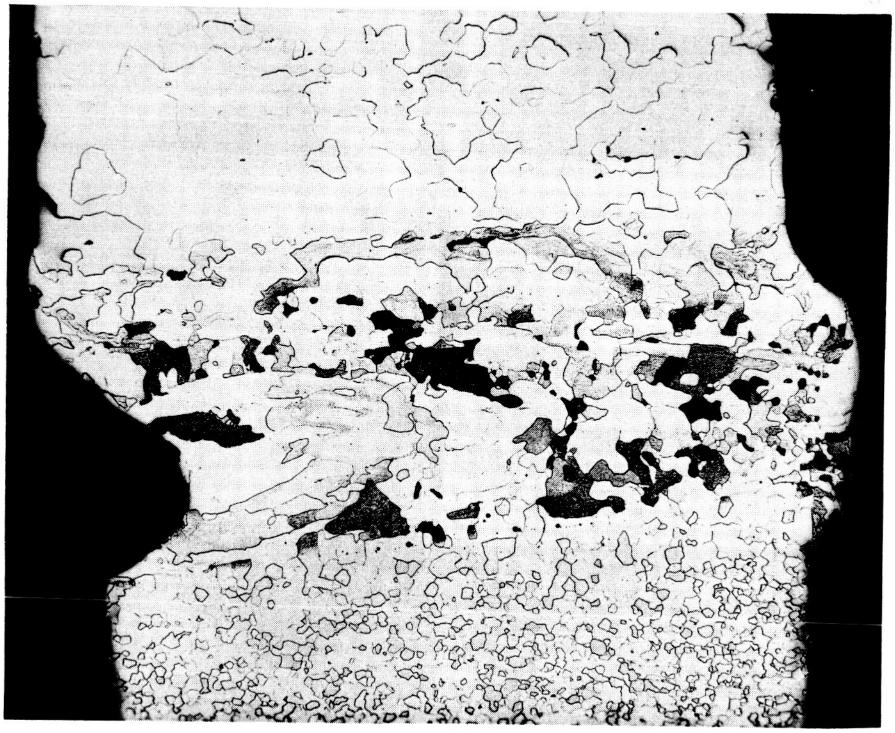

64-14235 3535 A

Figure 19E

75 X

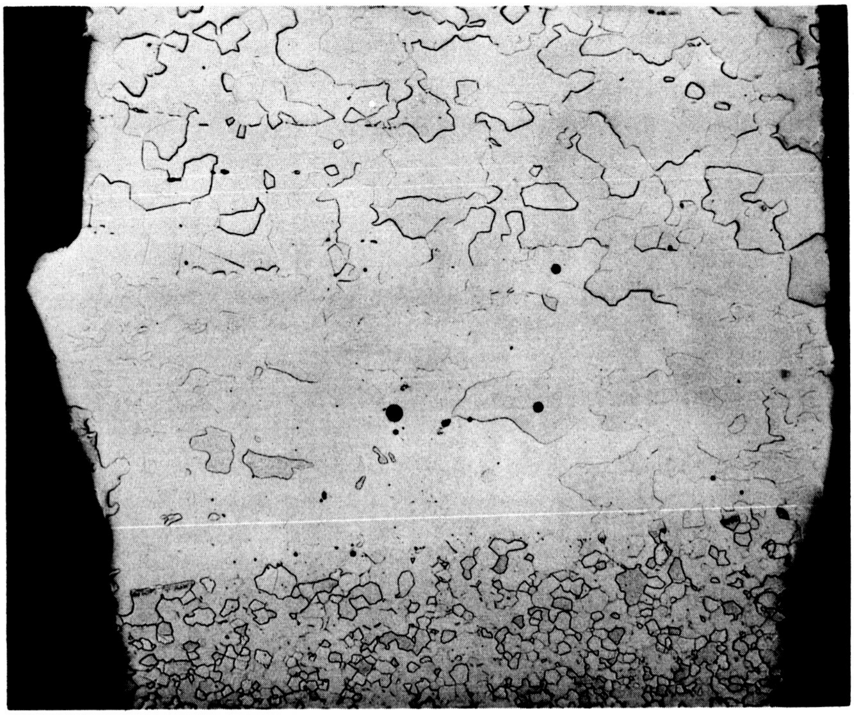

3535 B

Figure 19F

75 X

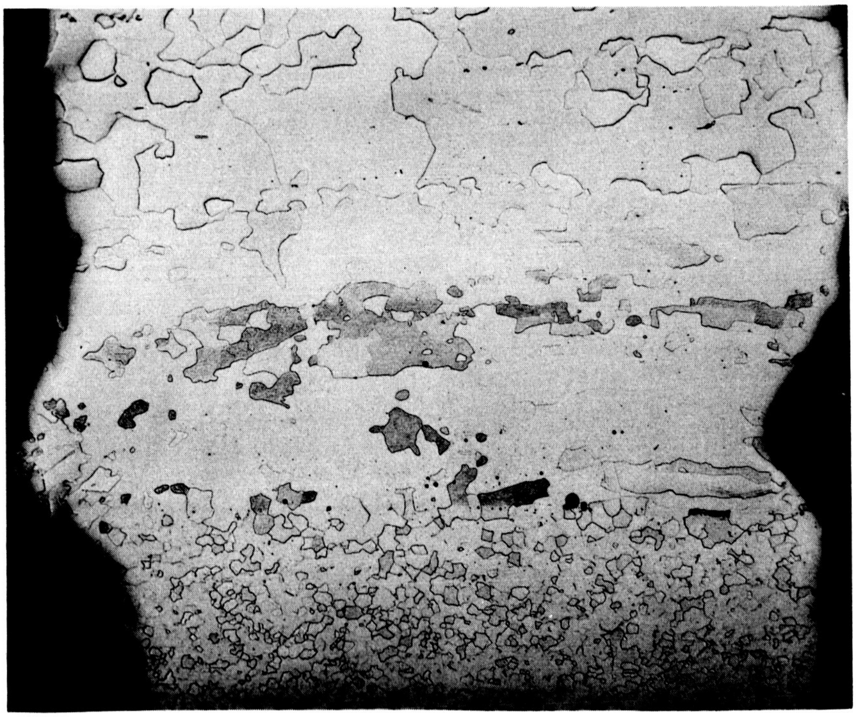

64-14236 3535 C

Figure 19G

75 X

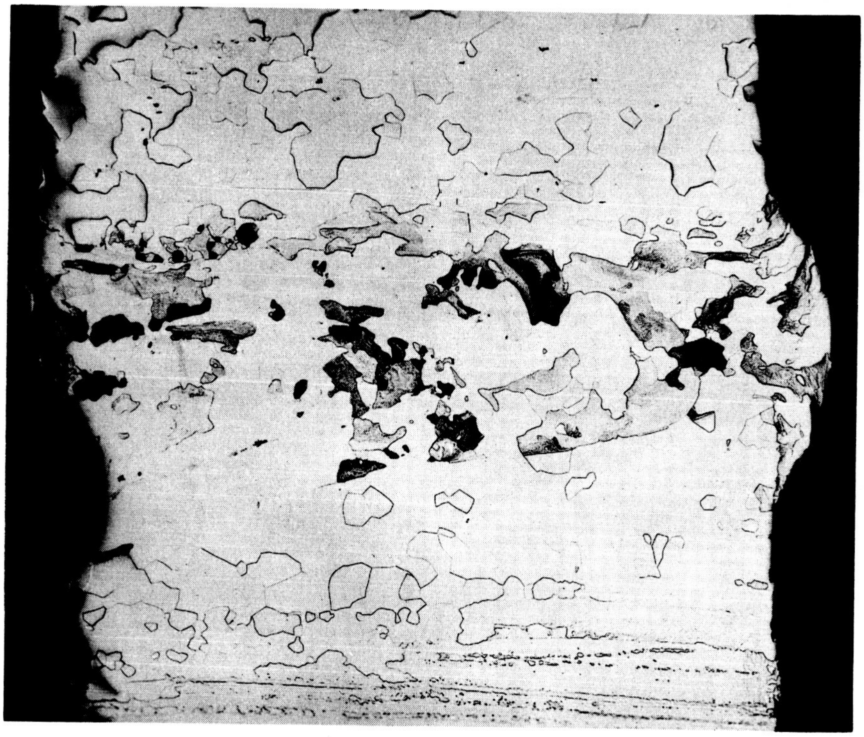

3535 D

Figure 19H

75 X

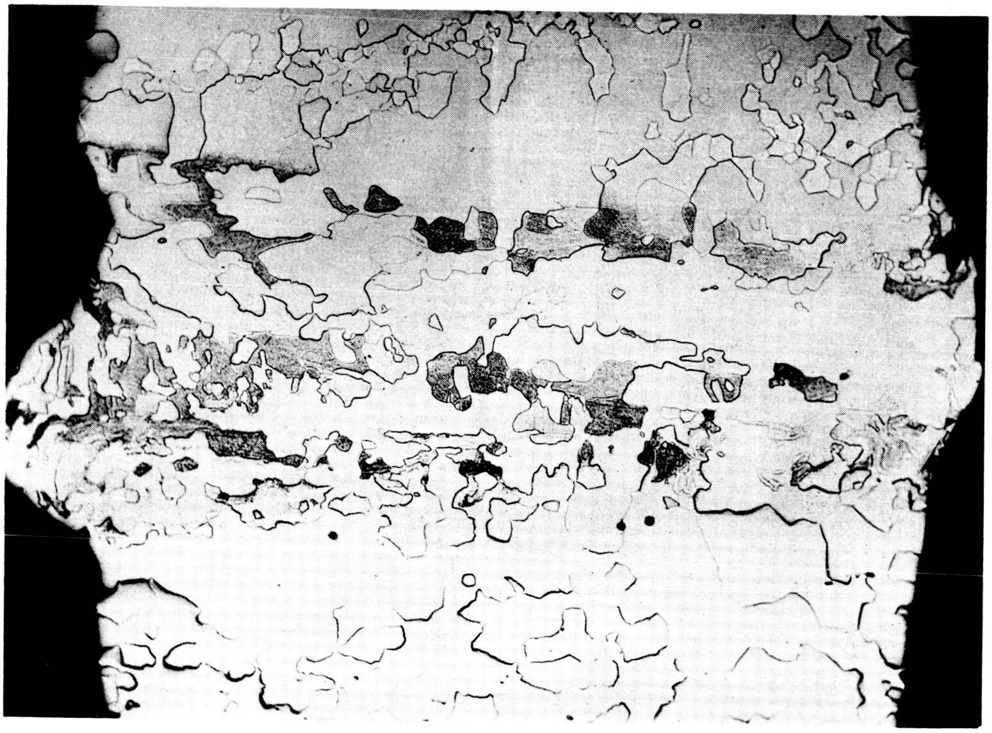

64-14237 3535 E

Figure 19I

75 X

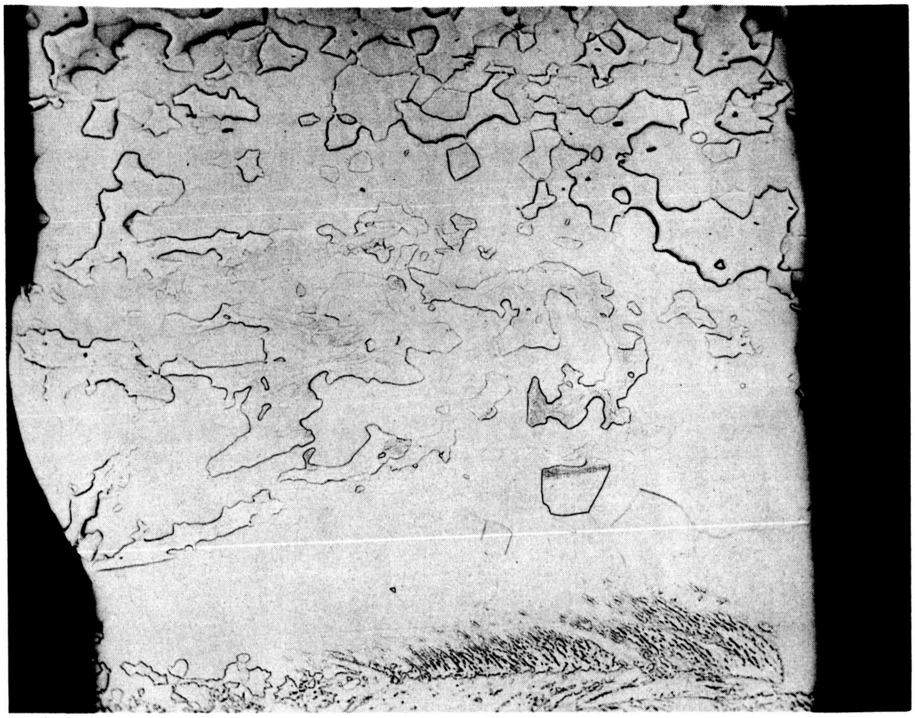

3535 F

Figure 19J

75 X

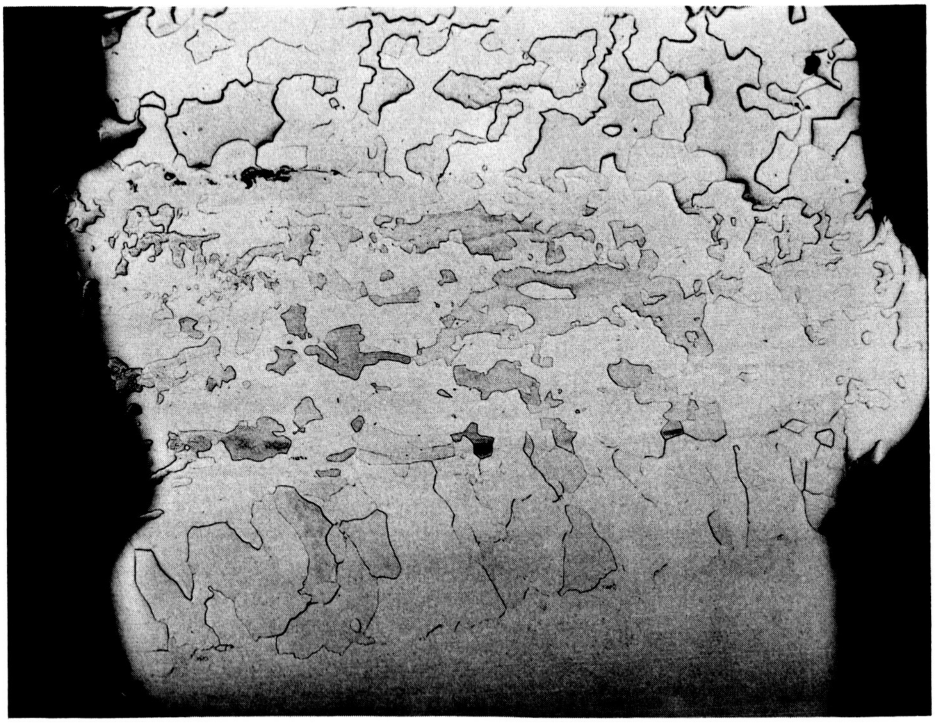

64-14238 3535 H

Figure 19K

75 X

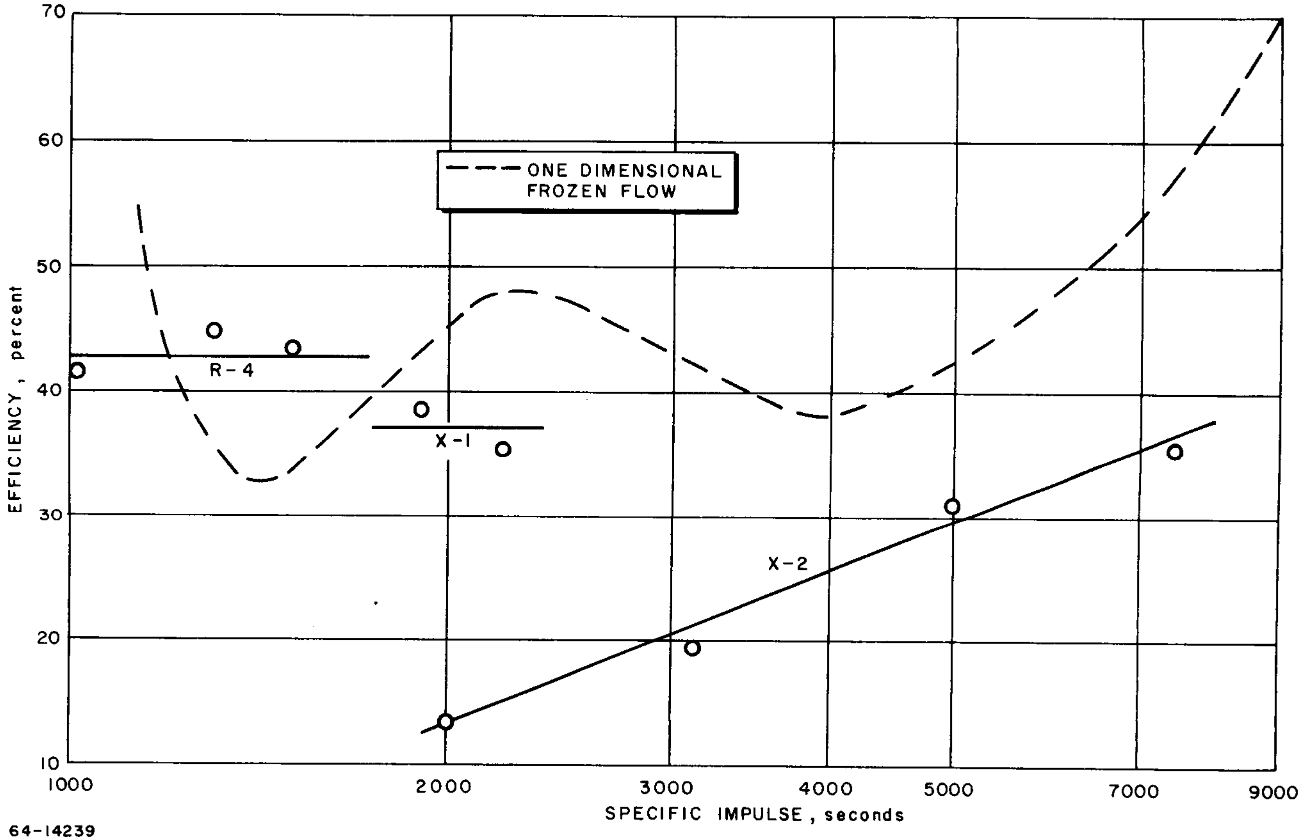

64-14239

Figure 20 EFFICIENCY VERSUS SPECIFIC IMPULSE; R-4, X-1, AND X-2 ARCJET ENGINES

III. APPLIED RESEARCH

A. INTRODUCTION

The applied research has been in three general areas; engine optimization studies, arc column studies and exhaust jet diagnostics. The optimization study has concerned itself with the effect of varying different portions of the internal geometry of the engine on operation and performance characteristics. The geometrical features that have been studies are the supersonic nozzle angle, the cathode tip shape and the position of the cathode within the plenum chamber.

The arc column study has five areas of investigation. The first section deals with an experiment to measure the axial voltage gradient in the constrictor section of the arc jet engine. The experimental results are discussed in terms of various analytical models which have been advanced to describe the constricted arc column.

Next, a two-fluid model for the constricted arc column is described. The model has been used to obtain a solution for a representative engine geometry and operating condition and these predictions are discussed in terms of the available relevant experimental data.

The next section deals with a calculation to find to what extent dissociative equilibrium exists in the throat (downstream) region of the constrictor. Section four describes an investigation of the nature of the arc attachment process in the anode section (supersonic nozzle) of the arcjet engine. The last section presents a series of measurements carried out to determine the effect on arc operation of varying flow rates of four different gases; hydrogen, nitrogen, ammonia and helium. These results are interpreted in terms of yielding information concerning those parameters which fix the arc voltage for a given arc current.

The diagnostic study of the exhaust jet mainly deals with the use of mass flux and impact pressure probes to obtain, eventually, the radial velocity and density profiles at the nozzle exit plane. The experimental results are interpreted using the Heller-Elenbaas model of the constricted arc as a framework. Further, the overall energy balance for the arcjet engine is discussed including a rough estimate of the frozen flow loss due to ionization and dissociative non-equilibrium that occurs in the supersonic expansion.

B. ENGINE OPTIMIZATION STUDIES

1. Introduction

The R-series 30 kw engines consist of a plenum chamber where the propellant is injected and where the body portion of the cathode resides, a converging section where the cathode tip is located, a constant area section, called a constrictor, in which the arc column is found and a supersonic nozzle which acts as the anode where the arc terminates. (See figure 21). The geometrical arrangement of the various portions which make up the engine influences the performance of the thrustor.

In this section is presented an experimental study of the results of varying certain features of the geometrical makeup of the engine in terms of the effect on arc current, thrust and overall thrust efficiency. The geometrical factors that have been isolated for study are the cathode tip shape, location of the cathode tip within the converging section connecting the plenum chamber to the constrictor and the expansion angle in the supersonic nozzle.

2. Cathode Shape and Gap-Length Variation

A systematic study has been carried out to determine the effect on the operating characteristics of the 30 kw arcjet engine due to various cathode-tip shapes and the position of the cathode within the inlet of the constrictor, as characterized by a gap length. The geometric meaning of the gap length is indicated in figure 22. The gap shape and gap length affect the inlet configuration which in turn could affect the portion of the flow in the constrictor which is ingested by the arc column.

A cathode of the shape normally used in propulsion engines (denoted as regular) has been employed as well as cathodes which are pointed, flat, and hollowed out at the tip to simulate erosion. Figure 23 shows the four different cathode-tip shapes employed in this investigation. For all cathodes, the included angle of the end of the cathode is the same (60 degrees).

The gap length is measured by inserting the cathode into the constrictor until contact is made between the cathode and the sides of the constrictor (see figure 22). The cathode is then withdrawn a distance which is termed the gap length.

The experiments were conducted on two different engines, denoted as engines 41 and 44. Engines 41 and 44 were built to the same specifications. After conducting one series of experiments on engine 41, the constrictor was bored out and a sleeve inserted with the effect that the 0.090-inch radius curve joining the constrictor and the converging conical section was transformed to a sharp corner. This modification is indicated in figure 24.

Engine 44 was operated at four gap settings for each of the four differently shaped cathodes. The positions of the cathodes within the body of the engine for each of the four gap settings are illustrated in figures 25 through 28. In every case, the minimum cross-sectional area of flow is the constrictor, i.e., in moving from the plenum chamber to the constrictor, the smallest cross-sectional area of flow is in the constrictor. The maximum cross-sectional area of flow varies between 9.5 and 11.5 times the constrictor area for the regular cathode as the gap setting varies from 0.090 to 0.0162 inch. The flow area in the plenum chamber is 4.85 times the constrictor area.

Tables 9 through 12 summarize the voltage-current and performance (thrust and overall efficiency) characteristics for the various gap settings for each of the four cathode shapes. In the discussion to follow, the data for engine 41 with the sharp corner (see figure 24) will not be included.

It is estimated that the thrust, mass-flow and efficiency measurements are accurate to 3, 3, and 6 percent (see appendix A). Referring to table 10, for a given current the voltage increases slightly while the efficiency and thrust show a slight maximum in going from a gap setting of 0.090 to 0.230 inch. In table 11, it is seen that for a given current, the voltage appears to be independent of gap setting while the efficiency and thrust indicate a minimum as the gap setting varies from 0:076 to 0.125 inch. Finally, for the hollow cathode, table 12 indicates that for a given current the voltage is approximately independent of gap setting while the efficiency and thrust fall off at the higher gap settings.

Figures 29 through 31 are plots of arc voltage, overall efficiency, and thrust versus current for each of three gap settings for the various cathode shapes. In figure 29, it is seen that for a gap setting of 0.090 inch at the higher powers, the pointed cathode gives consistently lower voltage, efficiency, and thrust for a given current than the other cathode shapes; the regular and flat cathode are quite similar. For the gap setting of 0.110 inch (figure 30), the pointed cathode also gives consistently lower arc voltages while the flat cathode results in a substantially lower efficiency. The hollow and regular cathode shapes are similar in thrust and consistently higher than the other cathode shapes. For the gap setting of 0.125 inch, again the pointed cathode leads to consistently lower arc voltages. The major consistent trend is that for all three gap settings the pointed cathode gives consistently lower arc voltages.

The data thus far presented are for a constant mass-flow rate of 0.25 gm/sec. Additional experiments have been conducted (engine 44) in which a constant power level of 30 kw is maintained but the mass-flow rate varied; the range of variation is from 0.175 to 0.25 gm/sec. Over this range, the arc voltage is relatively insensitive to mass-flow rate; in general, the arc voltage falls from between 10 and 20 volts as the mass-flow rate is decreased from 0.25 to 0.175 gm/sec. Hence, the arc current in general increases slightly with decreasing mass-flow rate. The overall efficiency shows a general trend of increasing slightly with decreasing mass flow rate although this increase is well within experimental error.

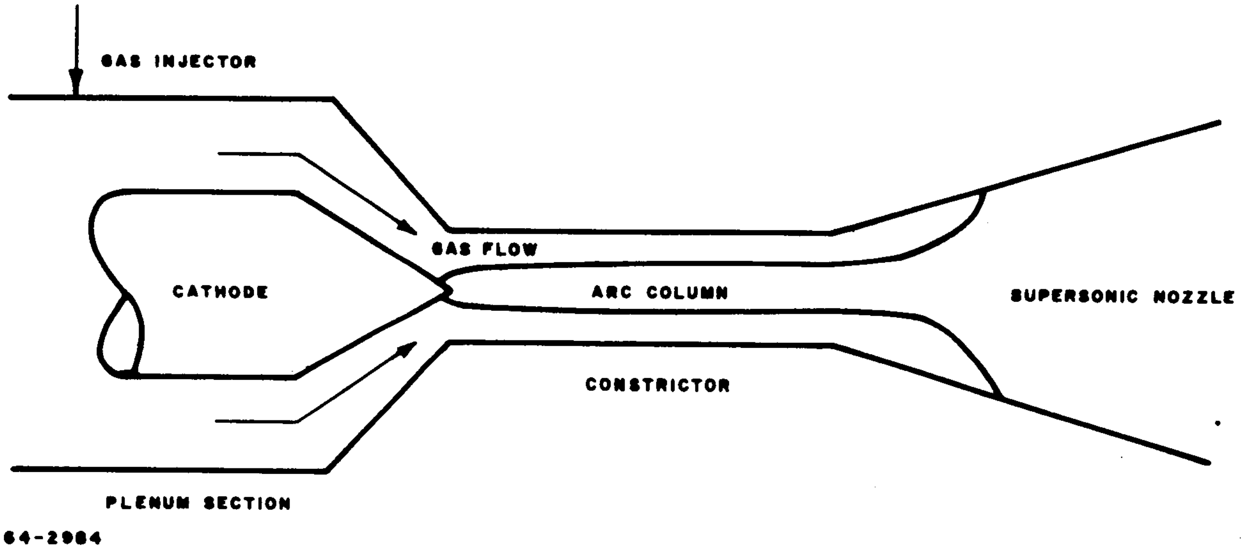
GAS INJECTOR
GAS FLOW
CATHODE
ARC COLUMN
SUPERSONIC NOZZLE
CONSTRICTOR
PLENUM SECTION
64-2984

Figure 21 SCHEMATIC ARC ENGINE OPERATION

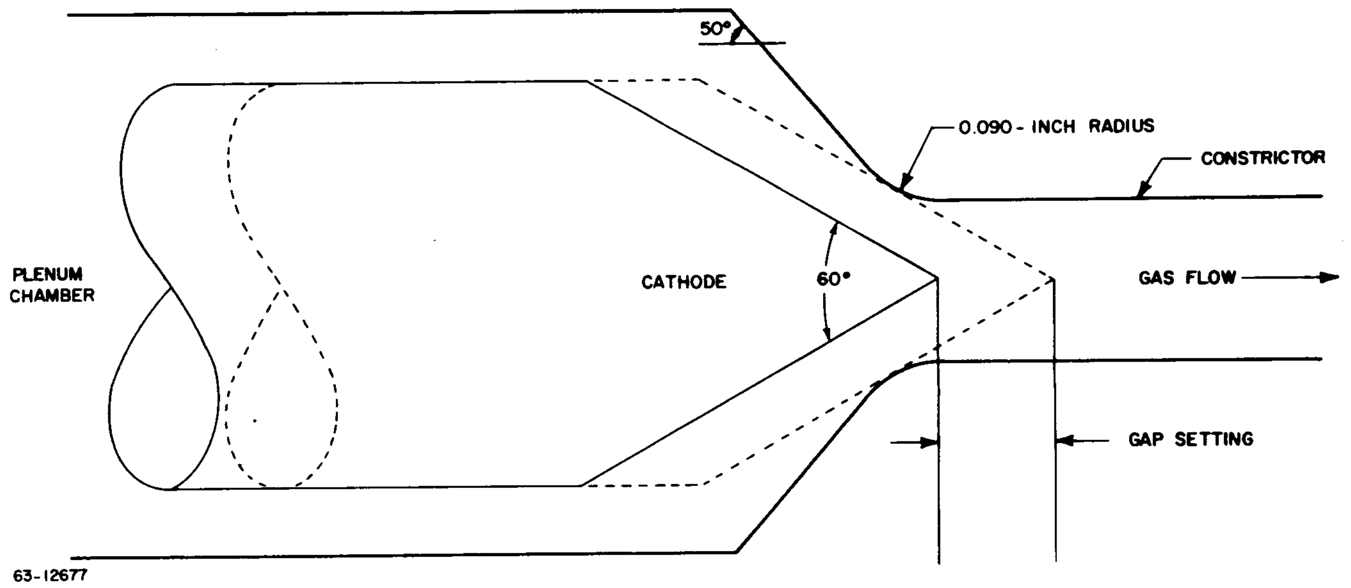
50°
0.090 - INCH RADIUS
CONSTRICTOR
PLENUM CHAMBER
CATHODE
60°
GAS FLOW
GAP SETTING
63-12677

Figure 22 SCHEMATIC DRAWING INDICATING THE GEOMETRIC MEANING OF GAP SETTING

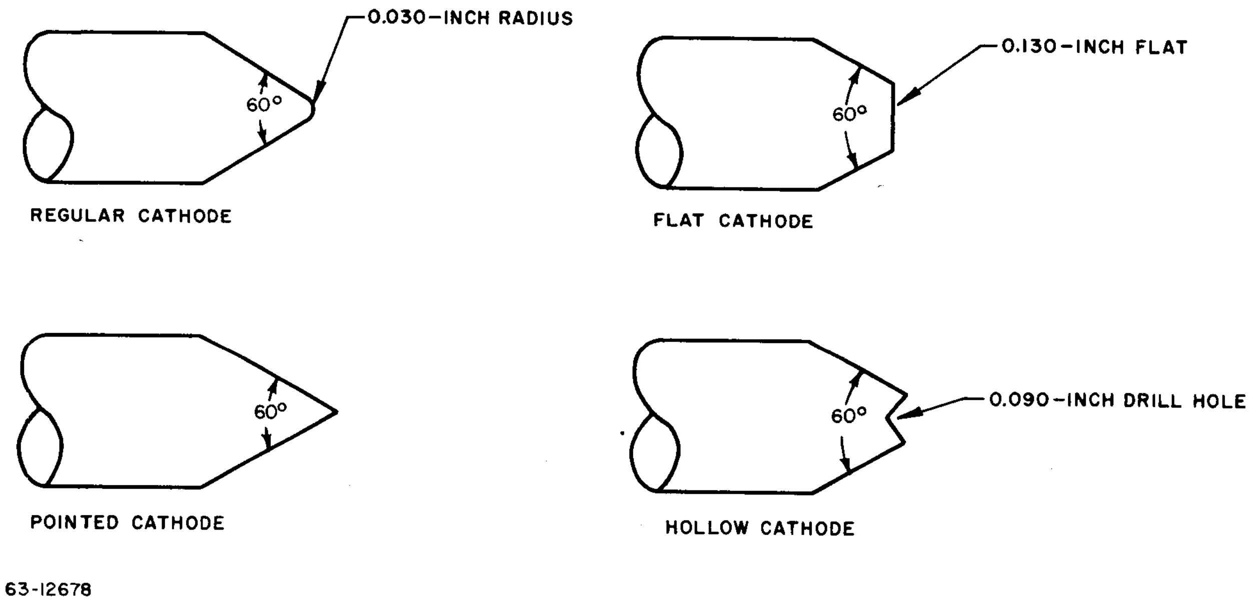
0.030-INCH RADIUS
60°
REGULAR CATHODE
0.130-INCH FLAT
60°
FLAT CATHODE
60°
POINTED CATHODE
0.090-INCH DRILL HOLE
60°
HOLLOW CATHODE
63-12678

Figure 23 SCHEMATIC DRAWING SHOWING FOUR CATHODE SHAPES

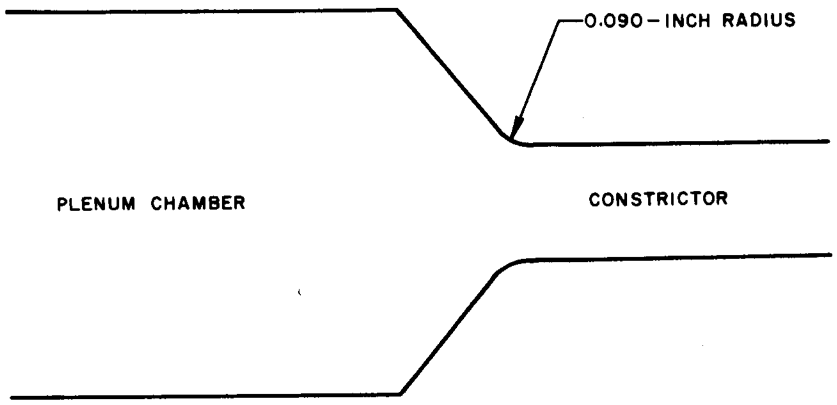
0.090 – INCH RADIUS
PLENUM CHAMBER
CONSTRICTOR

ENGINE 44 ; ENGINE 41 BEFORE MODIFICATION

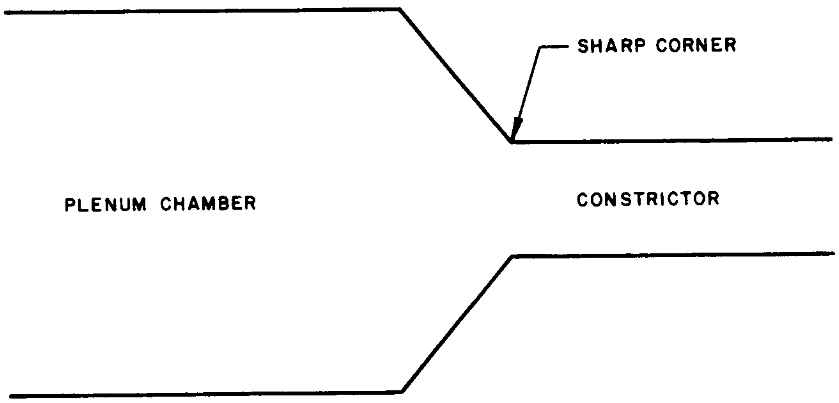
SHARP CORNER
PLENUM CHAMBER
CONSTRICTOR

ENGINE 41 AFTER MODIFICATION

63-12679

Figure 24 MODIFICATION OF ENGINE 41 TO OBTAIN SHARP CORNER

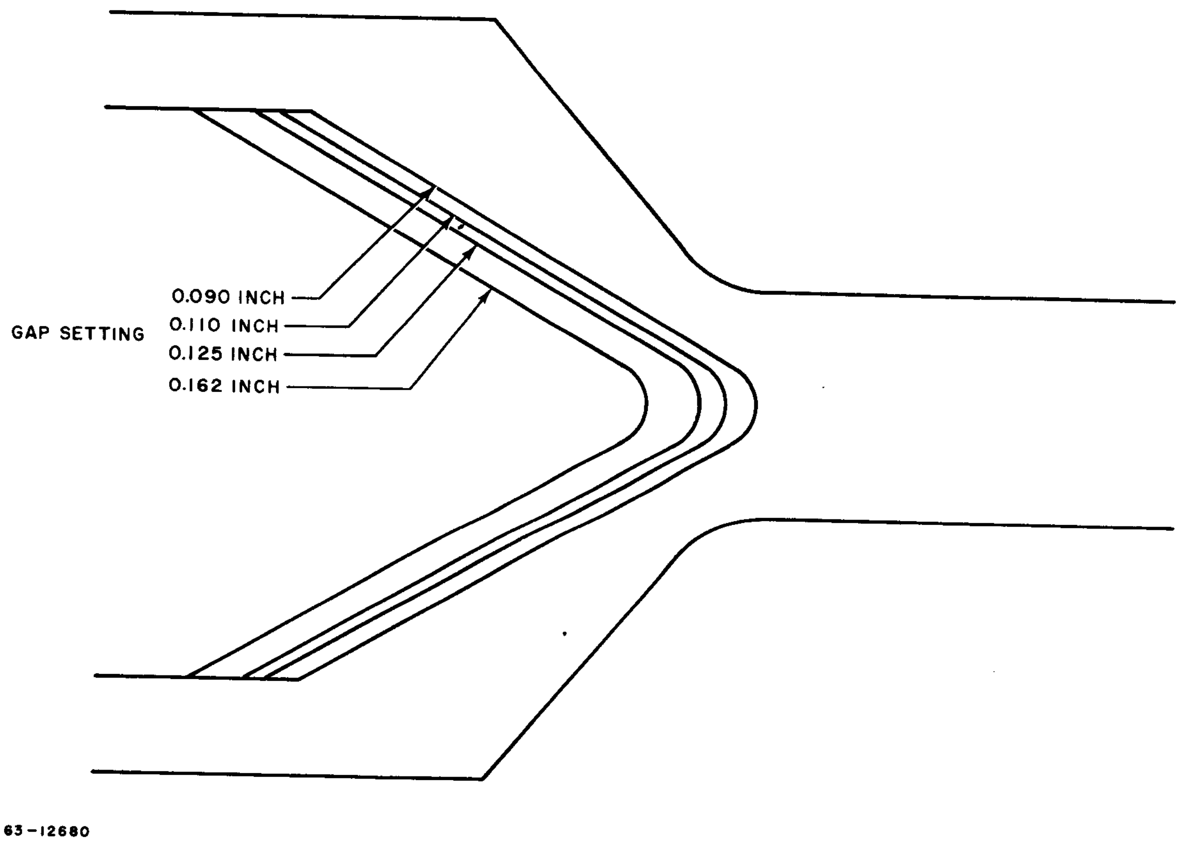
GAP SETTING
0.090 INCH
0.110 INCH
0.125 INCH
0.162 INCH
63-12680

Figure 25 POSITION OF REGULAR CATHODE FOR FOUR GAP SETTINGS

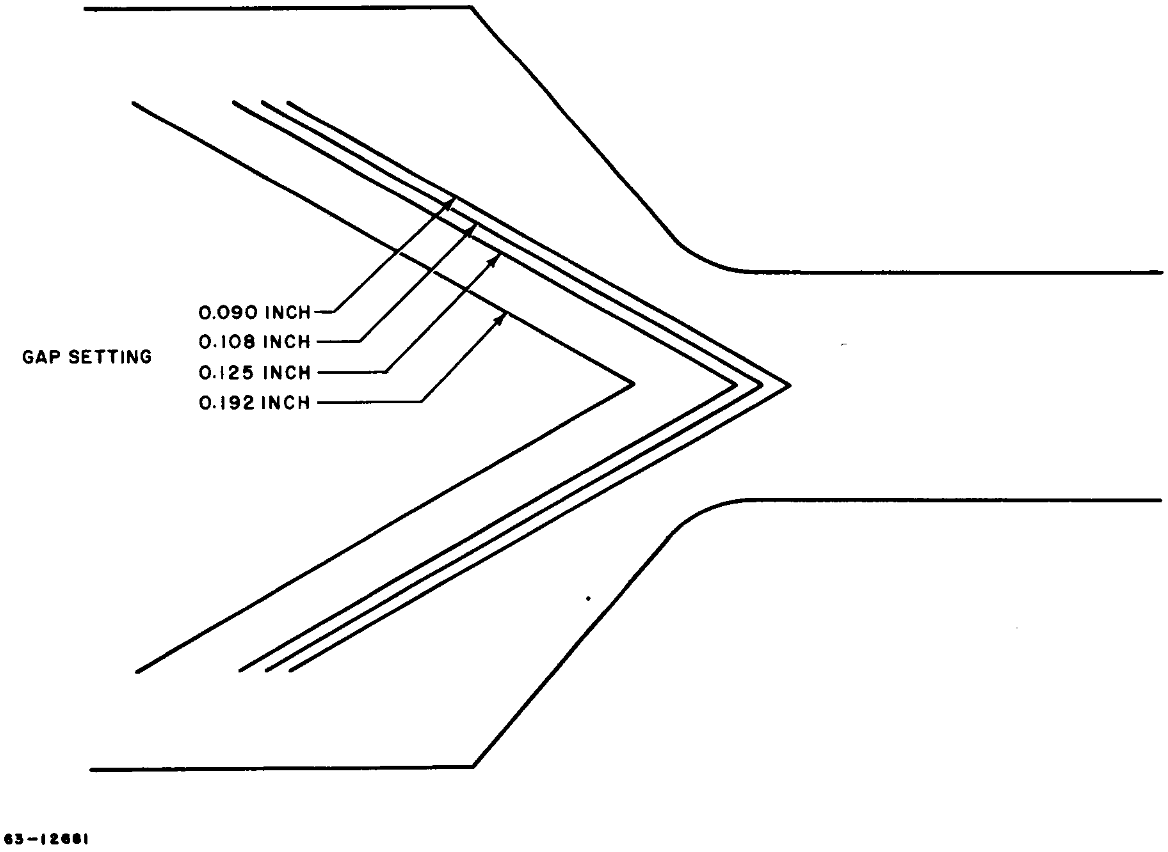
GAP SETTING
0.090 INCH
0.108 INCH
0.125 INCH
0.192 INCH
63-12681

Figure 26 POSITION OF POINTED CATHODE FOR FOUR GAP SETTINGS

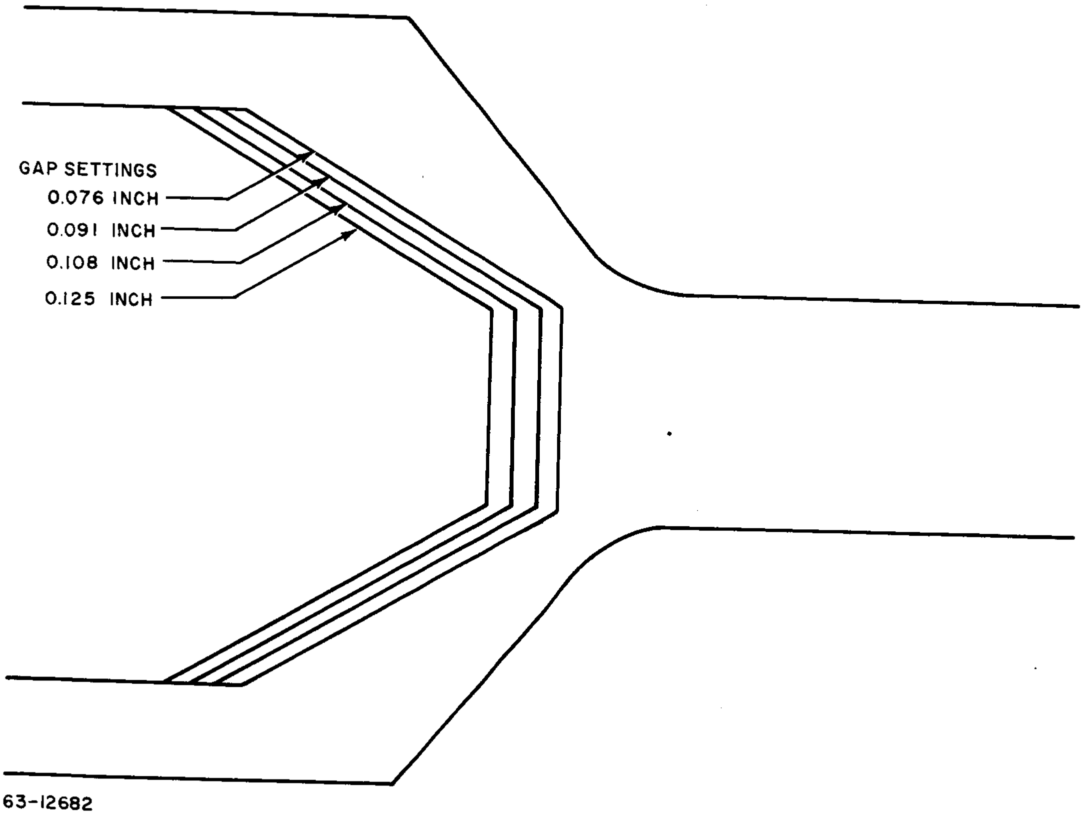
GAP SETTINGS
0.076 INCH
0.091 INCH
0.108 INCH
0.125 INCH
63-12682

Figure 27 POSITION OF FLAT CATHODE FOR FOUR GAP SETTINGS

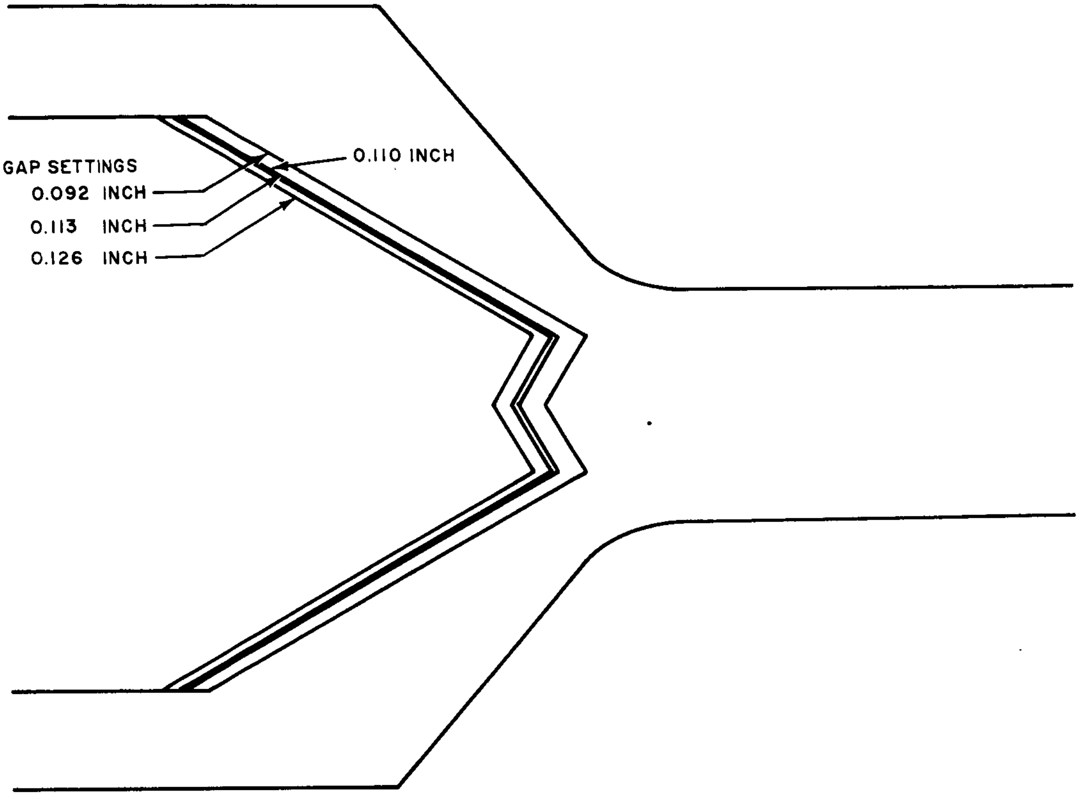
GAP SETTINGS
0.092 INCH
0.113 INCH
0.126 INCH
0.110 INCH

63-12683

Figure 28 POSITION OF HOLLOW CATHODE FOR FOUR GAP SETTINGS

TABLE 9. OPERATION AND PERFORMANCE CHARACTERISTICS FOR THE REGULAR CATHODE WITH DIFFERENT GAP SETTINGS, HYDROGEN PROPELLANT, MASS FLOW RATE = 0.25 gm/sec

	Engine 44 - 0.090" R											
Gap	0.090"			0.110"			0.125"			0.162"		
Currents (amps)	V	η	T	V	η	T	V	η	T	V	η	T
50	195	30.3	124	208	32.8	132	203	33.2	133	205	36.0	139
75	186	31.0	150	200	32.8	160	195	31.6	155	195	32.7	158
100	185	31.4	174	198	32.8	184	192	31.0	176	190	32.9	181
125	185	30.4	191	196	33.6	207	191	32.3	200	189	32.6	201
150	183	30.3	208	200	32.1	224	190	31.9	218	186	33.0	220
175	184	30.2	225	200	31.8	237	190	32.3	236	186	33.0	237

	Engine 41 0.090" R			Engine 41 Sharp Corner		
Gap	0.195"			0.123"		
Currents (amps)	V	η	T	V	η	T
50	210	34.3	138	190	39.7	140
75	202	31.6	158	180	39.7	167
100	196	31.8	180	175	36.5	182
125	195	29.6	193	173	37.0	204
150	192	33.0	223	170	35.7	218
175	190	30.5	230	169	34.9	232

List of Symbols:

V : total arc voltage (volts)

η : $\frac{\text{thrust power}}{\text{input power}} \times 100$

T : thrust (gmf)

TABLE 10. OPERATION AND PERFORMANCE CHARACTERISTICS FOR THE POINTED CATHODE WITH DIFFERENT CAP SETTINGS, HYDROGEN PROPELLANT, MASS FLOW RATE = 0.25 gm/sec

	Engine 44 - 0.090" R											
Gap	0.090"			0.108"			0.125"			0.192"		
Currents (amps)	V	η	T	V	η	T	V	η	T	V	η	T
50	187	31.0	123	193	32.1	127	186	35.0	130	203	39.8	145
75	176	29.8	143	181	29.1	148	177	30.5	145	194	40.4	175
100	175	28.8	162	177	31.3	170	175	32.4	172	191	37.0	192
125	174	29.4	182	175	31.0	188	173	32.7	192	185	37.2	212
150	174	27.6	194	175	31.4	207	175	32.3	210	182	35.0	223
175	170	27.7	207	175	29.5	217	175	32.5	228	180	35.1	240

	Engine 41 0.090"R			Engine 41 Sharp Corner		
Gap	0.230"			0.125"		
Currents (amps)	V	η	T	V	η	T
50	210	32.1	133	183	42.0	143
75	200	31.8	158	175	42.3	170
100	198	29.7	175	173	39.3	188
125	196	30.0	195	169	39.3	208
150	195	29.0	210	167	37.8	222
175	193	28.7	225	166	37.4	238

List of Symbols:

V : total arc voltage (volts)

η : $\frac{\text{thrust power}}{\text{input power}} \times 100$

T : thrust (gmf)

TABLE 11. OPERATION AND PERFORMANCE CHARACTERISTICS FOR THE FLAT CATHODE WITH DIFFERENT GAP SETTINGS, HYDROGEN PROPELLANT, MASS FLOW RATE = 0.25 gm/sec

	Engine 44 - 0.090" R											
Gap	0.076"			0.091"			0.108"			0.125"		
Currents (amps)	V	η	T	V	η	T	V	η	T	V	η	T
50	205	36.7	140	206	34.6	137	210	24.2	115	216	31.0	132
75	196	36.4	167	200	32.4	160	200	25.0	140	208	34.4	167
100	194	34.6	187	196	32.2	182	200	26.8	167	205	34.9	193
125	193	36.2	213	194	33.7	207	200	26.4	185	200	34.5	212
150	191	35.4	230	194	31.7	220	194	25.8	198	197	33.7	228
175	194	35.4	250	193	32.6	240	190	24.7	207	194	33.2	242

	Engine 41 0.090"R			Engine 41 Sharp Corner		
Gap	0.115"R			0.122"		
Currents (amps)	V	η	T	V	η	T
50	215	33.8	138	220	40.6	153
75	204	30.0	158	205	40.6	180
100	200	31.0	180	200	38.4	200
125	195	30.7	198	195	38.1	220
150	193	29.3	210	190	38.2	238
175	190	29.3	225	186	37.2	251

List of Symbols:

V : total arc voltage (volts)
η : $\frac{\text{thrust power}}{\text{input power}} \times 100$
T : thrust (gmf)

TABLE 12 OPERATION AND PERFORMANCE CHARACTERISTICS FOR THE HOLLOW CATHODE WITH DIFFERENT GAP SETTINGS, HYDROGEN PROPELLANT, MASS FLOW RATE = 0.25 gm/sec

	Engine No. 44 - 0.090" R											
Gap	0.092"			0.110"			0.113"			0.126"		
Currents (amps)	V	η	T	V	η	T	V	η	T	V	η	T
50	205	32.2	131	205	36.8	140	204	34.3	135	200	33.4	132
75	194	31.7	155	196	35.6	165	197	34.5	163	191	32.4	152
100	195	32.6	182	196	33.9	186	199	36.3	194	193	31.2	177
125	195	32.4	203	200	36.2	217	199	35.6	215	194	30.5	196
150	197	31.4	220	196	34.6	230	196	34.5	230	195	31.0	217
175	195	34.4	247	195	33.2	243	194	35.0	249	194	30.4	232

	Engine No. 41 0.090" R			Engine No. 41 Sharp Corner		
Gap	0.147"			0.125"		
Currents (amps)	V	η	T	V	η	T
50	214	33.8	138	206	44.8	155
75	201	30.5	155	197	42.2	180
100	196	30.0	175	194	43.7	210
125	192	30.1	194	190	41.9	228
150	190	29.2	208	188	41.7	248
175	186	29.1	222	185	39.8	259

List of Symbols:

V : total arc voltage (volts)

η : $\frac{\text{thrust power}}{\text{input power}} \times 100$

T : thrust (gmf)

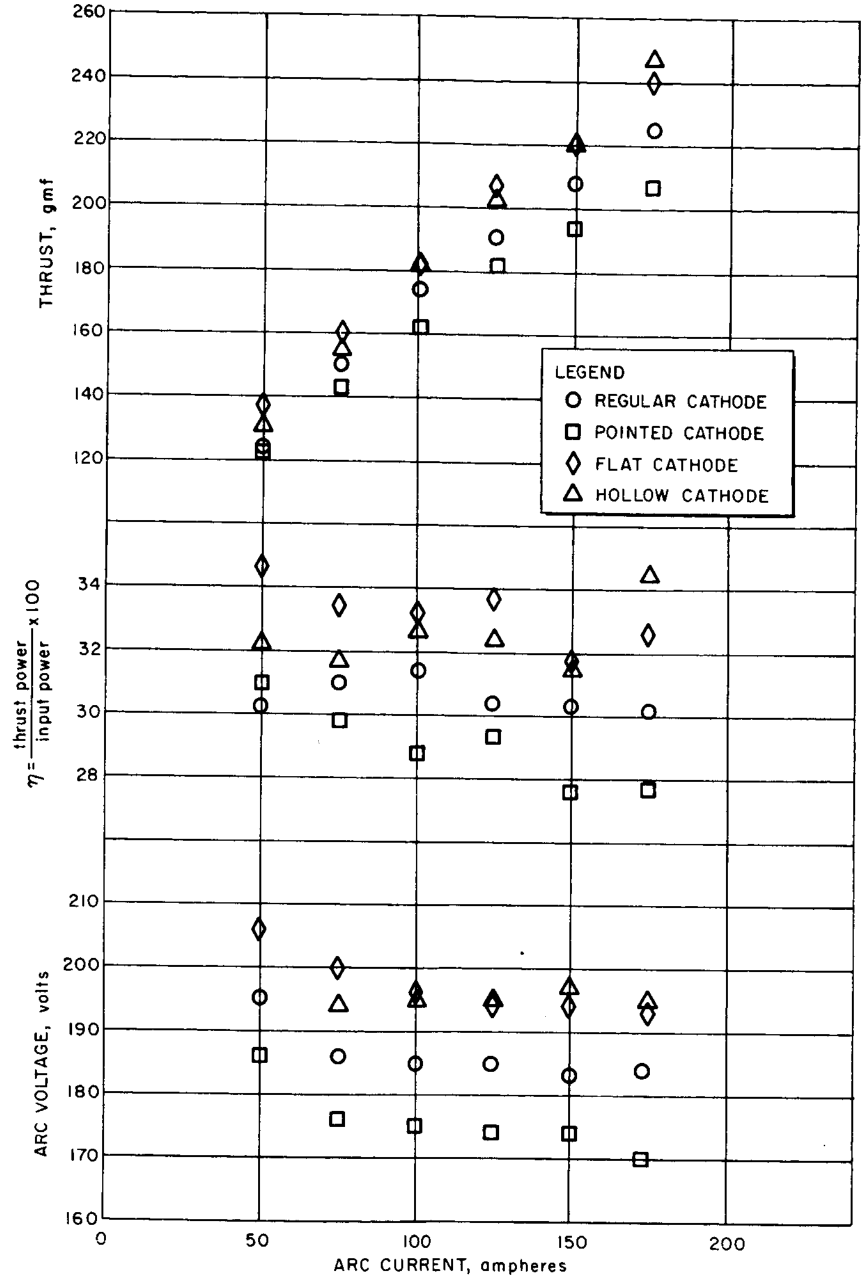

Figure 29 ARC VOLTAGE, EFFICIENCY, AND THRUST VERSUS CURRENT; GAP 0.090 INCH

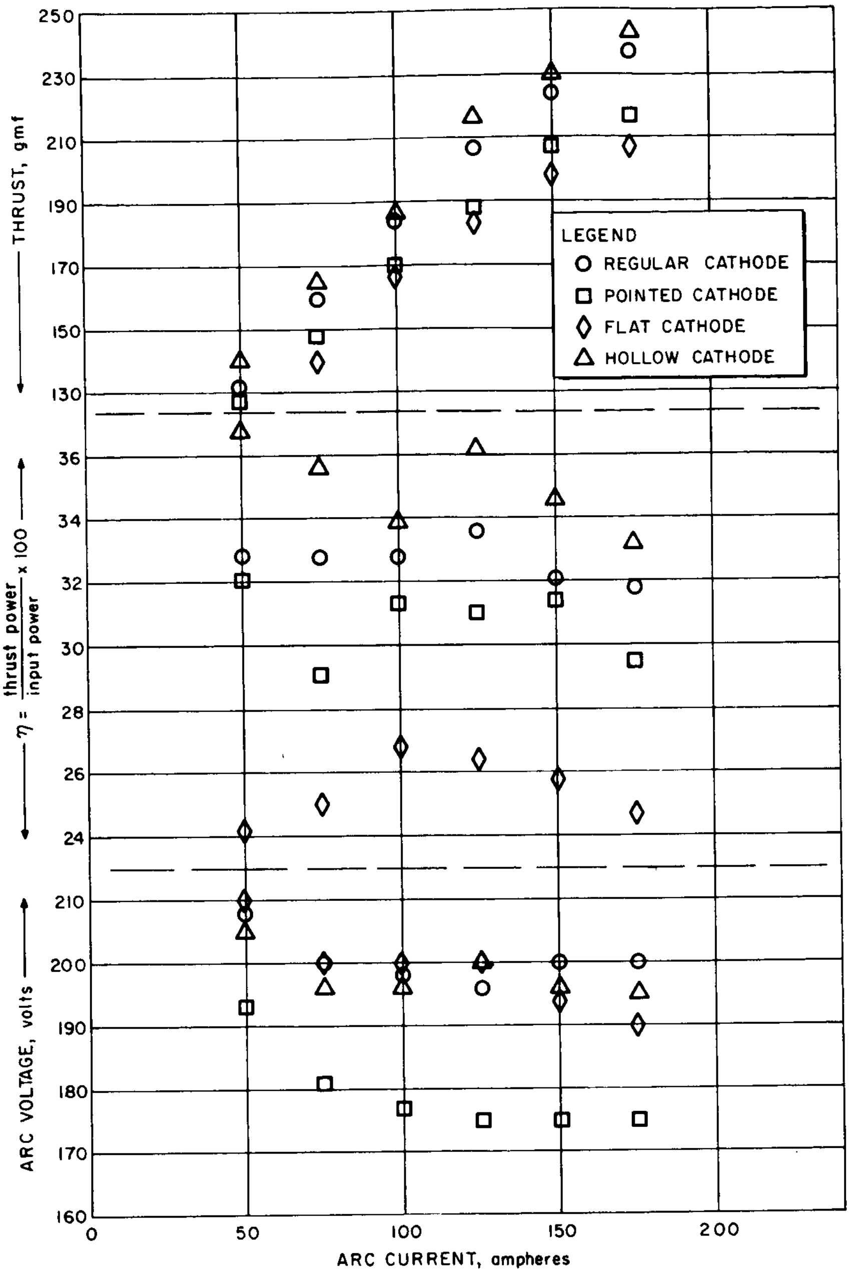

63-12685

Figure 30 ARC VOLTAGE, EFFICIENCY, AND THRUST VERSUS CURRENT; GAP 0.110 INCH

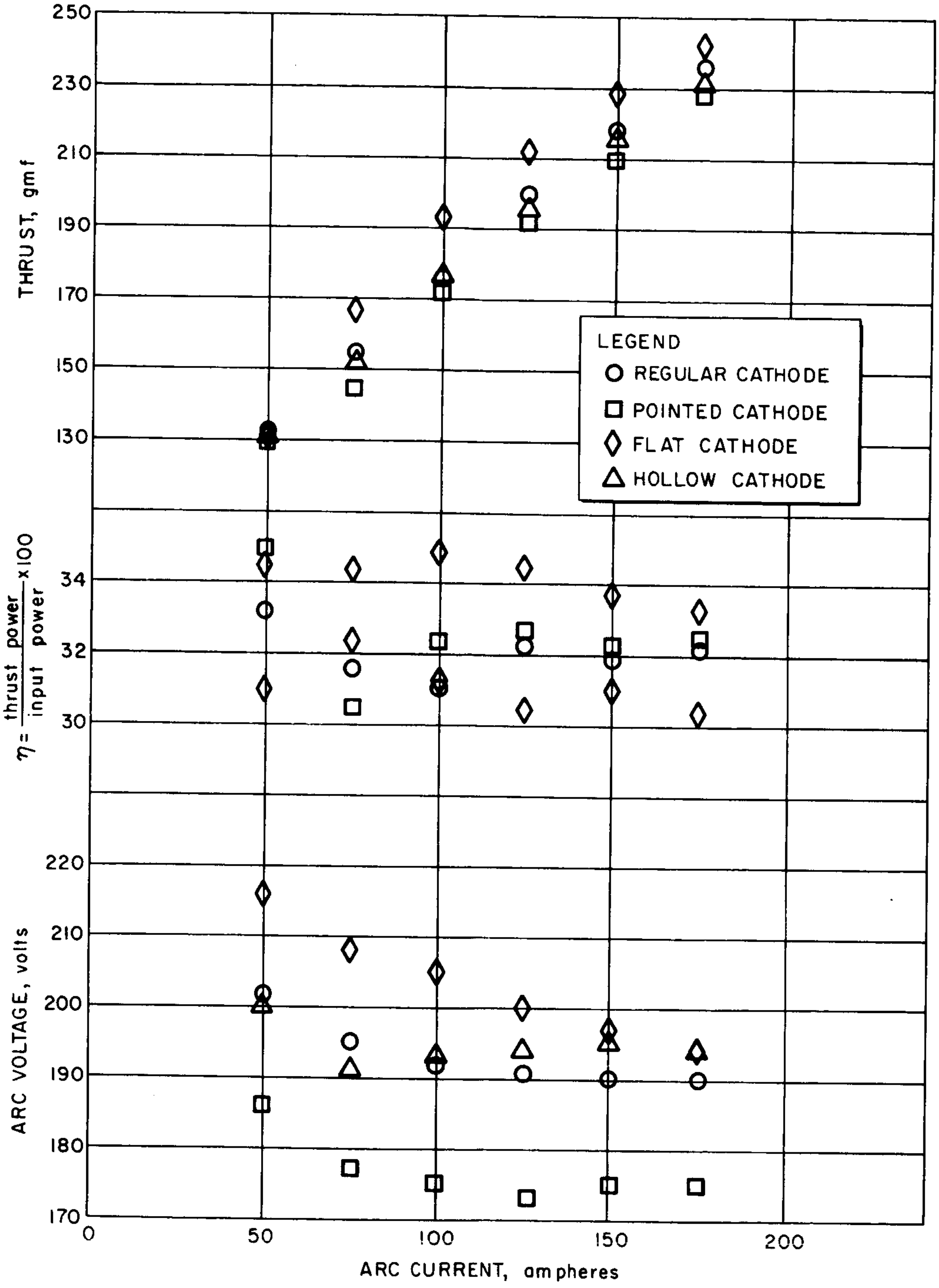

Figure 31 ARC VOLTAGE, EFFICIENCY, AND THRUST VERSUS CURRENT; GAP 0.125 INCH

The largest effect is that of an increase in specific impulse with a decrease in mass-flow rate. Figures 32 through 34 are plots of the specific impulse versus mass-flow rate for the four cathode shapes at each of three gap settings. For a gap of 0.090 inch (figure 32), the pointed cathode gives significantly less (approximately 10 percent) specific impulse for a given mass-flow rate than the other three cathode shapes. At a gap setting of 0.110 inch, the flat cathode yields approximately 12 percent less specific impulse for a given mass-flow rate than the other three cathode shapes. In contrast, for a gap of 0.125 inch, all cathode shapes are approximately equal.

Finally, table 13 is a comparison of the data obtained with an engine with a sharp corner and an engine with a 0.090-inch radius where the converging section joins the constrictor; the gap setting is 0.125 inch. It is seen that, in all cases, the configuration with the sharp corner gives lower arc voltages, the difference being greatest for the regular cathode shape. Also the sharp corner configuration consistently gives higher overall efficiency (the difference tends to decrease at the higher power levels) and is the most striking for the hollow-cathode shape and is least evident for the regular cathode shape. The same statements hold true for the thrust.

It is difficult to summarize the results of this investigation. It seems fair to say that within the range of variation of gap setting and cathode shape studied, no substantial improvement in the performance has been encountered. However, for certain configurations, a reduction in performance can be expected, as evidenced, for example by (1) the low efficiency and low specific impulse obtained with the flat cathode at a gap of 0.110 inch (figures 30 and 33) and (2) the low specific impulse obtained with the pointed cathode at a gap of 0.090 inch (figure 32). One rather clear trend is that the pointed cathode gives a lower total arc voltage for a given arc current. The configuration change due to altering the 0.090-inch radius to a sharp corner (see figure 24) seems to produce the biggest and most consistent effect on engine performance and operation.

3. Nozzle Angle Variation

The purpose of this investigation was to determine the effect on engine performance of varying the supersonic nozzle angle. In order to facilitate this and similar investigations a composite engine has been developed which can be employed to study the effect of various modifications of engine geometry such as the nozzle angle as well as constrictor length and diameter, gas injection pattern, etc. A detailed description of the composite engine along with an assembly drawing is given in appendix D. Briefly, great flexibility is obtained because the various engine components (plenum section, constrictor section, gas injection section and nozzle section) are removable; these sections are bolted together using C-rings. Hence, to study the effect of varying the nozzle angle, various nozzle sections are substituted thereby eliminating the costly and time consuming process of fabricating a new

TABLE 13 OPERATION AND PERFORMANCE CHARACTERISTICS FOR THE 0.090"R AND SHARP CORNER CONFIGURATION WITH A CONSTANT GAP SETTING OF 0.125"; HYDROGEN PROPELLANT, MASS FLOW RATE = 0.25 gm/sec

Currents (amps)	Regular Cathode						Pointed Cathode					
	0.090"R			Sharp Corner			0.090"R			Sharp Corner		
	V	η	T	V	η	T	V	η	T	V	η	T
50	203	33.2	133	190	39.7	140	186	35.0	130	183	42.0	143
75	195	31.6	155	180	39.7	167	177	30.5	145	175	42.3	170
100	192	31.0	176	175	36.5	182	175	32.4	172	173	39.3	188
125	191	32.3	200	173	37.0	204	173	32.7	192	169	39.3	208
150	190	31.9	218	170	35.7	218	175	32.3	210	167	37.8	222
175	190	32.2	236	169	34.9	232	175	32.5	228	166	37.4	238

Currents (amps)	Flat Cathode						Hollow Cathode					
	0.090"R			Sharp Corner			0.090"R			Sharp Corner		
	V	η	T	V	η	T	V	η	T	V	η	T
50	216	31.0	132	220	40.6	153	200	33.5	132	206	44.8	155
75	208	34.4	167	205	40.6	180	191	32.4	152	197	42.2	180
100	205	34.9	193	200	38.4	200	193	31.2	177	194	43.7	210
125	200	34.5	212	195	38.1	220	194	30.5	196	190	41.9	228
150	197	33.7	228	190	38.2	238	195	31.0	217	188	41.7	248
175	194	33.2	242	186	37.2	251	194	30.4	232	185	39.8	259

List of Symbols: V : total arc voltage (volts), η : $\frac{\text{thrust power}}{\text{input power}} \times 100$, T : thrust (gmf) engine for each nozzle section. A further advantage is that such an arrangement guarantees that there are no other variables except the one under consideration. The composite engine does have the drawback that a reliable seal cannot be obtained between the various component sections when the engine is operated at the 30 kw power level for time periods long compared to the start-up transient time of the engine. However, it is felt that by taking special care to reproduce the non-steady state condition, qualitative trends can be obtained and if something promising is indicated, then a standard series of engines can be used for a quantitative investigation.

In this study, axial length of the nozzle is fixed at 1.250 inch, while the nozzle half-angles are 1, 2, 3, 4, 5, 6, 7, 11, 15, and 20 degrees. The plenum chamber section is made of stainless steel and all other sections including the nozzles are molybdenum. The constrictor length and diameter are 0.300 inch and 0.150 inch respectively. The gap setting is 0.125 inch and the regular cathode is employed (see figures 22 and 23). Table 14 shows the exit area ratios for each nozzle angle.

TABLE 14

AREA RATIO CORRESPONDING TO NOZZLE HALF-ANGLE

Nozzle Half-Angle (degrees)	Exit Area Ratio
1	1.67
2	2.47
3	3.53
4	4.72
5	6.28
6	7.54
7	9.32
11	17.5
15	30.0
20	50.3

For each nozzle, the engine was operated at the same five mass flow rates (ranging from 0.250 to 0.176 gm/sec H_2) at a power level of 30 kw. Operation at this power level was for a time duration of 20 seconds. Measurements taken were arc current, total arc voltage, thrust, and plenum chamber pressure.

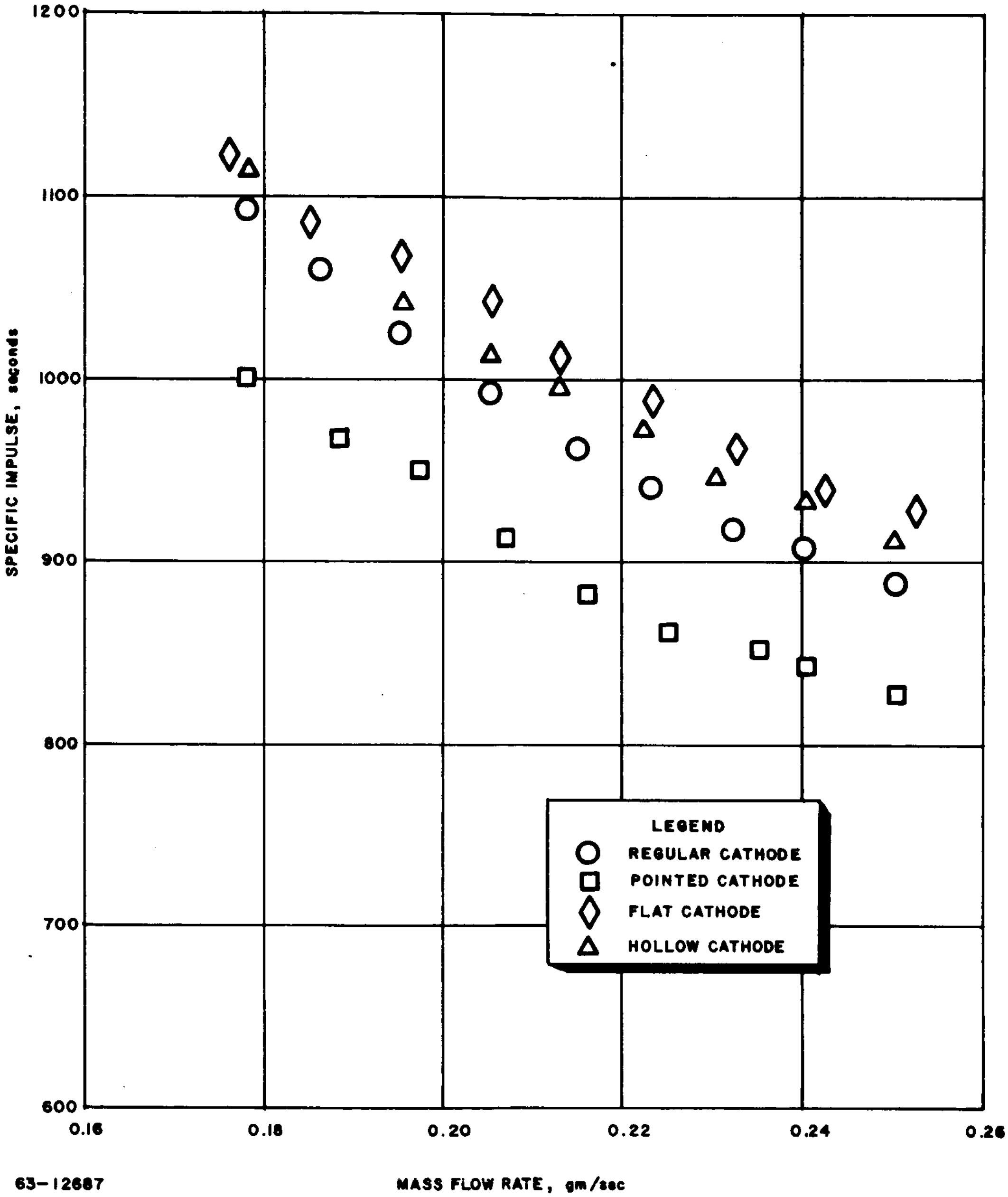

Figure 32 SPECIFIC IMPULSE VERSUS MASS FLOW RATE; GAP 0.090 INCH

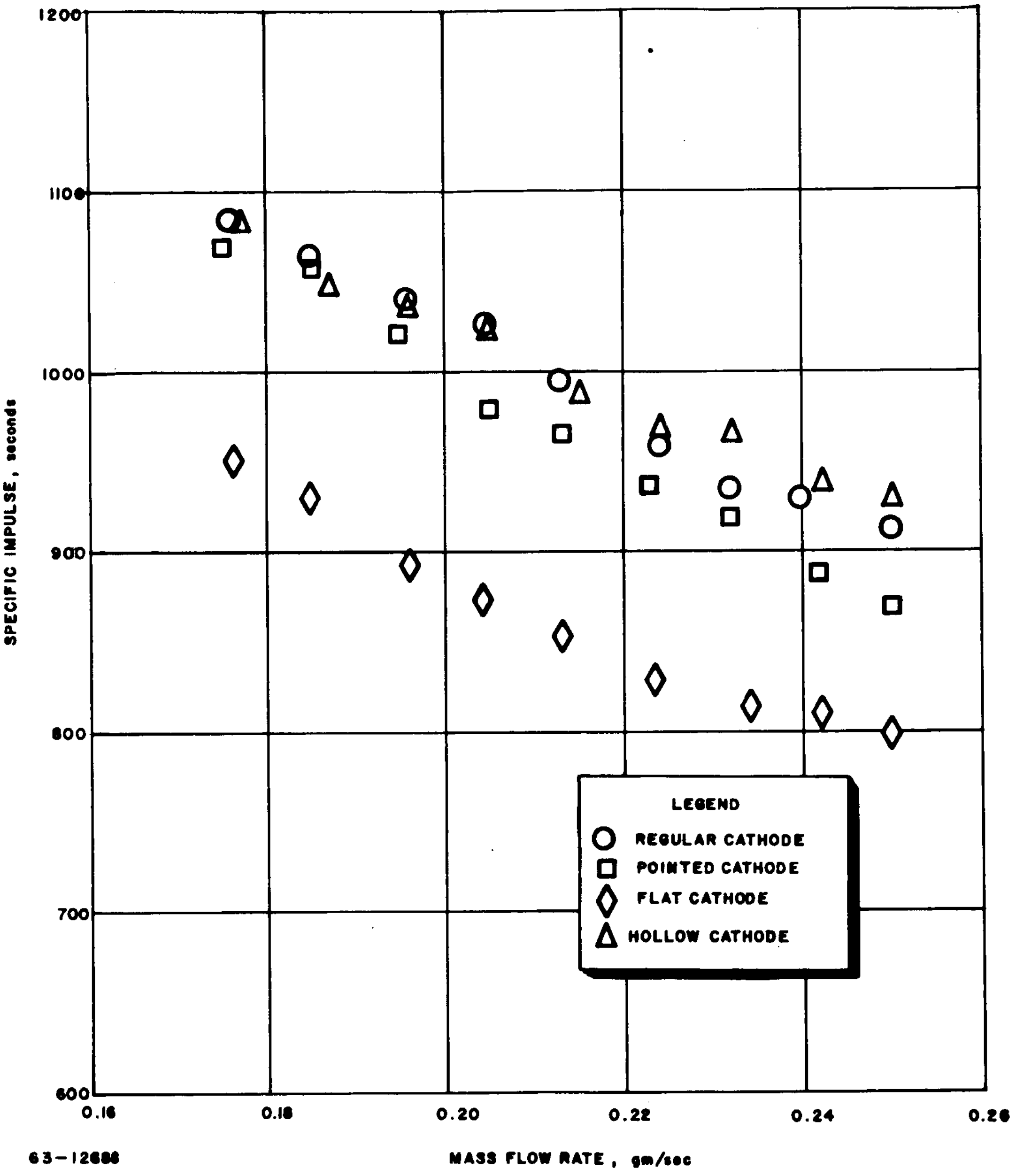

Figure 33 SPECIFIC IMPULSE VERSUS MASS FLOW RATE; GAP 0.110 INCH

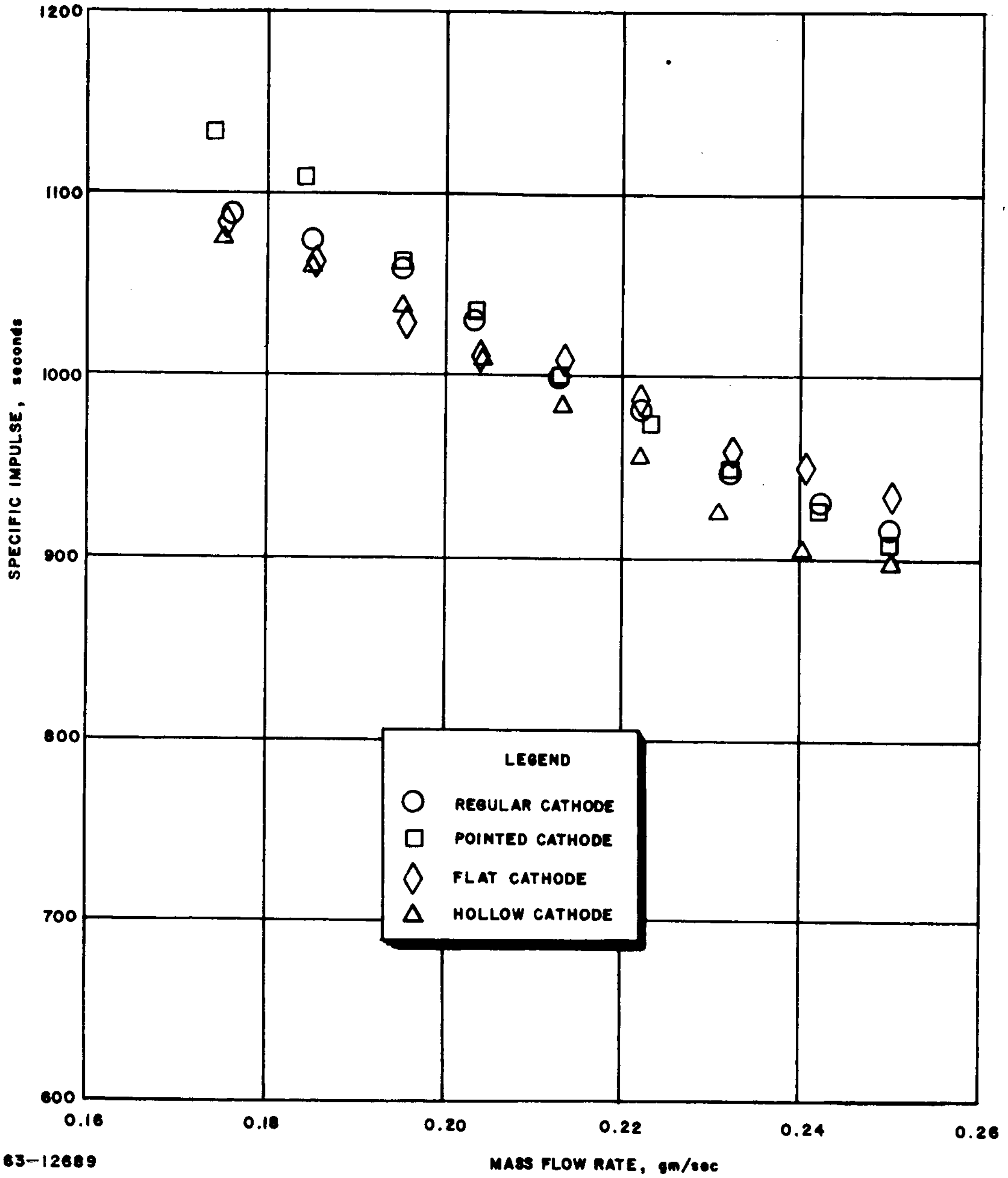

Figure 34 SPECIFIC IMPULSE VERSUS MASS FLOW RATE; GAP 0.125 INCH

Some of these data are shown in figures 35 through 37. Figure 35 is a graph of measured thrust versus nozzle half-angle for five different mass flow rates. For all mass flow rates it is seen that generally the thrust increases with nozzle half-angle up to a value slightly greater than 7 degrees and then decreases. Figure 36 is a graph of the propulsive efficiency (thrust power/input power) versus nozzle half-angle. For all mass flow rates, the propulsive efficiency increases with increasing nozzle half-angle up to a value slightly greater than 7 degrees and then decreases. Here the peak is more pronounced because the thrust power is $T^2/2\dot{m}$ where T is the thrust and $\dot{m}$ the mass flow rate. Finally, figure 37 is a graph of total arc voltage versus nozzle half-angle and it is seen that generally, the total arc voltage decreases with increasing nozzle half-angle.

Using the criteria of thrust, efficiency, or specific impulse, the data indicate that for a hydrogen propellant a nozzle half-angle in the neighborhood of 7 degrees is the optimum (this is the angle that has been used for all R-series hydrogen arc-jet engines).

Additional experimental work has shown that the above results have a rather low degree of reproducibility with regard to arc current and voltage although the thrust measurement reproducibility is excellent. It is thought that the transient condition of the engine during the measurement may be responsible for the lack of reproducibility. It is this transient condition that causes the low performance (low specific impulse) of the composite engine.

C. ARC COLUMN STUDIES

1. Introduction

This area of investigation concerns the interaction between the propellant flow and the arc discharge. Both the constrictor and the anode section where the arc terminates are involved. The purpose of these investigations is to gain a better understanding of the physical processes by which energy is added to the propellant flow from the arc discharge.

The discussion to follow deals with five areas of investigation; these are (1) voltage gradient measurements in the constrictor with a discussion of the results in terms of various column theories, (2) a two fluid column theory of the constricted arc, (3) an investigation of the possibility of dissociative non-equilibrium in the constrictor, (4) experiments conducted using the same molar flow of different gases and (5) an experimental investigation of arc attachment phenomena in the supersonic nozzle (anode).

2. Voltage Gradient Measurements

To measure the voltage difference between two points along the arc column, the usual constrictor section has been replaced with an electrically insulating

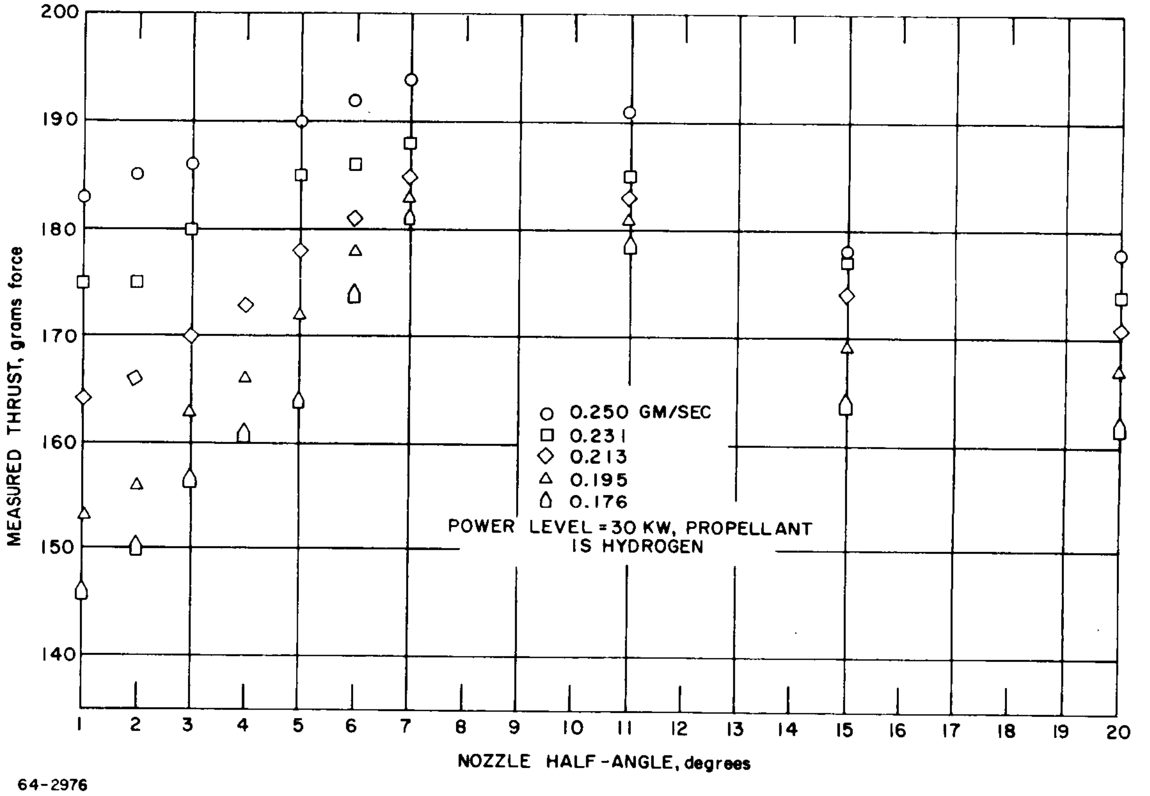

Figure 35 MEASURED THRUST VERSUS NOZZLE HALF ANGLE FOR VARIOUS MASS FLOW RATES

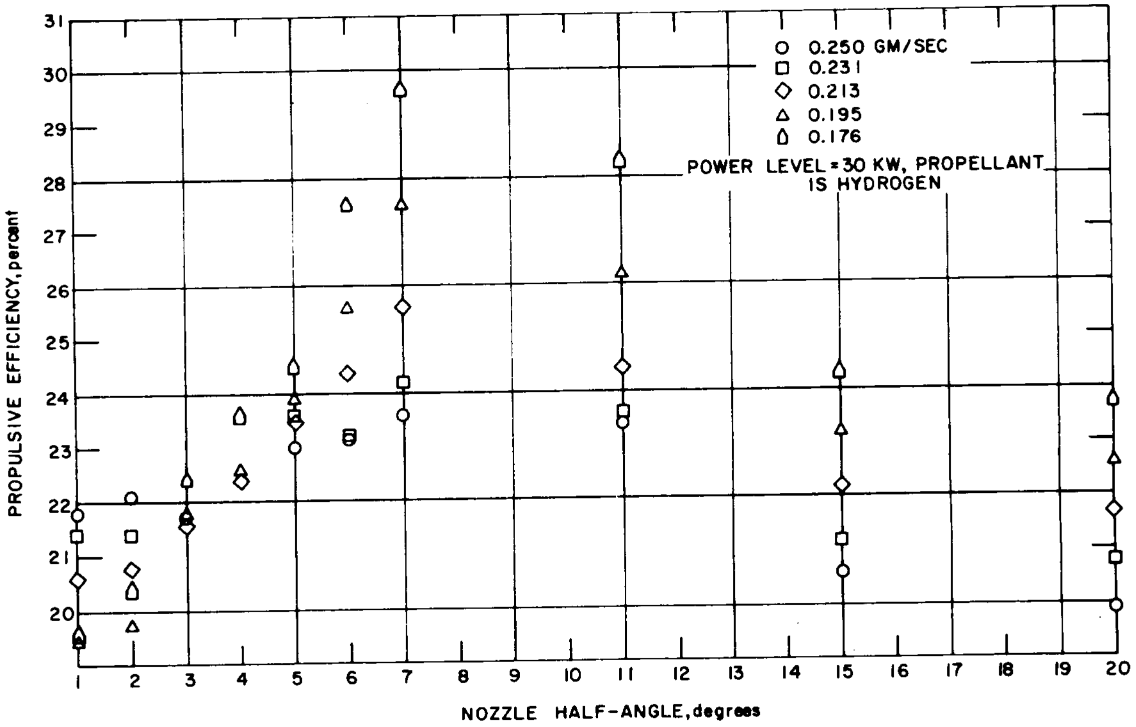

64-2977

Figure 36 EFFICIENCY VERSUS NOZZLE HALF ANGLE FOR VARIOUS MASS FLOW RATES

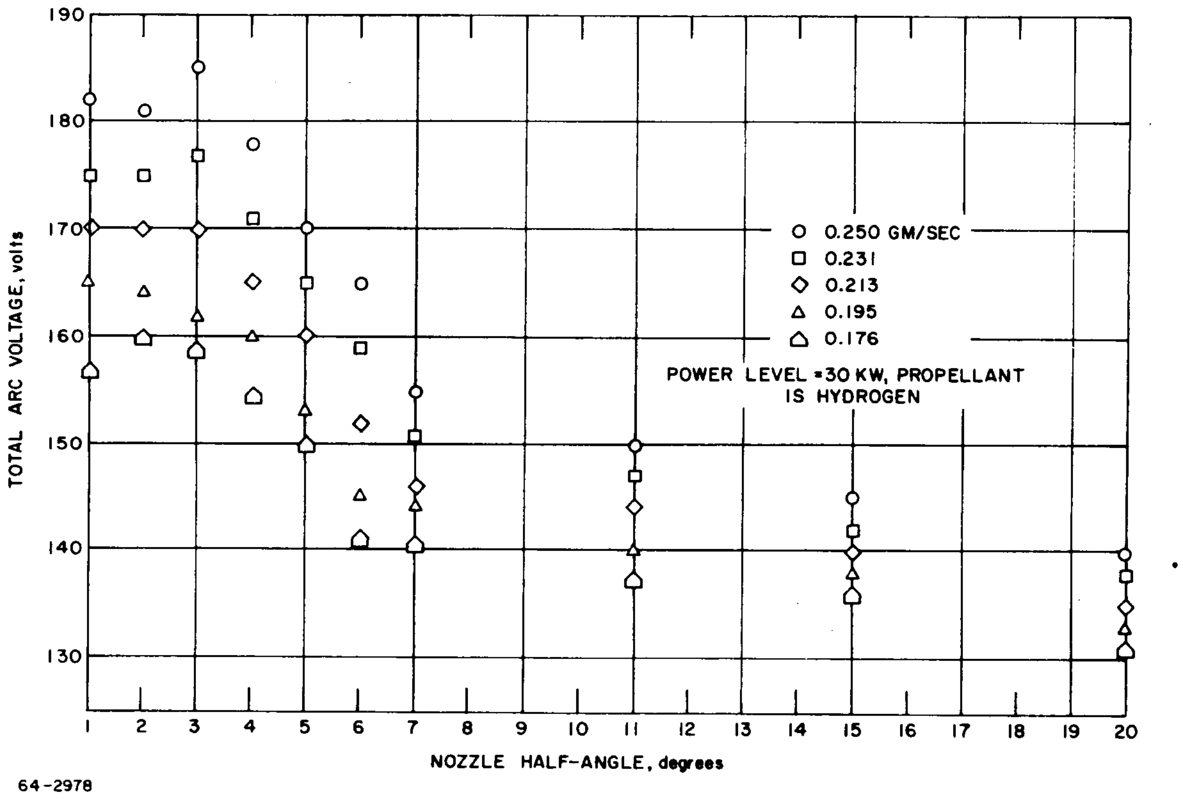

Figure 37 TOTAL ARC VOLTAGE VERSUS NOZZLE HALF ANGLE FOR VARIOUS MASS FLOW RATES

boron nitride structure (see figure 38). Holes are drilled through this boron nitride constrictor to permit the insertion of tungsten probes into the arc channel. These probe holes are sealed near the exterior surface of the boron nitride with rubber "O"-rings. The engine exhausts into a vacuum chamber which maintains an ambient pressure of 1 mm Hg with the hydrogen-mass flow rate employed. The main part of the engine is outside the vacuum tank and forms part of the vacuum envelope (see figure 39); this arrangement permits manual control of the probes. The probes are uncooled; the diameter of the probe tip is 0.015 inch.

a. Test Procedure

During the measurement procedure, the probes are initially withdrawn into the constrictor body; after the arc discharge has been established, the probes are manually inserted into the flow. Stops are affixed to the probes so that the distance of penetration can be closely controlled. In general, it is found that the voltage difference from probe to probe varies with the extent of penetration up to a point; from then on the voltage difference is insensitive to the depth of penetration. It is found that a penetration of 0.050 inch is within this insensitive region. At this penetration, the probes were able to withstand the constrictor environment for periods of the order of five seconds without noticeable ablation or erosion.

The probes are connected through one of several precision resistors in series with a microammeter; the voltage difference between probes is obtained as the product of the probe current and the series resistance.

The results of a series of voltage-probe measurements are presented in figure 40 for a hydrogen-mass flow of 0.25 gm/sec and an arc current of 175 amperes. Each horizontal line in figure 40 indicates a voltage gradient, obtained as the ratio of measured voltage to the centerline separation of the two probes. The end points of each line indicate the probe center locations. An average voltage gradient in the constrictor of 67 volts/cm represents the data within experimental uncertainties. Further measurements indicate the voltage drops associated with the cathode and nozzle-anode regions are approximately equal.

The use of tangible probes in plasma involves many uncertainties;[7] subsidiary experiments have been performed to evaluate the uncertainties inherent in these voltage gradient measurements. Three areas in particular have been investigated: (1) contact resistances at the probe tips, (2) contact potentials at the probe tips, and (3) contamination or other perturbation of the arc by the probes or by evaporated probe material. The effects of contact resistance at the probe tips has been investigated by varying the precision resistance in the probe-meter circuit. If the contact resistance is not small compared with the meter

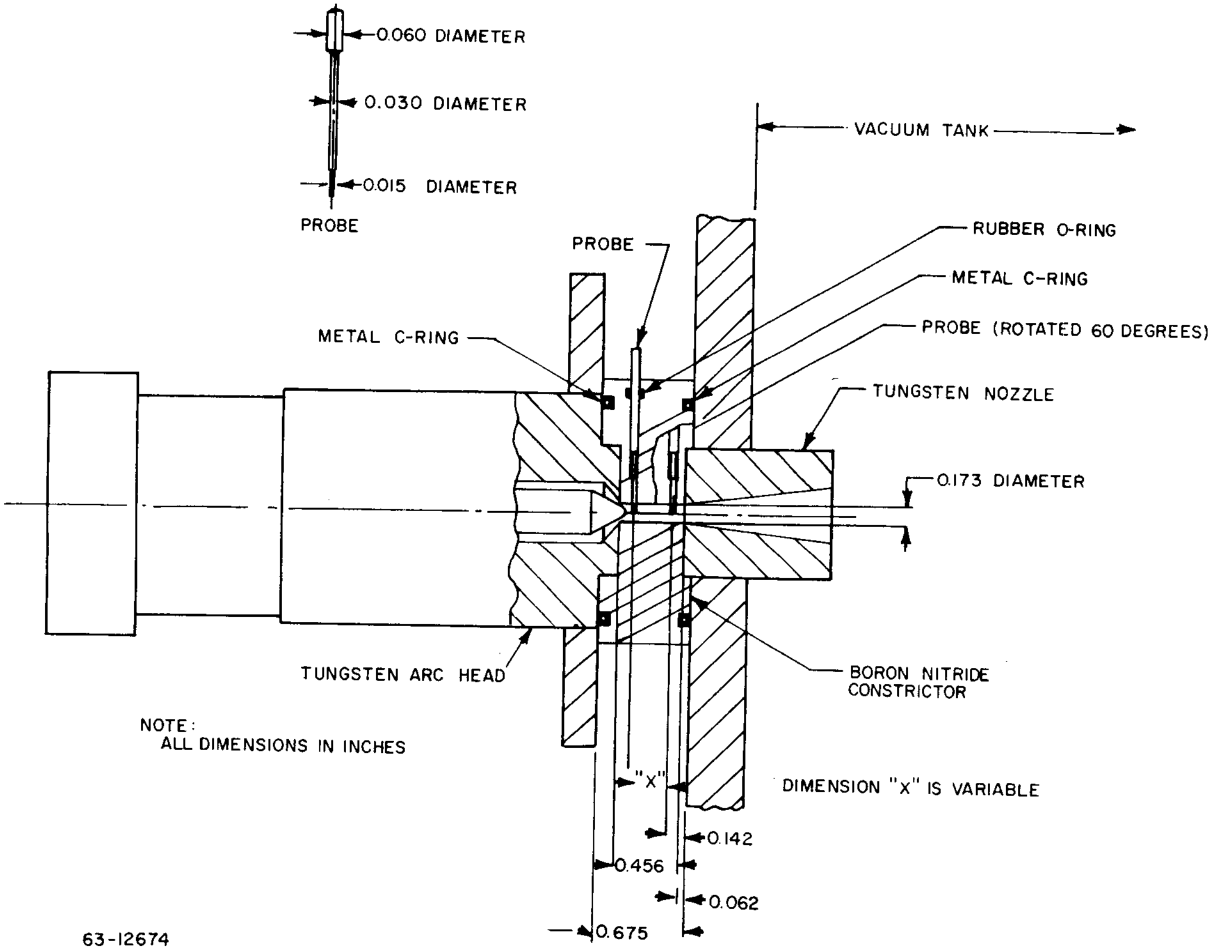
0.060 DIAMETER
0.030 DIAMETER
0.015 DIAMETER
PROBE
VACUUM TANK
PROBE
RUBBER O-RING
METAL C-RING
PROBE (ROTATED 60 DEGREES)
METAL C-RING
TUNGSTEN NOZZLE
0.173 DIAMETER
TUNGSTEN ARC HEAD
BORON NITRIDE CONSTRICTOR
NOTE:
ALL DIMENSIONS IN INCHES
"X"
DIMENSION "X" IS VARIABLE
0.142
0.456
0.062
0.675

63-12674

Figure 38 SCHEMATIC DRAWING OF VOLTAGE PROBE TEST SYSTEM

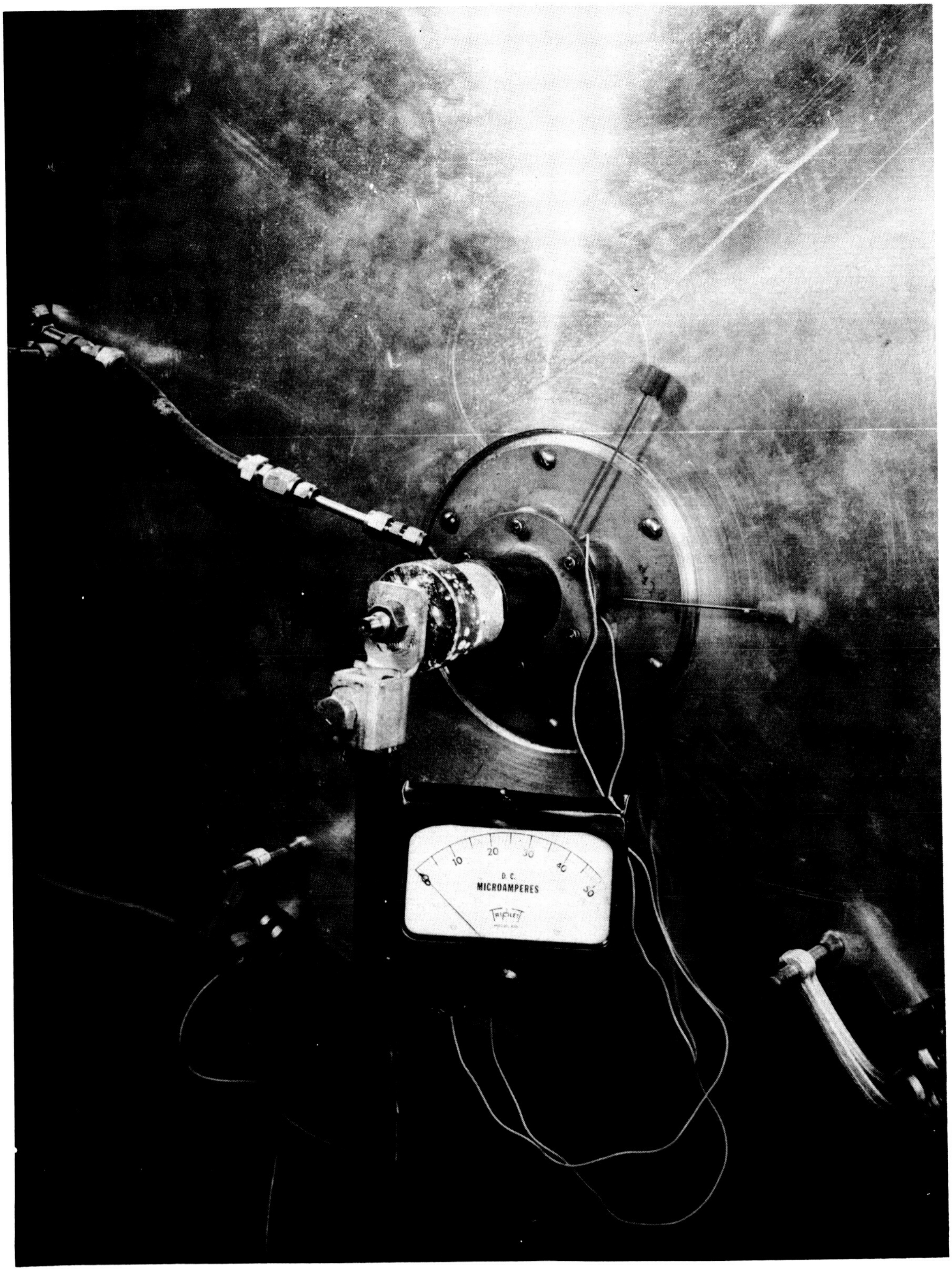
10
20
30
40
50
D.C.
MICROAMPERES
Triplett

Figure 39 PHOTOGRAPH OF VOLTAGE PROBE MEASURING SYSTEM

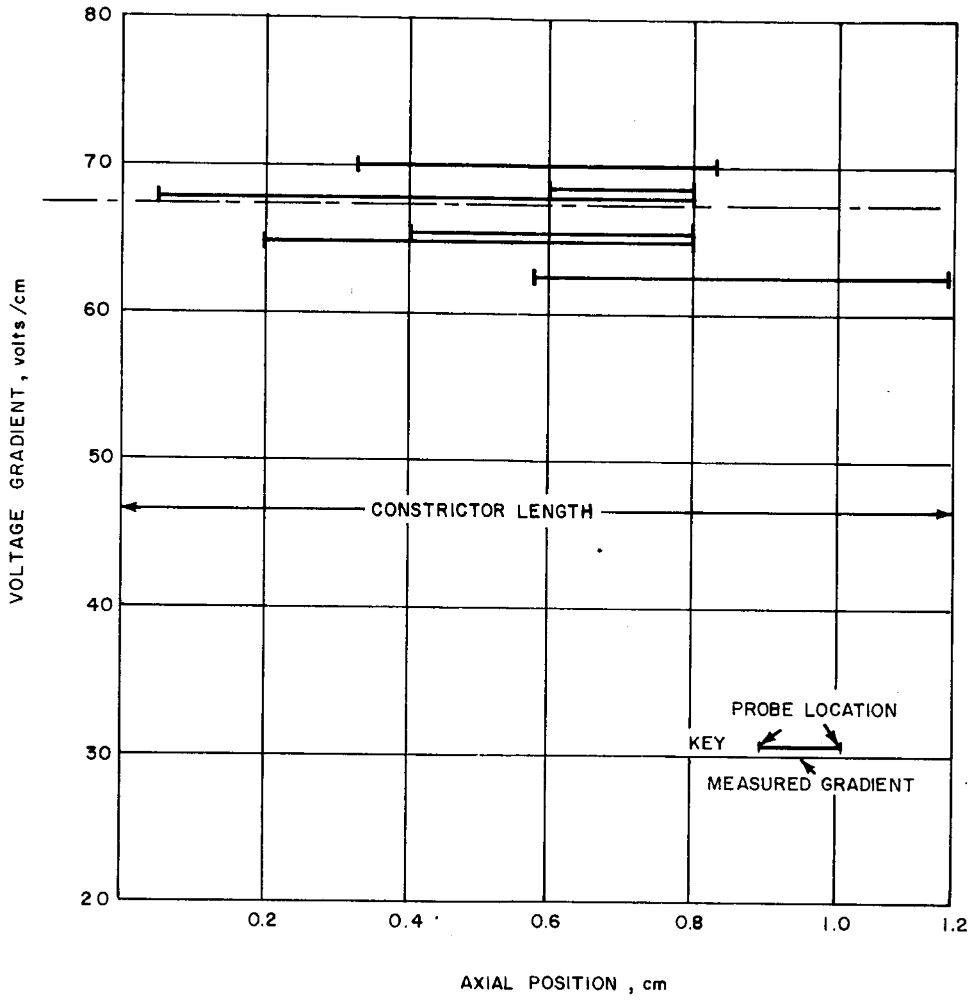

63-12675

Figure 40 VOLTAGE PROBE MEASUREMENTS AT THE 30 KW POWER LEVEL

resistance, then variation of the meter resistance will affect the apparent probe voltage. The measured probe-to-probe voltage is, in fact, insensitive to the meter resistance over a range of 1 to 5 megohms; resistors of this magnitude have, therefore, been used for all the reported measurements.

The effects of possible contact potentials have been investigated by reversing probe pairs, and by using a number of different probes. No measurable effects were detected. In addition, the measured gradients are insensitive to probe separation (i.e., to the actual voltage differences between probes). It has been concluded that either the contact potential effects are small or they are identical from probe to probe; in either case, the gradient measurements should be unaffected.

Finally, possible perturbation of the arc column has been investigated in two ways. First, the total arc voltage and current are monitored before and after probe insertion into the discharge column (total arc voltage is generally about 5 volts lower after probe insertion); secondly, several tests were made using three probes, two to measure a voltage gradient and a third to try to perturb the measurements. In no case was the voltage gradient between probes altered upon insertion of the test perturbing probe, whether this probe was inserted upstream, within, or downstream of the region in which the gradient was measured. However, insertion of the third probe generally had the effect of further reducing the total arc voltage by several volts. Finally, measurements' were made of the cathode-to-upstream probe, probe-to-probe, and downstream probe-to-anode voltages before and after inserting a perturbing third probe; again, the total arc voltage fell by several volts upon insertion of the perturbing probe, and the total drop occurred between the downstream probe and the anode. It has been concluded that the perturbing effects of the probes are small and concentrated almost entirely in that discharge region located downstream of the constrictor section. The probe measurements are thus thought to be a reliable guide to the actual constrictor voltage gradient.

b. Consequences of the Voltage-Probe Measurements

In light of the results of the voltage-probe measurements, it is of interest to look at two flow models which have been previously used in attempts to understand the arc-discharge process, and determine whether the Heller-Elenbaas and/or Stine-Watson core-flow models are consistent with the findings of the voltage-probe measurements.

1) Heller-Elenbaas Model[1, 8]

In this model, the arc column is independent of axial position and is governed by an energy equation (called Heller-Elenbaas equation) which includes joulean heating, radial heat conduction, and radiation but neglects convective-heat transfer. The annular region between the arc column and bounding (constrictor) wall is not treated by this model.

The boundary conditions are that the centerline temperature is specified and the (radial) temperature gradient at the centerline is zero. Numerical solutions have been generated in which the appropriate transport properties (electrical and thermal conductivities and power radiated per unit volume) are given plus the specification of the voltage gradient and centerline temperature. The solution is in the form of the temperature profile; other quantities that can be calculated are the arc current, the power radiated per unit length of arc column and the power conducted radially per unit length.

The experimentally known quantities for the discharge column developed in the constrictor of the 30-kw engine are the current, voltage gradient, and column luminosity diameter; in addition, spectroscopic measurements have been made to estimate the central temperature.

The Heller-Elenbaas model has incorporated in the formulation a constant voltage gradient, one of the results of the voltage-probe measurements. So, a test of the Heller-Elenbaas model will require using the experimental result that the voltage gradient is 65 to 70 volts/cm. Numerical solutions of the Heller-Elenbaas equation for hydrogen show that arc currents of the order of 150 to 200 amperes and a voltage gradient of 65 to 70 volts/cm yields a central temperature of 35, 000 to 40, 000°K and an arc diameter of 0. 22 to 0. 24 cm. The central temperature is not inconsistent with the lower limit of 20, 000°K obtained by spectroscopic measurements but the measured luminosity diameter is 0. 14 to 0. 16 cm. The numerical solutions of the Heller-Elenbaas equation for hydrogen at these currents and voltage gradients show that the temperature gradient near the outer edge of the column is steep; the thermal conductivity at the lower temperatures is small and hence large temperature gradients are required to produce the necessary heat flux. Therefore, the total column diameter is unlikely to depart from the luminosity diameter by 15 to 20 percent. This latitude is not sufficient to bring the measured diameters into line with the theoretical values.

Alternatively, an arc column with a current in the range of 150 to 200 amperes and a diameter of 0. 14 cm (luminosity) or 0. 16 to 0. 19 cm (overall) should have a voltage gradient of the order of 100 volts/cm. The discrepancy between this value and the measured value to 65 to 70 volts/cm is thought to be outside the margin of error associated with the measured values.

One possible source of the discrepancy between the experimental results and the Heller-Elenbaas calculation is the uncertainty of the transport properties used in the numerical solution of the Heller-Elenbaas equation. The transport properties (thermal and electrical conductivities) are known at best to 20 to 30 percent at the higher temperatures (above 10,000°K) due in part to the approximations in the treatment of the coulomb collisions.[9]

To determine the sensitivity of the calculated Heller-Elenbaas solutions to variations in the transport properties of hydrogen at temperatures above 10,000°K, the Heller-Elenbaas equation has been solved for nine sets of transport properties. These sets are identical for temperatures below 10,000°K. Above 10,000°K, one set consists of the best available theoretical values for the electrical (σ) and thermal (k) conductivities.[9*] The other eight sets consist of combinations of a 30-percent increase and decrease in the thermal and electrical conductivity. The nine resulting solutions of the Heller-Elenbaas equation are summarized in table 15. Reference to table 15 shows that (1) the central core temperature, T_o, is determined almost wholly by k; a ± 30-percent variation in k produces approximately ± 15-percent change in T_o; (2) the radius of the column is determined by both σ and k; r decreases with increasing k and increases with decreasing k, and (3) two combinations of k and σ (k-low, σ-high, and k-high, σ-low) produce an uncertainty (22 percent low and 29 percent high, respectively) in the column radius of the same general size as the uncertainty in the transport properties (30 percent).

The result of this calculation tends to render the discrepancy between the experimental results and the theoretical calculations less sharp but the discrepancy still appears to persist. Another way of ascertaining the applicability of the Heller-Elenbaas model is to consider the energy flux in the arc column. If the assumption is made that at the throat of the supersonic nozzle, the flow velocity is the local (equilibrium) sound speed and that the density and enthalpy are obtained from the temperature by equilibrium considerations, then the energy flow at the throat can be calculated. Assuming a voltage gradient of 70 volts/cm, an arc current of 200 amperes and a pressure of 0.6 atmospheres (typical conditions for operation at the 30-kw level), the resulting power in the arc core at the throat is approximately 27 kw; for a given current, the power increases with decreasing voltage gradient and decreases with decreasing pressure.

---

*The radiated power per unit volume is not varied because for the range of current, voltage gradient, and pressure at which the 30-kw arc-jet engine is operated, the power radiated is only 1 to 2 percent of the radial conducted power.

TABLE 15

VARIATION OF HELLER-ELENBAAS SOLUTION WITH TRANSPORT PROPERTIES

Transport Properties		Central Temperature	Core Radius	Power in Core (0.6 atm)
k		(°K)	(cm)	(kw)
high	high	32,800	0.104	23.3
high	Yos	33,600	0.120	30.6
high	low	32,700	0.142	43.2
Yos	high	37,900	0.095	20.8
Yos	Yos	38,000	0.110	27.1
Yos	low	37,800	0.130	38.0
low	high	43,800	0.086	17.7
low	Yos	41,700	0.098	22.8
low	low	43,600	0.117	32.8

Voltage gradient = 70 volts/cm; current = 200 amperes

Of course, the power in the core also is sensitive to the transport properties. This sensitivity has been ascertained in a manner identical to that previously described and the results are also summarized in table 15. It is seen that an uncertainty in the transport properties can yield values for the power in the core ranging from 18 kw (35 percent low) to 43 kw (59 percent high).

Now, if the assumptions of the Heller-Elenbaas model can be applied here, then this energy flow must be added to the propellant in a region near the cathode, for all the energy released in the column itself is conducted radially outward to the surrounding flow. The implication of this model is that the product of the current and the voltage drop in this cathode region must be equal to the energy flow rate at the throat. For a current of 200 amperes and an energy flow rate as low as 20 kw, a voltage drop of 100 volts must occur in the cathode region.

This is a factor of 2.5 higher than value determined from the voltage-probe measurements. It is seen that an increase in the power in the core leads to an even greater discrepancy.

To summarize, the Heller-Elenbaas model, though undoubtedly an oversimplified picture of the energy-transfer mechanisms, nevertheless describes certain features of the arc column such as the central-core temperature and column diameter to an accuracy that is quite amazing when the simplicity of the model is considered; this result indicates that the radial-heat conduction is probably the major energy transfer mechanism in the column region. Because the model is oversimplified, the fluid mechanics of the column region is not prescribed. Hence, information concerning the power flux or the mass flux in the column region requires further assumptions and it is in this sense that the Heller-Elenbaas column model is to be considered as unsatisfactory. An attempt to calculate the power flux at the throat leads to inconsistency between the predicted and measured voltage drop in the cathode region. The calculation of power flux is itself based on uncertain assumptions (e.g., sonic flow, no radial pressure gradient).

2) Stine-Watson model

The Stine-Watson theory[10] of the arc column differs from the Heller-Elenbaas model in that it includes an axial convection term in the energy equation. The Stine-Watson model contains the Heller-Elenbaas solution in the limit of large axial distances. An analytic solution of the Stine-Watson model can be obtained by making certain linearizing approximations of the transport properties; the resulting solution is separable in the radial and axial coordinates. Figure 41 illustrates the calculated longitudinal distribution of voltage gradient; the voltage gradient has been nondimensionalized by E_∞, the "large-distance" voltage gradient (same voltage gradient as would be given by the Heller-Elenbaas solution) and the axial distance has been nondimensionalized by the length Z_0 which depends upon the mass-flow rate and the transport properties. The physical interpretation of figure 41 is as follows.* There is a region in the arc column where the heat generated by joulean dissipation is both conducted radially outward and convected axially downstream. Moving downstream, the fraction of the energy convected axially decreases exponentially; this means the power in the arc column increases to some asymptotic value and hence the local voltage gradient must decrease exponentially as is indicated in figure 41. It is seen that Z_0 is a scale length which

---

*In this discussion, effects due to radiation are neglected.

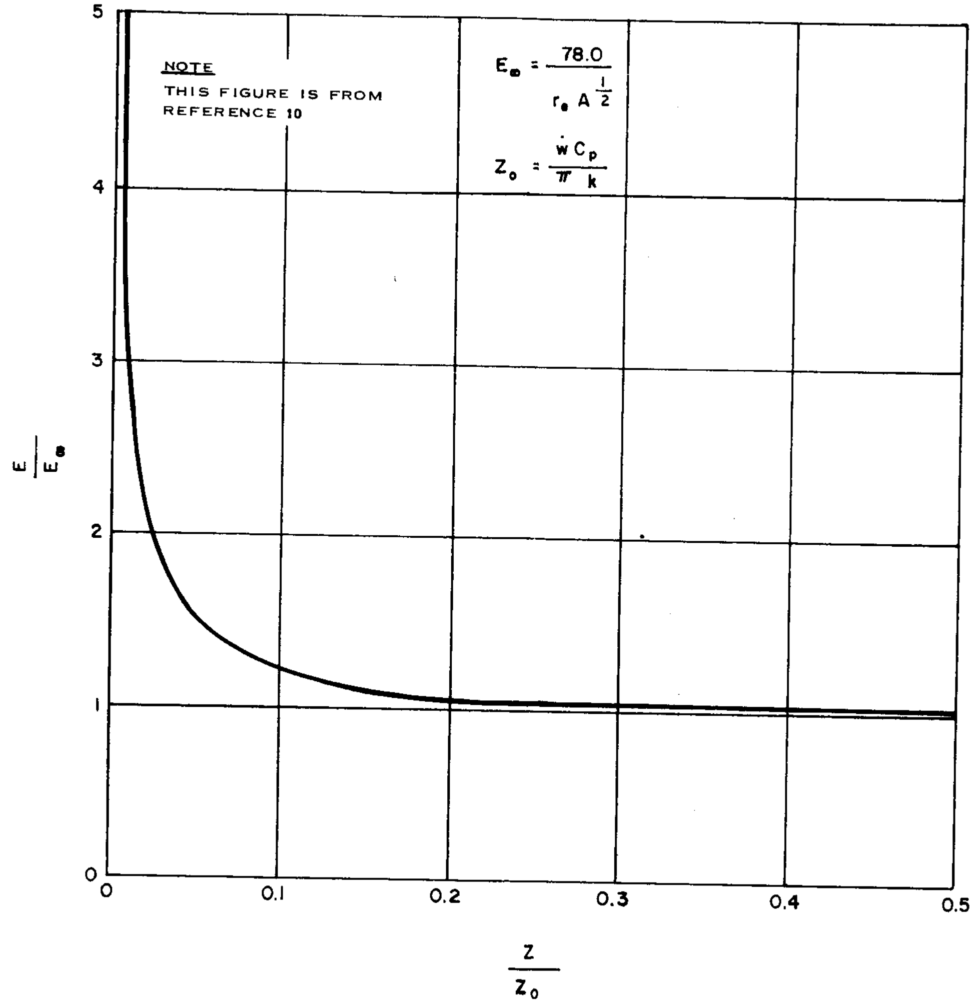

63-12676

Figure 41 LONGITUDINAL DISTRIBUTION OF LOCAL VOLTAGE GRADIENT ACCORDING TO STINE-WATSON THEORY

determines the distance that must be traveled before axial convection becomes negligible. For distances greater than Z_o, the joulean dissipation is balanced by radial conduction; the power in the column remains constant and the voltage gradient is a constant (Heller-Elenbaas).

The voltage-gradient measurements indicate that over a substantial portion of the constrictor (approximately 85 to 90 percent), the voltage gradient is constant. This result suggests that if the Stine-Watson solution has a region of validity, it is only in the beginning 10 percent of the constrictor, i.e., in a region quite close to the cathode. Another way of saying this is that if the Stine-Watson model is valid, $Z_0/Z_w << 1$ where Z_w is the length of the constrictor.

3. Two Fluid Model for the Constricted Arc Column

a. Introduction

The flow processes occurring in the constrictor of the arcjet engine are complex, involving the interaction of both fluid mechanic and electrodynamic phenomena and, up to the present, have proven intractable to exact analysis. As was discussed in the previous section, the Heller-Elenbaas model of the constricted arc column is partially successful in predicting certain properties of the arc column but because of its simplicity suffers the drawback of not taking into proper account the fluid mechanics in general and the interaction between the arc column flow and the flow in the surrounding cooler sheath region in particular.

To investigate the essential features of the column processes with a minimum of mathematical complexity, a simplified two-fluid model for the flow in the constrictor has been developed. Although the model is rather crude in its present state of development, it appears to give results which are at least in semi-quantitative agreement with experiment.

b. Description of the Model

In the model to be considered, the arc is assumed to strike through a straight cylindrical tube of length l and the uniform cross-sectional area A. The area column itself is represented by a hot central core region (see figure 42) whose properties are assumed to be uniform over the cross-sectional area A_1 and hence to depend only on the axial coordinate x. This hot core region is surrounded by a sheath of cold gas, region 2, whose properties are also assumed to depend only on x. These two flows are each treated as independent, quasi-one-dimensional flows subject to the coupling conditions that the pressures in the two flows at any axial position must be the same and that the cross-sectional areas for the two flows equal the total constrictor area A. The mass flow rate in the core region $\dot{m}$, is assumed to be negligible at the inlet of the constrictor, $X = 0$, and then to increase with increasing axial position due to heating of surrounding cold gas by thermal conduction from the core. It is important to realize that in this model, the boundary of the core region is an envelope containing the hot gas so the cross-sectional area of the core-region increases with axial position, ingesting more of the total mass.

In the present formulation of the model, all the power input from the arc is assumed to go into the hot core region so that the stagnation enthalpy of the outer flow (region 2) remains equal to the initial enthalpy for all x. This restriction should be relaxed in subsequent work to allow for possible heating of the outer flow as well.

c. Analysis

The details of the analysis are given in appendix E; here a rather general outline is presented. For the two regions the one-dimensional flow equations for conservation of mass, momentum, and energy along with appropriate equations of state are combined and integrated to yield nine simultaneous equations involving the 11 unknown quantities; P, ρ_1, v_1, h_1, A_1, ρ_2, v_2, h_2, A_2, $\dot{m}$, and V; where P = pressure, ρ = density, v = flow velocity, h = enthalpy, A = cross-sectional area, $\dot{m}$ = mass flow rate, and V = arc voltage; the subscripts 1 and 2 denote regions 1 and 2 respectively. The formal solution is completed by two additional relationships. One relation comes from including the effect of heat conduction from the core region to the surrounding sheath of cool gas which, in terms of this model, manifests itself in a mass transfer from region 2 to region 1; it is found that $\dot{m}_1 \sim x$. The other relation is supplied by Ohm's law for the column. The actual solution is obtained by an iterative procedure.

The solution contains five arc operation parameters which are the constrictor area, total mass flow rate, arc current, enthalpy of region 2 at $x = 0$, and the pressure at $x = 0$. These five parameters together with certain gas properties completely determine the solution. However, due to thermal choking phenomena, it is possible to have physically unmeaningful solutions. If the energy addition in the nozzle is not too large, then the sonic point is located near the (nozzle) end of the constrictor and this assumption is employed. This serves to determine one of the arc operating parameters, say the initial pressure, from the others.

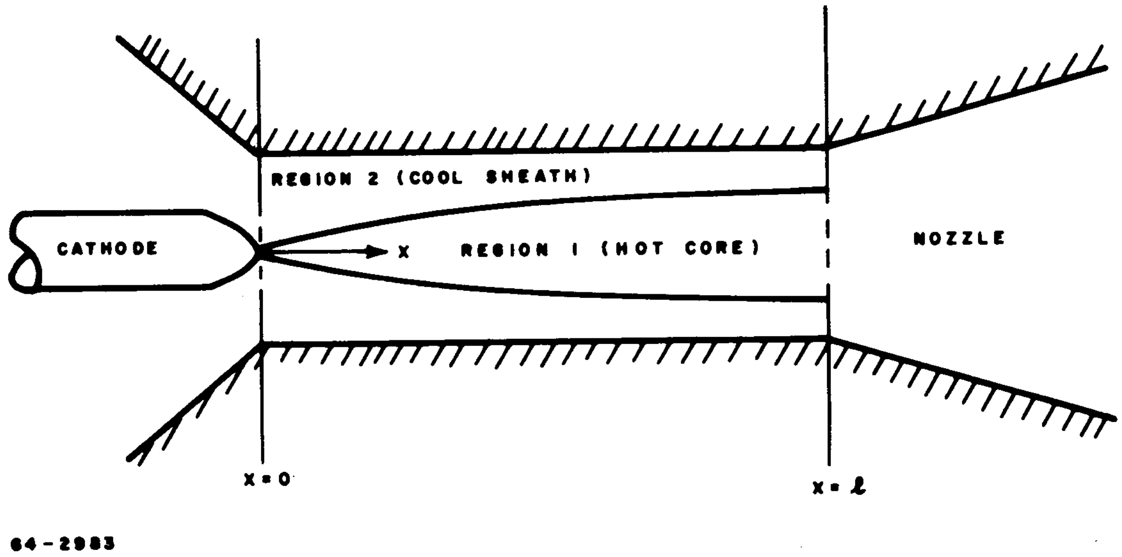
REGION 2 (COOL SHEATH)
CATHODE
X
REGION I (HOT CORE)
NOZZLE
X = 0
X = ℓ
64-2983

Figure 42 SCHEMATIC DRAWING OF THE TWO FLUID MODEL

d. Example

The solution to this model has been obtained for a set of arc operating parameters which are representative of a radiation-cooled 30-kw arc-jet engine. It is found that the arc voltage up to the axial position x is practically linear with x which is in agreement with voltage probe measurements and corresponds to a voltage gradient of 90 volt/cm in fair agreement with the measured value of 70 volt/cm. The column radius (region 1) is found to be qualitatively similar to the experimental observations for the region near the cathode tip but it is somewhat too large. However, this may be the result of differences in the experimental and theoretical definitions of column radius. Finally, the calculated pressure distribution is found to be linear with axial position over most of the constrictor. The linear pressure distribution and corresponding slope are in fair agreement with measured values obtained using a specially constructed pressure tap engine. The details are given in the appendix E.

e. Summary

Although the present model is rather crude, it nevertheless predicts many of the essential features of the experimental observations. Future work should include further refining of the model and solutions should be obtained for a variety of arc operating parameters and compared with experimental data.

4. Dissociative Non-equilibrium in the Constrictor

Based upon previous study[11] at this laboratory, doubt has been cast upon the assumption that the dissociation of H_2 molecules in the constrictor reaches an equilibrium value before the gas enters the nozzle. As reported in reference 11, various characteristic times were compared.

It was shown for a pressure of 1 atmosphere and for temperatures less than about 5000°K, the characteristic time for dissociation, T_d, is $\leq T_L$, the residence time; $T_d \approx T_L$ for $T \geq 5000°K$. Since a substantial fraction of the mass flow of the gas in the constrictor is in the relatively cool outer sheath, this result suggests that this portion of the gas flow may be heated without incurring an equilibrium degree of dissociation, thereby effectively relaxing the upper bound on propulsive efficiency implied by an equilibrium frozen flow loss. It is this possibility that has motivated an analysis which goes beyond comparing the characteristic times involved. Hence, the objective of this investigation is to determine, for a chosen model of the constrictor flow, the degree of dissociation reached at the end of the constrictor and to compare this value with the degree of dissociation implied by equilibrium.

The dissociation of H_2 proceeds through the two reactions

$$H_2 + H \underset{\alpha_1}{\overset{\beta_1}{\rightleftarrows}} H + H + H \tag{3}$$

and

$$H_2 + H_2 \underset{\alpha_2}{\overset{\beta_2}{\rightleftarrows}} H + H + H_2 \quad . \tag{4}$$

The equation for the production of H atoms through the dissociation of molecules is therefore

$$\frac{d}{dt} (N_1/2) = \beta_1 N_1 N_2 + \beta_2 N_2^2 - \alpha_1 N_1^3 - \alpha_2 N_1^2 N_2 \tag{5}$$

where N_1 is the concentration of H atoms (atoms/cm^3), N_2 is the concentration of H_2 molecules (molecules/cm^3), β_1 , and β_2 are the dissociation coefficients (cm^6/particle-sec); and α_1 and α_2 are the recombination coefficients (cm^6/particle^2/sec).

Numerical values of dissociation and recombination coefficients at temperatures to 5000°K are found in the literature (e. g., see references 12 through 15). For the purposes of this report let it suffice to say that values of the dissociation coefficients outside of the measured temperature range (2000-5000°K) obtained by extrapolation will tend to be overestimated due to lack of vibrational equilibrium.[16-19] For the calculation to be reported here, the effects of recombination are discarded altogether and the values of β_1 and β_2 were obtained by a straight line extrapolation on log-log paper over the temperature range needed. Both of these approximations tend to overestimate the effects of dissociation.

Disregarding recombination, equation (5) becomes

$$\frac{d}{dt} (N_1/2) = \beta_1 N_1 N_2 + \beta_2 N_2^2 \tag{6}$$

Setting $N_2 = N_2^\circ - N_1$ where N_2° is the initial concentration of H_2 molecules, equation (6) can be solved for N_1 (t). The result is

$$N_1(t) = N_2^\circ \beta_2 \frac{e^{2\beta_1 N_2^\circ t} - 1}{\beta_2 (e^{2\beta_1 N_2^\circ t} - 1) + 2\beta_1} \tag{7}$$

The initial density of H_2 molecules at the radius r is given by

$$N_2^o\,(t) = \frac{PN_o}{RT(r)} \tag{8}$$

where P is the pressure (assumed to be constant) N_o is Avogradro's number, R is the universal gas constant and $T(r)$ is the temperature at the radial point r. The propellant is assumed to move through the constrictor at the sonic velocity $V(r)$ given by

$$V(r) = {\frac{\gamma RT(r)}{M}}^{1/2} \tag{9}$$

where $\gamma = C_p/C_V$ and M is the molecular weight of H_2. The length of the constrictor is chosen to be 1 centimeter and the pressure as 0.5 atmosphere.

The total number of H_2 molecules entering the constrictor per unit time is then given by

$$N_2^{total} = 2\pi \int_o^{r_c} N_2^o\,(r)r\,dr \tag{10}$$

where r_c is the radius of the constrictor. From equation (7), the number of these H_2 molecules dissociated in passing through the constrictor is given by

$$N_2^{dissociated} = \frac{N_1^{total}}{2} = 2\pi \int_o^{r_c} \frac{N_1}{2}\,\frac{L}{V(r)}\,r\,dr \tag{11}$$

where $L/V(r)$ is the time the propellant at radius r spends in the constrictor (L = 1 cm).

A certain temperature profile is assumed to exist at the upstream end of the constrictor and to persist throughout its length. The temperature profile chosen is shown in figure 43. The curve was arrived at in combination empirical and analytic fashion. With a given temperature distribution along with the assumptions of (1) thermodynamic equilibrium, (2) constant pressure (chosen to be 0.5 atmospheres), and (3) sonic flow at the throat, profiles of enthalpy, flow velocity and density can be determined. From these profiles, the mass, power and momuntum flows through the engine can be computed and compared with measured quantities, thereby determing the degree to which the assumed temperature distribution is consistent with laboratory performance.

The profile in the vicinity of the center-line was chosen to be of the same general shape as given by the Heller-Elenbaas model using a current and voltage gradiant corresponding to a typical operating condition for the 30 kw arcjet engine. In addition,the temperature and temperature gradient at the constrictor wall were chosen to be those values indicated by a heat-transfer calculation given in reference 1. Finally, the temperature distribution in the region between the outer edge of the arc column (Heller-Elenbaas) and the constrictor wall was chosen to join smoothly with the temperature distribution in the arc column and near the wall, both in terms of absolute temperature and temperature gradient. The curve in figure 43 corresponds to mass flow of 0.15 gm/sec, a power of 32.4 kw and a thrust of 182 gmf. The measured thrust for this case was found to be 200 gmf.

It is remarked that for the puposes of this calculation, the temperature profile in figure 43 is assumed to hold not only at the throat but throughout the constrictor. The assumption that the hot core exists at the upstream end of the constrictor is not severe but the outer regions of the profile in figure 43 overestimate the temperatures for the upstream end of the constrictor.

The integrals in equation (10) and (11) have been evaluated numerically to give the results

$$N_2^{\text{dissociated}} = 1.36 \times 10^{16} \text{ molecules/sec}$$

and

$$N_2^{\text{total}} = 1.40 \times 10^{17} \text{ molecules/sec}$$

indicating that about 10 percent of the hydrogen propellant has been dissociated.

If it is assumed that dissociation equilibrium is reached for all temperatures in the constrictor, then a calculation similar to the one above shows that about 20 percent dissociation would be obtained.

In summary, the foregoing calculation indicates that it is likely that substantially less energy is lost in dissociating hydrogen in the constrictor of the 30 kw arcjet engine than is indicated from thermodynamic equilibrium considerations.

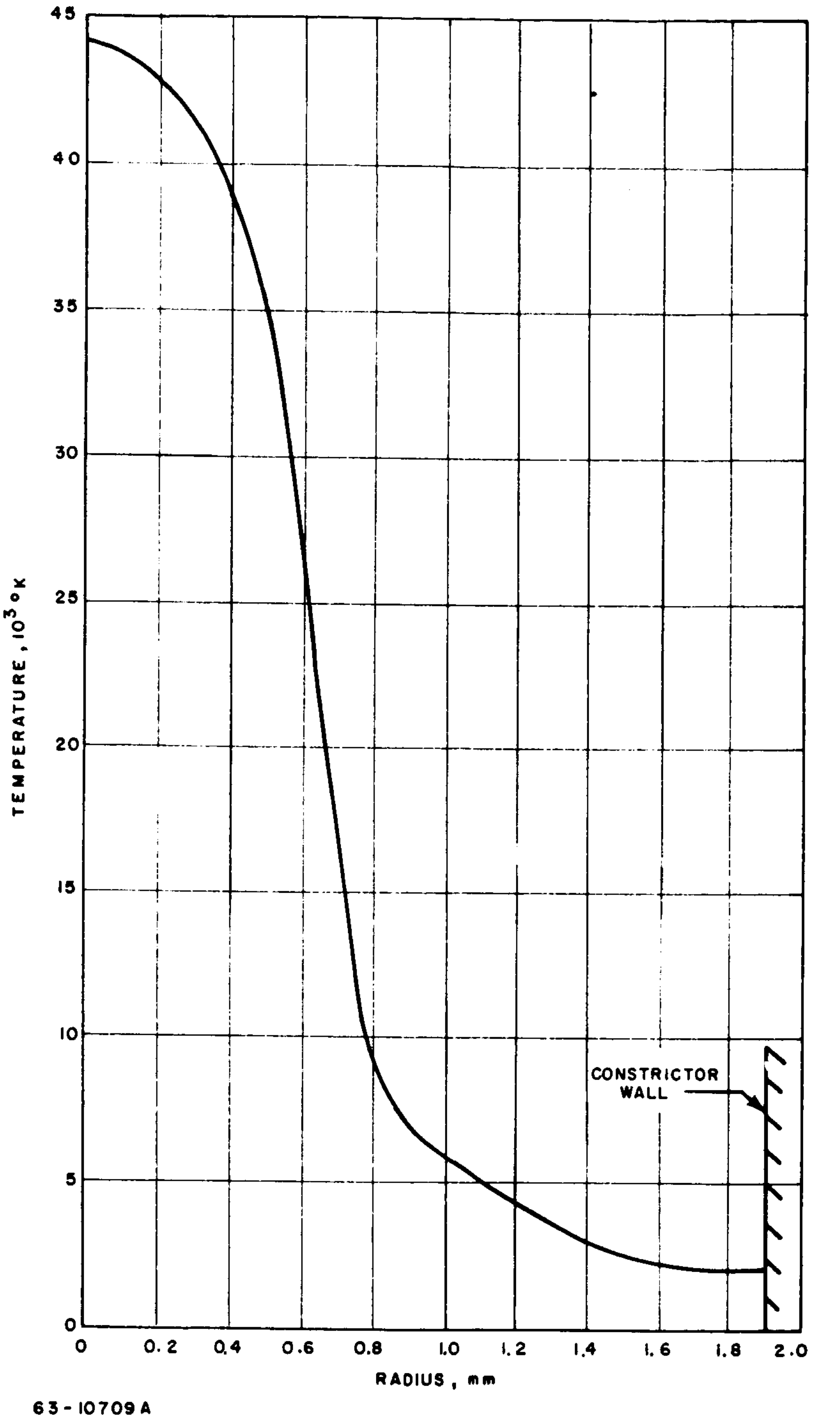

Figure 43 ASSUMED CONSTRICTOR TEMPERATURE PROFILE

5. Arc-Engine Voltages In Hydrogen, Nitrogen, Ammonia, and Helium

a. Introduction

A series of measurements has been carried out to determine the effect on arc operation of varying flow rates of four different gasses: hydrogen, nitrogen, ammonia, and helium. The purpose of these measurements is twofold: first, they lead to empirical relationships which can be used to predict the electrical characteristics of a specific engine when operated with one of these gases, if information already exists regarding its operation in another; second, interpretation of the data may be expected to yield information concerning those parameters which fix the arc voltage for given arc current. In turn, this may lead to an improved understanding of the energy-transfer processes within the engine.

b. Description of Measurements

Two sets of tests were made. The first, which is referred to as the preliminary set, was made to ensure that the mode of arc operation was similar for the four gases tested. That is, it was thought necessary to obtain visual evidence that the arc discharge was running from the cathode tip, through the constrictor, and attaching downstream of the nozzle throat. Previous experience with helium in an arc-jet engine[20] indicated that the arc might tend to strike short, attaching to the constrictor section or even upstream of the constrictor.

An experimental engine which has been used previously for visual inspection of the arc column, and which is sketched in figure 44, was employed for these observations. As indicated in figure 44, this engine has two holes bored radially from the outer circumference of the engine into the constrictor region. One hole is located so that it allows inspection of the discharge near the cathode, including the cathode tip. The second hole is downstream of the first one, allowing a field of view which extends almost to the nozzle throat. The hole diameters are 0. 125 inch and the center-to-center separation is 0. 187 inch. The center of the upstream hole is located at the point where the constrictor straight section begins. For this experimental engine the constrictor length is 0. 300 inch and the constrictor diameter 0. 136 inch.

In operation, the viewing holes are closed off at the engine exterior surface with a quartz plate. During operation, the quartz plate tends to heat, and to prevent destruction of this plate,runs are limited to periods of less than one minute and are generally made at low-power levels.

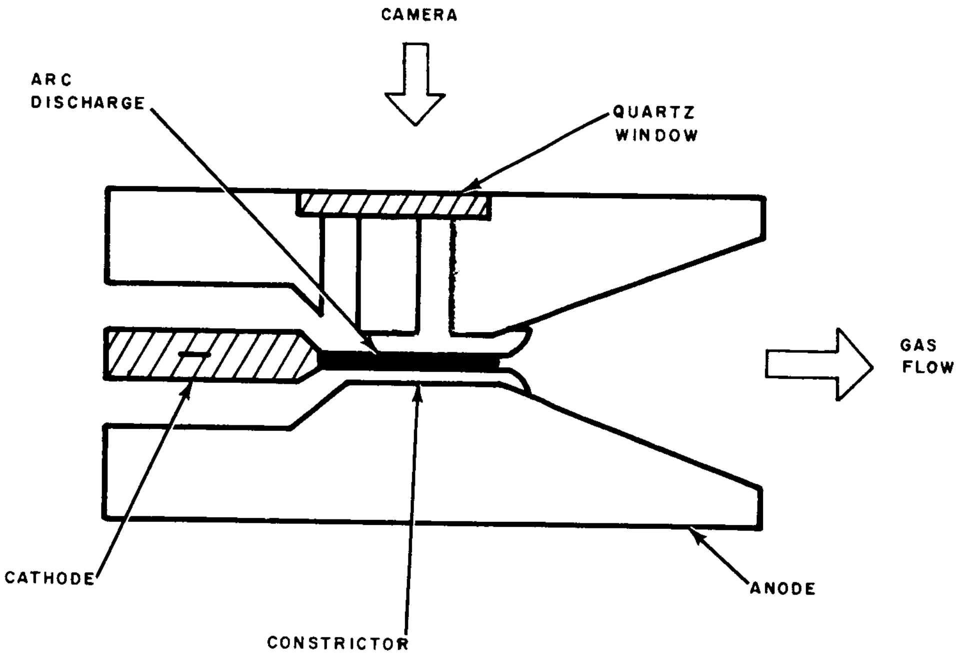
CAMERA
ARC DISCHARGE
QUARTZ WINDOW
GAS FLOW
CATHODE
ANODE
CONSTRICTOR

63-12697

Figure 44 EXPERIMENTAL ARCJET ENGINE FOR OBSERVATION OF THE ARC DISCHARGE

A series of tests was made with this experimental engine utilizing the gases hydrogen, nitrogen, ammonia, and helium. Photographs were made in each case, and four typical photographs are reproduced as figure 45. The test conditions under which the photographs of figure 45 were made are summarized in table 16.

TABLE 16

ENGINE OPERATING CONDITIONS FOR FIGURE 45

Gas	Flow Rate (gm/sec)	Arc Voltage (volts)	Arc Current (amperes)	Arc Power (kw)
H_2	0.120	88	100	8.8
NH_2	1.02	132	100	13.2
N_2	1.68	95	100	9.5
He	0.48	55	100	5.5

In each of the photographs of figure 45, the arc leaves the cathode-tip area and passes through the visible portions of the constrictor section. To this extent, the electrical characteristics of the arcs in different gases are comparable. It was observed that operation in this mode, which is achievable with relatively low mass flows of hydrogen, requires larger mass flows of the other gases. It appeared that comparison of the arc in different gases might be appropriate on the basis of comparable molar flow rather than mass-flow rates. Reduction of the mass flow rate of ammonia, for example, to 0.12 grams/second (which produces reliable operation in the strikethrough mode with hydrogen) resulted in failure of the arc to pass through the constrictor.

When these preliminary experiments had been carried out, a series of tests over a wide range of currents, powers, and mass-flow rates were made for the four gases employing a standard propulsion-type engine. This engine (No. 55) has a constrictor-length-to-diameter ratio of 0.400 to 0.200 inch. The main braze between the thoriated tungsten anode and the molybdenum plenum-chamber section is made with a chrome-vanadium brazing material, while the braze at the gas-entry tube is made with a 50 percent Cu--50 percent Pt brazing material. The gap setting of this engine for all runs was 0.095 inch. The nozzle exit diameter was 0.840 inch, the nozzle-area ratio was 17.7, and the nozzle angle was 36 degrees.

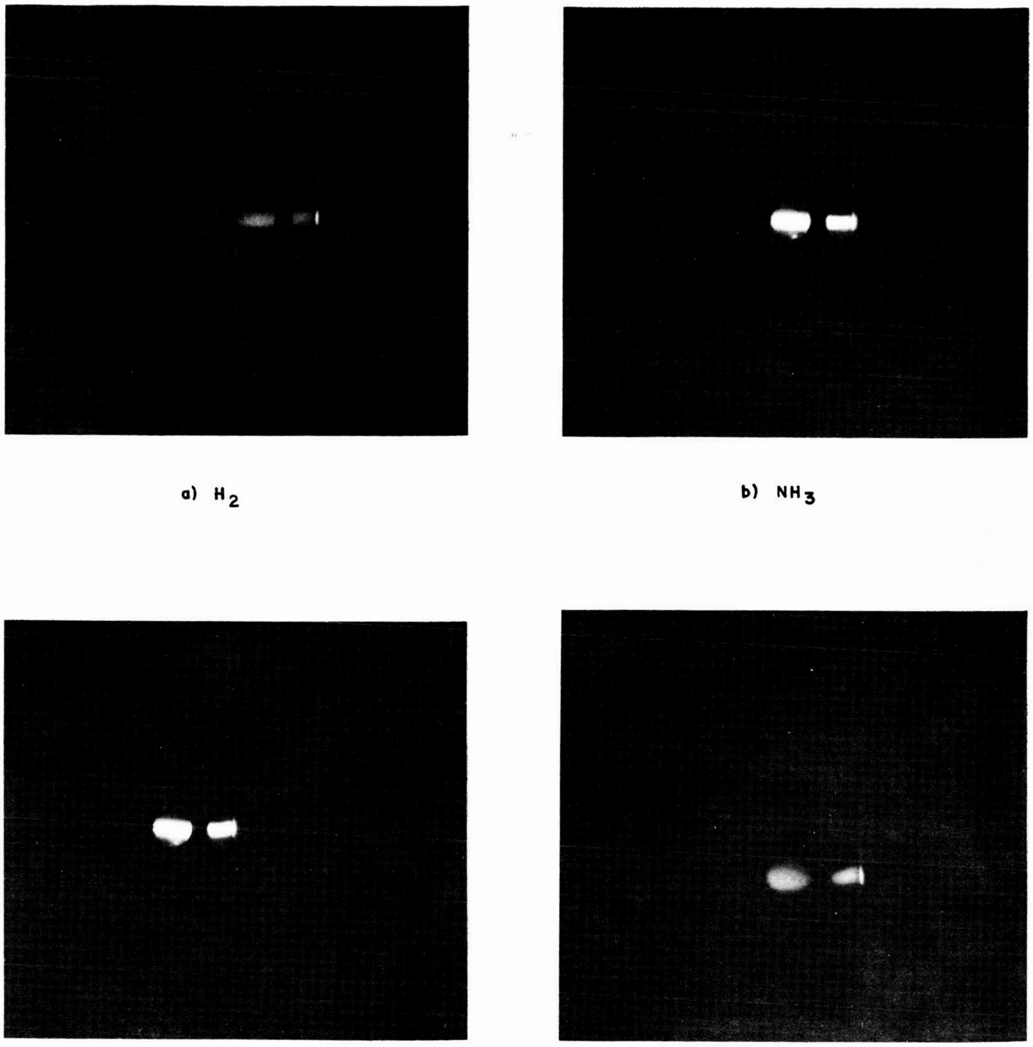

a) H_2

b) NH_3

c) N_2

d) He

OPERATING CONDITIONS GIVEN IN TABLE 9

63-12698

Figure 45 ARC COLUMN IN HYDROGEN, AMMONIA, NITROGEN, AND HELIUM

The test sequence was as follows: for the gas being tested, a desired mass-flow range was established bounded by the upper limits of the flowmeters being used and by the necessity of ensuring operation in the strikethrough mode at the lower limit; insofar as possible, a range of mass flows for each gas was employed so that an overlap among the molar-flow rates of the different gases was obtained; the gas flow then was set at the upper limit of the range chosen, and the arc run at a current of 100 amperes; when the engine had reached steady-state conditions, as indicated by the stability of all measured quantities with respect to time, data were recorded; the current then was increased to 125 amperes, and after a further waiting period to ensure stability the data were again recorded; in this way, an arc current of 225 amperes was reached in steps of 25 amperes; the mass-flow rate was then reduced slightly, and the arc run again at 100 amperes; this process was repeated until the entire mass-flow range was covered; the next gas then was introduced, and the same procedure was followed until all data had been recorded. In general, a time period of 15 to 20 minutes elapsed between the time the engine was started and the first data were recorded. An increase of current or a decrease of mass-flow was followed by a waiting period of 3 to 5 minutes before data were recorded. Time intervals of this length were required to reach steady-state operating conditions generally resulted in a change in engine-operating temperature; the time constant associated with the engine-temperature change is of the order of minutes. The order in which the gases were tested was: hydrogen, ammonia, nitrogen, helium, hydrogen. The second hydrogen test was made to ensure that the test setup gave reproducible results and that there had been no significant changes in the engine or the test system over the test program.

The data recorded were mass-flow rate, arc voltage, arc current, thrust, plenum-chamber pressure, vent pressure, and engine temperature at the exit plane (measured pyrometrically). Approximately 300 operating points were reached during the tests, which occupied three days.

c. Analysis

Figures 46 and 47 illustrate the data on voltage-current characteristics for each of the gas types for two different currents; figure 46 displays the measured voltage as a function of molar-flow rate at a current of 100 amperes and figure 47 presents the same parameters at a current of 200 amperes. The reproduciblity of these particular data can be judged by the two sets of points for hydrogen, one set of which was obtained from the first tests run while the other set came from the last tests run. (There was some concern on this account during the experiments, for the engine developed a leak at a "C"-ring seal during the first hydrogen test series; this affected the thrust measurements noticeably, but apparently had little effect on the measured voltages).

Perhaps the most striking feature of figures 46 and 47 is that the gases hydrogen, nitrogen, and ammonia offer very similar operating voltages at equivalent molar-flow rates. For example, at a molar-flow rate of 0.06 moles/sec, and a current of 100 amperes, hydrogen runs at 129 volts, nitrogen at 104 volts, and ammonia at 150 volts. Helium is substantially below this grouping, running at 44 volts, at 0.06 moles/sec. A second observation which can be made from figures 46 and 47 is that the operating voltage is relatively insensitive to current level in this current range. At a current of 200 amperes and a flow rate of 0.06 moles/sec hydrogen operates at approximately 120 volts, nitrogen at 103 volts, ammonia at 149 volts, and helium at 41 volts. This very slow variation of operating voltage with current is typical of arc discharges not exposed to flow, but its persistence in the flow situation does not automatically follow.

Finally, for each gas and for both currents the operating voltage increases with mass flow. Over much of the flow range the variation of voltage with flow is linear; however, there are indications, especially in figure 47 that at the low flow rates the dependence of voltage on flow rate becomes stronger.

To provide an analytical basis for these qualitative observations these data have been examined in terms of the core-flow model previously proposed.[1] According to this model, the arc discharge in the constrictor region is thought of as a heated wire, over which the gas flow passes. The characteristics of the discharge column itself are determined through the Heller-Elenbaas equation by the gas-transport properties (thermal and electrical conductivity and radiated power) and by two parameters which may be selected from the group including voltage gradient, current, column radius, column cooling rate, and central temperature. Specification of any two of these parameters specifies the others and leads to a complete column temperature profile. The imperfections of this model of the arc discharge (especially the neglect of axial flow through the column) are well-known, but this simplified model has proved useful in the past[1] as a basis for further work.

For the purposes of this analysis, it proved convenient to specify current and voltage gradient to determine an arc-column solution. The current is directly measured. However, the voltage gradient was not directly measured. A separate series of measurements described earlier in this report indicated that the voltage drop in the constrictor region, at least for hydrogen under certain running conditions, is approximately one-half of the total arc voltage.

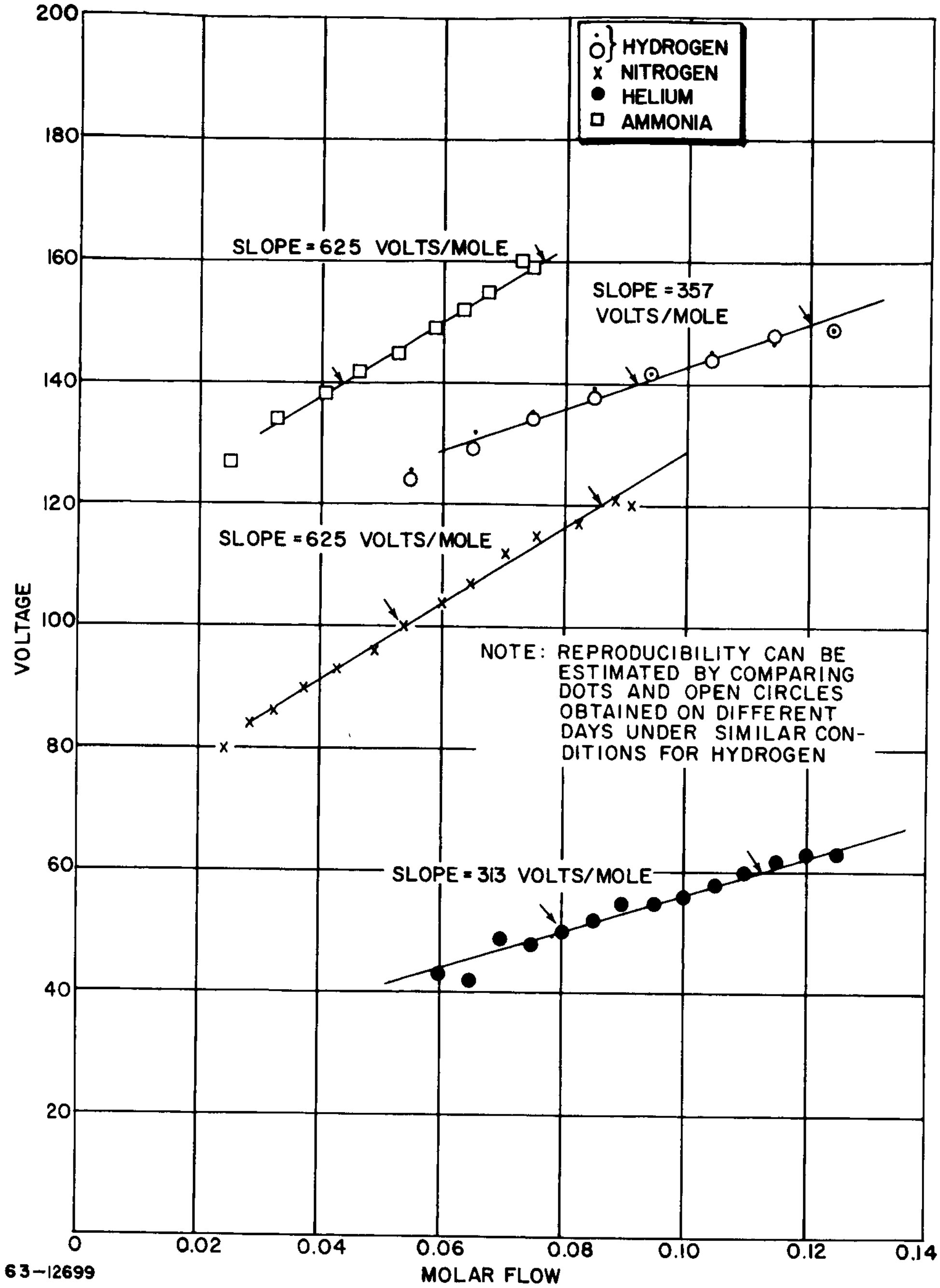

Figure 46 ARC VOLTAGE VERSUS MOLAR FLOW RATE, ARC CURRENT 100 AMPERES

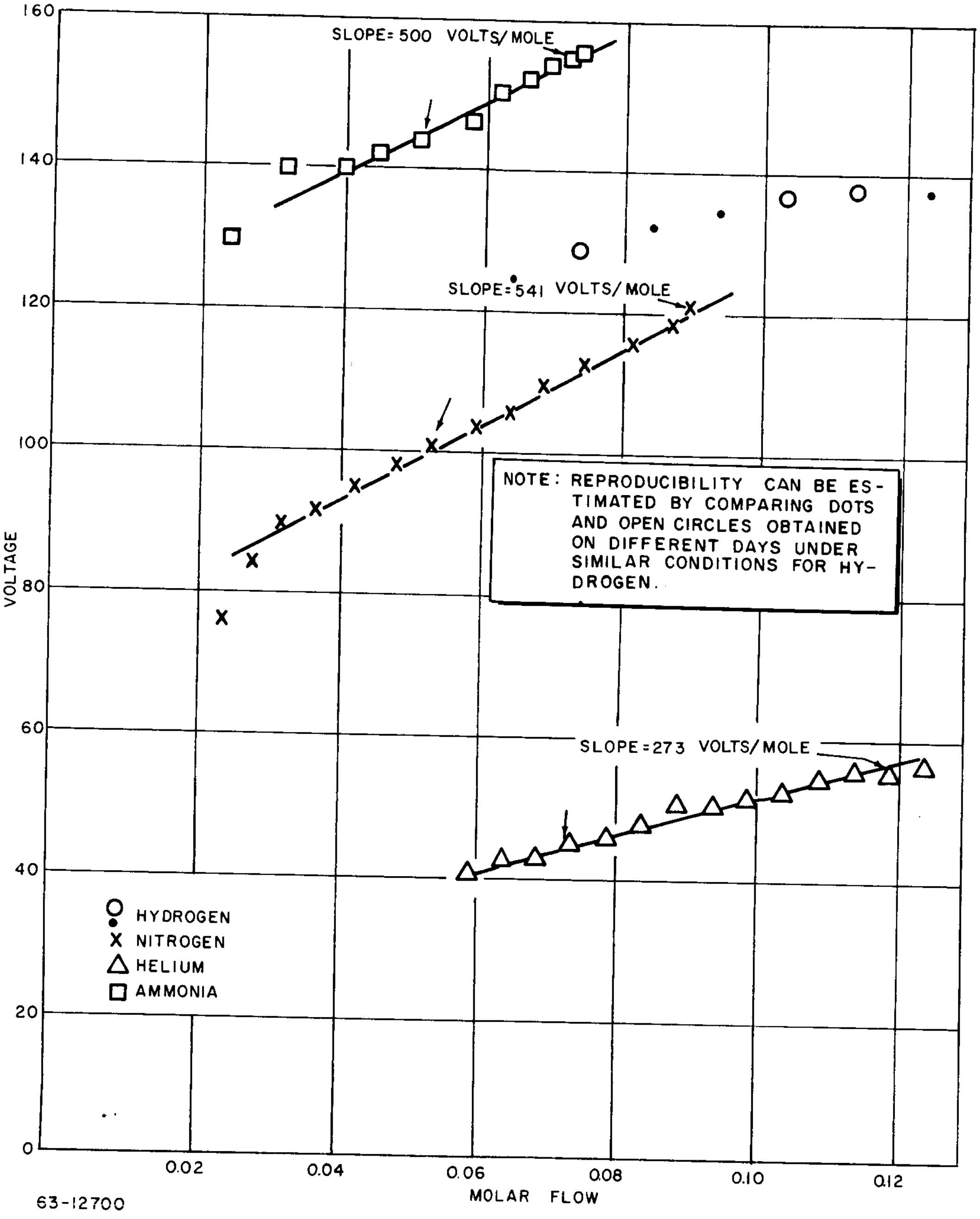

Figure 47 ARC VOLTAGE VERSUS MOLAR FLOW RATE, ARC CURRENT 200 AMPERES

If the assumption is made that this holds true for all of the gases tested over the range of molar-flow rates and currents employed and this voltage drop is combined with the constrictor length (almost exactly 1 centimeter for this engine), estimates can be made of the voltage gradients characteristic of each gas. These are summarized in table 17.

TABLE 17

ESTIMATED VOLTAGE GRADIENTS FOR AMMONIA, HYDROGEN, NITROGEN, AND HELIUM

Gas	Highest Voltage Gradient (volts/cm)	Lowest Voltage Gradient (volts/cm)	Representative Gradient (volts/cm)
NH_3	80	65	75
H_2	75	60	70
N_2	60	40	50
He	30	20	25

In the analysis which follows, the representative voltage gradients of table 17 will be used; variation of voltage with flow rate will then be discussed.

Solutions of the Heller-Elenbaas equation were obtained for currents of 100 and 200 amperes and for voltage gradients over a range including the representative voltage gradients listed in table 10 for each gas. The quantity desired for each solution was the column cooling rate, $(EI - W_r)/\pi d$, where E is the colume voltage gradient in volts/cm, I the current in amperes, W_r the radiated power per unit length of column in watts/cm, and d the column diameter in centimeters. The significance of this quantity is that it represents the rate per unit area of arc-column surface at which heat must be removed from the arc column by radial conduction. Since, according to the core-flow model, this heat is absorbed by the surrounding flow, it is thought that the column cooling rate should be the column parameter most directly affected by variation in the total propellant mass-flow rate or propellent type. That is, a low flow rate should imply a small-column cooling rate, while a large flow rate should correspond to a large-column cooling rate; additionally, if the gas type is such that the heat absorption of the flow is large this should correspond to a high cooling rate, while if the heat absorption of surrounding flow is small, again a low-cooling rate should be expected. Table 18 summarizes the results of the arc-column calculations in terms of column cooling rates.

TABLE 18

CALCULATED COLUMN COOLING RATES FOR ARC COLUMNS IN HYDROGEN, NITROGEN, AMMONIA, AND HELIUM, FOR CURRENTS OF 100 AND 200 AMPERES AND SELECTED VOLTAGE GRADIENTS

Gas	Current (amperes)	Voltage Gradient (volts/cm)	Column Cooling Rate (kw/cm^2)
H_2	100	70	9.5
	200	70	20.7
N_2	100	50	7.6
	200	50	12.4
NH_3	100	75	13.2
	200	75	23.5
He	100	25	0.65
	200	25	1.9

The indication of table 18 is that the cooling rates at each current for the different gases can be ordered in the same way as the voltage gradients; that is, the highest cooling rate goes with ammonia, followed by hydrogen, nitrogen, and helium in that order. Ammonia has by far the largest cooling rate, hydrogen and nitrogen are fairly close to each other, and helium has much the lowest cooling rate.

Next, the properties of each gas were examined to learn if, in fact, there is some correlation between the gas properties and the relative ability of each gas to cool an arc column. Figure 48 shows, for each of the four gases tested, the molar enthalpy as a function of temperature for a pressure of one atmosphere. If it is assumed that the surrounding gas stream cools the arc, and that the ability of the gas to absorb heat depends upon the temperature difference between the arc-column edges and the colling outer flow, it is clear that the larger the molar-heat capacity of a gas the more effectively it will be able to cool the arc. (The ability of the gas to transport heat also enters into this process.) It is expected, therefore, that if a gas has a high molar-heat capacity (or, equivalently, a high molar enthalpy at a given temperature) coupled with a high thermal conductivity, that it should be a good coolant. On the other hand, poor heat capacity or poor thermal conductivity should result in poor cooling ability.

Figure 48 shows that up to temperatures of the order of 7000° K, which are thought to be roughly characteristics of the flow immediately surrounding the arc column, the molar-heat capacities are, in descending order, ammonia, hydrogen, nitrogen, and helium. At about 7000° K the molar enthalpies of hydrogen and nitrogen cross over. This ordering is in agreement with the results of table 18. Inspection also has been made of the thermal conductivities at a pressure of one atmosphere summarized in table 19.

TABLE 19

THERMAL CONDUCTIVITIES OF AMMONIA, HYDROGEN, NITROGEN, AND HELIUM AT ONE ATMOSPHERE

(Units of k are mw/cm-° K)

Temperature ° K	NH_3	H_2	N_2	He
1000	2.72	4.37	0.67	--
2000	5.61	9.03	1.17	--
3000	45.2	69.0	1.64	8.6
4000	90.4	148.	2.36	10.9
5000	26.4	36.3	6.34	13.0
6000	32.5	22.4	23.1	15.2
7000	32.3	23.6	44.5	17.2

The indications of table 19 do not change the conclusions reached on the basis of figure 48. The thermal conductivity of hydrogen is somewhat larger than that of ammonia, but the heat capacity of ammonia may overcome this difference. The fact that the thermal conductivity of hydrogen is so much larger than that of nitrogen can account for their different cooling rates even though their heat capacities are not too different. Finally, the thermal conductivity of helium, though larger than that of nitrogen for much of the temperature range considered, may not overcome the rather low-heat capacity of helium.

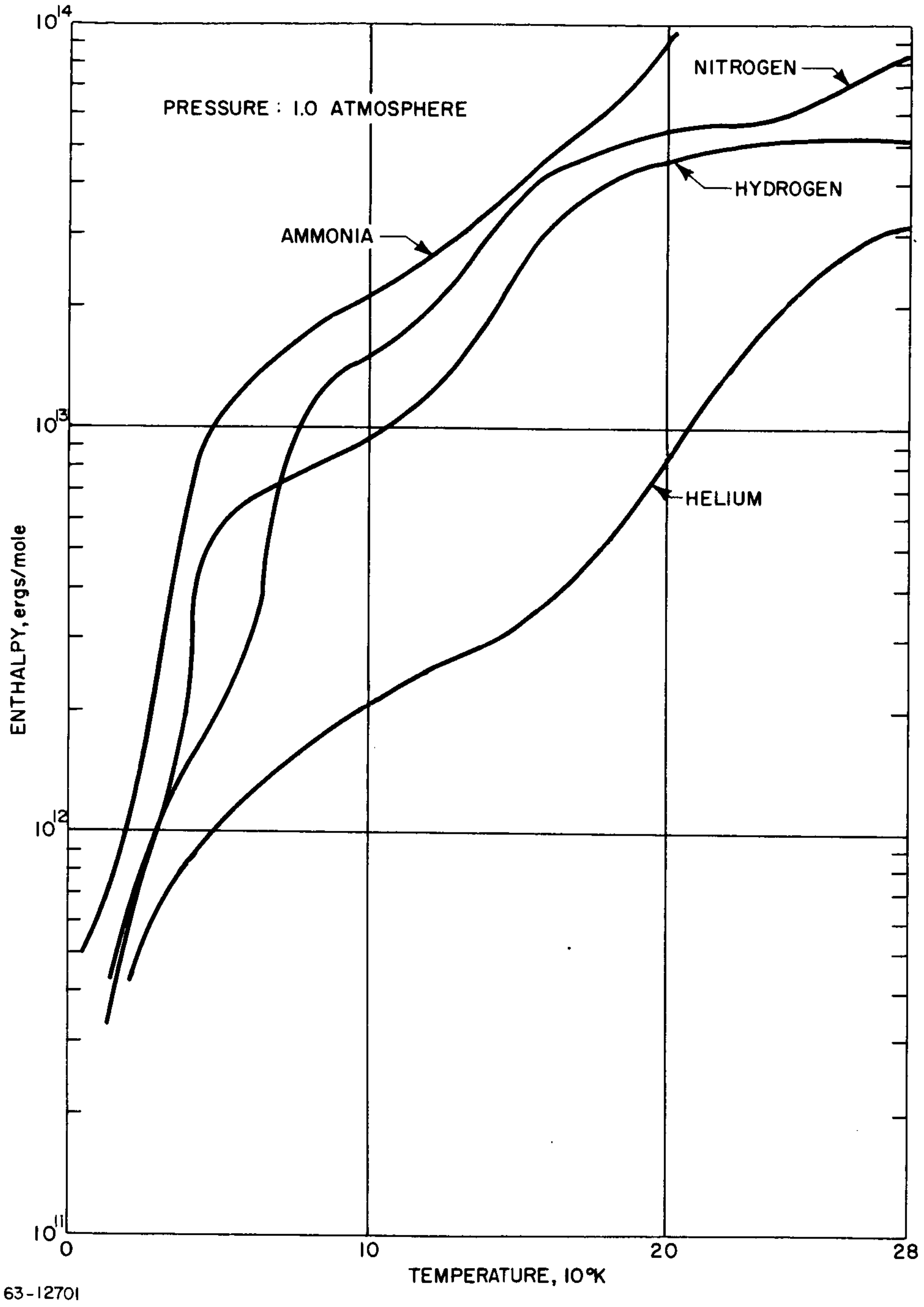

Figure 48 ENTHALPY VERSUS TEMPERATURE FOR HYDROGEN, AMMONIA, NIGROGEN, AND HELIUM

In summary, based on the core-flow model of arc operation, the voltage gradient associated with an arc column in a given gas and at a given current is determined by the ability of the surrounding gas flow to cool the arc (that is, to accept and carry away the heat which must be conducted radially out of the column). From experiments, estimates have been made of the voltage gradients obtained in a given engine configuration with each of four different gases. These estimated voltage gradients and the measured currents have been used to calculate the required cooling power of the surrounding flow. These required cooling powers have then been compared qualitatively with the molar-heat capacities and thermal conductivities of the four different gases; in the qualitative sense, there is agreement between the calculated cooling powers and the gas properties. That is, if the gases are ranked according to cooling power required by the measured voltages, the same ranking is found to describe the molar-heat capacity at temperatures up to 7000°K.

This qualitative agreement leaves several questions unanswered. In particular, why is the effect on arc voltage of a change in mass-flow rate for a given gas so small? For example, referring to figure 46, the voltage in hydrogen at a current of 100 amperes is 129 volts at a flow rate of 0.06 moles/sec, and 150 volts at a flow rate of 0.12 moles/sec. A partial answer to the question may be found in figure 49 where the calculated values of the column cooling rate for hydrogen are plotted against voltage gradient for currents of 100 and 200 amperes. From figure 49, a voltage gradient of 70 volts/cm at a current of 100 amperes corresponds to a cooling rate of 9.5 kw/cm^2. If this cooling rate is now doubled (to 19 kilowatts/cm^2), the voltage gradient is raised only to 96 volts/cm; hence, a conclusion of this Heller-Elenbaas based analysis is that the voltage gradient in a particular gas rises less rapidly than the column cooling rate. On this account, the relative insensitivity of arc voltage to propellant mass-flow rate may be understood. (It is stressed that only the trend is indicated by this brief analysis.)

A final feature of the electrical measurements of figures 46 and 47 should be observed. While the voltage is relatively insensitive to mass-flow rate, it is even less sensitive to arc current. The voltage data of figures 46 and 47 for currents of 100 and 200 amperes differ at most by a few percent. This is thought to have significance with regard to energy-transfer processes involving the arc column, as described below.

The first modifications of the core-flow model of arc-engine operation were concerned with energy transfer out of the arc column longitudinally by convection. That is, it was thought that the flow at the constrictor end, or nozzle throat, was likely to be sonic. In this case, using

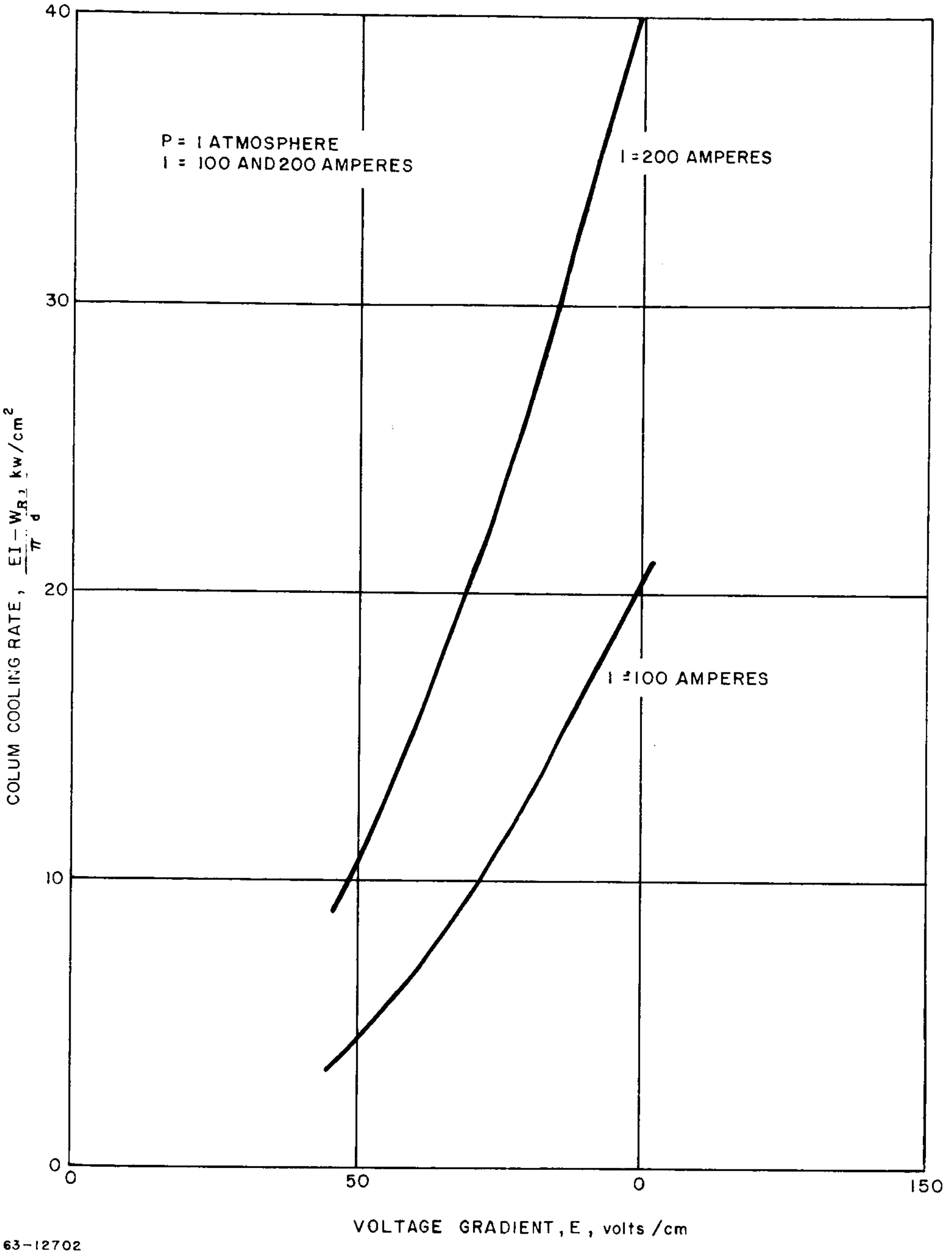

Figure 49 COLUMN COOLING RATE VERSUS VOLTAGE GRADIENT FOR THE FULLY DEVELOPED ARC COLUMN IN HYDROGEN

enthalpy profiles resulting from calculated temperature profiles based on the Heller-Elenbaas equation, it was possible to calculate the energy transported longitudinally out of the column at its downstream end, with the assumptions that the local density is given by the static pressure at the throat and the local temperature through the equation of state, and that the local velocity is sound speed at the calculated temperature. This energy-transport rate is given by the integral

$$P_{core} = 10^{-10} \int_{o}^{r_{col}} \rho u h \, 2 \pi r \, dr$$

where ρ is the local density in grams/cm^3, u is the local sound speed in cm/sec, h is the local enthalpy in ergs/gm, r_{col} is the column radius in centimeters, and P_{core} is the rate of energy transport longitudinally through the column in kilowatts.

P_{core} was calculated for a wide range of arc currents and voltage gradients (see figure 50) with the assumption that the static pressure at the throat was one atmosphere. (Subsequent experiments with an engine mounted with pressure taps indicated that this value should be approximately 0. 6 atmosphere. To a close approximation with the model assumed, P_{core} is proportional to the static pressure so that the earlier calculations may be used simply by multiplying the P_{core} obtained for one atmosphere by the constant 0. 6.) The results of these calculations showed that P_{core} is a significant fraction of the arc-column voltage drop multiplied by the arc current, so that the longitudinal transport of energy under this model was not negligible. Further, they indicated that P_{core} is relatively insensitive to current, but quite sensitive to voltage gradient, increasing as the voltage gradient decreases.

The experimental indications are that the arc voltage is insensitive to current; however, the arc power is approximately proportional to current because of the constancy of the voltage. Hence, since P_{core} is relatively insensitive to current, it represents a decreasing fraction of the total arc power as current is increased. If this is the case, it must be concluded that either the energy transfer processes in the arc undergo a significant change as current is increased, with P_{core} playing a smaller and smaller role compared with the total arc power; or, if the energy-transfer processes remain qualitatively the same as the current is increased, then P_{core} is probably overestimated at the lower current levels. It is thought that the most likely source of overestimation of P_{core}, if indeed this should turn out to be the case, is the gas density; vorticity may play a significant role in the constrictor. The static pressure near the center of the constrictor where the arc is established may be substantially lower than the static pressure measured at the constrictor wall, and the density may therefore be lower than has been thought. Careful gas-temperature measurements in the constrictor should establish the magnitude of radial heat conduction, and hence help to evaluate P_{core}.

d. Conclusions

i. Arc voltages have been obtained under a wide range of arc current and mass-flow rates of the four gases hydrogen, ammonia, nitrogen, and helium. These measurements will be useful in predicting the electrical characteristics of one of these gases in an engine once it has been run with another.

For example, electrical characteristics of hydrogen in an R-3 engine developed for use with ammonia can now be predicted. Further, an estimate can now be made of the minimum gas-flow rate to maintain the strike through mode of operation in a given engine configuration for one of these gases once it has been determined for another. It has been shown experimentally that the four gases tested are most easily compared on the basis of molar-flow rate.

ii. Comparisons of the measured voltages for each of the four gases are in qualitative agreement with the predictions of the core-flow model, based on the gas properties (heat capacity and thermal conductivity).

iii. The insensitivity of the arc voltage in a given gas to flow rate is in qualitative agreement with the predictions of the core-flow model.

iv. The insensitivity of the arc voltage to current implies either that the arc-engine energy-transfer mechanisms vary with current, or that longitudinal energy transport is less important than has been thought.

6. Arc Attachment Phenomena in a Supersonic Nozzle

In practical electrode-type plasma devices with a confluent arc and gas flow, long anode life is a necessity for reliable operation. This is particularly true since anode failures tend to be catastrophic. The heating load on the anode is higher than on any other solid boundary exposed to the arc. Hence, it is essential that locally intense and prolonged heating of the anode surface be eliminated.

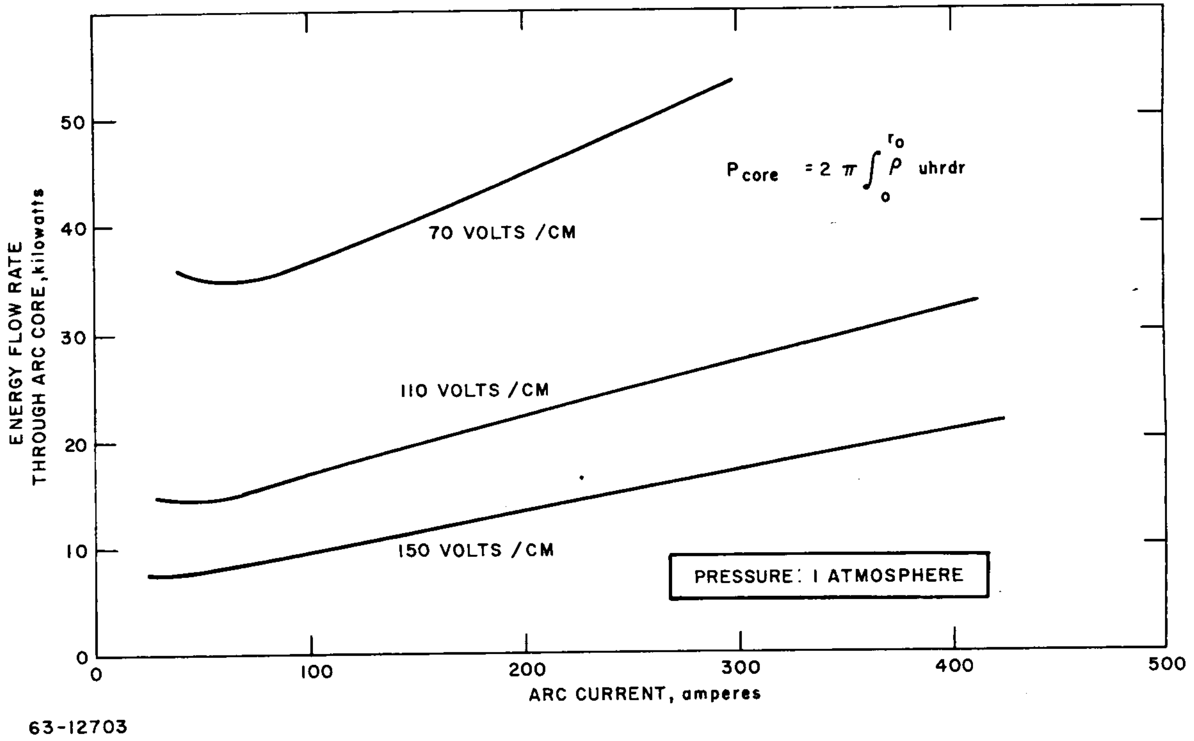

Figure 50 COLUMN ENERGY FLOW RATE VERSUS CURRENT FOR A FULLY DEVELOPED HYDROGEN ARC COLUMN

Various means have been devised to extend anode life. Intense swirling of the gas is often used to rapidly sweep the arc terminus over the anode surface. Simultaneously, the arc terminus tends to move axially along the anode with the gas flow.

It is the purpose of this investigation to study the electrical characteristics of arc-jet engine anodes, with particular emphasis on the interaction between the anode and the arc-heated gas flows, to provide a better understanding of the basic processes involved and a basis for the further improvement of arc-heater anodes and engines.

One of the apparent paradoxes of anode phenomena involves the mechanisms of electrical conduction to the anode. Since anodes with melting points below, say, 2000° C can be operated for long periods of time without being destroyed, it is generally concluded that the temperature of the gas near the anode wall must also be below 2000° C: Examining the equilibrium properties of gases in this temperature range, one finds that their electrical conductivity is very low. Predictions of the voltage drop across the cool boundary region yield values several orders of magnitude larger than the actual voltage drops across the entire arc.

It has been proposed that the cool sheath is, in reality, always hot and carrying a high current by means of a concentrated arc running from the conducting gas core of the arc to the anode surface. This implies an extremely large current density which, in turn, corresponds to very high temperatures. Current density is then a rather critical parameter in anode life and it is important to know how the current is distributed over the anode.

The long life of the anode is achieved by rapidly moving the arc terminus over the surface of the anode, thereby avoiding locally prolonged heating of the surface. The engineering developments leading to the achievement of long anode life have indeed coincided with the use of rapid sweeping of the arc terminus, leading to a desirable transient heat loading on the anode surface. As previously indicated, this has been accomplished by swirling the gas, and by using the gas flow to "blow" the anode attachment point down the gas flow duct (constrictor and nozzle).

One of the major objectives of this investigation has been the testing of the moving spot hypothesis; leading to a determination of the physical processes involved and the possible means of controlling them for the improvement of arc-jet engine design, performance and life.

The overall AC electrical characteristics of the arc have been experimentally determined for a hydrogen engine at various mass flow rates and power input levels. A schematic representation of the experimental arrangement is shown in figure 51. The trigger generator is used to trigger the two oscilloscopes simultaneously, thereby allowing direct comparison between the voltage and current at the same instant in time.

Figure 52 shows the voltage fluctuations at a mass flow of 0.28 gm/sec H_2 and a power level of 25 kw. The sawtooth shape of the voltage trace may readily be understood by the following argument. With an essentially constant current flow, the voltage across the cathode-anode is directly proportional to the impedance of the arc. As the arc length increases, its impedance also increases at the same rate. Thus, a linear lengthening of the arc is transformed into a linear rise of the voltage across the arc. The essentially constant slope of the voltage rise is thus indicative of an arc length which increases linearly, lending support to the hypothesis of an anode attachment point which moves axially along the anode surface at a constant velocity. When a new arc strikes nearer the cathode, the arc impedance drops and is directly observed by the rapid drop in the voltage. The fact that the voltage never seems to drop below a given value indicates that the new attachment point is always at very nearly the same axial position. The different maximum values show that the distance of travel does vary. The differences in voltage drop slopes are seen to be due to the fact that the time between the highest and lowest values is always the same.

Figure 53 shows the variation of the voltage trace at a mass flow of 0.19 gm/sec as a function of power input. Figure 54 shows the voltage variation at a power level of about 26.5 kw as a function of mass flow. It is evident from both figures that the voltage variation is smoothed out by an increase in specific enthalpy (arc power divided by mass flow) both in uniformity and in magnitude of variation.

An additional piece of useful information is obtained from the voltage-current traces, as seen in figure 55. The current and voltage ripples are of the order of 3 parts in 140, limiting the inaccuracy in total power input as measured using DC meters to less than 0.1 percent.

The results of this work led to the design and test of a segmented anode engine. In this engine the anode nozzle comprised four segments, separated along the flow direction by sheets of boron nitride insulation. The intention of experiments with this engine was to view directly the motion of the anode terminus, which would be evidenced by the pattern of current conduction through the individual anode segments. No unequivocal results were obtained with this segmented anode owing to the problem of electrical pickup between the circuits monitoring the current flow in each segment. The noise level associated with the transients as the anode termination moves from one segment to another is extremely high and ruled out quantitative measurements, although a number of steps were taken to minimize this noise problem. Qualitative indications were obtained that the current at the anode is indeed localized at a given time; one or two of the segments would carry current while the others did not. Also, qualitative indications were obtained that the terminus moved; at least, it is not always the same segments which carry current. However, these results are extremely preliminary.

Based on the overall electrical characteristics of the discharge in the engine, which could be carefully measured and which exhibited good reproducibility, the hypothesis that the arc attaches in a spot in the nozzle which is in cyclical motion is consistent with the data. The indications obtained with the segmented anode are also consistent with this picture in a qualitative sense, although there is little confidence in the quantitative value of the data.

D. EXHAUST JET DIAGNOSTICS

1. Introduction

A knowledge of the properties of the exhaust flow at the nozzle exit plane of the arcjet engine is directly applicable to evaluation of the arcjet engine loss mechanisms and limitations. In addition, the flow properties at the nozzle exit plane are useful in understanding flow phenomena occurring in the constrictor.

Measurements have been made on the exhaust jet yielding radial profiles of mass flux and impact pressure in the very near vicinity of the nozzle exit plane (approximately 0.1 nozzle diameters downstream). These measurements have been used to determine the radial distribution of the flow velocity and density and finally to compute the kinetic power of the exhausting propellant. Combining the kinetic power with estimates of the thermal power and radiated power, an estimate of the frozen flow loss (that power loss resulting from the presence of electrons and atoms) has been obtained.

The measurements were obtained using a modified R-4, Mod 1 arcjet engine with hydrogen as the propellant. The modifications were (i) no regenerative cooling passages and (ii) a nozzle exit diameter of 0.475 inch. The first modification was made for ease of fabrication and the second in order that the nozzle exit diameter be about twice that of the probe diameter.

The measurements were taken at the three operating conditions summarized in table 20. Probe lifetime considerations prevented measurements at the 30 kw level.

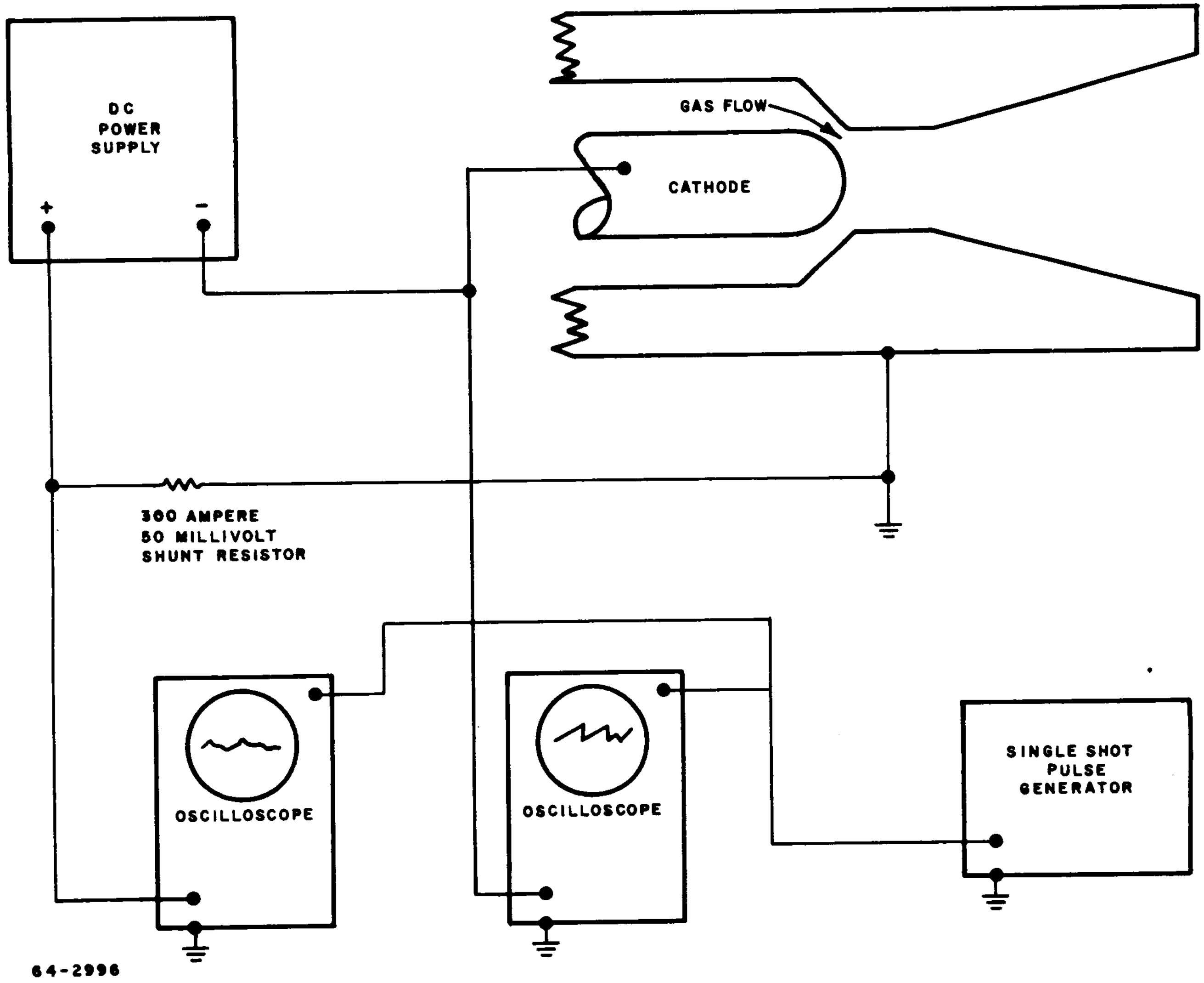
DC
POWER
SUPPLY
+
-
GAS FLOW
CATHODE
300 AMPERE
50 MILLIVOLT
SHUNT RESISTOR
OSCILLOSCOPE
OSCILLOSCOPE
SINGLE SHOT
PULSE
GENERATOR
64-2996

Figure 51 SCHEMATIC DRAWING OF CIRCUIT TO OBTAIN OVERALL AC CHARACTERISTICS

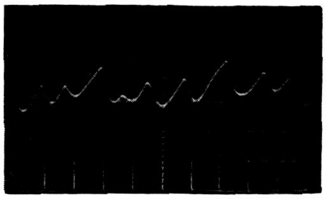

$\dot{m}$ = 0.28 GM/SEC H_2

ARC CURRENT = 156 AMPERES DC

ARC VOLTAGE = 160 VOLTS DC

ARC POWER = 25.0 KW

SWEEP SPEED = 2 μSEC/CM

VERTICAL SCALE = 5 VOLTS/CM

64-2997

Figure 52 TYPICAL AC VOLTAGE FLUCTUATION

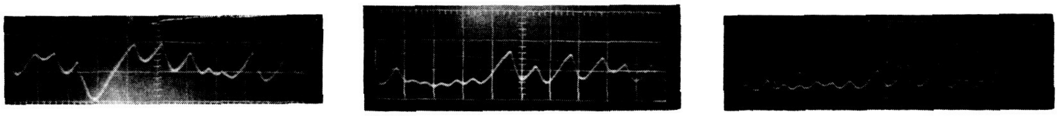

(a)

ARC CURRENT = 60 AMPERES DC

ARC VOLTAGE = 170 VOLTS DC

ARC POWER = 10.2 KW

(b)

ARC CURRENT = 120 AMPERES DC

ARC VOLTAGE = 150 VOLTS DC

ARC POWER = 18 KW

(c)

ARC CURRENT = 180 AMPERES DC

ARC VOLTAGE = 147 VOLTS DC

ARC POWER = 26.5 KW

$\dot{M}$ = 0.19 GM/SEC H_2

SWEEP SPEED = 2 μSEC/CM

VERTICAL SCALE = 5 VOLTS/CM

64-2998

Figure 53 EFFECT OF POWER LEVEL ON AC VOLTAGE FLUCTUATION

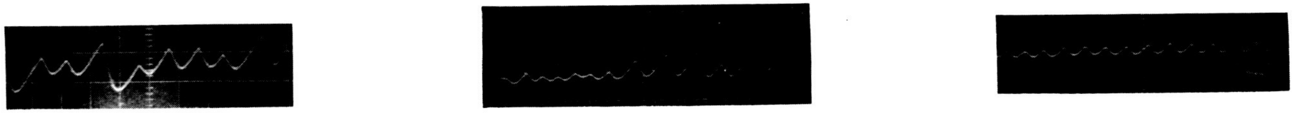

(A)
$\dot{M} = 0.25$ gm/sec H_2

(B)
$\dot{M} = 0.19$ gm/sec H_2

(C)
$\dot{M} = 0.13$ gm/sec H_2

POWER LEVEL ≈ 26 kw
SWEEP SPEED = 2 μ SEC/CM
VERTICAL SCALE = 5 VOLTS/CM

60-2999

Figure 54 EFFECT OF MASS FLOW RATE ON AC VOLTAGE FLUCTUATION

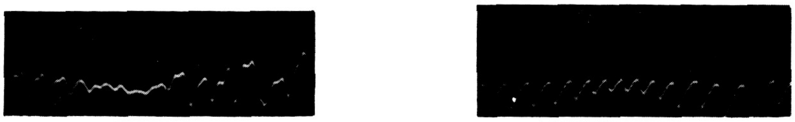

(A)
CURRENT
VERTICAL SCALE = 6 AMP/CM

(B)
VOLTAGE
VERTICAL SCALE = 5 VOLTS/CM

ARC CURRENT = 135 AMPERE DC
ARC VOLTAGE = 145 VOLTS DC
ARC POWER = 19.6 kw
$\dot{M}$ = 0.13 gm/sec H_2
SWEEP SPEED = 2 μ SEC/CM

64-3000

Figure 55. TYPICAL TIME-COINCIDENT AC VOLTAGE CURRENT FLUCTUATION

TABLE 20

OPERATING CONDITIONS USED FOR DIAGNOSTIC STUDY OF EXHAUST JET

Mass Flow Rate (gm/sec H_2)	0.20	0.15	0.20
Power (kw)	20	20	25
Arc Current (amperes)	131	136	168
Arc Voltage (volts)	153	147	149
Thrust (gmf)	165	146	181
Specific Impulse (sec)	825	1043	905
Overall Efficiency (%)	32.7	34.2	31.5

The measured impact pressure profiles are presented in Section 2, and the measured mass flux profiles in section 3. In section 4 the corresponding velocity and density profiles are displayed and in section 5 the discussion of energy partition and loss mechanisms in the arcjet engine is given; an extrapolation to the operating condition corresponding to 30 kw level is also presented.

2. Impact Pressure Profiles

a. Impact Pressure Probe and Associated Apparatus:

The impact pressure measurements were taken with a probe schematically represented in figure 56. The probe in figure 56 has a molybdenum tip; as work with the probes progressed, it was found that a copper tip with a very thin (≈ 0.030 inch) frontal surface was as good as the molybdenum tip from the point of view of withstanding the thermal environment in the exhaust jet and had the advantage of permitting a more reliable internal braze with the stainless steel tube through which the pressure is transmitted to the pressure measuring device.

The probe was cooled with water at a pressure of between 180-220 psi which corresponded to a flow rate of 1.6 gallons per minute through the probe. A strain gauge type transducer measured the pressure; the pressure measuring system was of extremely small volume permitting a steady state pressure trace in the order of one second.

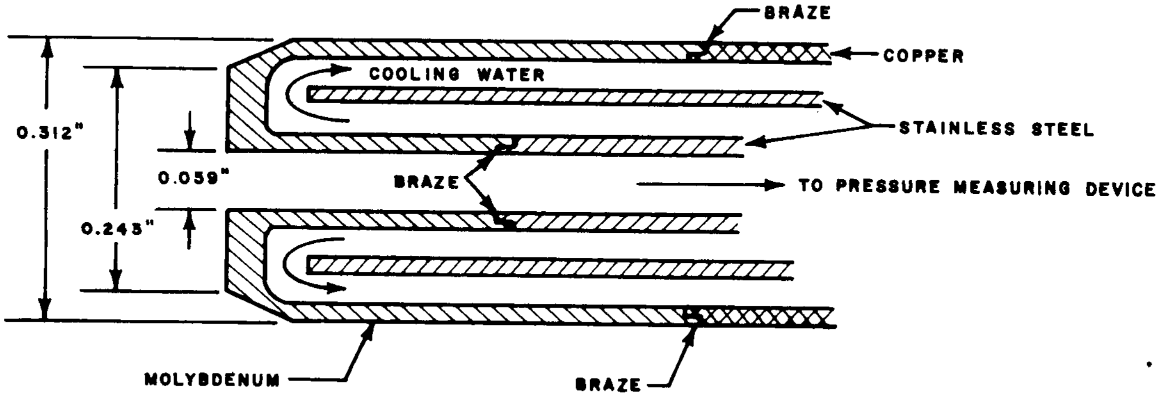
BRAZE
COPPER
COOLING WATER
STAINLESS STEEL
0.312"
0.059"
BRAZE
TO PRESSURE MEASURING DEVICE
0.243"
MOLYBDENUM
BRAZE

64-2992

Figure 56 FRONT PORTION OF EXPERIMENTAL IMPACT PRESSURE PROBE

The probe was hydraulically inserted into the exhaust stream for a measurement and then withdrawn. Figures 57 and 58 show two views of the probe insertion unit. The probe itself is mounted on top of a structure containing two Gilman slides which permit movement in the nozzle exit plane. Also shown is the 0-5 psia pressure transducer which is directly connected to the pressure outlet of the probe. Not shown are the copper cooling coils which are wrapped around the body of the transducer.

The Gilman slide structure rests on a bed in which are mounted two circular precision roller bearings which slide over the two case-hardened steel bars. The whole insertion unit is mounted on a sliding track in the test tank which permits adjustment of the axial position of the probe relative to the nozzle exit plane.

The Gilman slides are motor driven; a microswitch and two pins in the vernier head of each Gilman slide are arranged so that after every half turn of the lead screw to the slide (corresponding to a 0.0125 inch lateral motion) the motor stops automatically. Figure 59 shows the details for the horizontal motion slide. Both a mechanical counter and a channel on the recorder indicates the position of the probe tip during a radial traverse. It has been found that the probe insertion unit permits location of the probe tip to within a few thousandths of an inch throughout a traverse.

Not shown in figures 57 and 58 is a copper, water-cooled heat shield which protects the transducer, Gilman slide threads and bearing surfaces from the nozzle exhaust. Finally, figure 60 is a closeup of the probe tip.

A discussion of the theory of the impact pressure probe and the relation between the impact pressure measured by the probe and the momentum flux in the exhaust is given in appendix F.

b. Experimental Results:

The measurements were taken at a distance of 0.050-inch downstream of the nozzle exit plane. It was found that the measured impact pressure profiles show a lack of azimuthal symmetry. Comparison of the reproducibility of measurements obtained during a period of continued engine operation as compared to measurements taken during different periods of operation suggest that the lack of azimuthal symmetry is a real effect and may be due to an asymmetry in the arc-anode attachment phenomena which is not strictly reproducible in azimuth from one engine test to another. This possibility has led to averaging different sets of measurements all taken at the same mass flow rate and power level but during different periods of engine operation. The profiles so obtained tend to approximate an azimuthal average.

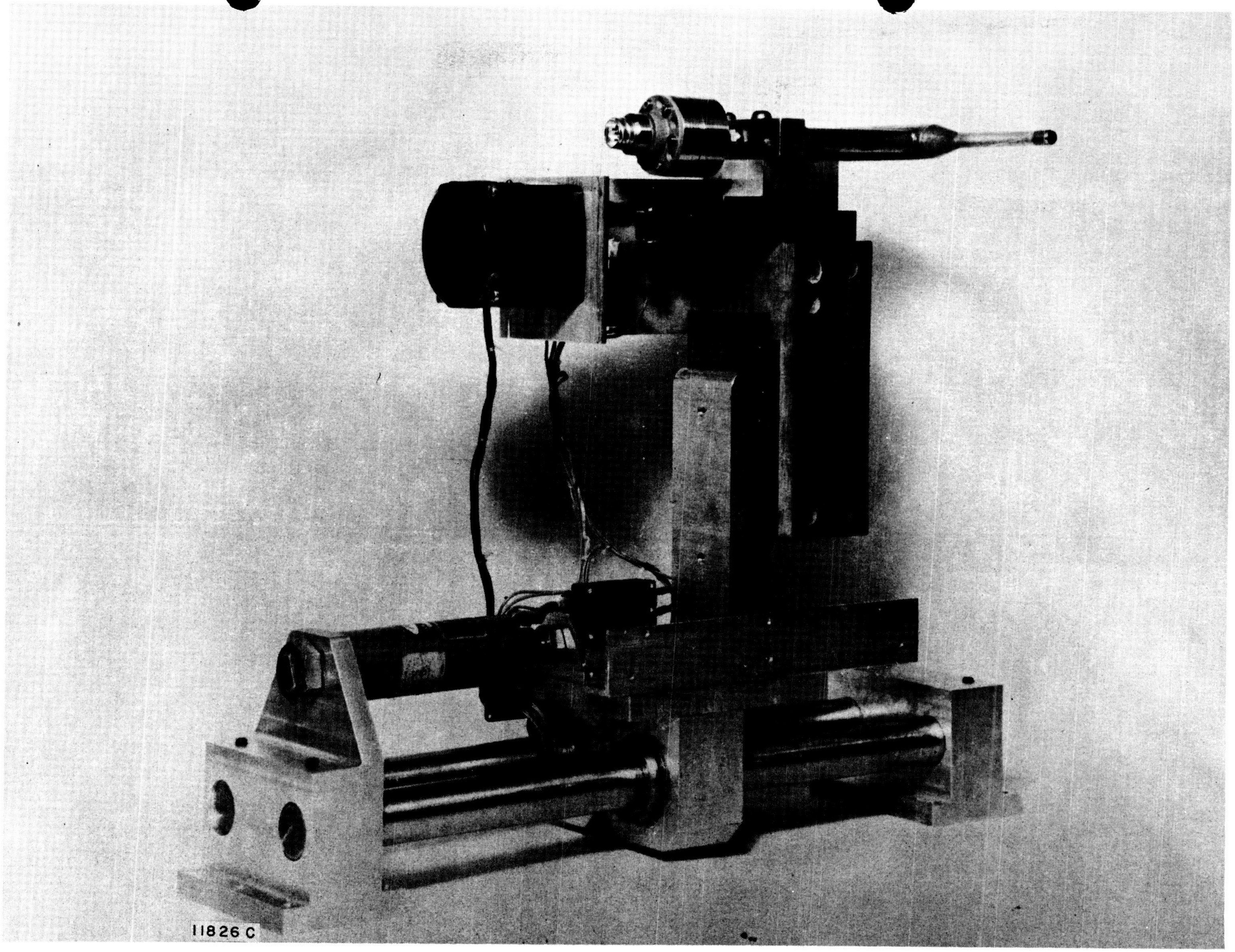

Figure 57 FRONT VIEW OF PROBE INSERTION UNIT

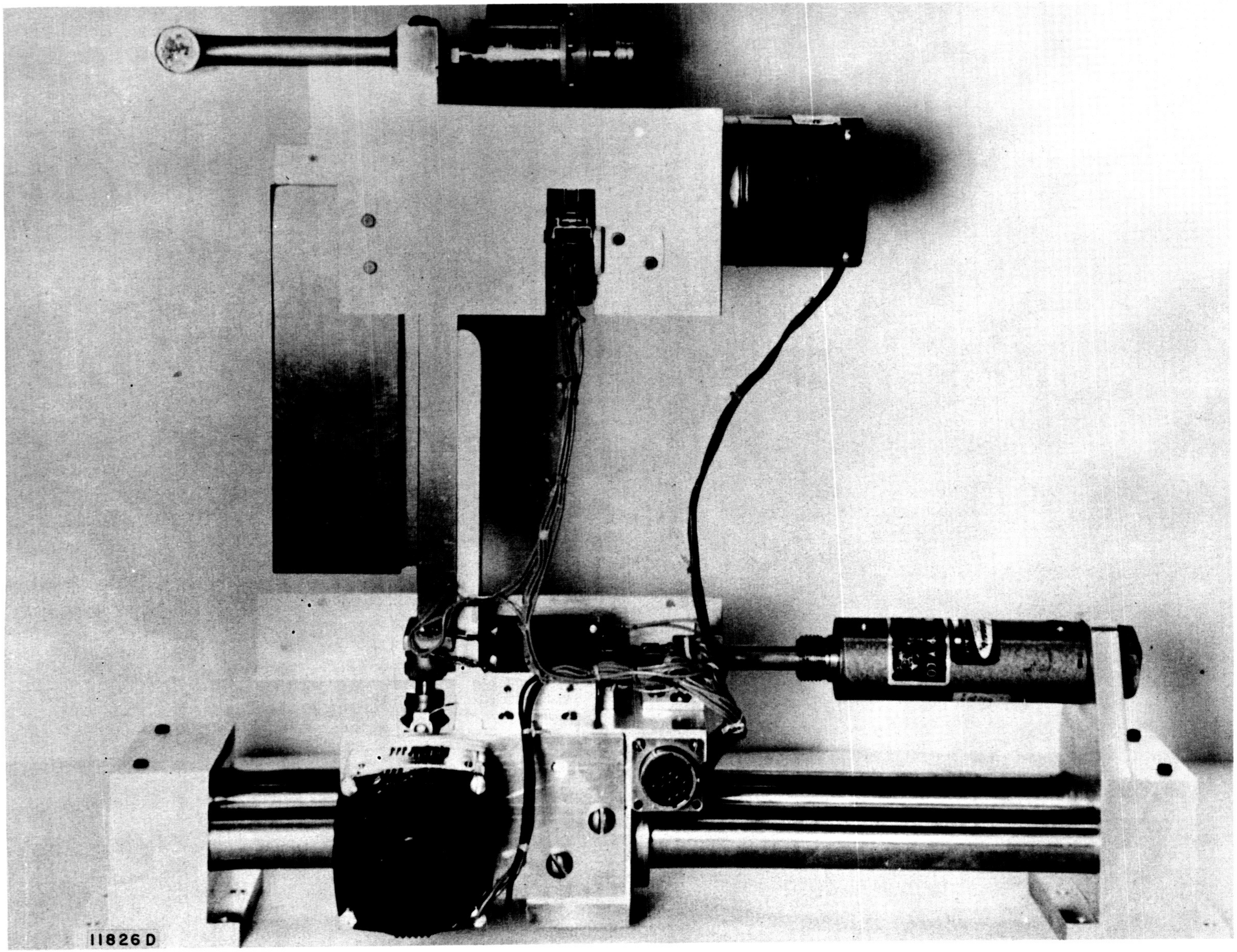

Figure 58 REAR VIEW OF PROBE INSERTION UNIT

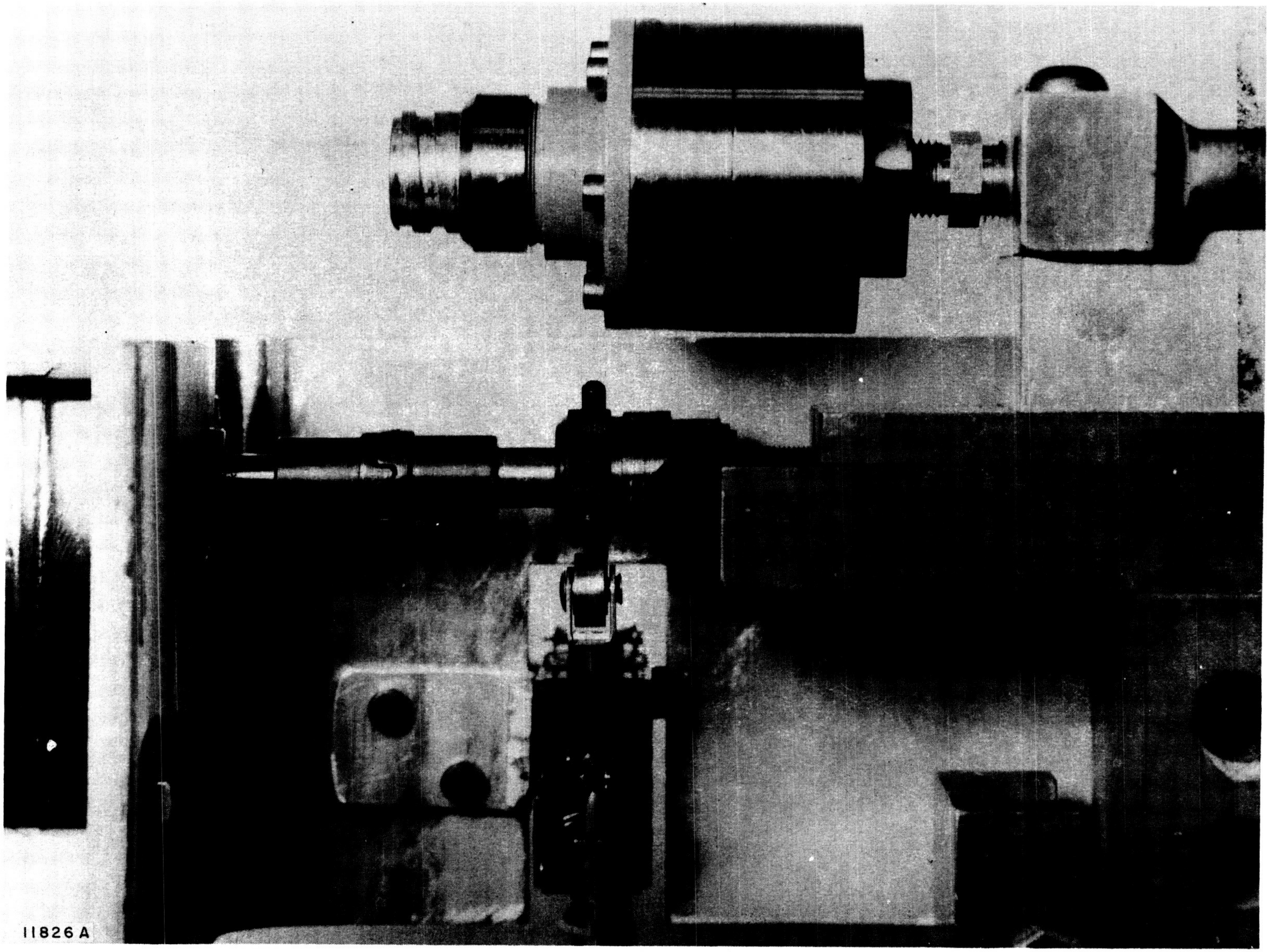

Figure 59 CLOSEUP OF MICROSWITCH FOR GILMAN SLIDE DRIVE ASSEMBLY

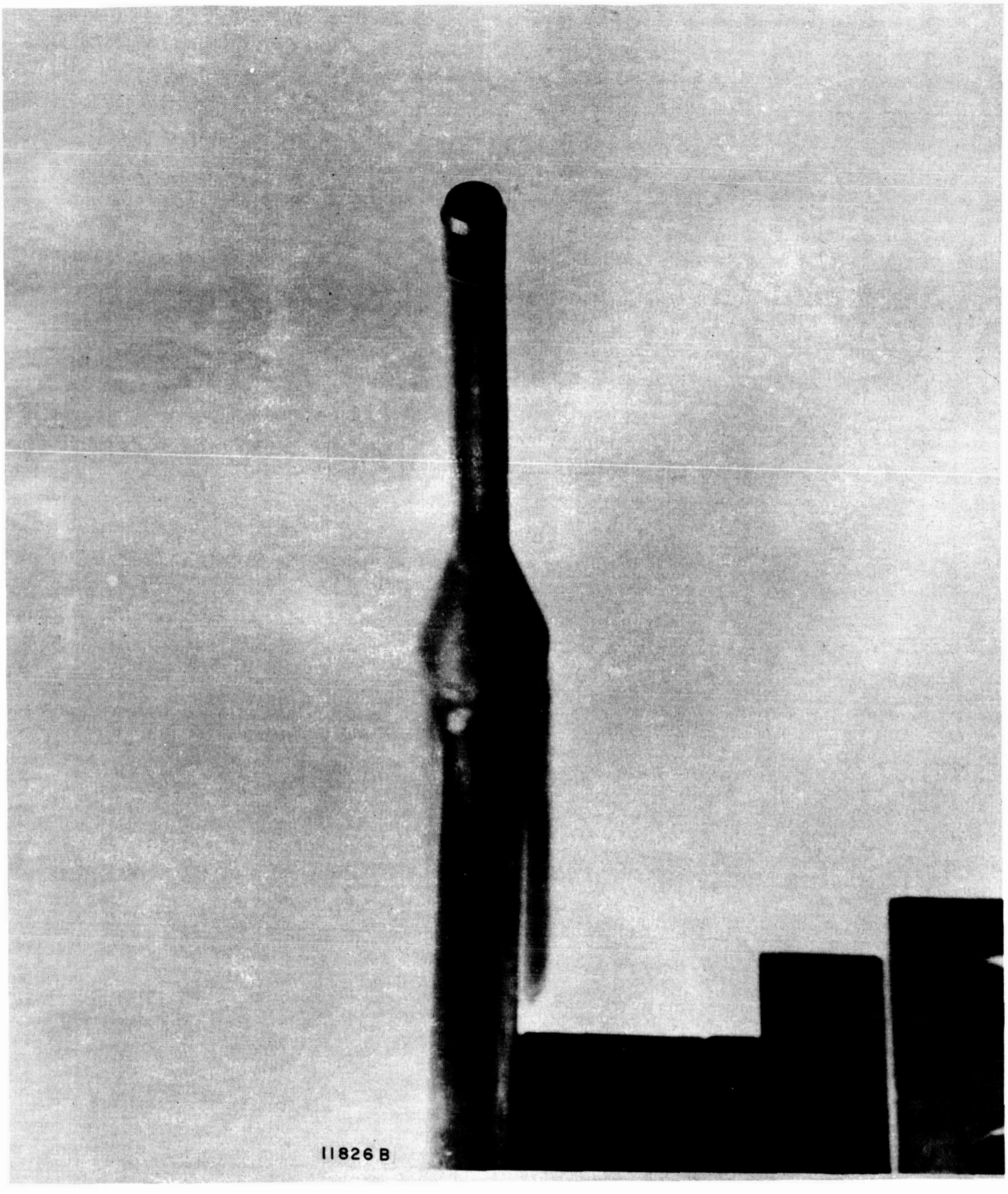

Figure 60 IMPACT PRESSURE PROBE WITH SUPPORTING STRUCTURE

The measured profiles are shown in figure 61. Of the three profiles one pair is at a constant mass flow rate but different power levels and one pair is at constant power level but two different mass flow rates.

The most striking characteristic exhibited by the profiles is that the central portion is approximately uniform although there is a slight dip. It is in this relatively flat central portion that the three profiles are substantially different. Further, the extent of the approximately uniform central portion is about the same for all three profiles and has a diameter of about 0.275 inch. It is of interest to note that measurements were made of the diameter of the very luminous portion of exhaust jet yielding a value of approximately 0.29 inch, for all three operating conditions. Such a measurement is subjective in character but it does indicate that the approximately uniform central portion of the impact pressure profiles corresponds roughly to the diameter of the visually bright region of the exhaust jet.

For the case of constant power but varying mass flow rate, the central portion of the profiles are similar in terms of impact pressure, while for the case of constant mass flow rate and varying power, the central portion of the profiles are different (higher power, higher impact pressure) in terms of impact pressure. If the diameter of the central region of the profile is taken to be the distance between peaks of the profiles, then the diameter of the central region is nearly the same for all three running conditions.

Some of these trends can be predicted by the Heller-Elenbaas model of the arc column. [1] This simplified model states that if, for example, the voltage gradient and arc current are the same for two arc columns then the temperature profile and column radius are the same. The Heller-Elenbaas model can be used to interpret the impact pressure profiles by identifying the central region of the profiles as encompassing that portion of the flow which passes through the arc column and by assuming that the voltage gradient in the constructor is the same for all three operating conditions because the total arc voltages are nearly the same (see table 20).

Returning to the case of constant power but different mass flow rate, since the arc current is practically the same, the Heller-Elenbaas model would predict the arc column would be the same, i. e., have the same radius and temperature profile. Although the Heller-Elenbaas model does not predict other features of the flow, it does say that within the framework of the model, the two arc columns are identical.

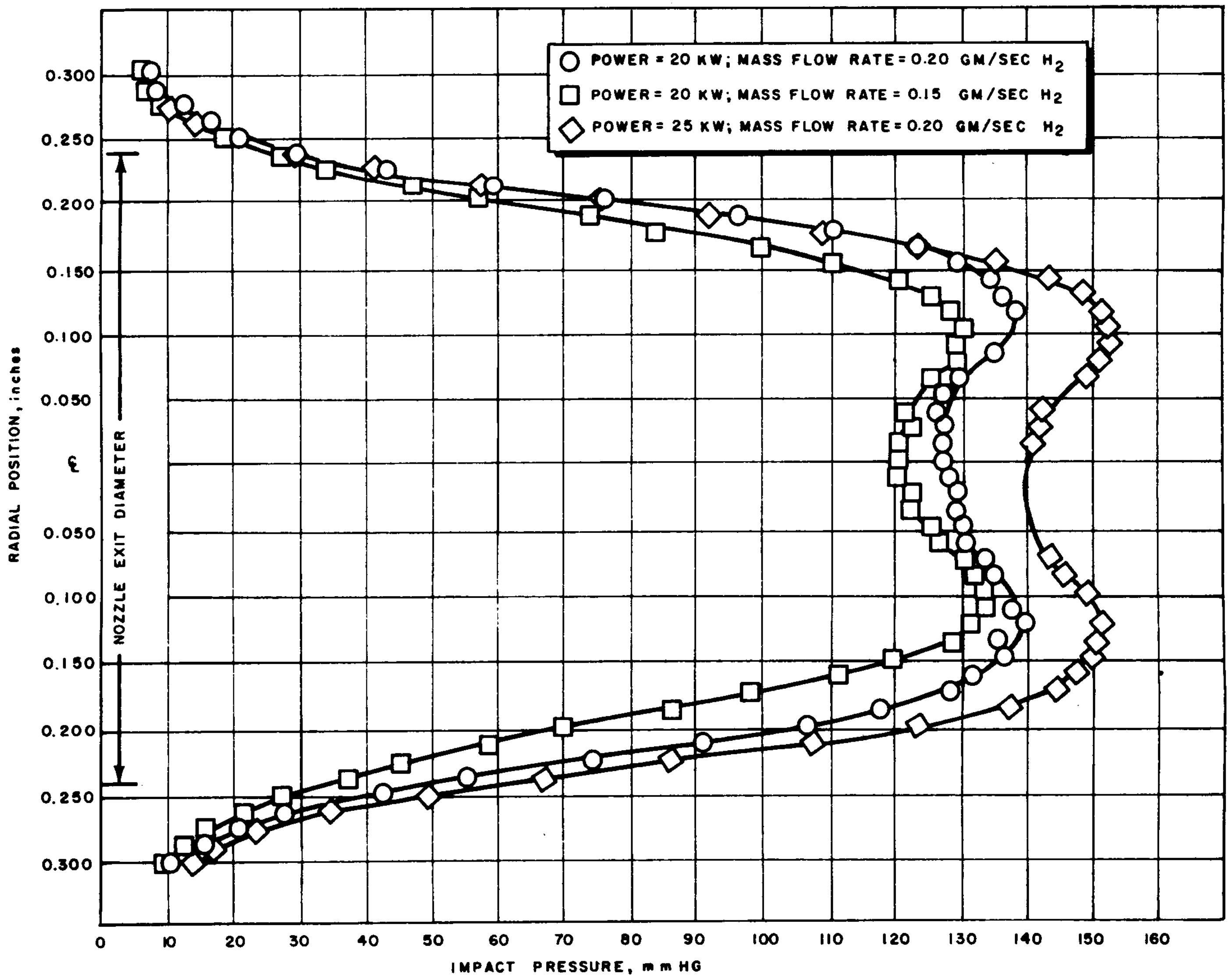

64-14241

Figure 61 IMPACT PRESSURE PROFILES AT 20 AND 25 KILOWATTS

For the case of constant mass flow rate but different power levels, the Heller-Elenbaas model predicts that for a voltage gradient of 70 volts/cm (see section III-C-2) and arc currents of 131 and 160 amperes (see table 20) the radii of the arc column are nearly the same though the central core temperature is higher for the higher power level.

Since the Heller-Elenbaas model doesn't take into account flow in the arc column it is not able to predict the magnitude of the impact pressure.

3. Mass Flux Profiles

A description of the mass flux probe and the associated apparatus is found in appendix G. The measured mass flux profiles at a distance of 0.050 inch (downstream) from the nozzle exit plane are presented in figure 62. The filled in points in figure 62 represent data taken with a removeable carbon probe tip while the open data points represent data taken with a copper tip probe. The carbon probe tips were employed in the central portion of the exhaust jet where the extreme environment was too severe for the copper probe tip to endure. These profiles are "averaged" in the same sense as the impact pressure profiles shown in figure 61.

Table 21 gives a comparison between the input mass flow rate as measured by the flow meter and the mass flow rate determined by integrating the measured mass flux profiles.

TABLE 21

COMPARISON OF MEASURED MASS FLOW RATE AND INTEGRATION OF MASS FLUX PROFILE

Power (kw)	Mass Flow Rate (gm/sec)	Result of Integration of Mass Flux Profile (gm/sec)	Difference (percent)
20	0.20	0.179	-11
20	0.15	0.122	-19
25	0.20	0.184	-8

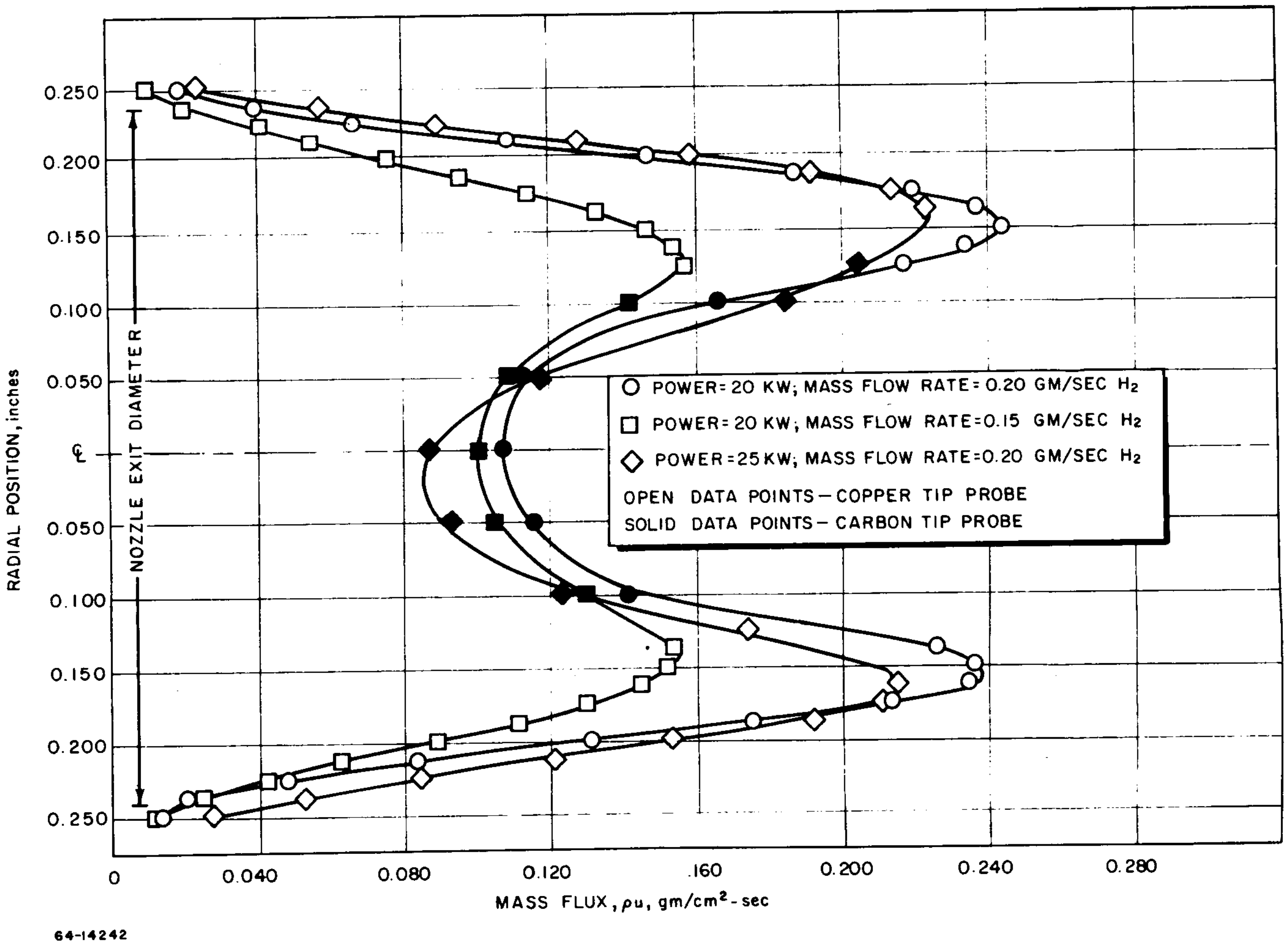

Figure 62 MASS FLUX PROFILES AT 20 AND 25 KILOWATTS

It can be seen that integrating the mass flux profiles gives a result which ranges from 8 to 19 percent too low. That the measured profiles tend to underestimate the mass flow rate is expected since if the shock is not completely swallowed then part of the incoming flow is deflected away from the probe. Further, near the outer edges of the profile, where it is thought that the relatively thick boundary layers may cause the flow to be subsonic, the probe would probably produce a low measurement because the incoming flow is deflected away from the entrance of the probe.

The profiles in figure 62 are characterized by a substantial dip in the center with peaks at the outer edges. The dip in the center represents evidence to support the statement that the core flow in the constrictor contains only a small portion of the total mass flow. The dip is probably more pronounced than that indicated in figure 62 due to the "graininess" of the measurements; the probe entrance tube has a diameter of 0.089 inch while the nozzle exit diameter is 0.475 inch.

The radial distance between the peaks is about the same for the two profiles corresponding to a mass flow rate of 0.20 gm/sec (about 0.30 inch) and is slightly smaller for the profile corresponding to a mass flow rate of 0.15 gm/sec (about 0.26 inch). Since the distance between the peaks corresponds approximately to the visual diameter of the luminous portion of the exhaust jet, then the region between the peaks can be tentatively identified with the inner flow of the core flow model.

Within 0.050 inch of the centerline the profiles corresponding to constant power are more similar than the profiles corresponding to constant mass flow rate. If the argument employing the Heller-Elenbaas model of the constricted arc introduced in discussing the impact pressure profiles is to hold, then this smaller central portion of the exhaust must correspond to the arc column in the constrictor. This is not unreasonable for it is to be expected that there would be an annular region surrounding the very hot core which is heated by, for example, mixing of the hot core and the surrounding cooler gas flow. Since the momentum flux (ρu^2) is much less temperature sensitive than the mass flux (ρu) it is expected that the mass flux profile would be much more sensitive to a temperature decay at the outer edges of the arc column than would the impact pressure profile, with the result that the mass flux profile should show a stronger radial variation near the center of the profile.

4. Velocity and Density Profiles

The corresponding mass flux and impact pressure profiles for each of the three operating conditions (see table 20) can be combined to give velocity and density profiles. In the discussion in appendix F it is shown that if the Mach number of the exhaust stream is sufficiently large, then the ratio of the impact pressure P_{o2}, as measured by the probe to the momentum flux in the exhaust stream, ρu^2 (where ρ is the gas density and u is the flow velocity) is independent of Mach number and the ratio is less than unity by between 5-8 percent depending on the value of the ratio specific heats, γ. As the Mach number of the exhaust stream decreases, the ratio $\rho_{o2/\rho u^2}$ increases. For example, for $\gamma = 1.3$, if the Mach number of the exhaust jet is greater than 1.5, then $P_{o2/\rho u^2}$ differs from unity by only 10 percent. Thus for the purpose of calculating the velocity and density profiles, it will be assumed that $P_{o2}/\rho u^2 = 1$.

The velocity and density profiles resulting from combining the impact pressure profile (now considered to be numerically equal to the momentum flux, ρu^2, and the mass flux (ρu) profile are shown in figures 63 and 64. In these figures, the profiles have been averaged about the center line.

Looking first at the velocity profiles it is seen that they are characteristically peaked at the center-line and decrease rapidly away from the center line. Further, it is seen that within the radial position 0.050 inch, for the case of constant power (20 kw) and different mass flow rates (0.15 and 0.20 gm/sec H_2) the profiles are substantially the same while for the case of constant mass flow rate (0.20 gm/sec) but different power levels (20 and 25 kw) the velocity profiles are quite different. Returning to the interpretation of the Heller-Elenbaas model of the arc column used in discussing the impact pressure and mass flux profiles, it is seen that the above result is to be expected. The Heller-Elenbaas model would predict a higher core temperature for the 25 kw operating condition than for the 20 kw condition. Since the flow velocity is roughly proportional to the square root of the temperature, the Heller-Elenbaas model would thus predict that the center line velocity in the suersonic flow would be greater for the power level of 25 kw than for the power level of 20 kw.

The density profiles show dips near the center-line. Again the profiles for constant power are substantially the same inside the radial position 0.050 inch while profiles for different power levels are different. Noting that the density would be expected to be roughly inverse temperature dependent, the Heller-Elenbaas model would predict a lower density for the 25 kw power level. Thus it appears that the major features of the inner regions of the various profiles can be understood in terms of the Heller-Elenbaas model of the arc column.

It is expected that the arc column flow would be modified in the supersonic expansion, the modification occurring initially at the outer edges of the core due to mixing with the surrounding cooler gas flow. It appears that the radial position of the arc column flow which remains relatively intact during the expansion process is of the order of 0.050 inch.

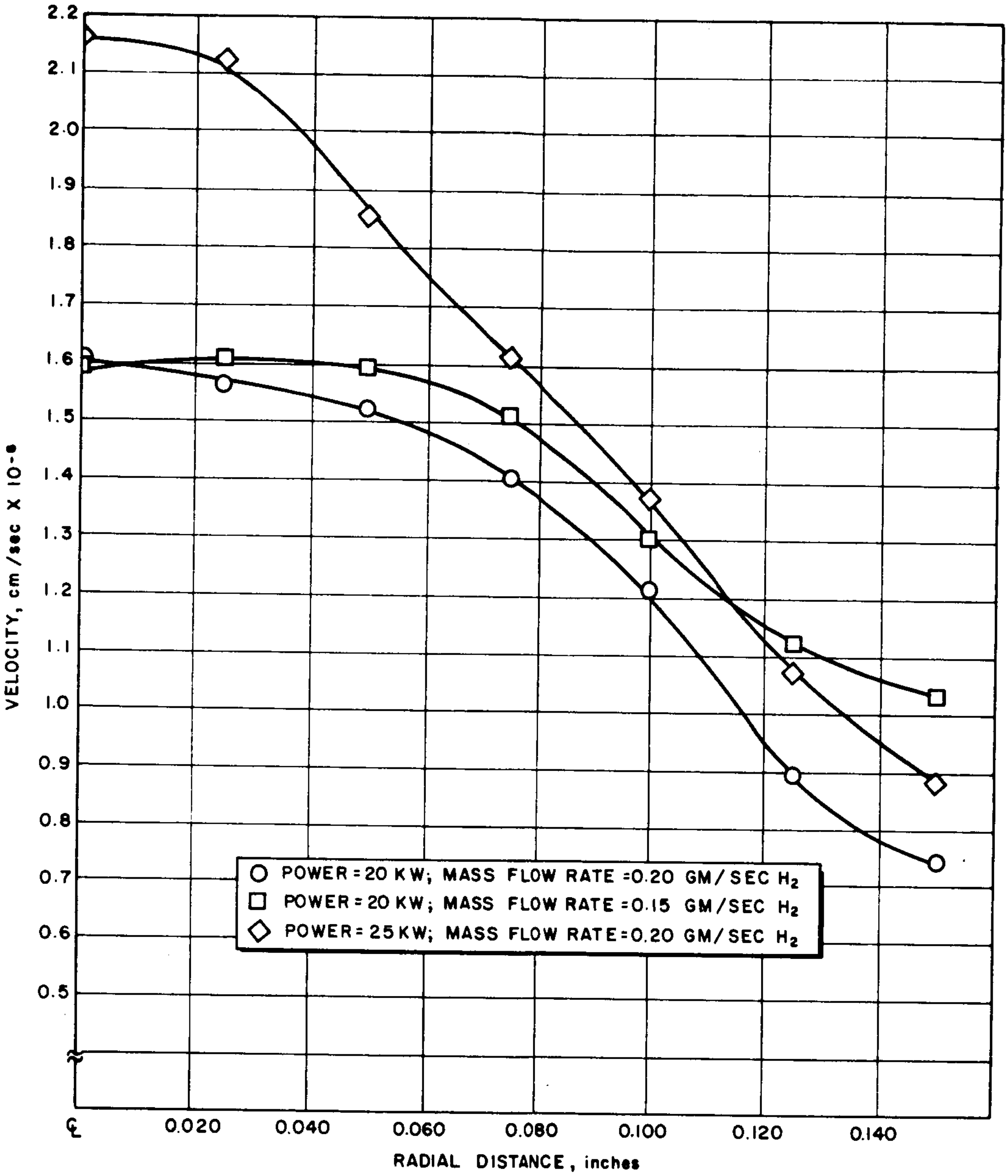

64-14243

Figure 63 DERIVED VELOCITY PROFILES AT 20 AND 25 KILOWATTS

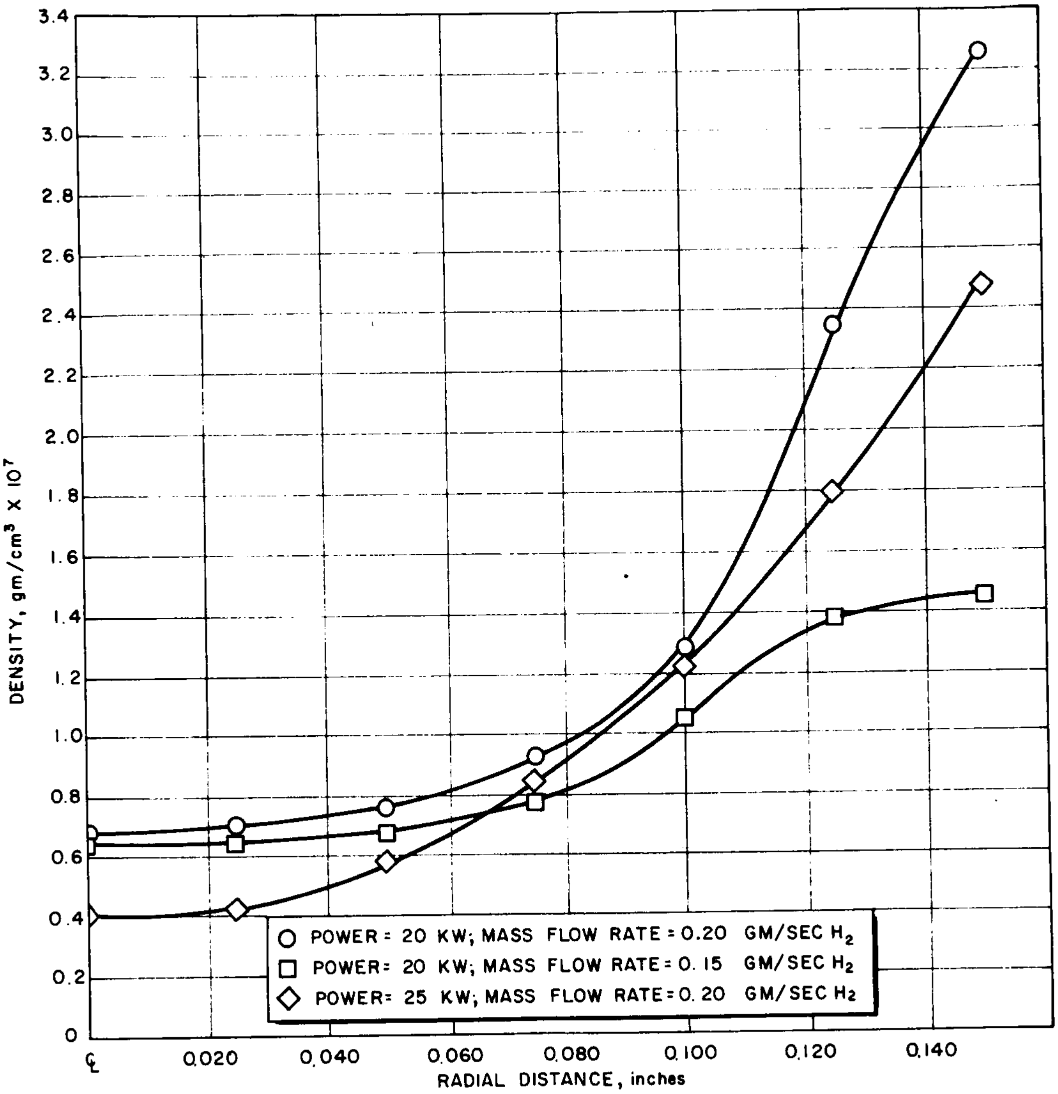

64-14244

Figure 64 DERIVED DENSITY PROFILES AT 20 AND 25 KILOWATTS

The velocity and density profiles are calculated out to a radial position of 0.150 inch while the nozzle exit radius is 0.28 inch. It is found that substantially beyond 0.150 inch the velocity appears to increase and correspondingly the density appears to decrease. These trends become extreme near the wall of the nozzle since near the wall of the nozzle the flow velocity should decrease to zero due to viscous effects. It is thought that the outer portions of the velocity and density profiles are unreliable.

There are several reasons why the probe data might be unreliable in the vicinity of the nozzle wall. Both the impact pressure and mass flux are small near the nozzle wall (due to the boundary layer) and a small absolute error in measurement of either could cause a large percentage error in the computed velocity and density. Another important consideration follows from the boundary layer itself. Various estimates[24] of the boundary layer thickness at the end of the supersonic nozzle have yielded results ranging from 10-25 percent of the nozzle exit radius. Choosing arbitrarily a value of 15 percent, the boundary layer thickness for the engine used during the diagnostic work is about 0.035 inch. The probe does not give a point-wise measurement but rather an average over the probe opening (0.060 inch for the impact pressure probe and 0.090 inch for the mass flux probe). This means that when the center-line of the probe is beyond a radial point of 0.150 inches, part of the probe opening is within the boundary layer. Within the boundary layer is a region where the flow is subsonic. In this subsonic region neither the impact pressure probe or the mass flux probe are reliable. (See appendixes F and G). The mass flux probe is most likely to read consistently low in a subsonic flow. With regard to the impact pressure probe, referring to figure F-2, appendix F, it is seen that for subsonic flow, the relation between momentum flux and impact pressure is very sensitive to Mach number and, in general, the ratio $P_{o_2}/\rho u^2 > 1$. Hence, in the vicinity of the nozzle exit radius, the momentum flux obtained by using $P_o 2/\rho u^2 = 1$ is too high. If in addition the mass flux probe reads too low, then it would be expected that the velocity as determined by the two probe readings would be much too high. This appears to be the case.

5. Arc Engine Power Balance

a. Introduction

The limitations and ultimate performance of the R Series 30-kw arcjet engines depends upon the various forms in which the input electrical power is distributed. The output power is either in the form of radiated power from hot engine surfaces or is contained in the propellant as it exhausts from the supersonic nozzle. Many phenomena are occurring while the propellant passes through the supersonic nozzle: the propellant continues to be heated by the arc until the arc terminates at some point on the nozzle surface; the density of the flow is decreasing rapidly so that recombination rates are inadequate to maintain thermodynamic equilibrium; thermal energy is converted to directed kinetic energy; propellant-nozzle wall interaction results in the formation of a region next to the wall where viscous effects are important producing surface drag and surface heating; radiation and recombination of atoms and ions that diffuse to the wall create additional heating; which is either partially recovered by regenerative cooling or conducted to and radiated from the nozzle outer surface. The remaining energy in the propellant as it exhausts from the engine consists of kinetic energy (essentially thrust), thermal energy (heat) and the energy implied by the presence of atoms and ions in the exhaust flow.

In the discussion to follow, the latter power form will be referred to as the frozen flow loss. A block diagram representation of the power balance is given in figure 65.

b. Kinetic power:

Evaluation of the portion of the power in the form of directed motion requires a knowledge of the velocity and density profiles at the nozzle exit plane. Let $\rho(r)$ and $u(r)$ be the density and velocity of the flow at the radial position r at the nozzle exit plane. Then the kinetic power of the exhausting propellant is given by

$$\text{Kinetic Power} = \frac{1}{2} \int_{o}^{R} \rho u^3 \, 2\pi r dr$$

where R is the nozzle exit radius.

From the experimental velocity and density profiles shown in figures 63 and 64, the kinetic power can be evaluated. The results are shown in table 22.

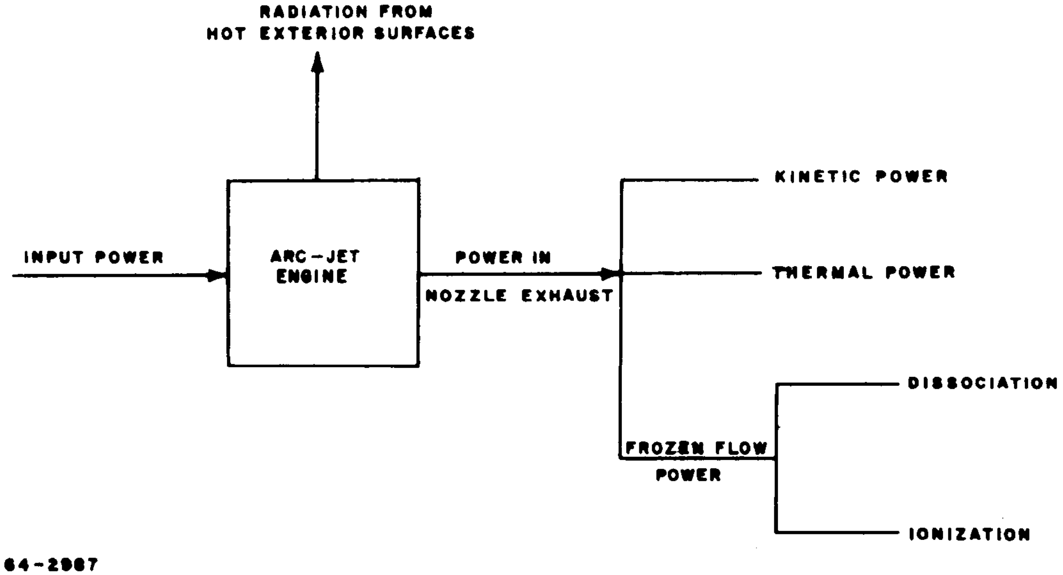
RADIATION FROM
HOT EXTERIOR SURFACES
INPUT POWER
ARC-JET
ENGINE
POWER IN
NOZZLE EXHAUST
KINETIC POWER
THERMAL POWER
FROZEN FLOW
POWER
DISSOCIATION
IONIZATION
64-2987

Figure 65 BLOCK REPRESENTATION OF POWER DISTRIBUTION IN ARCJET ENGINE

TABLE 22

EXPERIMENTALLY MEASURED KINETIC POWER

Power (kw)	Mass Flow Rate (gm/sec H_2)	Kinetic Power (kw)	Thrust Power (kw)
20	0.15	7.7	6.5
20	0.20	7.2	6.5
25	0.20	9.1	7.9

As pointed out in the previous section there is good reason to believe that the probe data at the outer edges of the profiles is unreliable. The following procedure was adopted to evaluate the integral. At the larger radial positions ($r > 0.175$ inch) where the velocity appeared to increase, the value at $r = 0.150$ inch was used out to the radial position $r = 0.225$ inch, and for the remaining 0.013 inch the velocity was assumed to be zero. The kinetic power flux, $\frac{1}{2} \rho u^3$, was calculated by using the momentum flux, ρu^2, as indicated by the impact pressure profile and the velocity adjusted in the manner described. Although this procedure is somewhat arbitrary, the kinetic power flux associated with the outermost radial positions is sufficiently small that the contribution to the total kinetic power is not large.

Also included in table 22 is the thrust power which is defined as $T^2/2\dot{m}$ where T is the measured thrust and $\dot{m}$ is the mass flow rate. For all three operating conditions, the thrust power is smaller than the kinetic power. The significance of this is seen by noticing that if the momentum flux, ρu^2, and the mass flux, ρu, were constant across the cross-section, then the definition of the thrust power is equivalent to the definition of the kinetic power. (This is not strictly true because the thrust contains, besides the momentum flux term, a term which depends on the pressure at the nozzle exit plane; however, for operating conditions of the Avco arcjet engine this additional term contributes only about 5 percent of the total thrust.) However, if the velocity distribution is not uniform, then the kinetic power is always greater than the thrust power. The difference between the two is called the non-uniform loss. Referring to table 22, the non-uniform or velocity profile loss increases both as the mass flow rate decreases at a given power and as the power increases for a given mass flow rate. Also, the non-uniform loss is quite small being on the order of 5 percent of the input power.

Of course it should be remembered that the non-uniform distribution of velocity with the accompanying non-uniform distribution of temperature is responsible for a much lower frozen flow loss than would be otherwise the case.

c. Thermal Power

The thermal power in the exhausting propellant is that power associated with the random thermal motion of the propellant gas. The calculation of the thermal power is difficult because the composition of the propellant at the nozzle exit plane is required; it is not enough to know the radial temperature and pressure profiles at the nozzle exit plane for the gas is not in equilibrium due to the rapid expansion in the supersonic nozzle. In appendix H a treatment of what measurements are necessary, in principle, to determine the non-equilibrium composition for the case of a hydrogen propellant is given.

d. Frozen Flow Power

The frozen flow power is that portion of the total exhaust power due to the presence of atoms, ions, and electrons. Like the thermal power the frozen flow power also requires a knowledge of the non-equilibrium composition of the exhaust propellant.

Appendix H gives a discussion of the frozen flow power, including methods to determine which portion is due to dissociation and which is due to ionization.

e. Radiated Power

The radiated power can be determined in at least two ways. One way is to calculate the power radiated from the hot exterior surfaces from measurements of the surface temperature, and a knowledge of the emissivity of the material involved. A set of measurements conducted at this laboratory using an optical pyrometer for the measurement of surface temperature (see appendix B) gave the result that the R series arcjet engines radiate less than 10 percent of the input power.

The radiated power can be indirectly measured by swallowing the exhaust stream with a calorimeter. The radiated power is then the difference between the input power and the power in the exhaust as measured by the calorimeter. These measurements[1] also indicate that the radiated power is about 10 percent the input power.

f. Incomplete Expansion Loss

From the previous discussion it is clear that from just the measured profile data, it is not possible to calculate the thermal power or the frozen power. However, it is possible to determine the sum of the thermal power and frozen power; this sum is the power in the exhaust due to incomplete expansion for if the expansion were perfect then in principle there would be no thermal energy left and equilibrium would exist because of complete recombination. The incomplete expansion power is the difference between the input power and the sum of the radiated power and the kinetic power. Table 23 shows the incomplete power loss for the three operating conditions considered; the radiated power was taken as 10 percent of the input power.

TABLE 23

INCOMPLETE EXPANSION POWER LOSS

Input Power (kw)	Mass Flow Rate (gm/sec H_2)	Kinetic Power (kw)	Radiated Power (kw)	Incomplete Power (kw)	Expansion (percent)
20	0.15	7.7	2.0	10.3	51.5
20	0.20	7.2	2.0	9.2	46.0
25	0.20	9.1	2.5	13.4	53.6

Table 23 indicates the trend that the fraction of the input power that goes into incomplete expansion power increases slightly both for decreasing mass flow rate at constant power and for increasing power at a constant mass flow rate. Also, it is seen that approximately one half of the input power goes into this form of incomplete expansion.

A very crude estimation of the thermal power can be made by using the average density (from the density profile) and assuming a constant pressure of about 10 mm Hg at the nozzle exit plane (at this ambient pressure the exhaust jet appears to be properly expanded.) Using the pressure and density and assuming the average molecular weight of the flow, an average temperature is found. An estimate of the thermal power then follows by multiplying the average temperature, the mass flow rate and a frozen specific heat at constant pressure, chosen to be consistent with the assumed average molecular weight.

A knowledge of the total power in the exhaust (input power minus radiated power), the kinetic power and the thermal power permits the calculation of the frozen flow power (see figure 65). An iteration of the assumed average molecular weight is then performed by estimating the degree of dissociation implied by the resulting frozen flow power. This degree of dissociation implies a new average molecular weight and the process is repeated.

This calculation gives a thermal power for the three operating conditions of between 3.5 and 4.5 kw. Any trends with power and mass flow rate are not considered as valid, since the calculation is crude. Using this estimation of the thermal power, the frozen flow efficiency, defined as the ratio of the frozen flow power to the input power is found to be between 65-70 percent for the three operating conditions. This means that 30-35 percent of the input power exhausts from the arcjet engine in the form of dissociation and ionization energies, manifested by the presence of ions, electrons and atoms, due to the lack of thermodynamic equilibrium.

This result for the frozen flow efficiency is much lower than would be anticipated using a one dimensional model for the flow in the arcjet engine with the assumption that the composition is frozen at the throat. For example, for the case of a mass flow rate of 0.20 gm/sec H_2 and a power of 25 kw, the one dimensional model would predict a frozen flow efficiency of about 45 percent. Again it is necessary to take into account the non-uniform radial temperature and velocity profiles in order to understand the thrust and efficiency capability of the arcjet engine.

E. SUMMARY AND CONCLUSIONS OF APPLIED RESEARCH

The preceding portions of this section have summarized the experimental procedures and results for a number of investigations of different aspects of arc engine operation. Each of the investigations has been aimed at improving understanding of the operation of the 30-kw arcjet engine, so that its energy loss mechanisms and ultimate limitations can be indentified.

The central feature of engine operation is that the engine is a complex of aerodynamic and electrodynamic phenomena dominated by the electrical characteristics and spatial extent of the arc discharge. Two empirical investigations aimed at observing the influence on engine operation of variations of the flow geometry have produced essentially negative results; these are the variations in cathode shape and location, and in nozzle opening angle and area ratio. The first of these geometrical variations should markedly affect the inlet flow conditions; the second, the supersonic expansion. The effects of each on arc engine operation were small, and such optima as were located correspond fairly closely with the configuration of the R-series engines.

The remainder of the investigations have dealt with the arc discharge and its effects upon the propellant flow. Voltage gradient measurements, coupled with measurements of the arc column diameter made during the previous year's effort, indicate that the properties of the arc column are approximately given by a very simple model which leads to the Heller-Elenbaas equation. Behavior of the arc column in different gases tends to support the approximate validity of this model.

The implications of this model for arc engine performance are that frozen flow losses in the specific impulse range 1000 to 1500 seconds, and probably up to at least 2000 seconds, are much less severe than one dimensional calculations would indicate; this is particularly the case when the likelihood that dissociative equilibrium is never attained is also considered. The penalty which operation of an arc engine in this mode imposes is the radial velocity profile at the nozzle exit plane with its attendant non-uniform flow loss. However, probe measurements in the exhaust indicate that this loss mechanism is not of major importance, and some improvement should be achievable by making the flow even less uniform. Additional gains in frozen flow efficiency would then outweigh the additional velocity profile loss.

The endurance of the engine is also attributable in large measure to this mode of operation. Although the anode investigations were not conclusive, they give strong indication that the anode attachment is in the form of a moving spot, which is, in a time averaged sense, equivalent to diffuse attachment. With the cool outer flow protecting the constrictor wall, and with regenerative cooling near the braze locations, the engine is shielded from the most adverse thermal loads. Still, at the highest engine operating temperatures there has been a great deal of difficulty in demonstrating engine life. An advance in engine materials may be necessary to obtain the desired life at the 1500 second specific impulse level or higher. The specific impulse range up to 1300 seconds is within reach insofar as engine life is concerned.

IV. PROGRAM DIRECTION

During this Third Year Development Program substantial progress was made in understanding the behavior of the 30-kilowatt engine in continuous operation. The major difficulties now appear to lie in the area of engine materials in order to demonstrate extended life at the 1500 second specific impulse level. The high specific impulse arcjet engine developments are encouraging. Future efforts are recommended in the areas of:

1. Engine material developments at the 30-kilowatt level, with the objective of demonstrating extended life at the 1500 second specific impulse level.

2. Development of the X-2 high specific impulse arcjet engine, with the aims of elucidating the thrust mechanism, improving the efficiency, and eventually operating with a storable propellant. If it proves possible, a radiation cooled version of this engine should be developed.

3. Pulsed mode operation of the radiation cooled arcjet engine should be investigated, particularly at low power levels.

V. REFERENCES

1. Thirty Kilowatt Plasmajet Rocket Engine Development Program, Summary Report on the Second Year Development Program, NASA CR-54044, 9 June 1963. Avco RAD TR-64-6.

2. Handbook of Chemistry and Physics, Chemical Rubber Publishing Co., Cleveland, Ohio.

3. Finkelnburg, W., and H. Maecker, Handbuch der Physik, 22, 254, (1956).

4. Cann, G.L., R.A. Moore, R.D. Buhler, and G.L. Marlotte, Thermal Arcjet Research, ASD-TDR-63-632, August 1963. (Confidential)

5. Weare, N.E., and R.E. Munroe, Welding and Brazing of Molybdenum, IMIC Report 108, March, 1959.

6. Defense Metals Information Center Memo 37, Battelle Memorial Institute, Columbus, Ohio.

7. Loeb, L.B., Basic Processes of Gaseous Electronics, University of California Press, Los Angeles (1960).

8. Elenbaas, W., Physica, 2, 155 (1935).

9. Yos, J.M., Transport Properties of Nitrogen, Hydrogen, Oxygen, and Air to 30,000°K, Avco RAD TM-63-7, March, 1963.

10. Stine, H.A., and V.R. Watson, Theoretical Enthalpy Distribution of Air in Steady Flow Along the Axis of a Direct Current Electric Arc, NASA TN D-1331 (August 1962).

11. Theoretical and Experimental Investigation of Arcjet Engine Nozzle Flow, S. Bennett, Avco RAD, TR-63-50, submitted under NAS 3-2506, July 1963.

12. Rink, J.P., J. Chem. Phys., 36, 262 (1962).

13. Sutton, E.A., J. Chem. Phys., 36, 2923 (1962).

14. Patch, R.W., J. Chem. Phys., 36, 1919 (1962).

15. Gardiner, Jr., W.C. and G.B. Kistiakowski, J. Chem. Phys., 35, 1765 (1961).

16. Rice, O.K., J. Chem. Phys., 67, 6 (1963).

17. Pritchard, H.O., J. Chem. Phys., 65, 504 (1961).

18. Marrone, P.V., and C.E. Treanor, Phys. Fluids, 6, 1215 (1963).

19. Wray, K.Z., J. Chem. Phys., 37, 1254 (1962).

20. Thirty Kilowatt Plasmajet Rocket Engine Development Program, Summary Report on the First Year Development Program.

21. Wheaton, J.R., and R.C. Dean, Research Report on Anode Gas-Sheath Electrical Breakdown in a High Pressure Arc Plasma Generator, Dartmouth, November 1961.

22. Harvey, J.K., P.G. Simkins, and B.D. Adcock, AIAA Journal, 1, 714 (1963).

23. McKee, H.B., R.C. Dean, and A. Pytte, On Cooled Anodes in Contact with Laminar Arc Heated Flows, Dartmouth, October 1963.

24. Effect of Non-Equilibrium Flow in Thermal Arcjet Engines, M. Chen, Avco RAD TR-62-25, September 1962, submitted under NAS 8-1607.

APPENDIX A

TEST SYSTEM CONSIDERATIONS

1. VACUUM TANK

Arc jet engine performance parameters are measured in an environmental system which maintains low ambient pressures and which removes the heat present in the engine exhaust and the heat radiated from the exterior surfaces of the engine.

The engine test systems employed at Avco RAD for thermal arc jet work comprise three basic components: test tank, heat exchanger, and vacuum pump. The test tank (see figure A-1) is cylindrical in shape, with a length of six feet and a diameter of either two feet or four feet. One end of the cylinder is readily removed for access to the engine and thrust stand, and the tank is equipped in addition with several viewing ports. The tank is double-walled, and water is circulated between the walls during engine operation. The double-wall construction is extended to the viewing ports.

The test tank is exhausted by a pumping system with a total capacity of 6000 scfm, sufficient to maintain the ambient pressure at levels of the order of 1 mm Hg during operation.

The vacuum pumps would deteriorate rapidly if they were to work directly on the hot engine exhaust. The pumps are therefore protected by a heat exchanger, placed in the test tank downstream of the engine and colinear with it. The hot exhaust impinges on the heat exchanger and is cooled there before entering the vacuum line.

2. POWER SUPPLY

Power for the d-c tests up to 300 kw is supplied from a bank of Miller selenium rectifiers. Each rectifier has a nominal power rating of 40 kw and an open circuit voltage of 160 volts. A total of ten units are available, and the options of series and Parallel connection allow continuous operation in the range of 160 to 1000 volts (open circuit), and 0 to 2000 amp. In the power range to 500 kw, a power supply comprising a set of two Perkins 500-kw saturable core reactor power supplies is available.

3. PERFORMANCE MEASURING EQUIPMENT

Engine thrust is measured by a liquid-cooled suspension-type thrust stand, of the type illustrated in figures A-2 and A-3.

Briefly, the engine is attached to an oil container which is suspended below a flat plate by means of four Kovar or stainless steel strips. A thrust produced by the engine results in a displacement of the engine and oil container until the restoring force produced by the strips is equal to the applied thrust. The entire suspension is oil-filled and water-cooled to isolate the system from thermal loads. Calibration is performed with standard pulley and string techniques. The slope of the calibration curve can be checked during a run of the engine. All calibration checks indicate proper functioning of the thrust stand; that is, the calibration curve slope is independent of the state of the engine operation; return to thrust stand zero upon cessation of a run is rapid and complete; and recorded thrusts do not deviate over periods of many hours.

Arc engine mass flow is measured with a rotameter flow meter, calibrated by standard gas bottle techniques. The manufacturer's calibration is claimed accurate to ± 1 percent. Flowmeters are periodically rechecked at this laboratory in a system whose accuracy is ± 3 percent. This recheck is useful in identifying large anomalies which would be characteristic of serious flowmeter defects. Mass flow measurements are believed to be accurate to ± 3 percent.

Power input to the arc is measured with precision d-c voltmeters and ammeters. Power supply ripple is small ($\leq$ 2 percent of d-c power) so that it is believed that a measurement of input power is accurate to ± 3 percent.

4. TEST ACCURACY

Using standard formulas for combination of independent errors, it is possible to deduce error limits for the important engine quantities, as follows:

a) Thrust: This is a measured quantity, with accuracy ± 3 percent

b) Specific Impulse: This quantity is derived from the relation

$$I_{sp} = T/\dot{m} \tag{A-1}$$

where I_{sp} is the engine specific impulse in seconds, T the measured thrust in grams, and $\dot{m}$ the measured mass flow rate in grams/second. The uncertainty in specific impulse is then given by:

$$\frac{\Delta I_{sp}}{I_{sp}} = \sqrt{\left(\frac{\Delta T}{T}\right)^2 + \left(\frac{\Delta \dot{m}}{\dot{m}}\right)^2}$$

or,

$$\frac{\Delta I_{sp}}{I_{sp}} = \sqrt{18 \times 10^{-4}} = 4.25 \times 10^{-2}, \text{ or 5 percent}$$

c) Overall Efficiency: This quantity is derived from the relation

$$E_{overall} = \frac{4.8 \times 10^{-5} \ T^2}{\dot{m} \ P_{in}} \qquad \text{(A-2)}$$

where E is the overall efficiency expressed as a fraction, and P_{in} is the input power in kilowatts. Customarily P_{in} is taken as the product of arc current and voltage, although strictly it should contain also the power content of the incoming gas flow. If the incoming gas flow is at room temperature, the incoming power content is 0.435 kilowatts for a flow rate of 0.1 gram/sec. For 30-kilowatt electrical input power at flow rates up to 0.25 gram/sec the error in input power made by neglecting this thermal input power is of the order of 3 percent, and closer to 1 percent at a mass flow rate of 0.1 grams/sec. The uncertainty in efficiency owing to the uncertainties in the measured quantities is then:

$$\frac{\Delta E}{E} = \sqrt{2\left(\frac{\Delta T}{T}\right)^2 + \left(\frac{\Delta \dot{m}}{\dot{m}}\right)^2 + \left(\frac{\Delta P_{in}}{P_{in}}\right)^2}$$

or,

$$\frac{\Delta E}{E} = \sqrt{36 \times 10^{-4}} = 6 \times 10^{-2}, \text{ or 6 percent}$$

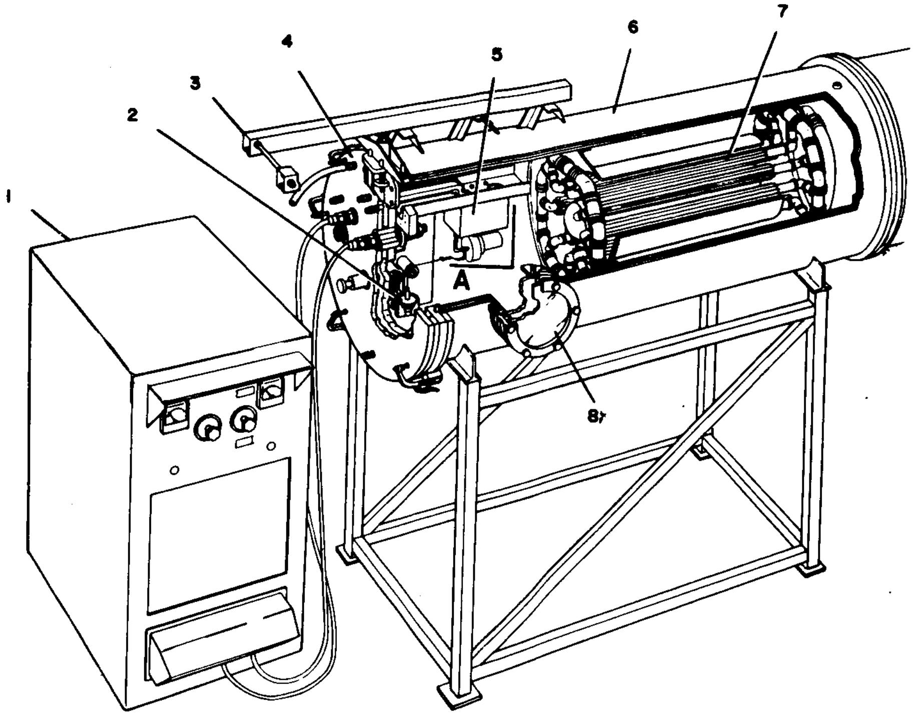

1. POWER SUPPLY
2. CALIBRATION WEIGHTS
3. TROLLEY SYSTEM (FOR COVER REMOVAL)
4. WATER – COOLED COVER ASSEMBLY
5. LIQUID COOLED THRUST STAND
6. WATER-COOLED DOUBLE WALL TANK
7. HEAT EXCHANGER
8. WATER-COOLED VIEWING PORT

Figure A-1 SCHEMATIC OF ENGINE TEST SYSTEM

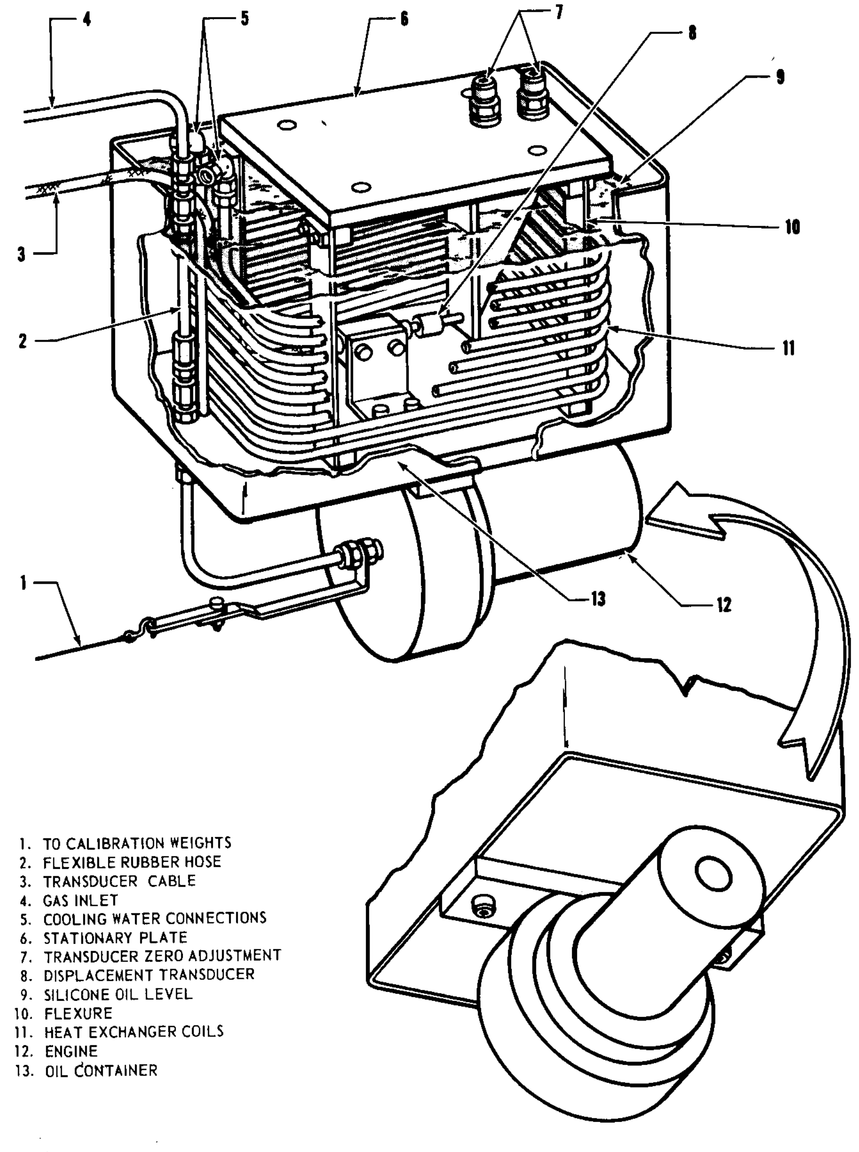

1. TO CALIBRATION WEIGHTS
2. FLEXIBLE RUBBER HOSE
3. TRANSDUCER CABLE
4. GAS INLET
5. COOLING WATER CONNECTIONS
6. STATIONARY PLATE
7. TRANSDUCER ZERO ADJUSTMENT
8. DISPLACEMENT TRANSDUCER
9. SILICONE OIL LEVEL
10. FLEXURE
11. HEAT EXCHANGER COILS
12. ENGINE
13. OIL CONTAINER

61-7000 A

Figure A-2 CUTAWAY DRAWING OF LIQUID COOLED THRUST STAND

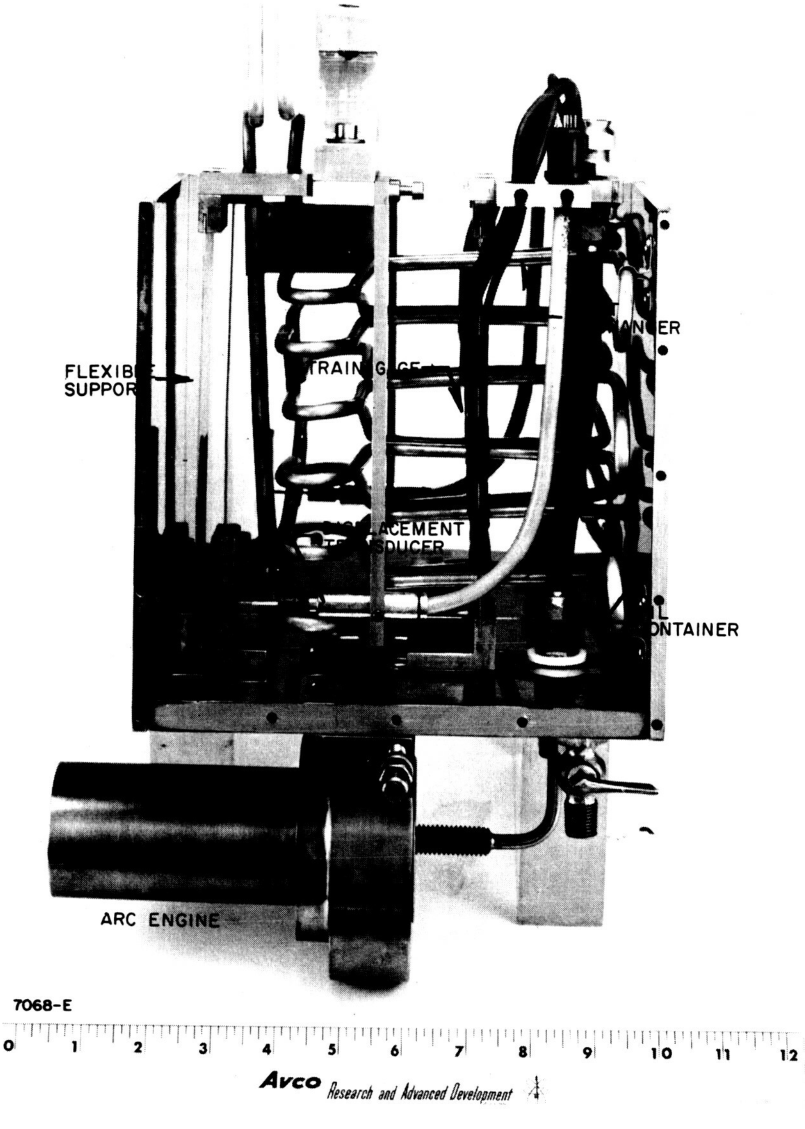
FLEXIB
SUPPOR
TRAIN G GE
ACEMENT
SDUCER
AN ER
NTAINER
ARC ENGINE
7068-E
0 1 2 3 4 5 6 7 8 9 10 11 12
Avco Research and Advanced Development

Figure A-3 PHOTOGRAPH OF LIQUID COOLED THRUST STAND

APPENDIX B

ARCJET SURFACE TEMPERATURE MEASUREMENT USING AN OPTICAL PYROMETER

1. GENERAL THEORY OF MEASUREMENT

An optical pyrometer has been used to measure the surface temperature of an arcjet engine. These measurements consist, in general, of a comparison between the apparent brightness of the surface and the brightness of a filament at a given temperature. The filament brightness is calibrated in terms of its brightness temperature, T_b, and when its brightness is the same as that of the surface being measured, the brightness temperature of the surface may be read directly from a meter in degrees centigrade.

The relationship between an object's true temperature and its apparent, or brightness, temperature may be derived using Wien's law. The energy distribution of radiation from a black body is given by

$$\Phi_\lambda = A C_1 \lambda^{-5} e^{-C_2/\lambda T} \tag{B1}$$

where Φ_λ is the spectral radiant heat intensity; A is the source area; C_1 and C_2 are constants equal to 1.77×10^{-12} watt/cm^2 and 1.439 cm degrees respectively; λ is the wave length in cm; and T is the temperature in degrees Kelvin.

In engine applications, the body is not black, and the radiant energy distribution is given by

$$\Psi_\lambda = \epsilon_\lambda \Phi_\lambda = A \epsilon_\lambda C_1 \lambda^{-5} e^{-C_2/\lambda T} \tag{B2}$$

where Ψ_λ is the spectral radiant intensity for a non-black body with spectral emissivity ϵ_λ.

The pyrometer yields the brightness temperature of the surface being measured; this temperature, T_B, is given by (B2) as

$$\Psi_\lambda = A \epsilon_\lambda C_1 \lambda^{-5} e^{-C_2/\lambda T_B} \tag{B3}$$

The true temperature is then given by

$$\frac{\Psi_\lambda}{\Phi_\lambda} = \epsilon_\lambda = e^{-\frac{C_2}{\lambda}\left(\frac{1}{T_B} - \frac{1}{T}\right)} \tag{B4}$$

or

$$\frac{1}{T} = \frac{1}{T_B} + \frac{\lambda}{C_2} \ln \epsilon_\lambda \tag{B5}$$

This relationship has been quoted by numerous authors.[B1-B4] It is of special value to note that the relation (B5) above is equally valid for all measurements which measure a reduced intensity, with ϵ_λ then denoting the ratio of measured intensity to true intensity. Thus, if the intensity reaching the instrument is reduced by absorbers in the light path to a value t_λ times the original intensity, then

$$\frac{1}{T_B} = \frac{1}{T_m} + \frac{\lambda}{C_2} \ln t_\lambda \tag{B6}$$

where T_m is the temperature read off the meter scale, and T_B is the brightness temperature, i.e., that value which would be read if not absorber were present.

If absorbers are present, then the relationship between true temperature, T, and measured temperature, T_m, is obtained by adding equations (B5) and (B6), yielding

$$\frac{1}{T} = \frac{1}{T_m} + \frac{\lambda}{C_2} \ln (\epsilon_\lambda t_\lambda) \tag{B7}$$

In principle, one should use Planck's law, in place of Wien's law, to determine the relationship between T and T_m. However, for the optical range and for temperatures up to about 4000°K, the error introduced is small enough to be neglected. The error introduced at 4000°K is only 4°, or 1/10 of 1 percent.[B5]

2. APPLICATION TO ARCJET ENGINE

In the case of measurements of an arcjet engine surface temperature, the gradient light passes through at least a 1 inch thickness of pyrex glass before reaching the pyrometer. In a large number of measurement situations, it must also pass through a second such window, separated from the first by 7/8 inch of water (see figure B1). The absorption of light by these bodies will cause a lower temperature reading on the pyrometer scale.

The reduction in the intensity reaching the pyrometer is caused both by a loss due to reflection at the boundaries between media of different indices of refraction, and by scattering and absorption of light in each medium.

For normally incident light, the fraction reflected from a boundary is given by[B6]

$$R = \left(\frac{n - m}{n + m}\right)^2 \tag{B8}$$

where n and m are the indices of the 2 media. We assume m = 1 for air, and m = 1.33 for water.

For the particular glass used, a simple determination of the index was made by measuring the displacement, d, in figure B2. The index may be determined from B7

$$d = t \sin \phi \left(1 - \frac{\cos \phi}{\sqrt{n^2 - \sin^2 \phi}}\right) \tag{B9}$$

where we have modified the equation by replacing n cos′ by the radical-obtained by using Snell's low.

The measurement yielded d = 0.315 inch ± 0.005 inch, which gives ($\phi = 45°$)

$$n = 1.46 \pm 0.02$$

Thus the value of R_{gw}, the fraction of light reflected at the glass-water boundary is essentially zero, and the introduction of water plus a second window should reduce the transmission by less than the addition of the second window alone.

A rather simple measurement of the total transmission of the glass using a thermopile yielded a transmission of about 8/9, with an accuracy estimated to be about 5 percent.

3. CALIBRATION

A series of measurements was performed using a calibrated tungsten lamp. The apparent temperatures were measured for seven different currents through the lamp, and for four different physical situations. Table B-I lists the measured temperatures (°C) for each situation.

Table B-II lists the values found for the total transmission of each system, using equation (B7) above, with ϵ_λ set equal to unity since comparison is with the brightness temperature T_B.

Table B-III lists the (calculated) values of temperature which would be measured if the value of t for each geometry were the average of the values measured. This is compared in the table with the values found. The agreement is quite good. In no case do the temperatures differ by $\geq$ 1/2 percent.

Figure B3 shows plots of T_m versus T_B for the various geometries.

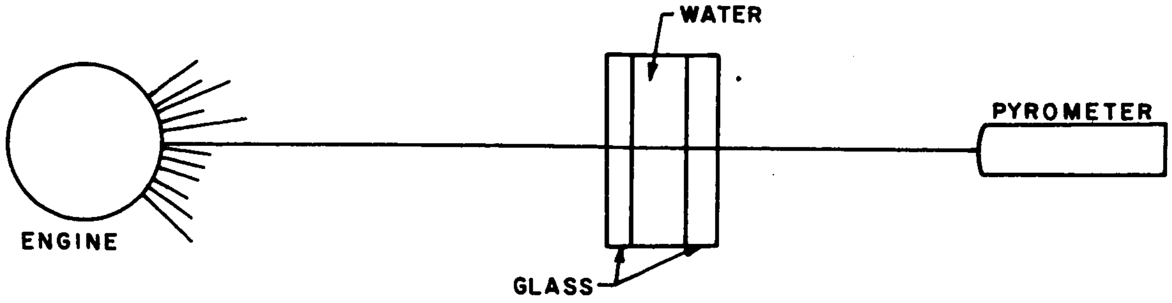
WATER
PYROMETER
ENGINE
GLASS

65-201

B-1

Figure B-1 SCHEMATIC DRAWING OF SYSTEM FOR ENGINE TEMPERATURE MEASUREMENT

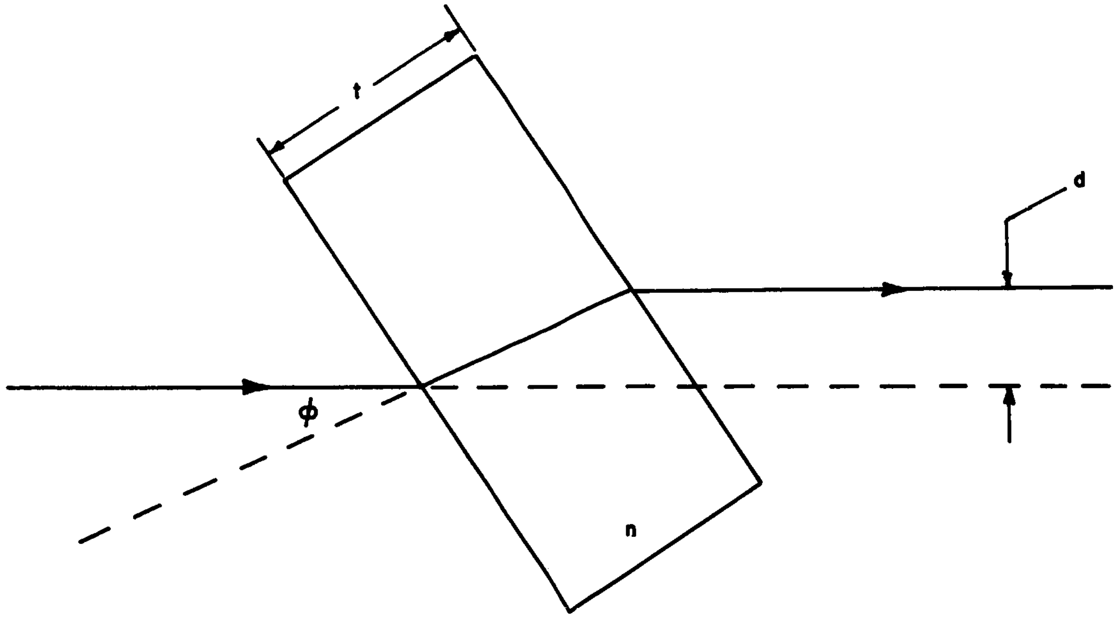

65-202

B-2

Figure B-2 IMAGE DISPLACEMENT BY GLASS PLATE

TABLE B-I

DEPENDENCE OF MEASURED BRIGHTNESS TEMPERATURE (°C) ON TYPE OF OPTICAL PATH

Lamp Current (Amperes)	Temperature (°C)				
	Type of Optical Path				
	Vacuum (From calibrated) Lamp	Air	One Window	Two Windows + Air	Two Windows + Water
32	1884	1886	1863	1833	1840
30	1804	1806	1786	1754	1761
28	1721	1724	1699	1670	1684
26	1633	1634	1610	1586	1596
24	1541	1540	1520	1499	1506
22	1444	1448	1426	1412	1417
20	1340	1341	1320	1311	1314

TABLE B-II

CALCULATION OF AVERAGE TRANSMISSION

T_{mc} (°C)	T_{mk} (°K)	$1/T_{mk}$ ($\times 10^8$)	(1/T) ($\times 10^8$)	$-\ln t$	T	$-\ln\bar{t}$	$\overline{(1/t)}$	Nature of Optical path
1884	2157	46360						Air
1804	2077	48146						
1721	1994	50150						
1633	1906	52465						
1541	1814	55125						
1444	1717	58241						
1340	1613	61996						
1863	2136	46816	456	0.0996	0.905			1 Glass
1786	2059	48567	421	0.0919	0.012			
1699	1972	50706	556	0.1214	0.886			
1610	1883	53106	641	0.1400	0.869			
1520	1793	55772	647	0.1413	0.868			
1426	1699	58857	616	0.1345	0.874			
1320	1593	62774	778	0.1699	0.844 0.880	0.1278	0.00585	

TABLE B-II (Concl'd)

T_{mc} (°C)	T_{mk} (°K)	$1/T_{mk}$ ($\times 10^8$)	$(1/T)$ ($\times 10^8$)	$-\ln t$	t	$-\ln \bar{t}$	$\overline{(1/t)}$	Nature of Optical Path
1833	2106	47483	1123	0.2453	0.782			2 Glass + Air
1754	2027	49333	1187	0.2592	0.772			
1670	1943	51466	1316	0.2874	0.750			
1586	1859	53792	1327	0.2898	0.748			
1499	1772	56433	1308	0.2857	0.751			
1311	1584	63131	1135	0.2479	0.780 0.767	0.2653	0.01215	
1840	2113	27326	966	0.2110	0.810			2 Glass + H_20
1761	2034	49164	1018	0.2223	0.801			
1683	1956	51124	974	0.2127	0.808			
1596	1869	53504	1039	0.2269	0.797			
1506	1779	56211	1806	0.2372	0.789			
1416	1689	59206	965	0.2108	0.810			
1314	1587	63011	1015	0.2217	0.801 0.802	0.2207	0.01011	

Note: For above calculations, $\lambda = 0.659$ microns.

TABLE B-III

COMPARISON OF CALCULATED AND MEASURED VALUES

$\overline{(1/t)}$	$\bar{t}$	T_{BK} (°K)	T_{MK} (^8K)	T_{BC} (°C)	T_{MC} (°C) Calculated	T_{MC} (°C) Measured	(°C)	Nature of Optical Path
0.00585	0.880	2157	2130	1884	1857	1863	+6	1 Glass
		2077	2052	1804	1779	1786	+7	
		1994	1971	1721	1698	1699	+1	
		1906	1885	1633	1612	1610	-2	
		1814	1795	1541	1522	1520	-2	
		1717	1700	1444	1427	1426	-1	
		1613	1596	1340	1323	1320	-3	
0.01215	0.767	2157	2101	1884	1828	1833	+5	2 Glass + Air
		2077	2026	1804	1753	1754	+1	
		1994	1947	1721	1674	1670	-4	
		1906	1863	1633	1590	1586	-4	
		1814	1774	1541	1501	1499	-2	
		1717	1681	1444	1408	1412	+4	
		1613	1582	1340	1309	1311	+2	

TABLE B-III (Concl'd)

$\overline{(1/t)}$	$\bar{t}$	T_{BK} (°K)	T_{MK} (^{8}K)	T_{BC} (°C)	T_{MC} Calculated (°C)	T_{MC} Measured (°C)	(°C)	Nature of Optical Path
0.01011	0.802	2157	2111	1884	1838	1840	+2	2 Glass + H_20
		2077	2034	1804	1761	1761	0	
		1994	1955	1721	1682	1683	+1	
		1906	1870	1633	1597	1596	-1	
		1814	1781	1541	1508	1507	-1	
		1717	1688	1444	1415	1416	+1	
		1613	1587	1340	1314	1314	0	

4. TRUE TEMPERATURE

The results of the temperature measurements indicate that the relationship between T_m and T_B is correctly given by

$$\frac{1}{T_B} = \frac{1}{T_m} - k \qquad \text{(B10)}$$

where k has the values

0.00585		1 window
0.01215	for	2 windows and air
0.01011		2 windows and water
0.		No absorber

The relationship between true temperature and brightness temperature depends upon the emissivity ϵ_λ. Using a value[B8] $\epsilon_\lambda = 0.438$ (corresponding to a temperature of 2000°K) for tungsten yields, finally

$$\frac{1}{T} = \frac{1}{T_m} - K \qquad \text{(B11)}$$

For the above situations K has the values

0.04367		1 window
0.04996		2 windows and air
0.04692	for	2 windows and water
0.03781		no absorber

5. ERRORS

Although the relationships derived from Wien's law are valid at each wavelength, the use of an optical pyrometer at just one wavelength - or very narrow band of wavelengths - is difficult because of the resulting lack of light intensity. One thus utilizes a wider band by using a red filter. This filter transmits a wider band of visible light and introduces the question of what the meanings of ϵ_λ, Φ_λ, Ψ_λ, t_λ, and λ itself are.

Since "brightness" depends upon the sensitivity of the eye to intensity, and since this sensitivity is a function of wavelength, an average human response to spectral intensity may be, and has been, plotted. By folding this response curve into the intensity distribution curve, for each temperature, we get an effective wavelength λ_e which depends both upon the temperature range, and the range of wavelengths used. For the red filter, for a temperature range $1500°K \leq T \leq 2500°K$, the variation in λ_e is only about 1.5mμ.[B9] The limiting value at $T = 2000°K$ is $\lambda_e = 0.659\mu$.

The choice of red for the filter is also due to the fact that over the range of wavelengths transmitted, the emissivity remains relatively constant. Over the range of temperatures above, the emissivity varies from 0.448 (at 1500°K) to 0.428 (at 2500°K), with a value of 0.438 at 2000°K.[B10]

The errors introduced may be estimated by (partial) differentiation of equation (B7).

$$\frac{dT}{T^2} = -\frac{\lambda}{C_2}\frac{d\epsilon}{\epsilon} \qquad \text{(B10a, b)}$$

or

$$\frac{dT}{T} = -\frac{\lambda T}{C_2}\frac{d\epsilon}{\epsilon}$$

For $T = 2000°$, $\lambda = 0.659$

$$\frac{dT}{T} \approx -0.1\frac{d\epsilon}{\epsilon}$$

Similarly,

$$\frac{dT}{T} \approx -0.1\frac{dt}{t}$$

The variation of emissivity of order 2.5 percent, and the uncertainty in transmission of order 5 percent, thus introduce uncertainties in the temperature measurement of about 1/4 percent and 1/2 percent, respectively.

The error introduced by the variation of λ_e with T is completely negligible. Again (partially) differentiating equation (B7)

$$\frac{dT}{T^2} = -\frac{\ln \epsilon t}{C_2}\,d\lambda$$

$$\frac{dT}{d\lambda} = -T^2\frac{\ln \epsilon t}{C_2} \qquad \text{(B11a, b)}$$

For $T = 2000°K$, and $\epsilon t \approx 1/2$,

$$\frac{dT}{d\lambda} \approx 0.2^{\mathrm{deg}/m\mu}$$

or about 1/4°K over the range from 1500°K to 2000°K. This may be entirely neglected.

The reproducibility of brightness match enters into the temperature uncertainty in just the same way as ϵ and t do. It has been found that an instrument reading is reproducible to within 5°. This is consistent with the results quoted by Forsythe and thus is the major cause of the uncertainty in transmission as determined by the measurements mentioned above.

Another effect which can introduce errors is the following. The use of $\epsilon = 0.438$ tacitly assumes that the pyrometer sights normally to the surface being measured. There is a Lambert's law correction if this is not so. Considering a 3 cm radius cylindrical engine, a displacement of about ± 5 mm on the surface corresponds to an angular displacement of about ± 10°K. Since the pyrometer can easily be set to within ± 5 mm from the center (normal sighting) the maximum error introduced corresponds to a decrease of intensity of about 1.5 percent. This is translated into a 0.15 percent error in temperature determination. Deviations from Lambert's cosine Law, due to the reflection from the non-black body, is given by Barber[B11] as only 0.3° at 1500°K for an angle of 15°, and is thus completely negligible.

The non-zero sighting angle also affects the reflection from the glass surfaces. For 20° the change in R is on the order of 1/2 percent.[B12] This affects the value of the transmission by less than 1/2 percent, and thus is further reduced to 1/10 x 1/2 percent in temperature determination.

The total uncertainty introduced by the effects enumerated is thus seen to be on the order of 1 percent in temperature determination.

6. CONCLUSIONS

The foregoing show that the determination of the temperature by using an optical pyrometer is correct to about 20°K in 2000°K. If anything, there is a tendency for the measured value to be translated into too low a true temperature.

The curves given in figure B3 may be used to determine the brightness temperature for any given measured value under each of the geometrical circumstances considered. The true temperature may be determined by using the values listed in the table in the Handbook of Chemistry and Physics,[B13] since these have also been computed for tungsten with $\epsilon \approx 0.438$.

Alternatively, one may plot the four curves given by equation (B11). This allows a direct reading from the graph. It is to be emphasized, that all values of T are in °K.

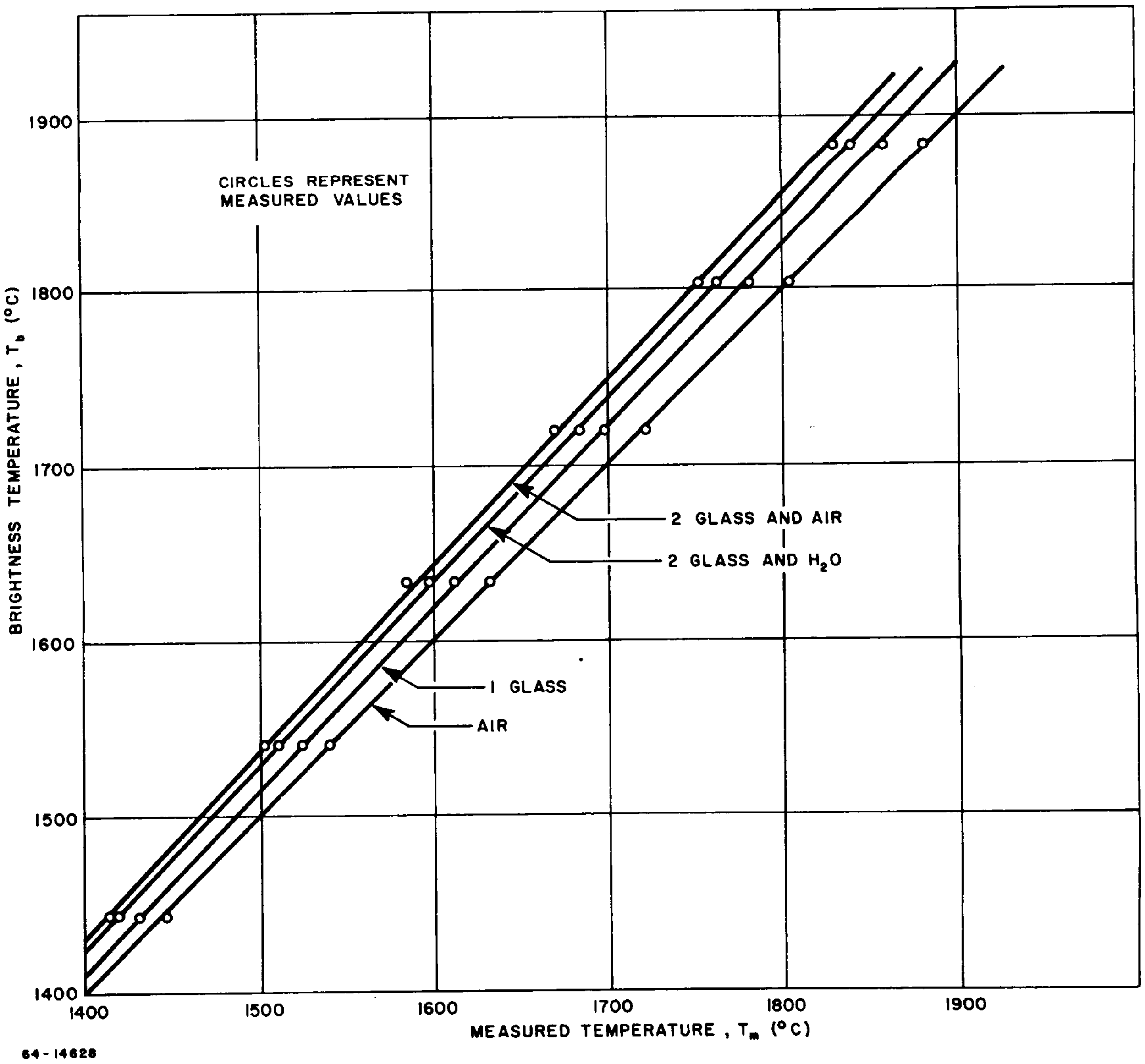

Figure B-3 CALIBRATION CURVES FOR BRIGHTNESS TEMPERATURE

REFERENCES

B1. W. E. Forsythe, Temperature - Its Measurement and Control in Science and Industry, Reinhold Publishing Corporation (1956), p. 1115.

B2. H. G. MacPherson, ibid, p. 1141.

B3. H. W. Russell and C. F. Lucks, ibid, p. 1159.

B4. A. G. Worthing, ibid, p. 1164.

B5. W. E. Forsythe, Loc. Cit.

B6. Jenkins and White, Fundamentals of Optics, Third Edition, McGraw-Hill Publishing Company (1957), p. 511.

B7. Ibid, p. 19.

B8. Handbook of Chemistry and Physics (1954-1955), Chemical Rubber Publishing Company, p. 2690.

B9. W. E. Forsythe, Loc. Cit.

B10. Handbook of Chemistry and Physics, Loc. Cit.

B11. C. R. Barber, Journal of Scientific Instruments, 23, 1946, p. 238.

B12. Handbook of Chemistry and Physics, p. 2679.

B13. Ibid, p. 2482.

APPENDIX C

INTERACTIONS OF CURRENT DISTRIBUTIONS WITH THE SELF MAGNETIC FIELD

Experiments with the X-2 High Specific Impulse arcjet engine have resulted in thrust measurements which are consistently higher than those which would be predicted from purely aerodynamic mechanisms. As a consequence, analytical investigations have been made of the forces in the thrust direction which could result from an interaction between a current distribution and its self magnetic field.

Two different thrust producing mechanisms have been identified. They are described as a magnetic blower and a magnetic pump. Analytical estimates have been made of the magnitudes of thrust which might result from each of these mechanisms.

1. Magnetic Blower

If, as is the case with the X-2 engine, the cathode is upstream of the anode and if the cross sectional area of the current distribution is larger at the anode than at the cathode, then:

i) there is a radial component of the current since the axial current density decreases in moving from the cathode to the anode, and

ii) there is an azimuthal magnetic field since the axial current density is different from zero.

The interaction of the radial current component with the azimuthal magnetic field results in a force in the axial direction. This force can directly accelerate the flow without an intermediate step of pressure buildup, hence the analogy to a blower rather than a pump. Numerical estimates of the force which can be produced by this mechanism are developed below.

We assume an arbitrary cylindrically symmetric current density $\vec{j}$ issuing from an anode and entering a cathode. The current density $\vec{j}$ can be expressed as:

$$\vec{j} = j_r(r,z)\,\hat{r} + j_z(r,z)\,\hat{z} \tag{C-1}$$

where j_r and j_z are the magnitudes of the radial and axial current densities, both permitted to be functions of r and z but not of the azimuthal coordinate θ (owing to the assumption of cylindrical symmetry); $\hat{r}$ and $\hat{z}$ are unit vectors in the r and z directions.

The current density $\vec{j}$ and the total current I are subject to the conditions:

$$\vec{\nabla} \cdot \vec{j} = 0 \tag{C-2}$$

$$I = \int_0^\infty 2\pi r\, j_z\, dr < \infty \tag{C-3}$$

The assumption of cylindrical symmetry allows us to write the divergence equation for $\vec{j}$ as:

$$\frac{1}{r} \frac{\partial r\, j_r}{\partial r} + \frac{\partial j_z}{\partial z} = 0 \tag{C-4}$$

Integrating equation C-4, we find:

$$j_z = -\int_0^z \frac{1}{r} \frac{\partial r\, j_r}{\partial r}\, dz + f(r) \tag{C-5}$$

where f(r) in equation C-5 is an arbitrary function of r.

Since the symmetry conditions require that H_r and H_z be zero, the equation for curl $\vec{H}$

$$\vec{\nabla} \times \vec{H} = 4\pi \vec{j} \tag{C-6}$$

yields

$$j_r = -\frac{1}{4\pi} \frac{\partial H_\theta}{\partial z} \tag{C-7}$$

and

$$j_z = \frac{1}{4\pi r} \frac{\partial r\, H_\theta}{\partial r} \tag{C-8}$$

Note, as a check, that integration of equation C-8 gives the familiar result:

$$H_\theta = \frac{1}{r} \int_0^r 4\pi r\, j_z\, dr + \frac{1}{r} h(z) = \frac{2I(r)}{r} \tag{C-9}$$

where the integration constant h(z) is set equal to zero to satisfy the requirement H_θ finite at $r = 0$.

Now, the axial force F_z is given by

$$F_z = \int j_r H_\theta \, d(\text{volume}) \tag{C-10}$$

$$= \int_{z_c}^{z_a} dz \int_0^\infty 2\pi r \, dr \left(- \frac{1}{4\pi} \frac{\partial H_\theta}{\partial z} \right) H_\theta$$

$$= \int_0^\infty 2\pi r \, dr \int_{z_c}^{z_a} - \frac{1}{8\pi} \frac{\partial (H_\theta)^2}{\partial z} \, dz$$

$$= - \frac{1}{4} \left[\int_0^\infty r H_\theta^2 \, dr \Big|_{z_a} - \int_0^\infty r H_\theta^2 \, dr \Big|_{z_c} \right]$$

Finally,

$$F_z = \int_0^\infty \frac{I_c^2 (r) - I_a^2 (r)}{r} \, dr \tag{C-11}$$

where $I_c (r)$ and $I_a (r)$ are the total currents inside radius r at the cathode and anode, respectively. This is as far as the analysis can proceed without further assumptions on the current distribution but note that the only requirement is to specify the distribution at the electrodes. In the region between electrodes only cylindrical symmetry has been assumed; the detailed dependence on r and on z is arbitrary.

Now, two additional assumptions are introduced to allow further manipulation of equation C-11.

i) $I_c(r) = I_a(\alpha r)$, or the current distributions at anode and cathode are similar, with a geometrical scaling parameter α.

ii) The current distributions cut off within a finite value of r. That is,

$$\int_o^R \frac{I_A^2(\alpha r) - I_A^2(r)}{r}\, dr = \int_o^\infty \frac{I_A^2(\alpha r) - I_A^2(r)}{r}\, dr$$

With these additional assumptions, equation C-11 becomes:

$$F_z = \int_o^{\alpha R} \frac{I_A^2(r)}{r}\, dr - \int_o^{R} \frac{I_A^2(r)}{r}\, dr$$

$$= \int_R^{\alpha R} \frac{I_A^2(r)}{r}\, dr = I^2 \int_R^{\alpha R} \frac{dr}{r}$$

or,

$$F_z = I^2 \ln \alpha \tag{C-12}$$

Hence, the total force depends on the square of the current and on the natural logarithm of the linear scaling factor α. Alternatively, equation C-12 can be written:

$$F_z = \frac{1}{2} I^2 \ln \alpha^2 \tag{C-13}$$

where α^2 is the area ratio of the current distribution at anode and cathode. Since electromagnetic units have been used to derive this relation, the force is given in dynes when the current is given in abamperes. To convert to forces of grams and currents of amperes, equation C-13 can be rewritten as:

$$F_z = 5.1 \times 10^{-6}\, I^2 \ln \alpha^2 \text{ grams} \tag{C-14}$$

a) Special Case, Purely Radial Discharge (figure C-2)

To test a special case, assume a purely radial discharge with current density j uniform as a function of z. Assume that the discharge occupies a length z_o on anode and cathode. Then, in the z interval 0 to z_o, and r interval r_c to r_a, the current density and magnetic field strength can be written as:

$$j_r = \frac{I}{2\pi r z_o} \qquad \text{(C-15)}$$

$$H_\theta = \frac{2I}{r}\left(1 - \frac{z}{z_o}\right) \qquad \text{(C-16)}$$

Hence, the axial force is

$$\int j_r H_\theta \, d(\text{volume}) = \frac{I^2}{\pi z_o} \int \frac{\left(1 - \frac{z}{z_o}\right)}{r^2} \, r \, dr \, d\theta \, dx$$

$$= I^2 \ln \frac{r_{\text{anode}}}{r_{\text{cathode}}} \qquad \text{(C-17)}$$

which is identical with equation C-12

b) Numerical Values

The X-2 High Specific Impulse Engine has been operated at current levels of the order of 2000 amperes. For this value of current, using equation C-14,

$$F_z = 20.4 \ln \alpha^2 \text{ grams}$$

If the anode area is set equal to the throat area, this is approximately 1 cm^2. No information yet exists about the current cross-section at the cathode. If the spot diameter were approximately 1 mm, then $A_{\text{cathode}} \sim 10^{-2}\ \text{cm}^2$, and $F \sim 94$ grams.

2. Magnetic Pump

In addition to the interaction between the radial current and the azimuthal field, which produces acceleration in the axial direction, there is also interaction between the axial current and the azimuthal field, which produces a radial force. This force raises the pressure within the current carrying

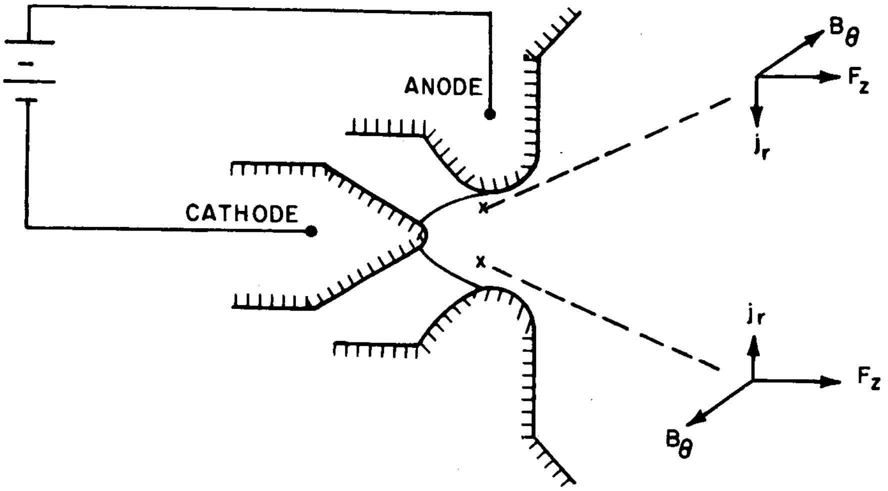
ANODE
CATHODE
x
x
B_θ
F_z
j_r
j_r
F_z
B_θ

Figure C-1 FORCE RESULTING FROM INTERACTION BETWEEN A CURRENT AND ITS OWN MAGNETIC FIELD IN AN ARCJET ENGINE CONFIGURATION

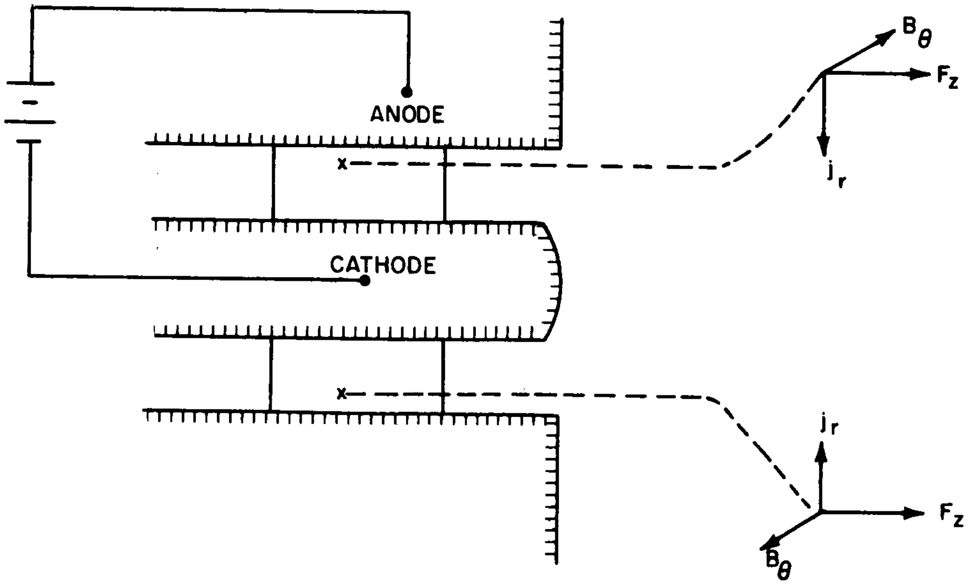
ANODE
CATHODE
x
x
B_θ
F_z
j_r
j_r
F_z
B_θ

64-14245

Figure C-2 FORCE BETWEEN CURRENT AND SELF MAGNETIC FIELD, PURELY RADIAL DISCHARGE

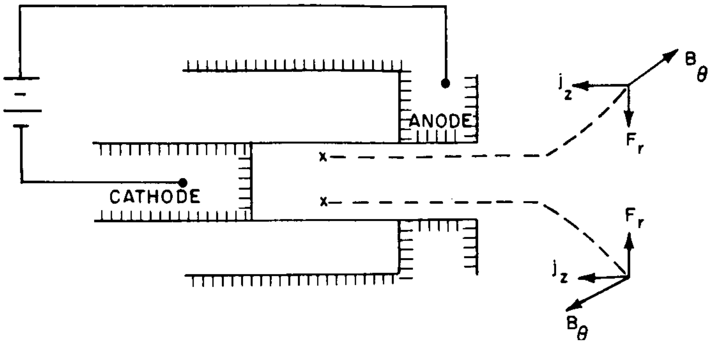
ANODE
CATHODE
x
x
j_z
B_θ
F_r
F_r
j_z
B_θ

Figure C-3 PINCH FORCE, UNIFORM AXIAL DISCHARGE

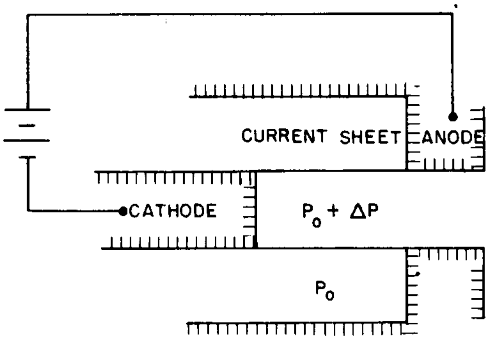
CURRENT SHEET
ANODE
CATHODE
P_o + ΔP
P_o

Figure C-4 PINCH FORCE, AXIAL SHEET DISCHARGE

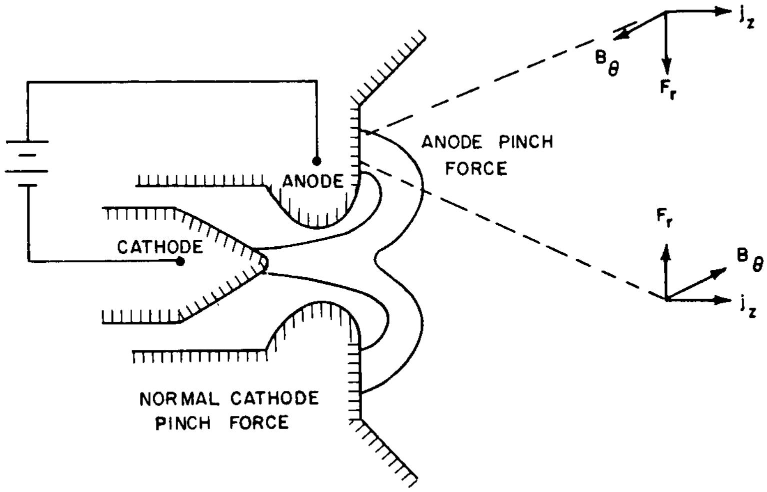
j_z
B_θ
F_r
ANODE PINCH FORCE
ANODE
CATHODE
F_r
B_θ
j_z
NORMAL CATHODE PINCH FORCE
64-14246

Figure C-5 PINCH FORCE INCLUDING EFFECT AT THE ANODE portion of the flow ("pinch") and this pressure rise can be translated into thrust and gas acceleration through gas-surface interaction. Two specific cases are worked out below.

a) Uniform current distribution, cylindrical symmetry (figure C-3)

The force on the cathode, for example, is given by:

$$F_z = \int P \, dA \tag{C-18}$$

where P is the pressure at the cathode surface.

Now, the pressure can be calculated by setting the radial pressure gradient equal to the radial magnetic force,

$$\frac{dP}{dr} = j_z H_\theta \tag{C-19}$$

So that

$$P(r) = P_o + \int j_z H_\theta \, dr \tag{C-20}$$

If the axial current distribution at the cathode is uniform over a circle of radius R,

$$j_z = \frac{I}{\pi R^2} \tag{C-21}$$

$$H_\theta = \frac{2I}{r} \left(\frac{r^2}{R^2} \right) = \frac{2\,Ir}{R^2} \tag{C-22}$$

Then, using equations C-20 and C-18,

$$P(r) = P_o + \int_o^r \frac{2I^2}{\pi R^4} \, r \, dr = P_o + \frac{I^2 r^2}{\pi R^4}$$

$$F_z = \int 2\pi r \, dr \left[P_o + \frac{I^2 r^2}{\pi R^4} \right]$$

$$F_z = \pi R^2 P_o + \frac{I^2}{2} \qquad \text{(C-23)}$$

The first term on the right hand side of equation C-23 represents the ordinary static pressure level, while the second term represents the additional magnetic pressure. Comparing this term to equation C-13, it can be seen that the magnetic pressure contribution to thrust is smaller than the direct acceleration by the factor ln a^2.

b) Cylindrical Sheet Current (figure C-4)

The sum of static and magnetic pressure at the outer boundary of the cylindrical sheet is $P_o + \frac{H^2}{8\pi}$ but H is given by

$$H = \frac{2I}{R}$$

The total pressure, therefore, is $\frac{I^2}{2\pi R^2} + P_o$.

The area over which the pressure acts is πR^2, so that

$$F_z = \frac{1}{2} I^2 + \pi R^2 P_o \qquad \text{(C-24)}$$

c) Numerical Values

Since the ambient pressure level P_o is accounted for in the X-2 engine data analysis as part of the aerodynamic thrust, we evaluate only $\frac{1}{2} I^2$. For a current of 200 abamperes, this is 2 x 10^4 dynes, or 20.4 grams. It should be noted that equations C-23 and C-24 are identical, and that neither depends upon the current cross-sectional area at the cathode. Further, if the current distribution is like that of figure C-5, a similar force will exist at the anode, and will also be in the direction of thrust. Hence, this mechanism can account for as much as 40 grams of thrust at the 2000 ampere level.

APPENDIX D

COMPOSITE ENGINE

In order to reduce the time and cost associated with the fabrication of experimental engines, a composite engine was designed and built. A detailed drawing of the composite engine is shown in figure D-1. Referring to figure D-1, the nozzle and constrictor sections are removable. This arrangement greatly simplifies the study of the influence of various geometrical changes such as nozzle shape (angle, area ratio and length), constrictor length and diameter, gas injection pattern, etc. on engine performance. Various constrictor and nozzle sections can be substituted thereby eliminating the need to build a separate engine for each test. The constrictor section can be modified so as to permit visual observation of the arc column through a quartz viewing port. Next to the constrictor section is a removable section which permits propellant injection at the converging section (joining the constrictor and the plenum chamber) with different entry geometries and angles of injection. These three removable sections are joined using bolts and sealed by means of "C"-rings.

The composite engine also provides a means of altering the gap setting by a micrometer adjustment which leads to the rear of the engine. A modification of the design removes this micrometer attachment and replaces it with the capability of injecting the propellant axially through the cathode.

The various parts of the composite engine can be fabricated of different materials including stainless steel, tungsten and molybdenum. The "C" -ring seals determine the limit of performance obtainable with the composite engine. The composite engine has been operated successfully at a specific impulse level in excess of 1000 seconds for periods of the order of a minute. It is thought that the experimental trends observed at this impulse level provide a useful basis from which to make modifications leading to optimum performance at higher impulse levels. The composite engine does have the important drawback that it can not be operated at the 30 kw power level in a steady state condition. However, careful attention to reproducing the transient operating condition can indicate qualitative trends which can then be quantitatively pursued using the standard engines.

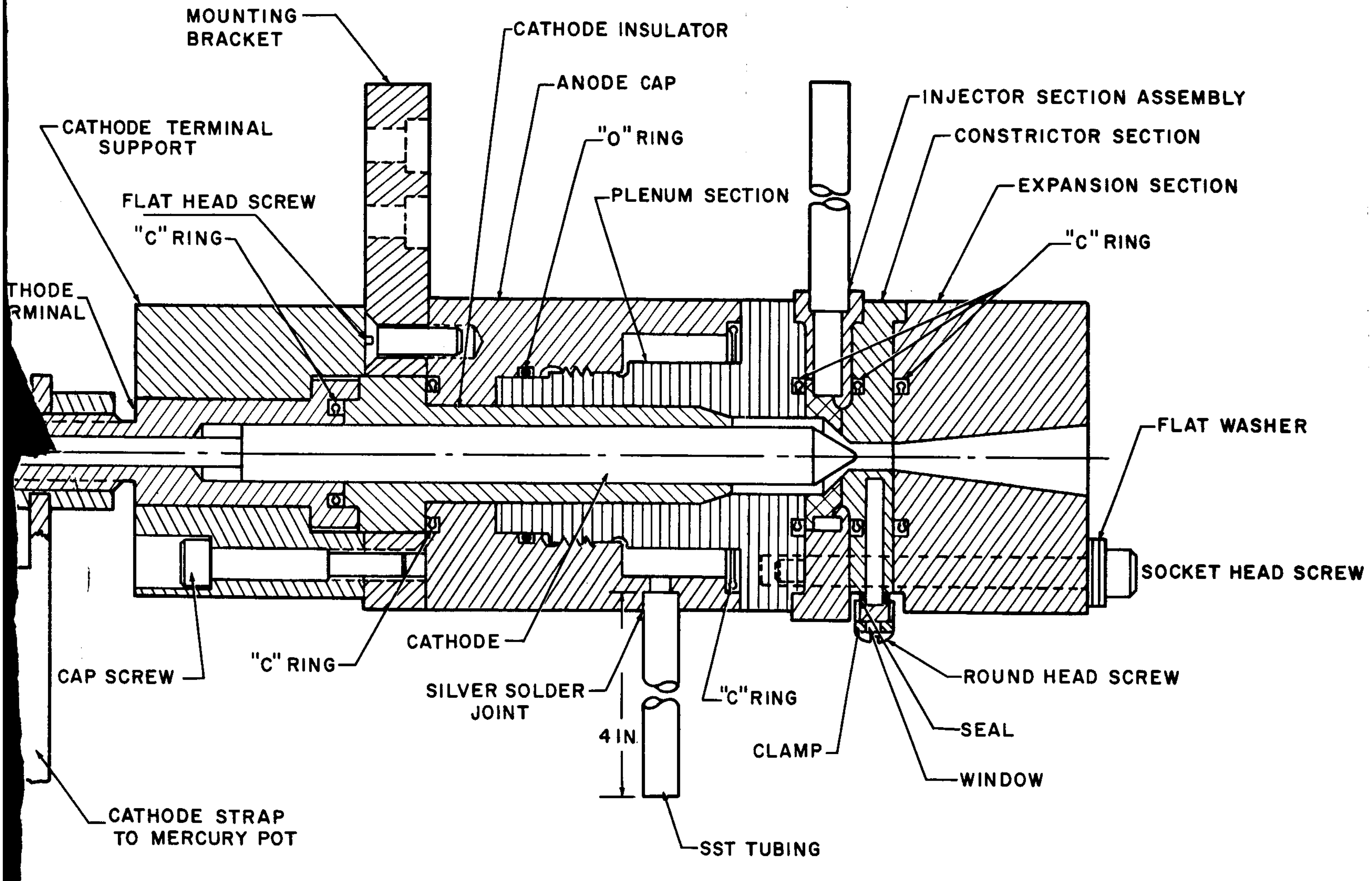
MOUNTING BRACKET
CATHODE INSULATOR
ANODE CAP
INJECTOR SECTION ASSEMBLY
CATHODE TERMINAL SUPPORT
"O" RING
CONSTRICTOR SECTION
EXPANSION SECTION
PLENUM SECTION
FLAT HEAD SCREW
"C" RING
"C" RING
THODE
RMINAL
FLAT WASHER
SOCKET HEAD SCREW
CATHODE
CAP SCREW
"C" RING
ROUND HEAD SCREW
SILVER SOLDER JOINT
"C" RING
SEAL
4 IN.
CLAMP
WINDOW
CATHODE STRAP TO MERCURY POT
SST TUBING

HIRTY KILOWATT COMPOSITE ARC ASSEMBLY

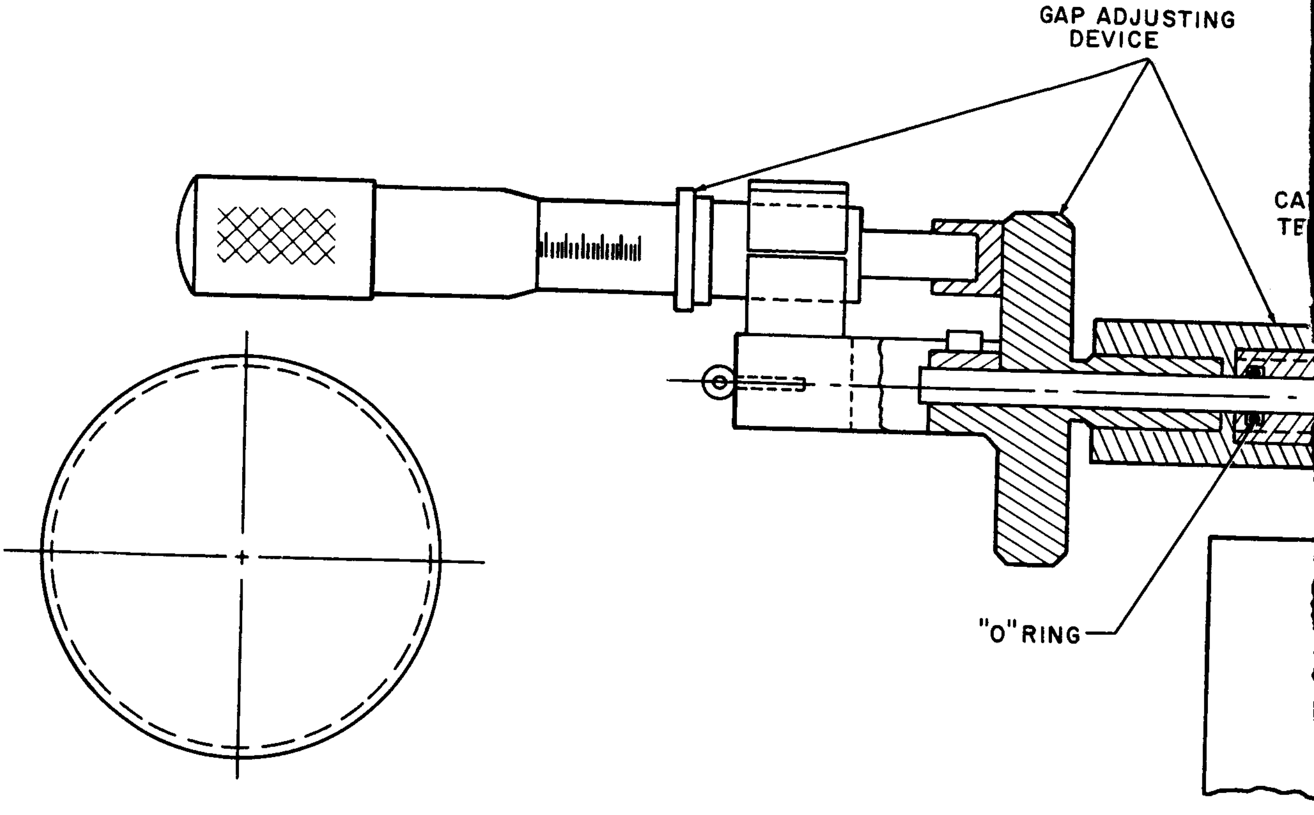
GAP ADJUSTING DEVICE
CA
TE
"O" RING

64-14247

Figure D-1

APPENDIX E

ANALYSIS OF TWO-FLUID MODEL FOR THE CONSTRICTED ARC

1. INTRODUCTION

To investigate the essential features of the arc column processes with a minimum of mathematical complexity, a simplified two-fluid model has been formulated; although the model is somewhat crude in its present state of development, it appears to give results which are in at least semiquantitative agreement with experiment.

The description of the model is given in the body of the text and it is here that the detailed analysis of the model is presented.

2. ANALYSIS

As previously discussed, the fluid-flows in both the arc core and in the cold sheath (see figure 42) are assumed to be governed by the equations of quasi-one-dimensional fluid-flow in a channel with mass and energy addition. For the cold-sheath flow these equations take the form

$$\frac{d}{dx}(\rho_2 V_2 A_2) = + \frac{d}{dx}\dot{m}_2 \qquad \text{(E-1a)}$$

$$A_2 \frac{dP}{dx} + \rho_2 V_2 A_2 \frac{dV_2}{dx} = 0 \qquad \text{(E-1b)}$$

$$\frac{d}{dx}\left(h_2 + \frac{1}{2} V_2^2\right) = 0 \qquad \text{(E-1c)}$$

where all symbols have their usual meaning and the subscript 2 indicates values of the quantities for the cold sheath; no subscript appears with the pressure for it is assumed to be the same in both regions. The term $- \frac{d}{dx}\dot{m}_2$ in equation (E-1a) represents the mass flux which is removed from the cold sheath and andded to the hot core region by the effects of heat conduction; this term will be discussed later and for the present may be taken as known.

Assuming the gas in the outer sheath satisfies the ideal equation of state

$$h_2 = \frac{\gamma_2}{\gamma_2 - 1} \frac{P}{\rho_2} \qquad \text{(E-1d)}$$

Equations (E-1) may be integrated immediately to obtain the usual adiabatic relations

$$\frac{P}{P_o} = \left(\frac{\rho_2}{\rho_o}\right)^{\gamma_2} \qquad \text{(E-2)}$$

$$h_2 + \frac{1}{2} V_2^2 = h_o + \frac{1}{2} V_o^2$$

$$\rho_2 V_2 A_2 \equiv \dot{m}_2 = \dot{m} - \dot{m}_1$$

where the subscript o indicates initial conditions and $\dot{m} = \rho_o V_o A$ is the total mass flow rate; the subscript 1 denotes the core region. Since, as will be seen below, the mass flow rate in the core, $\dot{m}_1$, is usually only a small portion of the total mass flow rate, $\dot{m}$, it follows from equations (E-2) that the cross-sectional area A_2 of the sheath at any axial position x is determined essentially only by the pressure drop to that point. Since the areas of the core and sheath flows are related by the condition on the total area

$$A_1 + A_2 = A \qquad \text{(E-3)}$$

the interesting conclusion is reached that the relationship between the core area A_1 and the pressure p is determined primarily by the properties of the cold-gas sheath surrounding the core and is largely independent of what occurs in the core itself.

In the case of the hot core, the equations of quasi-one-dimensional flow take the form

$$\frac{d}{dx} (\rho_1 V_1 A_1) = \frac{d}{dx} \dot{m}_1 \qquad \text{(E-4a)}$$

$$A_1 \frac{dP}{dx} + \dot{m}_1 \frac{dV_1}{dx} + (V_1 - V_2) \frac{d}{dx} \dot{m}_1 = 0 \qquad \text{(E-4b)}$$

$$\dot{m}_1 \frac{d}{dx}\left(h_1 + \frac{1}{2} V_1^2\right) + \left[\left(h_1 + \frac{1}{2} V_1^2\right) - \left(h_2 + \frac{1}{2} V_2^2\right)\right] \frac{d}{dx} \dot{m}_1 = I \frac{dV}{dx} \qquad \text{(E-4c)}$$

where the term $(V_1 - V_2) \frac{d}{dx} \dot{m}_1$ in equation (E-4b) represents the momentum required to accelerate the mass of gas which is added to the core flow from the velocity V_2, which it had in the cold sheath, to the velocity V_1 of the core. Similarily, the term $[(h_1 + 1/2 V_1^2) - (h_2 + 1/2 V_2^2)] \frac{d}{dx} \dot{m}_1$ in equation (E-4c) represents the energy required to heat this added gas from the temperature of the sheath to the temperature of the core, and the term $I \frac{dV}{dx}$ represents the energy addition to the core from the arc current; V is the arc voltage. (As previously mentioned, it has been assumed in this preliminary analysis that all the energy given up by the arc goes into heating the gas in the core region.)

The equations (E-4) for the core flow can be integrated readily by adding them to the corresponding equations for the cold-sheath flow (equation (E-1) to obtain the conservation equations for the flow as a whole. Integration proceeds by making use of equations (E-2) and (E-3) to give

$$\rho_1 V_1 A_1 = \dot{m}_1 \tag{E-5}$$

$$PA_1 + \dot{m}_1 V_1 + \dot{m} V_2 = \text{constant} = (P_o + \rho_o V_o^2) A \quad .$$

$$\dot{m}_1 \left(h_1 + \frac{1}{2} V_1^2\right) + \dot{m}_2 \left(h_2 + \frac{1}{2} V_2^2\right) = \dot{m} \left(h_o + \frac{1}{2} V_o^2\right) + IV$$

where the constants of integration have been evaluated assuming that the mass flow rate $\dot{m}_1$ in the core region is equal to zero initailly (at $x = 0$) and that the arc voltage V is zero at $x = 0$. Equations (E-1d), (E-2), (E-3), and (E-5) together with the equation of state

$$h_1 = h_1 (P, \rho_1) \tag{E-6}$$

for the core flow provide a system of nine simultaneous equations involving the eleven unknown quantities P, ρ_1, V_1, h_1, A_1, ρ_2, V_2, h_2, A_2, $\dot{m}_1$ and V. These equations can be solved to yield expressions for any nine of these variables in terms of the remaining two, which for example may be $\dot{m}_1$ and V. To complete the solution of the problem it is thus necessary to obtain expressions for the quantities $\dot{m}_1$ and V as functions of the axial position coordinate x.

3. THE EFFECTS OF HEAT CONDUCTION

One of the additional relationships required to specify the problem is provided by considering the effects of heat transfer from the hot core to the surrounding sheath of cold gas. Since by definition the core flow region is part of the total gas flow which has been heated, it follows that the cold gas which is heated due to the transfer of heat from the hot core must subsequently be counted as part of the core flow itself; the net effect of heat conduction in this model is to cause a transfer of mass from the cold gas region 2 to the hot core region 1. Since $\frac{d}{dx} \dot{m}_1$ represents the mass flow rate per unit time per unit length into the arc column due to this cause, then the total heat involved per unit length of column in heating this gas to the column enthalpy is simply

$$Q = (h_1 - h_2) \frac{d}{dx} \dot{m}_1 \qquad \text{(E-7)}$$

If it is assumed that this heat is provided by heat conduction out of the column then it follows that

$$Q = -2\pi r_c k \frac{\partial T}{\partial r} = -2\pi r_c \frac{k}{c_p} \frac{\partial h}{\partial r} \qquad \text{(E-8)}$$

where k is the thermal conductivity of the gas, c_p is the specific heat at con-constant pressure, and r_c is the column radius. Combining equations (E-7) and (E-8) then gives an expression for $\frac{d}{dx} \dot{m}_1$ in terms of the radial enthalpy gradient $\frac{\partial h}{\partial r}$: i. e.,

$$\frac{d}{dx} \dot{m}_1 = -2\pi \frac{k}{c_p} \frac{r_c}{h_1 - h_2} \frac{\partial h}{\partial r} \qquad \text{(E-9)}$$

The radial enthalpy gradient $\frac{\partial h}{\partial r}$ occurring in equation (E-9) cannot be evaluated within the framework of the present model since in this model a discontinuity in the enthalpy at the interface between the core and sheath regions has been assumed. To proceed further it is necessary to introduce some approximation for determing $\frac{\partial h}{\partial r}$. For simplicity, it is assumed that $\frac{\partial h}{\partial r}$ is proportional to $-\frac{(h_1 - h_2)}{r_c}$ so that equation (E-9) becomes simply

$$\frac{d}{dx} \dot{m}_1 = 2\pi a \frac{k}{c_p} \qquad \text{(E-10)}$$

where the proportionality constant a depends on the shape of the radial enthalpy distribution and must be evaluated from independent considerations. For a parabolic distribution, for example, it is found that

$$a = 4 \qquad \text{(E-11)}$$

Figure (E-1) shows a plot of $\frac{k}{c_p}$ versus temperature for hydrogen at atmospheric pressure. It is seen that over the range of temperatures of interest for arc operation the value of $\frac{k}{c_p}$ tends to oscillate over a limited range of values and shows no distinct trend with increasing temperature. For a first approximation $\frac{k}{c_p}$ is simply taken equal to a constant average value, $\overline{k/c_p}$ so that equation (E-10) may be integrated immediately to give the remarkably simple relationship

$$\dot{m}_1 = 2\pi a \left(\frac{k}{c_p}\right) x \qquad \text{(E-12)}$$

where again the boundary condition $\dot{m}_1 = 0$ at $x = 0$ has been used. Thus, within the accuracy of the approximation of equation (E-12), the mass flow rate in the hot core region depends only on the length of the arc and the gas and is independent of all other arc parameters.

4. OHM'S LAW

The final relationship required to determine the model is supplied by Ohm's law for the column,

$$\frac{dV}{dx} \equiv E = \frac{I}{\bar{\sigma} A_1} \qquad \text{(E-13)}$$

where E is the axial electric field at x and $\bar{\sigma}$ is the average electrical conductivity of the column. If the enthalpy profile in the column is assumed to be known then $\bar{\sigma}$ is known function of the average column enthalpy, h_1. From equations (E-1) through (E-6) and equation (E-12) however, the column enthalpy h_1 and the area A_1 are known functions of V and x, so that the right-hand side of equation (E-13) becomes an ordinary nonlinear differential equation

$$\frac{dV}{dx} = F(V,x) \qquad \text{(E-14)}$$

which could be solved by standard numerical procedures to obtain the electric potential V as a function of x. This solution could then be substituted into equations (E-1) throug (E-6) and (E-12) to obtain expressions for the other arc properties of interest as functions of x.

As was pointed out in the discussion of the effects of heat conduction, the radial enthalpy distribution in the core region which is required to evaluate the function $\bar{\sigma}(h_1)$ in equation (E-13) cannot be obtained within the framework of the present model but must be assumed independently. Figure (E-2) shows a plot of $\bar{\sigma}$ versus h_1 for two different assumed enthalpy profiles in the core region, namely a constant enthalpy over the core region cross-section and a parabolic enthalpy distribution. It is seen that the $\bar{\sigma}$ functions calculated from these two different enthalpy profiles do not differ much from one another; thus it appears that errors in $\bar{\sigma}$ due to an incorrect choice of the column enthalpy profile does not lead to a major source of error in the final results of the calculation.

5. SOLUTION OF THE EQUATIONS

Although equation (E-14) presumably could be solved without too much difficulty by direct numerical integration, a somewhat simpler approximation procedure has been adopted which is suggested by the experimental observation that the axial electric field strength E is approximately constant over most of the arc length (see voltage gradient measurement section under Arc Column Studies). In this procedure a new quantity $V_c = V_c(x)$ is introduced and defined by the relation

$$V_c \equiv V - x \frac{dV}{dx} \equiv V - Ex \tag{E-15}$$

and which evidently represents the voltage which would be obtained by extrapolating the actual voltage and field strength at the point x back to the origin $x = 0$, assuming a constant field strength. Thus if E is only a slowly varying function of x, V_c should be nearly constant. Substituting the value of $\frac{dV}{dx}$ from equation (E-15) into equation (E-14) gives the algebraic equation

$$\frac{V - V_c}{x} = F(V,x) \tag{E-16}$$

Equations (E-15) and (E-16) now constitute a pair of simultaneous equations for the two unknown quantities V and V_c as functions of x. To solve these equations an approximate interative procedure is employed which is based on the fact that V_c is only a slowly varying function of x. For the first approximation a constant value of V_c is assumed in equation (E-16) and the resulting algebraic equation is solved for $V(x)$. This value of $V(x)$ is then substituted into equation (E-15) to obtain a new value of $V_c(x)$ and the procedure is repeated until satisfactory convergence is obtained. The question of how well this procedure leads to convergence has not been studied in any detail; however an example of the results obtained from the first iteration for a typical case is shown in figure E-3. It is seen that for this case at least the approximation of constant appears to be very well satisfied indeed.

Looking back over equations (E-1) through (E-6) and equation (E-12) which define the function $F(V,x)$ in equation (E-14), it is seen that $F(V,x)$ is a function of five arc operation parameters which might, for example, be taken to be the constrictor area A, arc current I, mass flow rate $\dot{m}$, initial enthalpy h_o, and the initial pressure p_o. Although these five parameters together with the gas properties are sufficient to completely determine the solution of equation (E-14), they are not the most convenient set for most applications. The reason for this is the occurrence of "thermal choking" phenonema in the solutions, i. e., for given values of the arc operating parameters, equation (E-14) does not have real solutions for values of x greater than some critical value $x = x_c\ (A, I, \dot{m}, h_o, p_o)$. An example of the effect is seen clearly in figure E-3 where the solution is seen to turn back on itself when x reaches the value of about 0.77 cm. This behavior is completely analogous to the well-known chocking effect which occurs at the sonic point in an ordinary quasi-one-dimensional flow, through in the present case it turns out that neither of the flows need be sonic at the critical point.

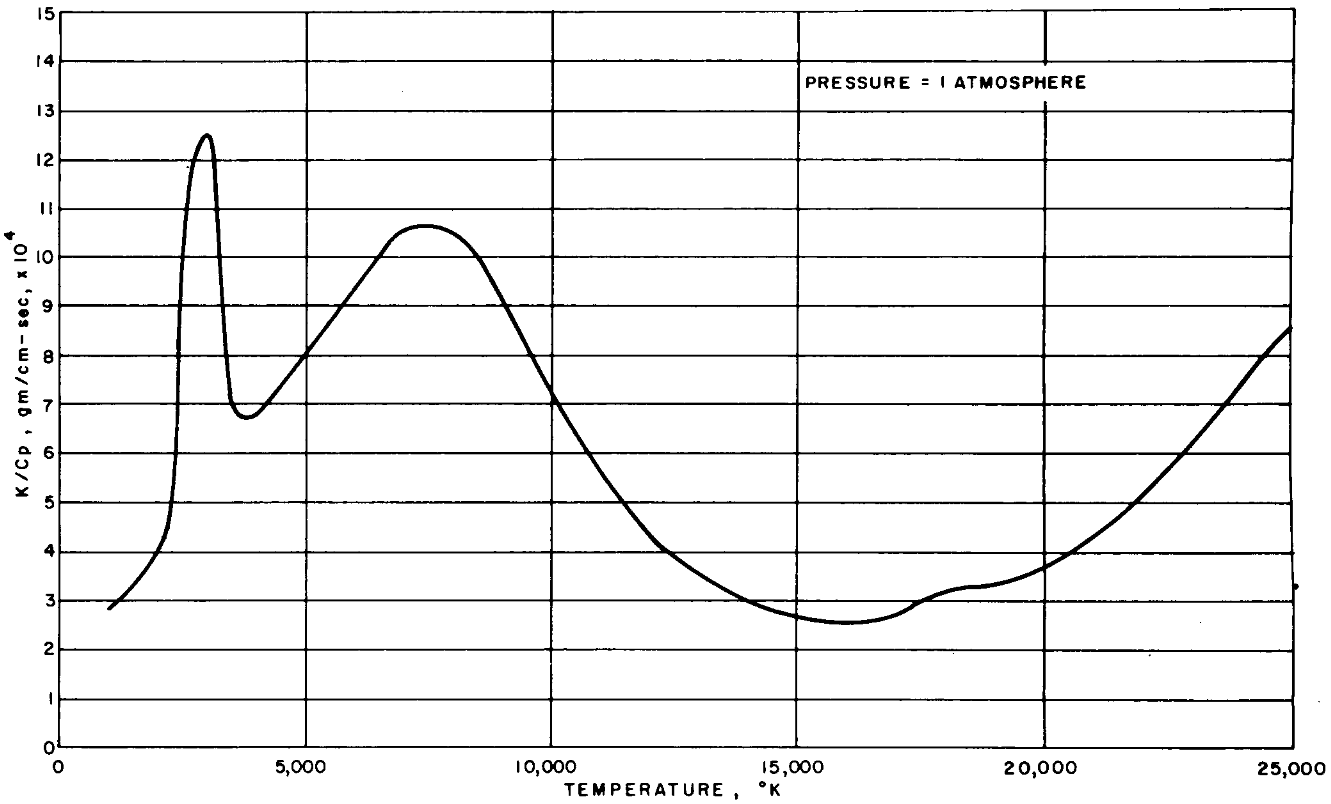

64-3003

Figure E-1 K/C_p VERSUS TEMPERATURE FOR HYDROGEN

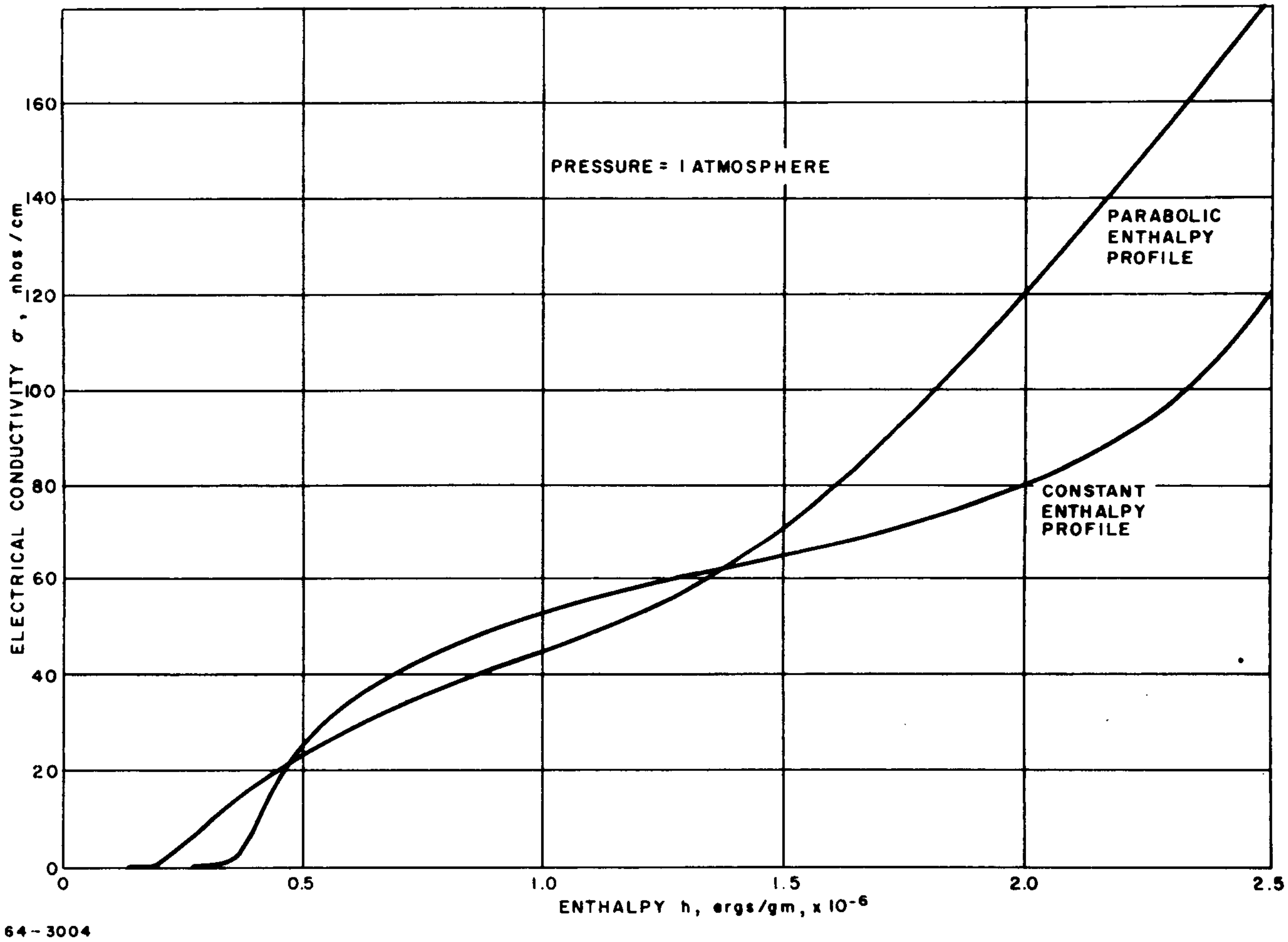

Figure E-2 ELECTRICAL CONDUCTIVITY VERSUS ENTHALPY FOR HYDROGEN

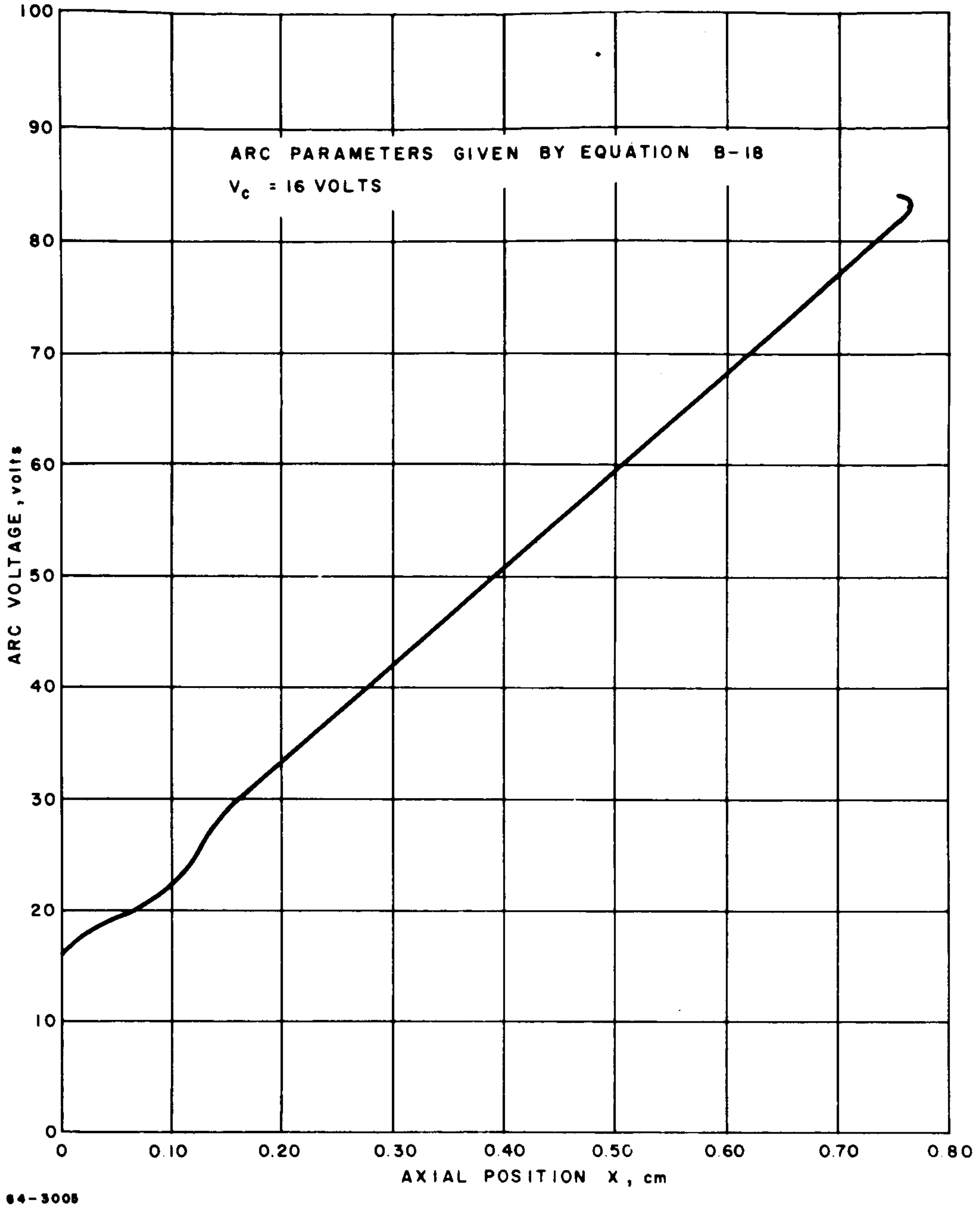

Figure E-3 ARC VOLTAGE VERSUS AXIAL POSITION AS GIVEN BY THE TWO FLUID MODEL

To obtain physically meaningful solutions of equation (E-14) it is thus necessary to choose the arc operating parameters in such a way that the critical length x_c is not less than the length of the constrictor tube (see figure 42). To determine the actual position of the critical point, l it is necessary$l$ to know the complete solution for the flow in the constrictor tube and in the supersonic nozzle; however, in analogy to the case of ordinary quasi-one-dimensional flow, it is expected that if the energy addition in the expansion nozzle is not too large, the critical point will be located near the end of the constrictor tube, so that

$$x_c \approx l \qquad \text{(E-17)}$$

Equation (E-17) can then be used to determine one of the arc operating parameters, say the initial pressure P_o, from the others.

6. EXAMPLE

A solution of equation E-16 for the column properties of a hydrogen arc has been obtained for the following typical case:

$A = 0.079 \text{ cm}^2$

$I = 180$ amperes

$\dot{m} = 0.1$ gm/sec

$T_o = 1030$ °K

$$x_c = l = 0.77 \text{ cm} \qquad \text{(E-18)}$$

In these calculations the gas was assumed to be ideal with the ratio of specific heats $\gamma = 1.2$, the value of V_c was taken equal to 16 volts and a parabolic enthalpy distribution was used in evaluating the quantities a and $\bar{\sigma}$ in equations (E-12) and (E-13). The arc voltage $V(x)$ obtained from this calculation is shown in figure E-3. It is seen that $V(x)$ is very nearly linear with x and gives an axial electric field strength of $E = 86$ volts/cm, in fair agreement with the experimental value of $E = 70$ volts/cm. The column radius is plotted versus x in figure E-4; it is seen that the shape of the column is qualitatively similar to the experimental observations but that it is somewhat too wide. However, this may be the result of the differences in the theoretical and experiment definitions of column radius. Finally, figure E-5 shows a plot of the calculated pressure distribution versus axial position which is in qualitative agreement with measured values obtained using a specially constructed pressure tap engine.*

---

*Bennett, S., Theoretical and Experimental Investigation of Arc Jet Engine Nozzle Flow, (Contract NAS-3-2506). Technical Report RAD-TR-63-50, July, 1963.

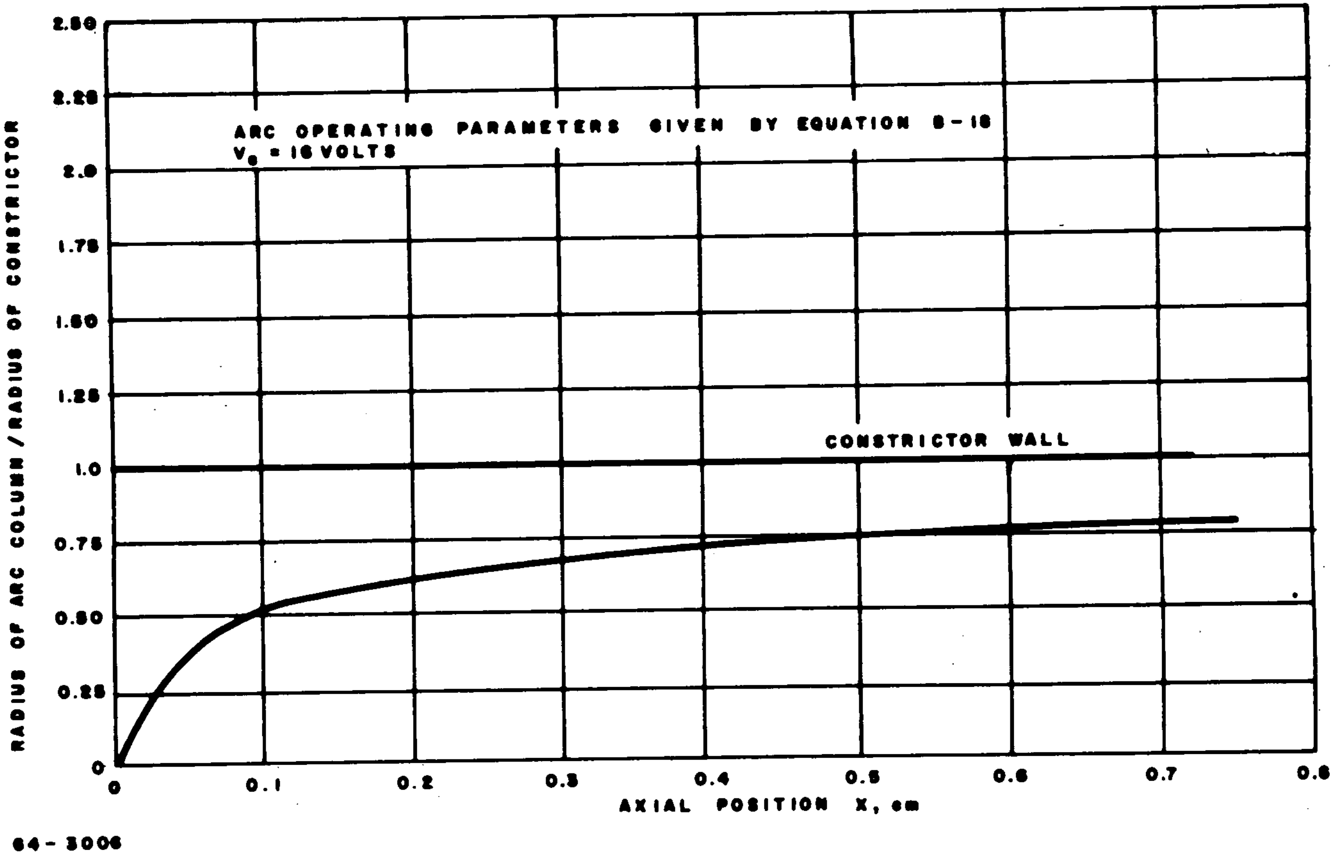

Figure E-4 CORE RADIUS VERSUS AXIAL POSITION AS GIVEN BY THE TWO FLUID MODEL

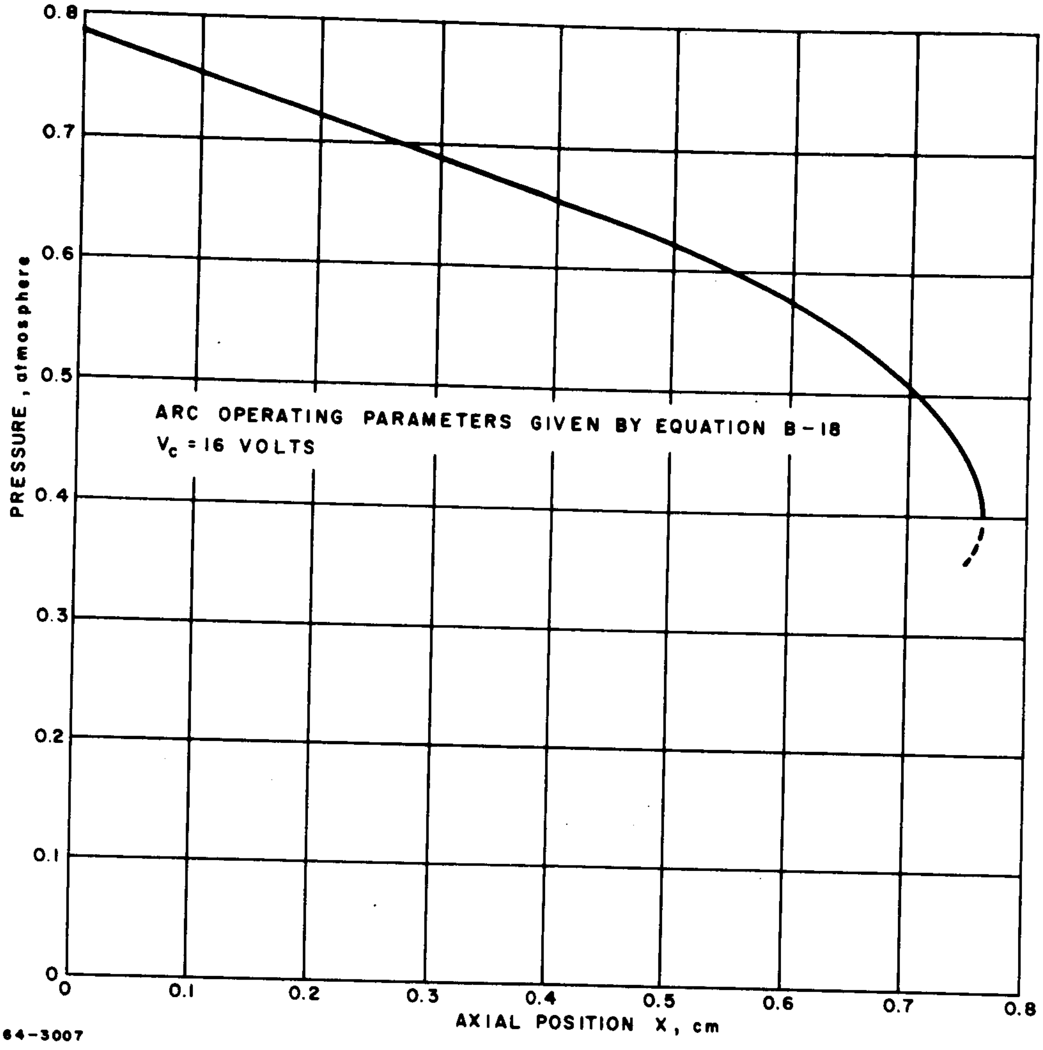

Figure E-5 PRESSURE DISTRIBUTION IN THE CONSTRICTOR AS GIVEN BY THE TWO FLUID MODEL

APPENDIX F

THEORY OF THE IMPACT PRESSURE PROBE

1. RELATION BETWEEN IMPACT PRESSURE AND MOMENTUM FLUX

The theory of the supersonic impact-pressure probe is based on the assumption that over the extent of the diameter of the probe orifice, the detached shock situated in front of the probe tip can be considered normal; this requires that the probe tip be blunt. The situation is depicted in figure F-1. The flow is assumed to be brought isentropically to rest within the probe and the resulting pressure is termed the impact pressure. It will now be shown that under certain conditions the impact pressure is closely related to the momentum flux in the flow upstream of the shock.

This relationship can be seen in a qualitative way by considering the statement of conservation of momentum for flow across a normal shock. Letting the subscript 1 denote conditions upstream of the shock and the subscript 2 denote conditions downstream of the shock, then the statement of conservation of momentum takes the form.

$$P_1 + \rho_1 u_1^2 = P_2 + \rho_2 u_2^2 \tag{F-1}$$

where P, ρ, and u denote the static pressure, density, and flow velocity respectively. If the supersonic flow (region 1) is characterized by a high Mach number, i. e., $M_1 >> 1$ then $\rho_1 u_1^2 >> P_1$. Consequently, the flow immediately downstream of the shock has a low Mach number so that P_2 is substantially larger than $\rho_2 u_2^2$ with the result that $P_2 \approx \rho_1 u_1^2$. The pressure measured by the probe is the total or impact pressure, P_{o2} which is the pressure that results when the flow is brought isentropically to rest. If the flow in region 2 has a low Mach number then $P_2 \approx P_{o2}$ so that the final result is $P_{o2} \approx \rho_1 u_1^2$.

The above discussion shows that in a qualitative way it is to be expected that when $M_1 >> 1$, the impact pressure is approximately equal to the momentum flux $\rho_1 u_1^2$ in the flow. The quantitative relation can be established by considering the complete normal shock equations rather than just the conservation of momentum. This can be done with the use of normal shock tables in the following way: The Mach number M is defined as u/a where a is the sound speed. For a perfect gas, the sound speed is given

$$a = \sqrt{\frac{\gamma P}{\rho}} \tag{F-2}$$

where γ is the ratio of the specific heat at constant pressure to the specific heat at constant volume. Then

$$\frac{P_{o2}}{\rho_1 u_1^2} = \frac{P_{o2}}{P_1}\,\frac{P_1}{\rho_1 u_1^2} = \frac{1}{\gamma M_1^2}\,\frac{P_{o2}}{P_1} \qquad \text{(F-3)}$$

For a gas for which γ does not change across a shock, then P_{o2}/P_1 is only a function of the Mach number M_1 and γ. Going to the normal shock tables (e.g., reference F1), one can calculate how $P_{o2}/\rho_1 u_1^2$ varies with M_1 for a given γ. Figure F-2 is a plot of $P_{o2}/\rho_1 u_1^2$ versus M_1 for $\gamma = 1.2$, 1.3 and 1.4. For a given γ, as $M_1 \to \infty$, $P_{o2}/\rho_1 u_1^2$ approaches a limiting value given by

$$\frac{P_{o2}}{\rho_1 u_1^2} \xrightarrow[M_1 \to \infty]{} \frac{2}{\gamma + 1}\left[1 + \frac{(\gamma - 1)^2}{4\gamma}\right]^{\gamma/\gamma - 1} \qquad \text{(F-4)}$$

In particular,

$$\frac{P_{o2}}{\rho_1 u_1^2} \xrightarrow[M_1 \to \infty]{} \begin{cases} 0.9555 & \gamma = 1.2 \\ 0.9367 & \gamma = 1.3 \\ 0.9197 & \gamma = 1.4 \end{cases} \qquad \text{(F-5)}$$

From figure F-2 it is seen that for a given γ, if M_1 is large enough (say greater than five), then $P_{o2}/\rho_1 u_1^2$ is practically independent of M_1 and is given essentially by the limiting values in equation F-5. Moreover, if $M_1 < 5$ but not too small, then $P_{o2}/\rho_1 u_1^2$ while dependent on M_1 increases towards unity as M_1 decrease. The Mach number at which $\frac{P_{o2}}{\rho_1 u_1^2}$ is unity depends on γ; in general as γ decreases, the higher the Mach number for which $P_{o2}/\rho_1 u_1^2$ is unity. As an example, for $\gamma = 1.3$, if $M_1 \geq 1.7$, then $\rho_1 u_1^2$ equals P_{o2} to within 7 percent. Various theoretical models of the expansion in the nozzle indicate that the effective γ is in the range 1.3 to 1.4 and the exit Mach number is in the range 2.5 to 4 for the typical nozzle geometries. Thus the Avco arc-jet engine operates in the range of exit Mach numbers where the impact pressure profiles at the nozzle exit plane can be converted into a momentum-flux profile to an accuracy of about 10 percent. If M_1 can be measured directly, or a good theoretical model of the flow in the nozzle developed, then this accuracy can be improved.

It is necessary to discuss briefly to what extent the above conclusions are affected when the propellant is at a temperature such that chemical reactions are occurring and γ is not constant across a shock. Experience has shown that the stagnation pressure downstream of a shock is insensitive to chemical effects. This has been verified for a particular case which is representative of the normal operating conditions of the Avco arc-jet engine.

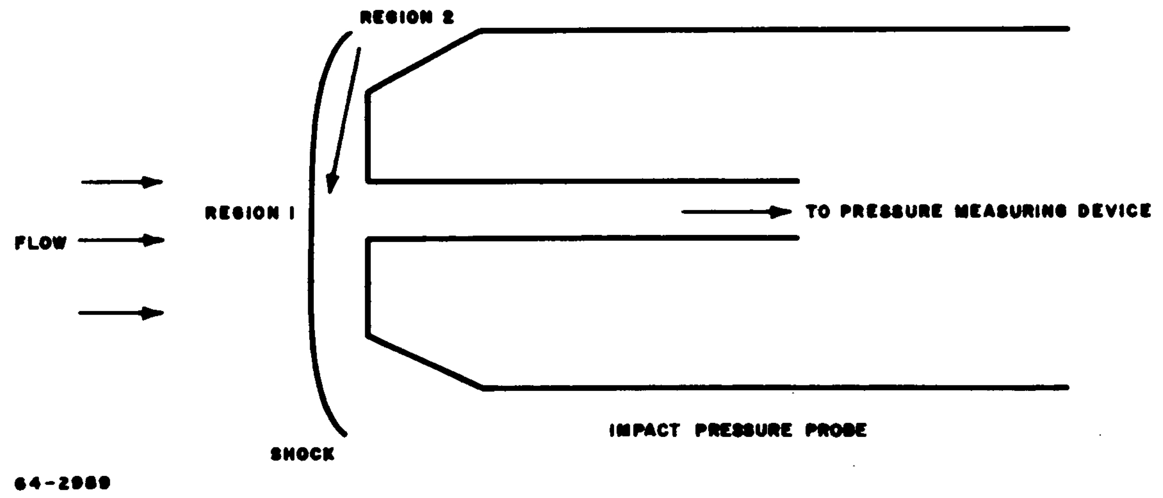
REGION 2
REGION I
FLOW
TO PRESSURE MEASURING DEVICE
IMPACT PRESSURE PROBE
SHOCK
64-2989

Figure F-1 REPRESENTATION OF IMPACT PRESSURE PROBE IN SUPERSONIC STREAM

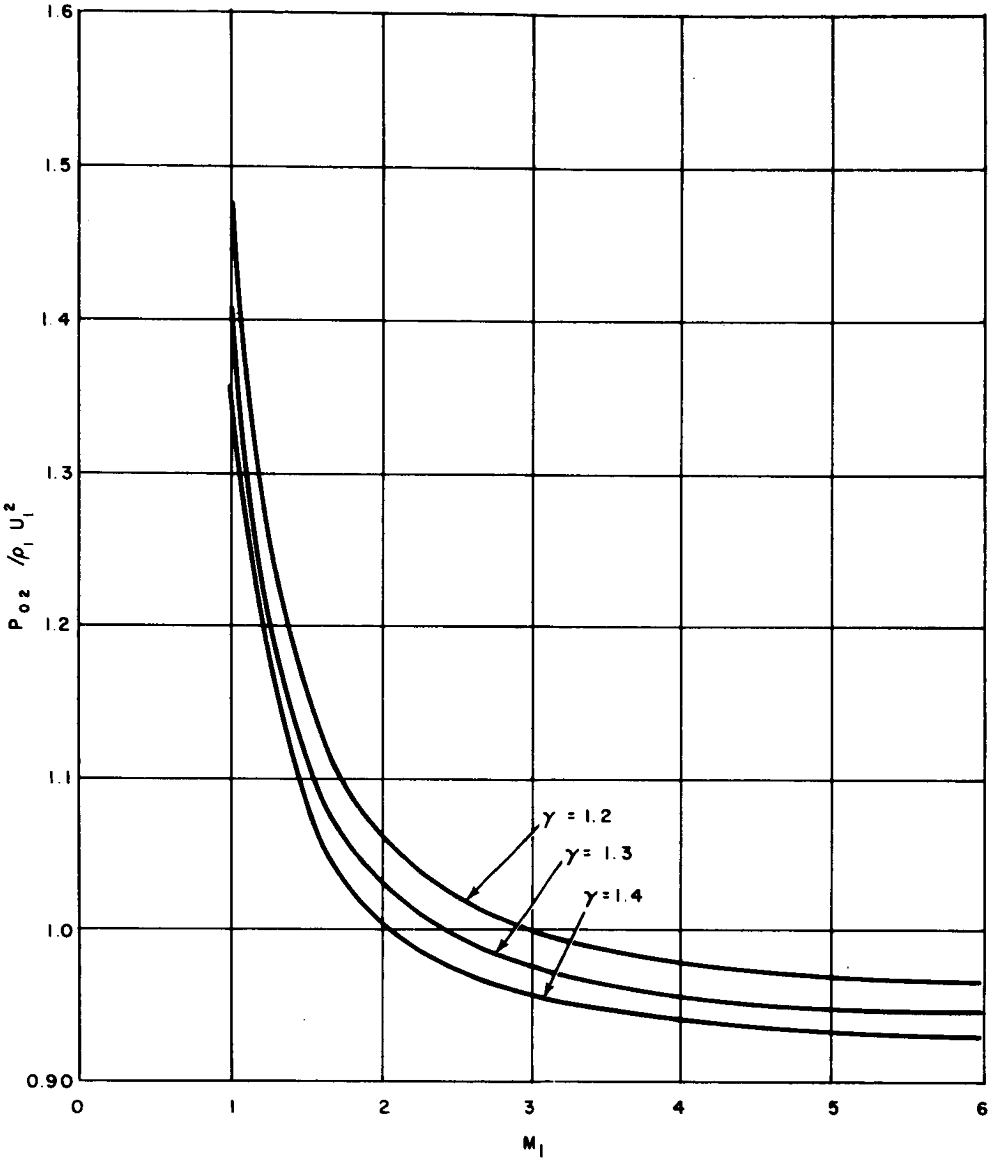

Figure F-2 PLOT OF $P_{02}/{}_1 u_1^2$ VERSUS M_1

The test calculation proceeds as follows. A set of throat conditions is derived, based on a one dimensional model of the flow in the constrictor. This model, is admittedly crude because of the large radial variation in velocity, temperature and density. However, certain predictions of the one-dimensional model have been found to be approximately correct and for the purposes of this calculation such an approach is adequate.

The throat conditions are determined by assuming the flow is sonic and in equilibrium. The following equations must be satisfied:

$$\dot{m} = \rho U^* A \qquad (F\text{-}6)$$

$$h_o = \frac{\text{Power in Flow at Throat}}{\dot{m}} \qquad (F\text{-}7)$$

$$h_o = h + \frac{U^{*2}}{2} \qquad (F\text{-}8)$$

$$U^{*2} = \left(\frac{\partial\, ln P}{\partial\, ln P}\right)_{\text{entropy}} \frac{P}{\rho} \qquad (F\text{-}9)$$

$$f(P, T) = 0 \text{ (Equation of state)} \qquad (F\text{-}10)$$

$$h = h(T, P) \qquad (F\text{-}11)$$

where

$\dot{m}$ = mass flow rate

h_o = stagnation enthalpy at throat

h = static enthalpy at throat

U^* = sound speed at throat

P = pressure at throat

ρ = density at throat

T = temperature at throat

A = area of throat

It is assumed that $\dot{m}$, A and the power at the throat are given. The remaining six unknowns, h_o , h , P , ρ, T and U^* are determined by solving equations (F-6) through (F-11). This has been done numerically using the appropriate thermochemical tables which provide the equation of state and the enthalpy as a function of temperature and pressure.

A solution for the case $\dot{m} = 0.25$ gm/sec H_2, $A = 0.114$ cm^2 and a power at the throat of 27 kw is given in table F-1.

TABLE F-1

Throat Conditions for One Dimensional Model

$P = 0.815$ atm

$h = 9.85 \times 10^{11}$ erg/gm $= 23.5$ kcal/gm

$h_o = 1.08 \times 10^{12}$ erg/gm $= 25.8$ kcal/gm

$U^* = 4.31 \times 10^5$ cm/sec

$\rho = 5.08 \times 10^{-6}$ gm/cm^3

$T = 3295°$ k

The throat conditions in table F-1 are used to generate the flow conditions at the nozzle exit plane. This is done by assuming an isentropic expansion in the nozzle using the "frozen" ratio of specific heats, γ_f, which for the solution given in table F-1 has the value $\gamma_f = 1.347$. The use of γ_f is the assumption that the composition is constant in the supersonic nozzle due to the rapid expansion of the flow.

The calculated exit plane conditions are given in table F-2.

TABLE F-2

Nozzle Exit Plane Conditions for $\gamma = 1.347$ and Throat Conditions in table I

$P_1 = 0.0150$ atmosphere
$u_1 = 9.348 \times 10^5$ cm/sec
$\rho_1 = 2.617 \times 10^{-7}$ gm/cm^3
$h_1 = 6.408 \times 10^{11}$ erg/gram $= 15.31$ kcal/gm
$T_1 = 1177°K$
$M_1 = 3.63$

To relate flow conditions downstream of the normal shock (subscript 2) to flow conditions immediately upsteam of the shock (table F-2), the conservation equations for a normal shock must be satisfied. They are:

$$\rho_1 u_1 = \rho_2 u_2 \qquad \text{Conservation of mass}$$

$$P_1 + \rho_1 u_1^2 = P_2 + \rho_2 u_2^2 \qquad \text{Conservation of momentum}$$

$$h_1 + \frac{u_1^2}{2} = h_2 + \frac{u_2^2}{2} \qquad \text{Conservation of energy}$$

$$f(P_2, T_2) = 0 \qquad \text{Equation of state}$$

Solving these equations numerically assuming equilibrium after the shock gives $P_2 = 0.192$ atmosphere, $h_2 = 25.25$ kcal/gm, $u_2 = 2.025 \times 10^5$ cm/sec, $M_2 = 0.476$, $\gamma_2 = 1.242$ and the entropy is 30.58 cal/gm-°K. To find the pressure resulting from bringing the flow isentropically to rest, P_{o2} is determined by moving along the entropy line 30.58 cal/gm-°K to the point where the total enthalpy is 25.76 kcal/gm. Using the thermochemical tables it is found that $P_{o2} = 0.2165$ atmosphere. Hence, it is found that for this example, $\frac{P_{o2}}{\rho_1 u_1^2} = 0.959$. If the calculation, is performed for the same Mach number, $M_1 = 3.63$, but assuming no chemical effects, i.e., γ is constant across the shock and during the isentropic deceleration to rest, it is found that for $\gamma = 1.347$, $\frac{P_{o2}}{\rho_1 u_1^2} = 0.955$. Thus for this example there is a change of about 0.5 percent due to chemical effects.

2. GENERAL DESIGN CONSIDERATIONS

In designing an impact pressure or ρu^2 probe for probing the nozzle exhaust of the Avco arc-jet engine, certain requirements must be met. To see what these requirements are, it is necessary to look at certain geometrical consideration which are shown in figure F-3. The Avco arc-jet nozzle has a (diverging) half-angle of 7 degrees and an exit plane diameter D_o of approximately 1 centimeter or slightly less than 1/2 inch.

For the detached shock to appear normal over the extent of the probe entrance tube D_a should be two or three times larger than D_i. To get good spatial resolution, it is required that $D_i << D_o$. However, D_i cannot be too small for the assumption of continuum flow requires that $D_i >> \lambda$ where λ is the average mean free path of the gas particles. A calculation shows that for conditions at the nozzle exit plane, λ is of the order of 0.01 cm for hydrogen Another requirement is that the Reynolds number not be too low so that viscous effects do not disturb the impact pressure measurement (see reference F-2); the Reynolds number in the supersonic stream is estimated to be approximately 500, using 1 centimeter as the reference length.

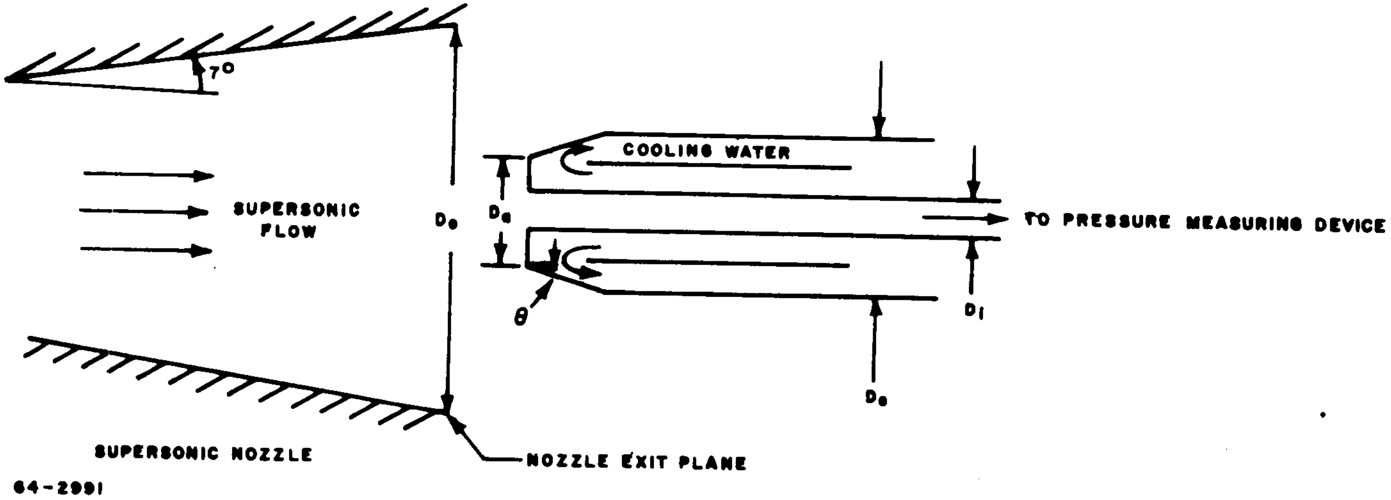
7°
SUPERSONIC FLOW
D_e
D_a
θ
COOLING WATER
TO PRESSURE MEASURING DEVICE
D_i
D_o
SUPERSONIC NOZZLE
NOZZLE EXIT PLANE
64-2991

Figure F-3 GEOMETRICAL CONSIDERATIONS IN DESIGN OF IMPACT PRESSURE PROBE

The diameter D_e should be sufficiently smaller than D_o so that the disturbance created by the presence of the probe in the flow is as small as possible. If the diameter of the front surface of the probe D_a is smaller than D_e and the probe tip is shaped like a truncated cone with a diverging angle θ of 15 to 20 degrees, the tendency of the probe to block the flow when it is in the outer radial positions (near the nozzle wall) is reduced.

Since the probe is to be water-cooled, the cross-sectional area available for water flow is small (approximately $\frac{\pi}{4}(D_e^2 - D_i^2)$) and high pressures are required to secure enough cooling for the probe to withstand the severe environment within the nozzle exhaust. This in turn means that the actual fabrication of the probe is complicated.

The tip portion of the probe that has been used for the impact pressure measurements is shown in figure 56. Using the notation of the previous discussion (see figure F-3), $D_i = 0.059$ inches, $D_a = 0.243$ inch, $D_e = 0.312$ inch and $\theta = 20$ degrees. The tip of the probe has been made of either molybdenum or copper. A thinner heat transfer surface at the front has been obtained with copper plus the advantage that a more reliable internal braze is obtained at the joint joining the copper tip to the stainless steel tube than with the molybdenum tip (see figure 56). It was found that using a line pressure of about 220psig., a water flow of about 1.6 gallons per minute is obtained and this permitted the probe to withstand the hottest portion of the exhaust (central portion) for a period of about 5 seconds when the engine was operated at a power level of 25kw and a mass flow rate of 0.20 gm/sec H_2.

To summarize, probing the exhaust of the Avco arc-jet engine presents two main problems. The small exit diameter of the nozzle requires that the probe be small so as not to unduly disturb the flow and to give adequate resolution. On the other hand, the requirement of a small probe and a high cooling rate capacity gives rise to fabrication problems.

Reference:

F-1 NACA Report 1135, Equations, Tables and Charts for Compressible Flow (1953).

F-2 Sherman, F. S., NACA Technical Note 2995 (1953).

APPENDIX G

MASS FLOW PROBE

1. DESIGN CONSIDERATIONS

The mass flux probe tip geometry is quite different from that of the impact pressure probe. Instead of being blunt the probe tip is streamlined as shown in figure G-1. The basic idea behind this type of probe is that when valve 1 is opened, the low pressure in the collecting tank causes the bow shock standing in front of the probe tip to be swallowed, producing oblique conical shocks emanating from the probe tip edge. To ensure that the probe is intercepting a streamtube equal to the orifice area, it is necessary that the edge of the probe tip entrance tube be sharp; if the edge were too blunt, then detached bow shocks would form, deflecting part of the streamtube away from the probe. The sharp edge is particularly vulnerable to the high temperature environment in the nozzle exhaust for it is difficult to place the cooling passages close enough to the edge to carry away the high local heat flux.

It is of paramount importance for the operation of the probe that the shock be swallowed. This requirement imposes geometrical restraints of the same general character as mentioned in the discussion of the impact pressure probe. The entrance tube diameter must not be too small so that boundary layer effects impede the shock from being swallowed while if it is too large the resolution is poor. The probe should not unduly affect the stream during the measurement while a probe with a small outside diameter is difficult to cool.

2. ASSOCIATED EQUIPMENT

To measure the mass of gas passing through the probe, a collecting tank with two valves is used. (See figure G-1) The valves are of the solenoid type and open in about 0.015 second. The time interval that valve 1 is open is adjusted by a mechanical counter; the time interval is measured with a binary electronic timer to 0.001 second. The pressure in the collecting tank is measured with a 0 to 20 mm Hg absolute pressure gage. The collecting tank has a volume of 4630 cm^3 and is situated inside the test tank but is located such that it is not directly exposed to radiation from the hot engine. In addition, the collecting tank is water-cooled so that the gas in the tank is the temperature of the cooling water.

If the pressure in the collecting tank, p_f, is close to the pressure obtained by leaving the valve open indefinitely, $p_f{}^*$, (approximately the impact pressure) then the mass flow to the collecting tank is not linearly proportional to p_f. Experimentally it has been found that if $p_f / p_f{}^* \leq 0.3$ to 0.4 the mass flow through the probe is essentially not affected by the pressure buildup in the collecting tank. It is found that for the size of the collecting tank and the size of the entrance tube of the probe (0.060 to 0.100 inch) this leads to a time interval of 1-2 seconds during which valve 1 is open.

The mass-flux probe is inserted into the exhaust stream during the actual measurement and withdrawn after the measurement. The same insertion apparatus is used for the mass-flux probe as for the impact-pressure probe and has been previously described.

3. PROBE FABRICATION

During the course of the diagnostic program, the mass flux probe went through several stages of evolution. The first attempt at a mass flux probe used a removable carbon tip. The idea here was that this is the easiest and quickest type of probe to fabricate and it was felt that this approach should be followed to see if a mass flux probe could be made to work satisfactorily. Although the main body of the probe was water-cooled, the tip itself was not and it was found that even at an operational power level of 20 kw the carbon tips were damaged when measurements were taken in central portion of the exhaust jet. This necessitated the replacement of the damaged tip for every measurement; this entailed stopping the engine, removing the vacuum from the test tank, opening the test tank, inserting the new probe tip, reestablishing the position of the probe tip, closing the test tank, pumping down the test tank and restarting the engine. It was found that the integrated value of the mass flux profile at the nozzle exit plane agreed with the mass flow rate to the engine as measured by the flow meter to within 10-15 percent. Measurements were also made under cold flow conditions with axial injection of the propellant where it was possible to establish a satisfactory analytical check for a pointwise measurement rather than comparing through an integrated profile. On the basis of these results, it was felt that the mass flux probe would work satisfactorily.

From that point on, the main effort was directed toward fabricating a probe tip that could withstand the severe environment found in the nozzle exhaust without suffering damage and hence could be used for repeated measurements.

This goal led to a probe with a molybdenum tip, brazed to the copper afterbody on the outside and to a stainless steel internal gas tube on the inside (see figure G-2). It was found that this probe failed due to melting at the probe tip. It was felt that the failure was due to the large distance (≈ 0.2 inch) between the front edge of the tip and the closest distance cooled by the water.

The next effort was to decrease this distance by going to a large cone angle (40 degrees; this probe tip is shown in figure G-3). For this probe the distance from the front edge of the probe tip to the cooling water was reduced to about 0.080 inch. Upon testing this design it was found that the probe failed but not due to tip melting but rather due to a failure in the braze joining the molybdenum tip to the stainless steel gas tube.

Another probe was made where copper was used for the tip rather than molybdenum; this probe had a cone angle of 20 degrees and is shown in figure G-4. This probe also failed but again the failure was at the brazed joint.

These two failures led to changing the material of the gas tube from stainless steel to copper. Another probe was built, similar to that shown in figure G-4, but with a copper gas tube having a diameter of 0.090 inch. It was found that upon testing, the probe failed in the central portion of the nozzle exhaust due to local melting of the probe tip edge. Hence, to obtain measurements in this region, recourse was made to the removable carbon tip probe. When the carbon tip probe was used, a measurement of the diameter of the probe tip opening was made before and after a data point along with the mass lost from the tip during its exposure to the nozzle exhaust.

4. TEST PROCEDURE

The procedure during a set of profile measurements is as follows. The probe is centered with respect to the nozzle exit plane using a specially made jig which permits the location of the probe at the geometrical center-line of the nozzle exit plane to within a few thousands of an inch. The probe tip is located at a distance of about 0.050 inch downstream of the nozzle exit plane. A "point" on the profile is obtained by inserting the probe into the exhaust stream, using the probe insertion unit described in the discussion of the impact pressure probe, and immediately opening valve 1 (figure G-1) for a time period of approximately one second after which the valve is closed and the probe withdrawn from the exhaust stream. Typically, the probe is in the exhaust stream for about three seconds. The amount of gas intercepted by the probe is reflected by the increase in pressure in the collecting tank (figure G-1): the initial (low) pressure in the tank is measured; it is established by means of a separate vacuum system and is typically a few tenths of a millimeter of mercury. Experiments showed that no discernible difference in a measurement was detected when the collecting tank was evacuated to the same pressure as the collecting tank. This indicates that the impact pressure is sufficiently high (even in the boundary layer) that the small amount of flow due to having the collecting tank pressure (0.2 mm H_g) lower than the ambient pressure in the test tank is negligible.

The collecting tank is water-cooled and is in a shadow as far as exposure to radiation from the hot engine and exhaust jet is concerned. Before the measurement the gas in the tank is at essentially the temperature of the cooling water and after the measurement, the gas has the same temperature if a sufficient length of time has elapsed.

The mass of gas collected is given by

$$m = \frac{MV}{RT}(P_f - P_i)$$

where M is the gram molecular weight of the propellant, V is the volume of the collecting tank, R is the universal gas constant, T is the temperature of the water cooling the collecting tank and P_f and P_i are the final and initial pressure of the collecting tank.

The mass flow rate $\dot{m}$ is the mass of gas collected divided by the length of time, t , that valve 1 is open. It is necessary that P_f be small compared to the impact pressure at the radial position in the exhaust stream under consideration so that for a given P_i , P_f is approximately linear with t. Then the local mass flux ρu is given by $\underline{\dot{m}}$ where A is the area of the probe tip orifice.

After each such measurement, the probe tip is moved a known amount by means of the probe insertion unit in preparation for a measurement at a different radial position in the nozzle exhaust stream. At the end of the run, the probe tip is returned to the center-line as indicated by the counters on the probe insertion unit and this centerline position is checked using the centering jig.

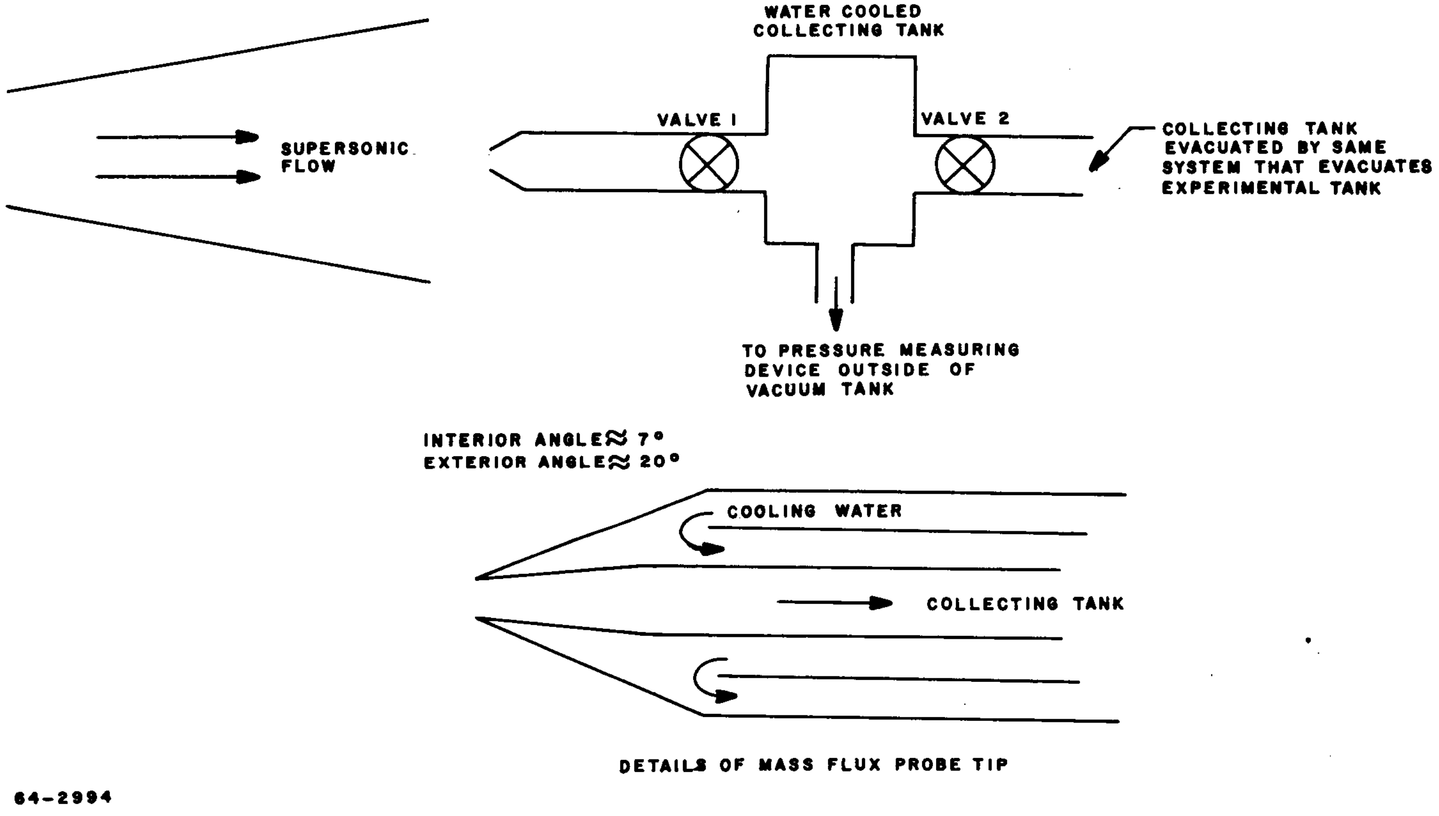
WATER COOLED
COLLECTING TANK
SUPERSONIC
FLOW
VALVE 1
VALVE 2
COLLECTING TANK
EVACUATED BY SAME
SYSTEM THAT EVACUATES
EXPERIMENTAL TANK
TO PRESSURE MEASURING
DEVICE OUTSIDE OF
VACUUM TANK
INTERIOR ANGLE ≈ 7°
EXTERIOR ANGLE ≈ 20°
COOLING WATER
COLLECTING TANK
DETAILS OF MASS FLUX PROBE TIP
64-2994

Figure G-1 SCHEMATIC DRAWING OF MASS FLUX PROBE AND ASSOCIATED EQUIPMENT

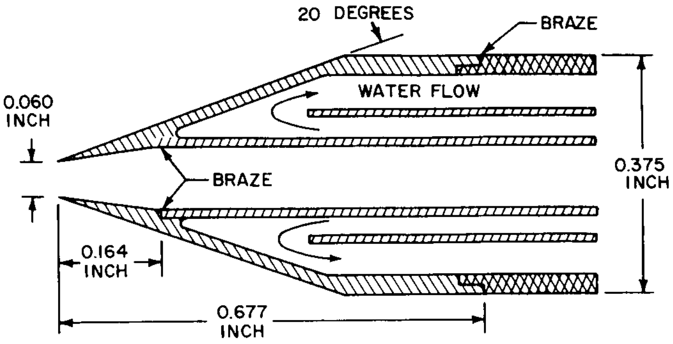
20 DEGREES
BRAZE
WATER FLOW
0.060
INCH
0.375
INCH
BRAZE
0.164
INCH
0.677
INCH

Figure G-2 MASS FLUX PROBE TIP GEOMETRIES

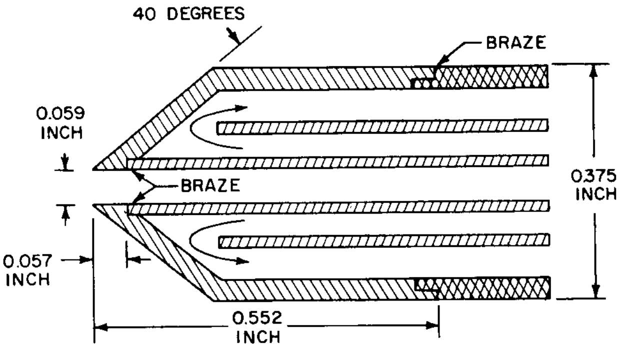
40 DEGREES
BRAZE
0.059
INCH
BRAZE
0.375
INCH
0.057
INCH
0.552
INCH

Figure G-3 MASS FLUX PROBE TIP GEOMETRIES

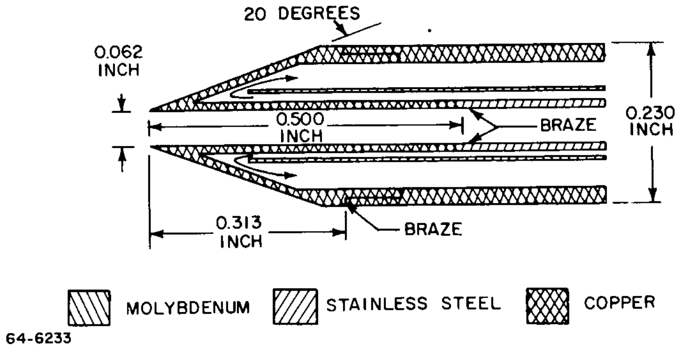
20 DEGREES
0.062
INCH
0.500
INCH
BRAZE
0.230
INCH
0.313
INCH
BRAZE
MOLYBDENUM
STAINLESS STEEL
COPPER
64-6233

Figure G-4 MASS FLUX PROBE TIP GEOMETRIES

APPENDIX H

NONEQUILIBRIUM IN NOZZLE EXHAUST

An analysis of the flow through the Avco arcjet engine shows that some dissociation and ionization nonequilibrium is to be expected in the nozzle exhaust. In simple terms, this nonequilibrium occurs because the residence time is much shorter than the recombination time. Because energy is unavoidably invested in dissociating and ionizing the propellant, the lack of dissociative and ionization equilibrium gives rise to a power loss which is termed the frozen flow loss. Hence it is of interest in terms of ascertaining the propulsive efficiency and thrust potential of the Avco arcjet engine to determine the extent of the nonequilibrium in the nozzle exhaust and the accompanying frozen flow loss.

In the discussion of the power balance in the arcjet engine in section III-C, it was pointed out that the velocity and density profiles at the nozzle exit plane are not sufficient information to calculate the thermal and frozen flow power. Here is presented an outline of how the thermal and frozen flow power can be calculated if in addition to the velocity and density profiles, profiles of total (equilibrium) enthalpy, electron concentration and electron temperature at the nozzle exit plane are available. The total enthalpy profile is presumed to be obtainable with an enthalpy probe and the electron concentration and temperature are assumed to be measured using spectroscopic techniques.

In discussing the nonequilibrium flow in the supersonic nozzle, it is useful to think in terms of a specific model. The model that is tenatively advanced has the following details:

1. The propellant is considered to be hydrogen

2. Beyond some axial position in the nozzle, termed the freeze line, the flow is in dissociative and ionization nonequilibrium. However, it is assumed that translational and vibrational equilibrium exists for the heavy particles, H_2 , H and H^+, hydrogen molecule, atom and ion respectively so that a temperature exists for these components of the exhaust gas. In addition, it is assumed that in the radial region where the electron concentration is the greatest (in the vicinity of the center-line of the exhaust) an electron temperature exists. It is remarked that the assumption of vibrational equilibrium for the heavy particles may be unrealistic but the assumption is made here for convenience.

3. In this model it is assumed that the static pressure of the gas mixture is given by the sum of the partical pressures of the heavy particles and the electrons. This assumption deals with the core part of the exhaust where an electron temperature is assumed to exist.

4. The static pressure profile is sufficiently uniform that to a good approximation, it can be considered constant.

The measurements that are considered are:

a. An impact pressure profile which can be translated into the momentum flux, ρu^2 where ρ is the density and u is the velocity.

b. A mass flux profile which yields ρu

c. A total (equilibrium) enthalpy profile

d. Spectroscopic measurements to yield profiles of the electron temperature and electron concentration. These profiles are to be obtained at the nozzle exit plane.

The (constant) static pressure P, can be determined by varying the ambient pressure of the test tank until the exhaust jet appears neither underexpanded or overexpanded. When this condition is reached, the static pressure at the nozzle exit plane is equal to the ambient pressure in the test tank.

From these measurements, then, the following quantities are determined as a function of radial position.

$$\left.\begin{array}{lcl} \rho(r) & = & \text{gas density} \\ u(r) & = & \text{gas velocity} \\ h_t(r) & = & \text{total equilibrium enthalpy} \\ T_e(r) & = & \text{electron temperature} \\ n_e(r) & = & \text{electron number density} \\ P & = & \text{static pressure} \end{array}\right\} \text{nozzle exit plane} \qquad \text{(H-1)}$$

It will now be shown that these above known quantities and the assumed model of the nozzle flow imply a gas temperature T for the heavy particles and the composition at the nozzle exit plane. This in turn permits calculation of the magnitude of the various forms (kinetic, thermal, and frozen flow) of the nozzle power flux.

The power flux in the nozzle exhaust at the radial position r is given by

$$\rho u h_t = \frac{\rho u^3}{2} + \frac{n_H A u}{2} + n_e B u + \frac{\rho_u}{\bar{M}} \Big[\Psi_H M_H h_H + \Psi_{H_2} M_{H_2} h_{H_2}$$

$$+ \Psi_{H^+} M_{H^+} h_{H^+} + \Psi_e M_e h_e \Big] \qquad \text{(H-2)}$$

where the subscripts H, H_2 , H+, and e denote hydrogen atoms, molecules, ions, and electrons respectively, n is the number density, Ψ is the mole fraction, M is the gram molecular weight, h is the thermal enthalpy and $\bar{M}$ is the average molecular weight of the gas mixture and is given by

$$M = M_H \Psi_H + M_{H_2} \Psi_{H_2} + M_{H^+} \Psi_{H^+} + M_e \Psi_e \tag{H-3}$$

The left-hand-side of equation (H-2), is self-explanatory. The first term on the right-hand-side is the power in the form of kinetic motion. The second term is the power invested in dissociation; the constant A contains the dissociation energy of the hydrogen molecule. The third term is the power invested in ionization; the constant B contains the ionization energy of the hydrogen atom. The last four terms in the right-hand-side of (H-2) make up the thermal power carried in the exhaust, i. e. the power associated with the random motion of the gas particles; there is a term for each of the four types of particles. The terms h_H and h_{H_2} are the enthalpies of the hydrogen atom and molecules and depend only on temperature; the temperature dependence can be found in the JANAF tables.^{H1} The enthalpy of the hydrogen ions, h_{H^+} is given by

$$h_{H^+} = \frac{5}{2} \frac{RT}{M_H} \tag{H-4}$$

where T is the temperature of the heavy particles (H, H_2 and H^+) while the enthalpy of the electrons is given by

$$h_e = \frac{5}{2} \frac{RT_e}{M_e} \tag{H-5}$$

where T_e is the temperature of the electrons.

It is to be noticed that in equation (H-2), the (directed) velocity of all the particles is assumed to be the same. Possibly the only serious objection would concern the electrons. It is noted that with the condition of charge neutrality, a slip velocity between electrons and ions would lead to charge separation with accompanying very strong electric fields.

Substituting equations (H-3), (H-4), and (H-5) into equation (H-2 and noting that $M_{H_2} = 2M_H$, $M_{H^+} \approx M_H$, $M_e << M_H$ and $\Psi_e = \Psi_{H^+}$, gives the result

$$\rho u h_t = \frac{\rho u^3}{2} + n_H u A + n_e u B \tag{H-6}$$

$$+ \rho u M_H \frac{\left[\Psi_H h_H + 2\Psi_{H_2} h_{H_2} + 5/2\, \Psi_e RT/M_H + 5/2\, \Psi_e R T_e/M_e\, M_e/M_H\right]}{M_H (\Psi_H + 2\Psi_{H_2} + \Psi_e)}$$

Dividing by ρu and using the relation that $\Psi_i = n_i/n$ where n is the number density of all particles, equation (H-6) becomes

$$h_t = \frac{u^2}{2} + \frac{1}{\rho}\left(\frac{n_H}{2} A + n_e B\right) + \frac{n_H h_H + 2 h_{H2} + 5/2 \, \frac{n_e R}{M_H} (T + T_e)}{h_{H2} + 2 n_{H_2} + n_e} \qquad \text{(H-7)}$$

The gas density, ρ is given by

$$\rho = m_H (n_H + 2 n_{H_e} + n_e) \qquad \text{(H-8)}$$

where m_H is the mass of the hydrogen atom. Substituting equation (H-8) into equation (H-7) and using the fact that $\frac{R m_H}{M_H} = \frac{R m_H}{N_o m_H} = k$ where N_o is Avogadro's number and k is the Boltzmann constant, gives the result

$$h_t = \frac{u^2}{2} + \frac{1}{\rho}\left\{ n_H \left(\frac{A}{2} + m_H h_H\right) + 2 n_{H_2} m_H h_{H_2} + n_e [B + 5/2 \, k (T + T_e)] \right\} \qquad \text{(H-9)}$$

Finally, the static pressure is assumed to be given by

$$P = (n_H + n_{H_2} + n_e) k T + n_e k T_e \qquad \text{(H-10)}$$

Considering equations (H-8) to (H-10), the unknows are n_H, n_{H_2} and T for h_H and h_{H_2} are functions only of T. Hence equations (H-8) to (H-10) constitute 3 equations in 3 unknowns and permit the calculation of the gas temperature and number density of H and H_2 at the nozzle exit plane. By comparing the composition so obtained with the equilibrium composition implied by the pressure and the density profile, the extend of nonequilibrium in the nozzle exhaust can be determined. Finally, the kinetic, thermal, dissociation, and ionization components of the nozzle power flux can be calculated.

Reference:

H-1 Dow Chemical Comapny, Midland, Michigan, JANAF Thermochemical Tables.

APPENDIX I

EFFECT OF SUPERSONIC HEAT ADDITION ON ARC-JET ENGINE PERFORMANCE

The configuration of typical arc jet propulsion device is shown in figure I-1. Experiments with such devices have indicated that the arc can be expected to attach to the wall of the nozzle downstream of the sonic point in the diverging section. Therefore some portion of the total power supplied to the propellant is introduced in the supersonic stream. Since heat addition to a supersonic stream, in the absence of other effects, causes a decrease in velocity and Mach number, it can be expected that the exit velocity with such heat addition to the supersonic flow will be less than in the case when the same total power is provided upstream of the sonic point. This memo presents expressions based on a one dimensional analysis for the decrease in exit velocity and specific impulse under such conditions. A calculation for a typical case is also presented.

The equation governing flow with area variation and heat addition is, according to Shapiro:[I1]

$$dM^2 = F_A \frac{dA}{A} + F_{To} \frac{dTo}{To} \qquad \text{(I-1)}$$

where F_A and F_{To} are influenced coefficients for area change and stagnation temperature change respectively:

$$F_A = - \frac{2M^2 \left(1 + \frac{\gamma - 1}{2} M^2\right)}{1 - M^2}$$

$$F_{To} = - \frac{M^2 (1 + \gamma M^2) \left(1 + \frac{\gamma - 1}{2} M^2\right)}{1 - M^2}$$

Constant γ and molecular weight have been assumed.

The area of the diverging section may be written as the following function of downstream distance (see figure I-1):

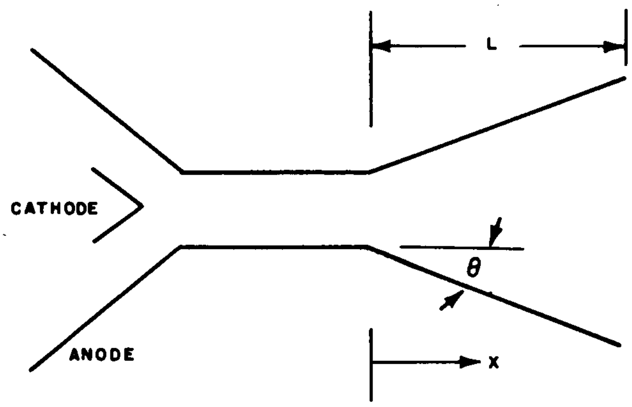
L
CATHODE
θ
ANODE
X

64-14248

Figure I-1 ARC ENGINE CONFIGURATION

$$A = \frac{\pi}{4}\left(\sqrt{\frac{4A^*}{\pi}} + 2\,x\,\tan\theta\right)^2$$

so that:

$$\frac{dA}{A} = \frac{2\tan\theta}{\sqrt{\frac{A^*}{\pi}} + x\tan\theta}\,dx \qquad \text{(I-2)}$$

The stagnation temperature anywhere in the diverging section is assumed to be given by a relation of the form:

$$To = To^* + (To_e - To^*)\left(\frac{X}{mL}\right)^n \qquad 0 \leq x \leq mL$$

$$To = To_e \qquad x > mL$$

where subscript e indicates exit values, * indicates values at the sonic point, L is the length of the channel, and mL is the value of x at which the arc attaches (assumed to be the end of heat addition). Then

$$\frac{dTo}{To} = \frac{(To_e - To^*)\,(n/mL)\,(x/mL)^{n-1}}{To^* + (To_e - To^*)(x/mL)^n}\,dx \qquad 0 \leq x \leq mL \qquad \text{(I-3)}$$

$$\frac{dTo}{To} = 0 \qquad x > mL$$

Substituting (I-2) and (I-3) in (I-1) and dividing by F_A gives:

$$\frac{dM^2}{F_A} = \frac{2\tan\theta}{\sqrt{\frac{A^*}{\pi}} + x\tan\theta}\,dx + \frac{F_{To}}{F_A}\,\frac{\left(To_e - To^*\right)\frac{n}{mL}\left(\frac{x}{mL}\right)^{n-1}}{To^* + (To_e - To^*)\left(\frac{x}{mL}\right)^{n}}\,dx \qquad \text{(I-4)}$$

$$0 \leq x \leq mL$$

$$\frac{dM^2}{F_A} = \frac{2\tan\theta}{\sqrt{\frac{A^*}{\pi}} + x\tan\theta}\,dx \qquad x > mL$$

Integrating equation (I-4) between the limits 0 and L (where $M = 1$ at $x = 0$ and $M = Me$ at $x = L$) gives:

$$\ln \frac{1}{Me}\left[\frac{2\left(1 + \frac{\gamma - 1}{2} Me^2\right)}{\gamma + 1}\right]^{\frac{\gamma+1}{2(\gamma-1)}} = 2\ln \frac{\sqrt{\frac{A^*}{\pi}} + L\tan\theta}{\sqrt{\frac{A^*}{\pi}}} \qquad \text{(I-5)}$$

$$+ (To_e - To^*)\frac{n}{mL}\int_0^{mL} \frac{F_{To}}{F_A}\,\frac{\left(\frac{x}{mL}\right)^{n-1}}{To^* + (To_e - To^*)\left(\frac{x}{mL}\right)^{n}}\,dx$$

The last term must be integrated numerically since it contains functions of both Mach number and distance.

If P is the total power provided to the propellant in kilowatts, then the total heat added per pound of propellant, Q, is $P/1.0548\ w$, where w is the flow rate in lbs/sec. If f now represents the fraction of Q added prior to the sonic point, and if $To_i \approx T_i$ is the temperature at which the propellant is supplied, then the following relations hold:

$$Q = C_p (T_{oe} - T_{oi})$$

$$fQ = C_p (T_o{}^* - T_{oi})$$

$$(1 - f)\, Q = C_p (T_{o_e} - T_o{}^*)$$

$$H_{o_i} = C_p\, T_{o_i} = \text{inlet total enthalpy}$$

Using these relations, (I-5) becomes:

$$\ln \frac{1}{M_e} \left[\frac{2\left(1 + \frac{\gamma - 1}{2} M_e^2\right)}{\gamma + 1} \right]^{\frac{\gamma+1}{2(\gamma-1)}} = 2 \ln \frac{\sqrt{\frac{A^*}{\pi}} + L \tan\theta}{\sqrt{\frac{A^*}{\pi}}} \tag{I-6}$$

$$+ \; (1 - f) \frac{n}{mL} \int_o^{mL} \frac{F_{To}}{F_A} \; \frac{(x/mL)^{n-1}}{f + 1.0548\, Ho_i\, w/P + (1 - f)\,(x/mL)^n} \, dx$$

Solution of equation (I-6) for $f = 1$ gives:

$$\frac{A_e}{A^*} = \frac{1}{Me_1} \left[\left(\frac{2}{\gamma + 1}\right) \left(1 + \frac{\gamma - 1}{2} Me_1^2\right) \right]^{\frac{\gamma+1}{2(\gamma-1)}} \tag{I-7}$$

where subscript 1 indicates $f = 1$.

The ratio of the exit velocity for $f \neq 1$ to the exit velocity which would be obtained with all heat added upstream of the sonic point ($f = 1$) is:

$$\frac{Ve}{Ve_1} = \frac{Me}{Me_1} \sqrt{\frac{Te}{Te_1}} = \frac{Me}{Me_1} \sqrt{\frac{1 + \frac{\gamma - 1}{2} Me_1^2}{1 + \frac{\gamma - 1}{2} Me^2}} \tag{I-8}$$

since T_{o_e} is the same for all cases.

The specific impulse of a rocket engine is given as:

$$I_{SP} = \frac{F}{w} = \frac{\lambda Ve}{g} + \frac{A_e (P_e - P_a)}{w}$$

where

$\lambda = \frac{1}{2} (1 + \cos \theta)$

F = Thrust

w = Weight flow rate (maintained constant under all conditions)

P_a = Ambient pressure

Since w does not change:

$$\frac{\rho_e}{\rho_{e_1}} = \frac{Ve_1}{Ve}$$

Rearranging (I-8):

$$\frac{Te}{Te_1} = \left(\frac{Me_1}{Me}\right)^2 \left(\frac{Ve}{Ve_1}\right)^2$$

Applying the perfect gas relation:

$$\frac{Pe}{Pe_1} = \frac{\rho_e}{\rho_{e_1}} \frac{Te}{Te_1} = \left(\frac{Me_1}{Me}\right)^2 \frac{Ve}{Ve_1} \qquad \text{(I-9)}$$

Forming the ratio of vacuum specific impulses ($P_a = 0$):

$$\frac{I_{SP}}{I_{SP_1}} = \frac{\dfrac{\lambda Ve}{g} + \dfrac{Ae\, Pe}{w}}{\dfrac{\lambda Ve_1}{g} + \dfrac{Ae\, Pe_1}{w}} = \frac{Q\,\dfrac{Ve}{Ve_1} + \dfrac{\rho_e}{\rho_{e1}}}{1 + Q} \qquad \text{(I-10)}$$

where

$$Q = \frac{w \lambda Ve_1}{Ae\, \rho_{e_1} g} = \frac{\lambda Ve_1^2}{R\, Te_1} = \lambda \gamma Me_1^2$$

Combining (I-8), (I-9), (I-10) and the definition of Q gives:

$$\frac{I_{SP}}{I_{SP_1}} = \frac{Me}{Me_1}\,\frac{\lambda\gamma + 1/Me^2}{\lambda\gamma + 1/Me_1^2}\sqrt{\frac{1 + \dfrac{\gamma - 1}{2} Me_1^2}{1 + \dfrac{\gamma - 1}{2} Me^2}} \qquad \text{(I-11)}$$

Thus, once the three parameters, m, n, and f have been specified, knowledge of the arc jet engine configuration (A^*, L, θ) and operating conditions (w, P H_{o_i}, γ) allows the calculation of the exit Mach number from (I-6) for $f \neq 1$ and from (I-7) for f = 1. These values are then used in (I-8) and (I-11) in order to find the desired exit velocity and specific impulse ratios.

The following sample calculation will illustrate the use of the equations. Typical arc jet engine parameters are assumed:

$Ae/A^* = 10$

$A^* = 0.0177$ in^2

L = 1.32 in

$\theta = 7°$

w = 0.25 gm/sec

P = 27 Kw

H_{o_i} = 1200 Btu/lb

$\gamma = 1.6$

In addition, the following input parameters are specified:

$m = 0.5$

$n = 1.0$

These values correspond to the case where the arc attaches half-way between the throat and the exit plane, and the stagnation temperature increases linearly between the sonic point and the point of arc attachment.

Equation (I-6) was written in a finite difference form in order to perform the numerical integration. Subscripts i and f indicate initial and final values of the variables for each interval Δx :

$$\ln \frac{M_i}{M_f} \left[\frac{1 + \frac{\gamma - 1}{2} M_f^2}{1 + \frac{\gamma - 1}{2} M_i^2} \right]^{\frac{\gamma + 1}{2(\gamma - 1)}} - 2 \ln \left[\frac{1 + \sqrt{\frac{\pi}{A^*}}\, x_f \tan\theta}{1 + \sqrt{\frac{\pi}{A^*}}\, x_i \tan\theta} \right]$$

$$= \overline{(F_{To}/F_A)} \; \frac{(1 - f)\,(n/mL)\,(\bar{x}/mL)^{n-1}}{f + (1.0548\, Ho_i\, w/P) + (1 - f)\,(\bar{x}/mL)^n} \; \Delta x$$

where $\bar{x} = \frac{x_f + x_i}{2}$ and $\overline{F_{To}/F_A}$ is the ratio of influence coefficients corresponding to $\bar{M} = (M_f + M_i)/2$. Calculations were performed using the above values with $\Delta x = .2$ in. The results of those calculations are shown in figure (I-2) for several values of f . The values of Mach No. at the nozzle exit were read from figure (I-2) and used in equations (I-8) and (I-11) to produce figure (I-3).

It can be seen that the decrease in both exit velocity and specific impulse is not large for the range of values considered. The specific impulse ratio is greater than the exit velocity ratio due to the increase in exit pressure with decreasing f .

Reference:

I-1 Shapiro, A.H., The Dynamics and Thermodynamics of Compressible Fluid Flow, Vol 1, Ronald Press, New York, 1953.

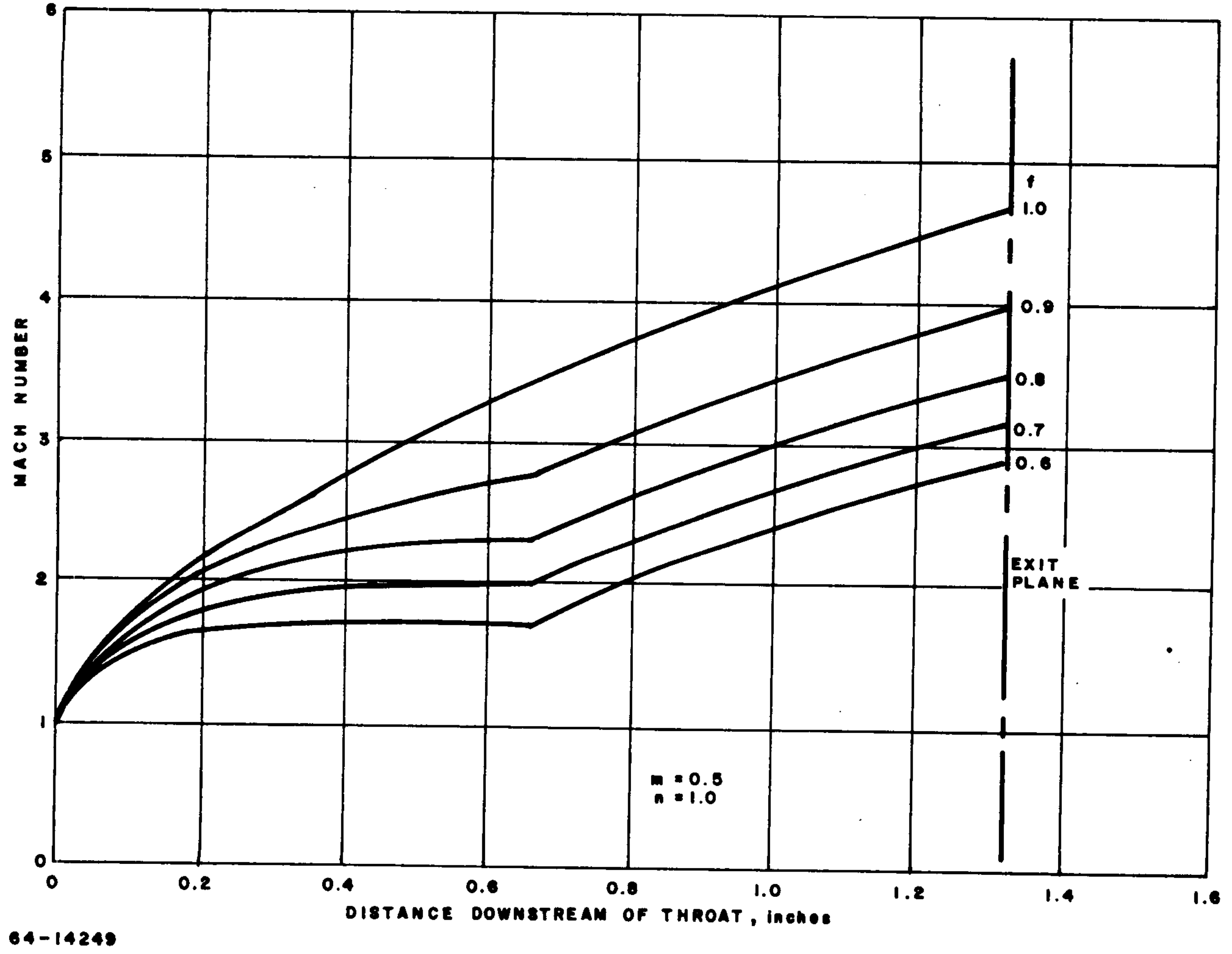

Figure I-2 MACH NO. VERSUS AXIAL POSITION, AS A FUNCTION OF HEATING IN THE SUPERSONIC NOZZLE

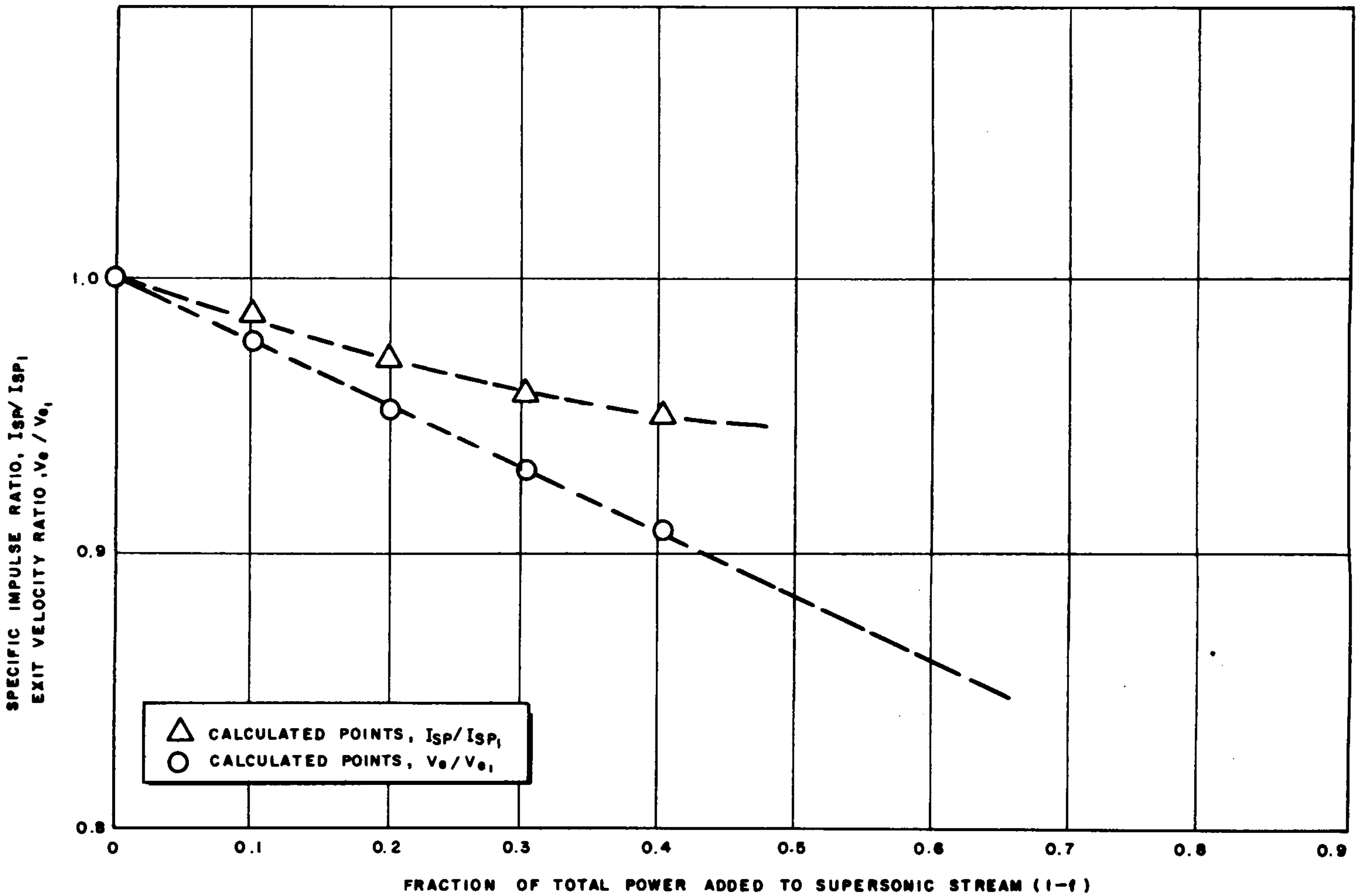

64-14250

Figure I-3 EXIT VELOCITY AND SPECIFIC IMPULSE RATIOS AS A FUNCTION OF HEATING IN THE SUPPERSONIC NOZZLE

DISTRIBUTION

Addressee	No. of Copies
1. NASA-Lewis Research Center Spacecraft Technology Division 21000 Brookpark Road Cleveland, Ohio 44135 Attn: H. Hunczak	6
2. NASA-Lewis Research Center Spacecraft Technology Procurement Section 21000 Brookpark Road Cleveland, Ohio 44135 Attn: John H. DeFord	1
3. NASA-Lewis Research Center 21000 Brookpark Road Cleveland, Ohio 44135 Attn: Library	2
4. NASA-Lewis Research Center Electric Propulsion Laboratory 21000 Brookpark Road Cleveland, Ohio 44135 Attn: J. Jack	1
5. NASA-Lewis Research Center 21000 Brookpark Road Cleveland, Ohio 44135 Attn: Technology Utilization Office	1
6. NASA Headquarters FOB-10B 600 Independence Avenue, N. W. Washington, D. C. Attn: RNT/J. Lazar	2
7. NASA-Ames Research Center Moffett Field, California Attn: Library	1
8. NASA-Ames Research Center Moffett Field, California Attn: Dr. G. Goodwin	1

DISTRIBUTION (Cont'd)

Addressee	No. of Copies
9. NASA-Goddard Space Flight Center Greenbelt, Maryland Attn: W. Isley Bldg. 6, Code 622	1
10. NASA-Marshall Space Flight Center Building 4488 Huntsville, Alabama Attn: Mr. G. Heller	1
11. NASA-Marshall Space Flight Center Building 4488 Huntsville, Alabama Attn: Dan Gates (MS-T)	1
12. NASA Marshall Space Flight Center Huntsville, Alabama Attn: Dr. E. Stuhlinger (M-RP-DIR)	1
13. Commander Aeronautical Systems Division Wright Patterson Air Force Base, Ohio Attn: ASRMPE, F. L'Hommedieu	1
14. Commander Aeronautical Systems Division Wright-Patterson Air Force Base, Ohio Attn: AFAPL (APIE), R. Supp	1
15. Headquarters, USAF Office of Scientific Research Washington 25, D. C. Attn: Dr. M. Slawsky	1
16. United States Army Research Office (Durham) Box CM Duke Station Durham, North Carolina Attn: Dr. P. Kosting	1
17. Jet Propulsion Laboratory 4800 Oak Grove Drive Pasadena, California Attn: G. Robillard	1

DISTRIBUTION (Cont'd)

	Addressee	No. of Copies
18.	NASA-Lewis Research Center Spacecraft Technology Division 21000 Brookpark Road Cleveland, Ohio 44135 Attn: J. H. Childs	1
19.	Gianinni Scientific Corporation 3839 South Main Street Santa Ana, California Attn: Dr. Gabriel Gianinni and Mr. Andriano Ducati	2
20.	Electro-Optical Systems, Inc. 125 North Vinedo Avenue Pasadena, California Attn: Dr's. G. Cann and R. Buhler	2
21.	Thrust Systems Company 1641 Monrovia Costa Mesa, California Attn: W. Stoner	1
22.	NASA Scientific and Technical Information Facility Box 5700 Bethesda, 14, Maryland Attn: NASA Representative RQT-2448	6
23.	AFWL Kirtland Air Force Base, New Mexico Attn: WLPC/Capt. C. F. Ellis	1
24.	The Marquardt Corporation 16555 Saticoy Street Van Nuys, California Attn: Mr. Russell Page	1
25.	General Electric Company Flight Propulsion Laboratories Evendale, Ohio Attn: Dr. M. Bromberg	1

DISTRIBUTION (Concl'd)

Addressee	No. of Copies
26. Space Dynamics Corporation Plasmajet Systems Division 2215 Florence Avenue Cincinnati 6, Ohio Attn: Dr. M. Ghai	1
27. NASA-Lewis Research Center 21000 Brookpark Road Cleveland, Ohio 44135 Attn: Report Control Office	1
28. Aerospace Corporation P.O. Box 95085 Los Angeles, California 90045 Attn: Library Technical Documents Group	1
29. Westinghouse Astronuclear Laboratories Pittsburgh 34, Pennsylvania Attn: H. W. Szymanowski, Manager Electrical Propulsion Laboratory	1
30. NASA Headquarters FOB-10B 600 IndependenceA venue, NW Washington, D. C. 20546 Attention: RNT/J. Mullen	1
31. NASA Marshall Space Flight Center Library Huntsville, Alabama 35812	1
32. NASA Marshall Space Flight Center R-RP-T Bldg. 4488 Huntsville, Alabama 35812 Attention: W. Jones	1
33. NASA Langley Research Center Langley Station Library Hampton, Virginia 23365	1

DISTRIBUTION (Cont'd)

Addressee	No. of Copies
34. NASA Goddard Space Flight Center Library Greenbelt, Maryland 20771	1
35. Aerospace Research Laboratories Wright-Patterson AFB, Ohio 45433 Attention: Mr. Soehngen, Bldg. 45	1
36. Commander Aeronautical Systems Division Wright-Patterson AFB, Ohio 45433 Attention: AFAPL (APIE), P. Lindquist	1
37. AVCO-Everett Research Laboratory Everett, Massachusetts Attention: R.M. Patrick	1
38. Ling-Temco-Vought, Inc. Advanced Systems, Astro. Division Box 6267 Dallas 22, Texas Attention: F.T. Esenwein	1
39. Aerojet General San Ramon, California Attention: Dr. J.S. Luce	1
40. Convair Mail Zone 6-181 San Diego, California Attention: Dr. F. Boynton	1
41. Philco Corporation Newport Beach, California Attention: R. Spongberg ATC	1
42. McDonnell Aircraft Corporation Box 516 St. Louis 66, Missouri Attention: Dr. W. van Camp	1

DISTRIBUTION (Concl'd)

Addressee	No. of Copies
43. Department of Mechanical Engineering University of Minnesota Minneapolis, Minnesota Attention: Dr. E. Ecker	1
45. Thorpe Arc-Flame Assoc., Inc. Concord, New Hampshire Attention: Mr. M. Thorpe, Pres.	1
46. Institute of Plasma Physics c/o Max Planck Institute Munich/Garching, Germany Attention: W. von Jashowsky	1
47. Grumman Aircraft Eng. Company Thermodynamics & Propulsion Section Plant No. 5 Bethpage, New York Attention: I. Tobias	1
48. General Dynamics/Astronautics P.O. Box 1128 San Diego, California Attention: Dr. T. Gooding	1
49. Los Alamos Scientific Laboratories Los Alamos, New Mexico Attention: Dr. T. S. Stratton	1
50. NASA Langley Research Center Langley Station Hampton, Virginia Attention: Mike Ellis	1
51. Central Files	1
52. Research Library (+1 reproducible)	35